Characterization of the circulation around, above and across (through fracture zones) the Reykjanes Ridge

Tillys Petit

UNIVERSITE SCIENCES BRETAGNE DE LA MER LOIRE ET DU LITTORAL

UBO
Université de Bretagne Occidentale

THESE DE DOCTORAT DE

L'UNIVERSITE
DE BRETAGNE OCCIDENTALE
COMUE UNIVERSITE BRETAGNE LOIRE

ECOLE DOCTORALE N° 598

Sciences de la Mer et du Littoral
Spécialité : *Océanographie Physique et Environnement*

Par

Tillys PETIT

Caractérisation de la circulation autour, au-dessus et à travers (via des zones de fracture) la dorsale de Reykjanes

Thèse présentée et soutenue à Brest, le 15 Novembre 2018
Unité de recherche : IFREMER, UFR Brest, CNRS, IRD, Laboratoire d'Océanographie Physique et Spatiale (LOPS), IUEM

Rapporteurs avant soutenance

Gilles REVERDIN Directeur de recherche, CRNS, LOCEAN
Achim WIRTH Directeur de recherche, CNRS, LEGI

Composition du Jury

Alain COLIN DE VERDIERE
Professeur d'université, UBO, LOPS / *Président*
Gilles REVERDIN
Directeur de recherche, CRNS, LOCEAN / *Rapporteur*
Achim WIRTH
Directeur de recherche, CNRS, LEGI / *Rapporteur*
Pascale BOURUET-AUBERTOT
Professeur, Sorbonne Université, LOCEAN / *Examinateur*
Sophie CRAVATTE
Chargé de recherche, IRD, LEGOS / *Examinateur*
Herlé MERCIER
Directeur de recherche, CNRS, LOPS / *Directeur de thèse*
Virginie THIERRY
Chercheur, IFREMER, LOPS / *Co-directeur de thèse*

Remerciements

Je tiens à remercier IFREMER et la Région Bretagne pour avoir financé ma thèse dans le cadre du projet RREX, mais aussi toutes les personnes qui m'ont accompagnée et en ont fait une aventure passionnante.

Tout d'abord, je tiens particulièrement à remercier Herlé Mercier et Virginie Thierry pour m'avoir soutenue pendant ces 3 années, pour leur disponibilité permanente, pour m'avoir fait confiance dans ce projet et pour avoir été présent dans les moments importants. La mission en mer restera une expérience inoubliable et particulièrement enrichissante. J'ai beaucoup de chance d'avoir appris à leur côté, ils ont su me faire aimer le monde de la recherche et je les en remercie.

Ensuite, je veux remercier chaleureusement toute l'équipe du laboratoire que j'ai eu le plaisir de côtoyer pendant mes travaux, chercheurs, techniciens et secrétariat, pour leur aide et leur bonne humeur au quotidien.

Enfin, je remercie toutes ces personnes extérieures, parents et amis, pour leur soutien indéfectible et précieux.

Contents

1 Introduction

1.1 Role of the North-Atlantic Ocean on the climate system

The global ocean largely governs the climate system by being a major sink for carbon dioxide over more than 70% of the Earth surface. Because it stores as well more than 90% of the excess of atmospheric heat caused by the actual human activity, the global ocean is crucial to regulate the climate. In a context of global warming, it is recognized that climate change has direct impacts on our societies and environments, which fosters our interest in better characterizing the heat uptake and storage of anthropogenic carbon dioxide by the oceans. The Intergovernmental Panel on Climate Change (IPCC, 2013) report suggests a slowdown of this carbon storage by the inhibition of convection areas at high latitudes, and highlights the roles of the North-Atlantic Ocean and Southern Ocean in the storage of anthropogenic carbon dioxide at depth.

As part of the ocean circulation, the meridional overturning circulation (MOC), also known as the *Great Conveyor Belt* (Figure 1.1), is the primary mechanism for storage and meridional transport of heat, freshwater and other substances involved in the ocean primary productivity (Lozier, 2010). The MOC is driven by large-scale meridional gradients in density between the high and low latitudes that are formed by air-sea buoyancy exchanges and by wind-driven upwelling around Antarctica. While the salinity field decreases by precipitation and sea ice melting in the Polar Regions, it increases by evaporation in the Tropical Regions.

In the North-Atlantic Ocean, the MOC is characterized by a northward transport of warm and salty upper-waters toward the Polar Regions, and is balanced by a compensating southward transport of cold and fresh lower-waters toward the Equator. In the northern North-Atlantic Ocean, horizontal wind-driven ocean circulation, which is known as the North-Atlantic SubPolar Gyre (NASPG), is superimposed to the vertical circulation of the MOC. The

NASPG is characterized by a cyclonic circulation pattern that extends roughly from 50°N to 65°N and between Europe and North America. The northward warm and salty upper-waters of the MOC are deflected eastward at mid-latitudes by the wind stress curl such that they first join the Eastern Basin and then continue northward (Figure 1.2). The combined horizontal and vertical circulations of the MOC and NASPG set the sea surface temperature of the North-Atlantic (Delworth et al., 2007; Knight et al., 2005; Robson et al., 2012; Yeager et al., 2012), which impacts the summer climate over Europe and North America, as well as weather phenomena such as hurricane activity over the eastern coast of North America (Knight et al., 2006; Smith et al., 2010; Sutton & Hodson, 2005; Zhang & Delworth, 2006). As a consequence, the scientific community pays particular attention in better understanding the northern North-Atlantic circulation and its dynamical processes.

In section 1.2, we first detail the main branches of ocean circulation in the subpolar North-Atlantic. The water masses formed in the northern North-Atlantic Ocean are presented in section 1.3. Then, we focus on the impacts of the bottom topography on the ocean circulation and give examples of well-documented interactions in the North-Atlantic Ocean (section 1.4). By reviewing these sketchy circulations and dense water mass formation in the vicinity of the Reykjanes Ridge, we highlight our lack of knowledge about the impacts of the Reykjanes Ridge on the ocean circulation and properties (section 1.5). We finally introduce the main questions of the PhD thesis in section 1.6.

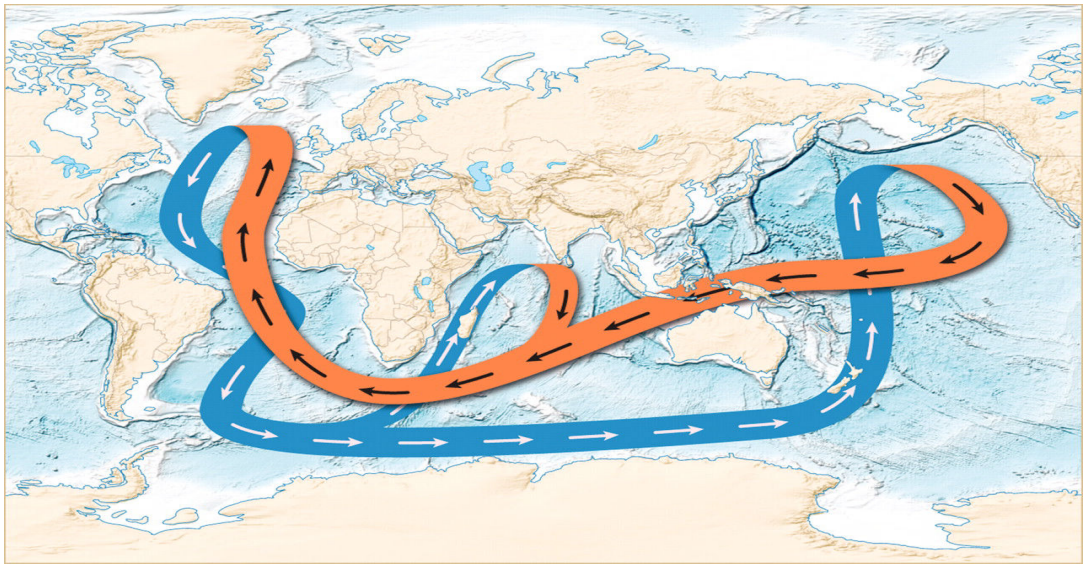

Figure 1.1: Schematic of the global thermohaline circulation (also called *Ocean Conveyor Belt*). Black and white arrows indicate the direction flow. Orange shows the warm and salty pathway of the upper limb, and blue shows the cold and fresh pathway of lower limb. Source: Lozier (2010).

1.2 Mean circulation in the northern North-Atlantic Ocean

The circulation scheme in Figure 1.2 is an overall view of the mean circulation in the northern North-Atlantic Ocean from Daniault et al. (2016), which combines OVIDE data analysis with results of previous studies in this region. From the subtropical gyre, the Gulf Stream flows northward into the northern North-Atlantic Ocean by carrying warm and salty water masses in the upper limb of the MOC (red arrows in Figure 1.2). The North-Atlantic Current (NAC) is an extension of the Gulf Stream that is deflected eastward near Flemish Cap in the Newfoundland Basin (indicated as the Northwest Corner in Figure 1.2 at about 45°W/45°N). There, the warm and salty upper-waters are joined by southward flow of fresher and colder water masses from the Labrador Sea. The northeastward NAC flows into three main branches and bounds the cyclonic circulation of the subpolar gyre to the south. The central NAC branch flowing near 50.5°N is characterized by a sharp salinity front and is generally refer to in the literature as the Sub-Arctic Front (SAF) (Daniault et al., 2016). At the Mid-Atlantic Ridge (MAR), the three branches of the NAC are dynamically constrained to cross the ridge across its deeper fracture zones. The northern branch follows the Charlie Gibbs Fracture Zone (CGFZ) at 35°W/52.5°N, the SAF follows the Faraday Fracture Zone (FFZ) at 35°W/50.5°N, and the southern branch follows the Maxwell Fracture Zone at 35°W/48°N (Bower & von Appen, 2008; Bower & Furey, 2017; Roessler et al., 2015; Schott et al., 1999). The northern NAC branch and the SAF flow around the Rockall Plateau and continue cyclonically in the Iceland Basin. The southern NAC branch splits into two branches after crossing the MAR. Its northern branch joins the cyclonic circulation through the Rockall Trough while its southern branch veers southward in the Western European Basin (Daniault et al., 2016). Before cyclonically turning along the Icelandic shelf north of 60°N, part of the NAC continues toward the Nordic Seas via the Iceland-Scotland Ridge as part of the upper limb of the MOC. In the Nordic Seas, the water masses become fresher and colder and sink to the bottom. This deep water feeds the lower limb of the MOC in the Iceland Basin by crossing back southward the Iceland-Scotland Ridge (blue arrows in Figure 1.2).

Located at the northern part of the MAR between the Iceland Basin and the Irminger Sea, the Reykjanes Ridge is a major topographic feature of the northern North-Atlantic Ocean (Figure 1.2). From Iceland southwestward till the CGFZ, the Reykjanes Ridge bounds the cyclonic circulation in the Iceland Basin to the west and deflects southwestward the two limbs of the MOC. This top-to-bottom current lying along the eastern flank of the Reykjanes Ridge was named East Reykjanes Ridge Current (ERRC) by Treguier et al. (2005). To join the Irminger

Sea, the ERRC crosses anticyclonically the Reykjanes Ridge at specific areas. RAFOS float trajectories identified the Bight Fracture Zone (BFZ) at 34°W/57°N as a preferential pathway to the westward branch of the subpolar gyre (Bower et al., 2002). Observations (Saunders, 1994) and model outputs (Xu et al., 2010; Zou et al., 2017) also showed the importance of the BFZ and CGFZ for the deepest water masses. Interestingly, other analyses based on measurements perpendicular to the ridge axis suggested that the subpolar gyre takes additional pathways across the Reykjanes Ridge. For instance, the Ovide project provided series of indirect transport estimates showing significant westward transports north of the BFZ (Daniault et al., 2016; Lherminier et al., 2010). Once in the Irminger Sea, the westward branch of the subpolar gyre flows northeastward along the western side of the Reykjanes Ridge within the Irminger Current (IC). Våge et al. (2011) defined the IC as a two-branch surface-intensified northeastward flow of about 200-km wide west of the top of the Reykjanes Ridge. In the literature, the source of IC water comes from the NAC that quickly leaves the Iceland Basin after crossing the Reykjanes Ridge (Lavender et al., 2005; Ollitrault & Colin de Verdière, 2014; Våge et al., 2011).

In the Irminger Sea, the two limbs of the MOC shift southwestward along the eastern coasts of Greenland and form a strong boundary current (Lherminier et al., 2007) named East-Greenland Irminger Current (EGIC). The EGIC is fed at depth by southwestward overflows from the Nordic Seas that join the Irminger Sea through the Denmark Strait. Near Cap Farewell, the EGIC recirculates in the western part of the Irminger Sea and forms a narrow cyclonic recirculation named the Irminger Gyre (Våge et al., 2011). This part of the Irminger Sea is known as a deep convection area (de Jong et al., 2018; Pickart et al., 2003; Anne Piron et al., 2016). After Cap Farewell, the EGIC becomes the West Greenland Current as it continues along the western coasts of Greenland toward the Labrador Sea. Around the outer rim of the Labrador Sea, strong air-sea interactions form large amount of deep waters that sink carbon dioxide (Talley & McCartney, 1982; Yashayaev & Loder, 2016). This water flows toward the Newfoundland Basin where part joins the NAC and part continues toward the southern North-Atlantic Ocean.

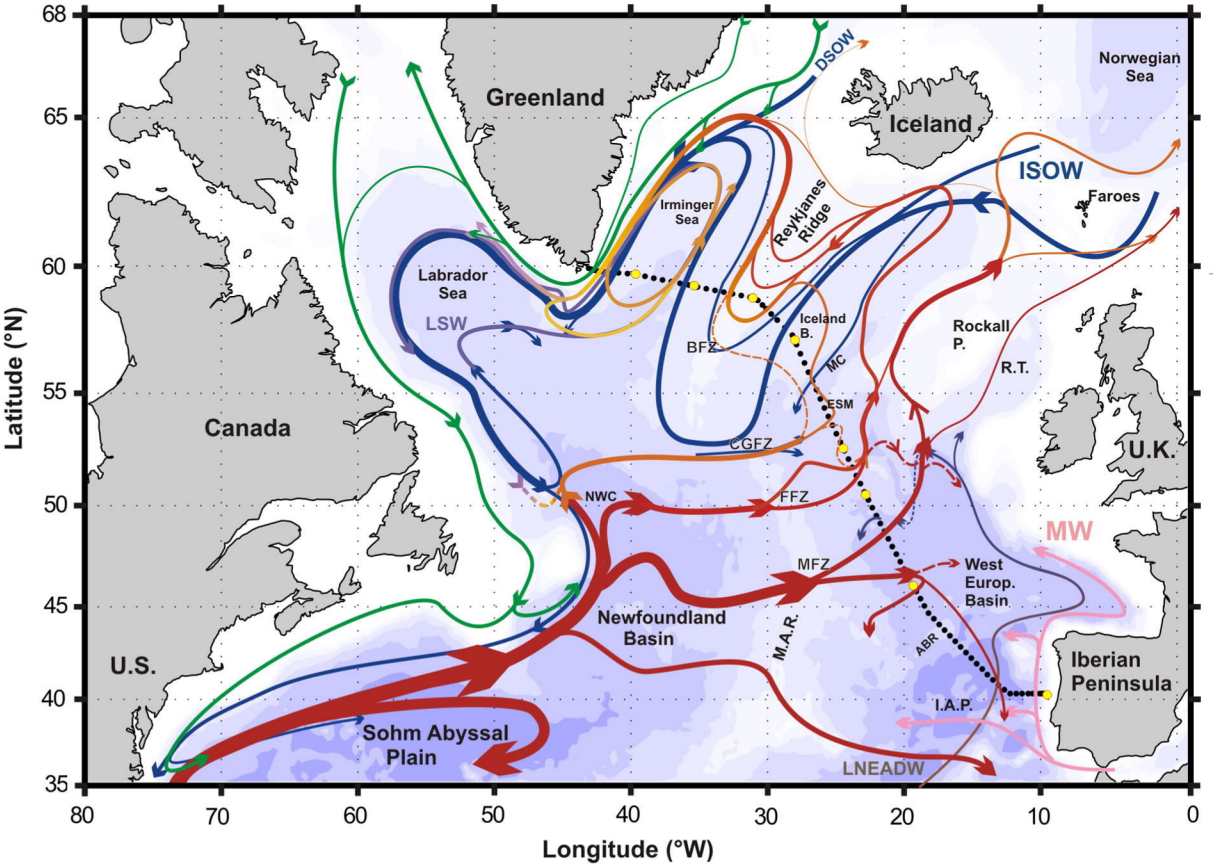

Figure 1.2: Schematic of the large-scale circulation in the northern North with locations of the OVIDE hydrographic stations (black dots). Bathymetry is plotted in color with color changes at 100 m, 1000 m and every 1000 m below 1000 m. Topographical features and currents of North Atlantic are indicated as follows: Bight Fracture Zone (BFZ), Charlie-Gibbs Fracture Zone (CGFZ), Faraday Fracture Zone (FFZ), Maxwell Fracture Zone (MFZ), Mid-Atlantic Ridge (MAR), Azores-Biscay Rise (ABR), Iberian Abyssal Plain (I.A.P.), Northwest Corner (NWC), Rockall Trough (RT), Rockall Plateau (Rockall P.) and Maury Channel (MC). The main associated water masses are indicated: Denmark Strait Overflow Water (DSOW), Iceland-Scotland Overflow Water (ISOW), Labrador Sea Water (LSW), Mediterranean Water (MW) and Lower North East Atlantic Deep Water (LNEADW), which is called Lower Deep Water (LDW) in the following. Source: Daniault et al. (2016).

1.3 State of the art of North-Atlantic water masses

Many water masses in the vicinity of the Reykjanes Ridge undergo modifications in the Iceland Basin and Irminger Sea via air-sea exchange in the mixed layer, isopycnal and diapycnal mixing at intermediate depths, or entrainment in the deep overflows. This section provides a short review of these water masses as they are described in the literature.

1.3.1 SubPolar Mode Water

SubPolar Mode Water (SPMW) composes the upper layers of the North-Atlantic Ocean. Formed by winter air-sea interactions and convection, SPMW is characterized by nearly

uniform hydrological properties (density, temperature, salinity) in the thick winter mixed layer, and is located between the permanent and seasonal pycnoclines in summer (Talley & McCartney, 1982). Because of its recent contact with the atmosphere, SPMW is also characterized by higher oxygen concentration than the surrounding water masses. In the literature, SPMW is thus often identified by its low potential vorticity (Brambilla & Talley, 2008; Thierry et al., 2008).

These past few years, the scientific community was particularly interested in better characterizing this mode water because of its importance in the transfer of warm and salt between the subtropical and the subpolar gyres (de Boisséson et al., 2012; Brambilla & Talley, 2008; Thierry et al., 2008). Indeed, the SPMW properties vary along the horizontal cyclonic pathway of the subpolar gyre such that its density gradually increases from the Iceland Basin to the Irminger Sea. Along the trans-Atlantic Scotland — Greenland section AR7, the SPMW potential temperature varied from 9 — 10°C in the Rockall Trough, to about 6°C over the Reykjanes Ridge, and to 3 – 3.5°C in the Irminger Sea (Van Aken & De Boer, 1995). As a consequence, García-Ibáñez et al. (2015) defined three different varieties of SPMWs along the Ovide line depending on their potential temperatures. Two were situated in the Iceland Basin with temperatures of 7 and 8°C, while another SPMW variety was situated in the Irminger Sea with colder temperature. Once in the Labrador and Nordic Seas, the water mass contributes to the formation of deep water that feeds the lower limb of the MOC (Sarafanov et al., 2012). Thus, the densification of SPMW in the eastern subpolar gyre paves the way for further densification occurring downstream.

Over the Reykjanes Ridge, a variety of SPMW, called Reykjanes Ridge Mode Water (RRMW), is identified in Figure 1.3. This mode water is formed in the Iceland Basin by winter convection of surface and central waters from the NAC (de Boisséson et al., 2012; Brambilla & Talley, 2008; Talley, 1999; Thierry et al., 2008). RRMW may also incorporate underlying intermediate and deep waters when the winter mixed layer is deep enough. Brambilla and Talley (2008) showed in Figure 1.4 that the RRMW density increases southward from $27.3\sigma_0$ north of 60°N to $27.5\sigma_0$ south of 57°N. This feature is related to the NAC water properties that feed the upper layer of the Iceland Basin (de Boisséson et al., 2012). Based on Lagragian tools, de Boisséson et al. (2012) investigated the origins of the particles that cross the Reykjanes Ridge as part of RRMW (Figure 1.5). They showed that the NAC particles connected to the Reykjanes Ridge flow west of the Rockall Plateau. The northern branch of the NAC reaches the southern part of the Reykjanes Ridge with higher

proportion of subpolar water than the southern branch of the NAC, which is connected to the northern part of the Reykjanes Ridge.

Finally, Thierry et al. (2008) showed strong temporal variability of the RRMW properties at 58.5°N over the Reykjanes Ridge. Between 1990 and 2006, they showed that the RRMW density decreased from $27.56\sigma_0$ in the early 1990s to $27.45\sigma_0$ in the mid-2000s. More recently, Grist et al. (2016) showed that during winter 2013 – 2014, extreme air-sea heat loss resulted in a strong cooling of the subsurface subpolar gyre and in a formation of particularly dense SPMW. Zunino et al. (2017) argued that this cooling added to the cooling of the subpolar gyre took place since 2006.

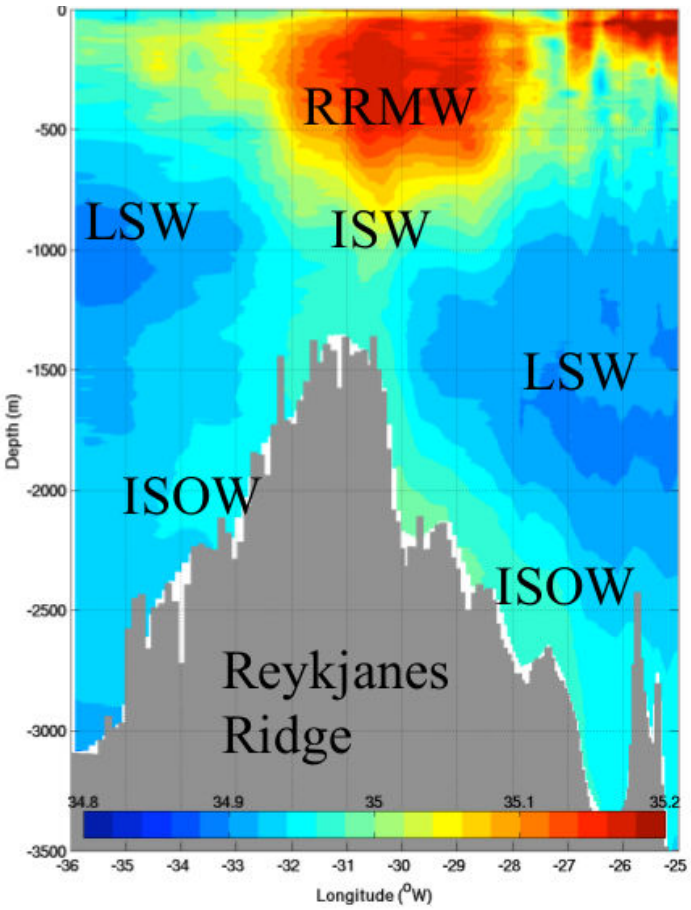

Figure 1.3: Mean 2002 – 2010 salinity section along part of the Ovide line and localized above the Reykjanes Ridge. The main associated water masses are indicated: Iceland-Scotland Overflow Water (ISOW), Labrador Sea Water (LSW), Icelandic Slope Water (ISW) and Reykjanes Ridge Mode Water (RRMW).

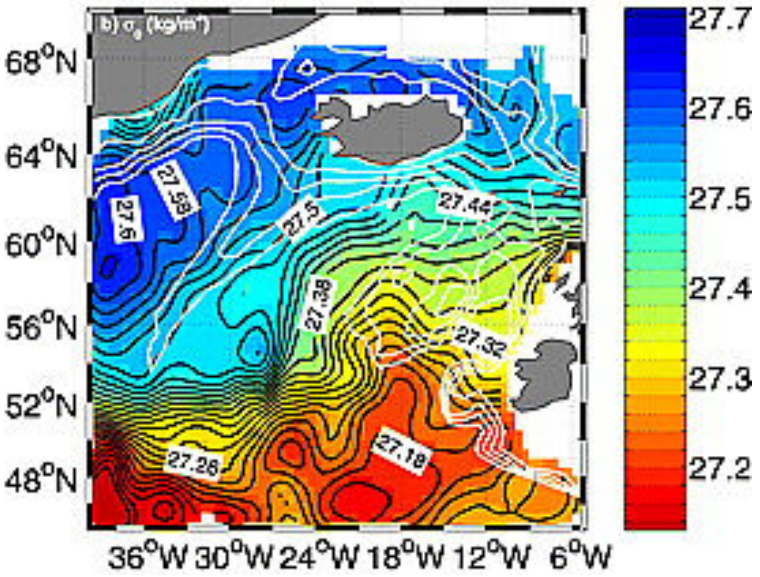

Figure 1.4: Potential density σ_0 at the PV minimum with contour interval of 0.02 kg m^{-3}. White contours are the topography from 10 m to 2000 m with contour interval of 500 m. Source: Brambilla and Talley (2008).

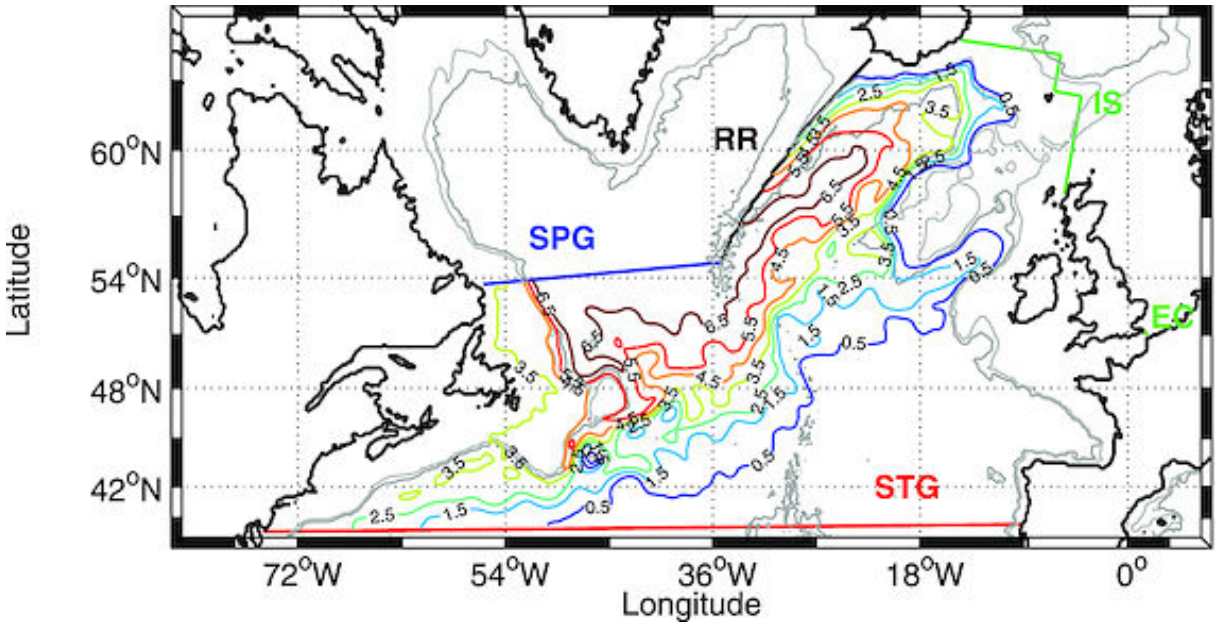

Figure 1.5: Mean stream function (Sv) of particles that come from the STG and SPG sections and estimated by the Lagrangian tool during the summer 1990. Gray lines indicate the 1000 and 2000-m isobaths. Source: de Boisséson et al. (2012).

1.3.2 Intermediate Water

In the eastern part of the NASPG, Intermediate Water (IW) bounds the permanent pycnocline below. At the intersection of the subpolar and subtropical gyres, IW is formed by isopycnal mixing of Antarctic Intermediate Water, Sub-Arctic Intermediate Water and Mediterranean Water in the Eastern Basin (Harvey & Arhan, 1988). IW then mixes with surrounding water masses along the subpolar gyre such that this category of IW is not found in the western NASPG. In the Iceland Basin, IW is marked by a relative maximum of potential vorticity and a relative minimum of oxygen concentration (O_2 < 5.6 ml l^{-1}) as showed by Read (2001) in Figure 1.6. The IW is also biogeochemically defined by maxima of NO_3 due to the old-aged Antarctic Intermediate Water that partly composes the IW and to mineralization processes taking place in the Iceland Basin (Van Aken & De Boer, 1995).

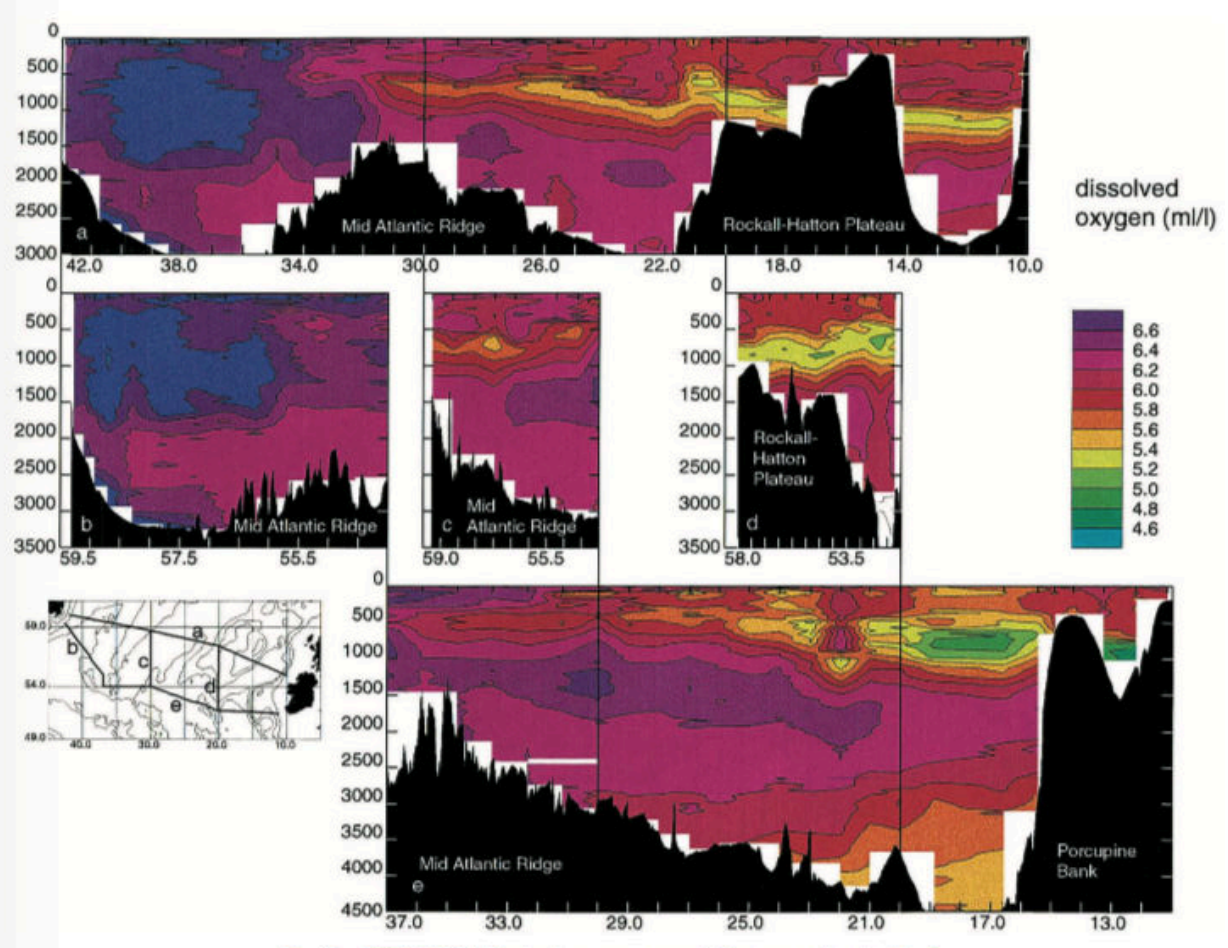

Figure 1.6: Dissolved Oxygen concentration of the CONVEX-91 secions. The minimum of oxygen concentration (O_2 < 5.6 ml l^{-1}) along section (a) is associated with Intermediate Water. Source: Read (2001).

1.3.3 Labrador Sea Water

Labrador Sea Water (LSW) is a major water mass found all over the NASPG. Large amount of LSW are formed each year by deep winter convection in the western NASPG. The Labrador Sea is a well-known convection area (Talley & McCartney, 1982), but more recently, Pickart et al. (2003) showed that LSW was also formed in the center of the Irminger Sea. At these two locations, LSW is characterized by its unique low salinity and high oxygen concentration between 1 000 and 2 000-m depths (Van Aken & De Boer, 1995). In the Irminger Sea, the newly formed LSW is slightly saltier (0.04) and warmer (0.3°C) than LSW formed in the Labrador Sea (de Jong et al., 2018; Anne Piron et al., 2016). After formation, LSW spreads toward other regions of the NASPG. Advected southeastward by the Deep Western Boundary Current and subsequently by the NAC (Rhein et al., 2002; Talley & McCartney, 1982), LSW reaches the Iceland Basin in about 4 – 5.5 years from the Labrador Sea (Straneo et al., 2003; Sy et al., 1997; Yashayaev et al., 2007). Because the water mass transits for a long period of time and along various pathways over the subpolar gyre, a large range of LSW properties can be seen along the trans-Atlantic section AR7. In the Iceland Basin, Figure 1.7 shows that LSW is saltier by up to 0.1 than the variety of LSW found in the Labrador Sea, and saltier by up to 0.04 than the variety of LSW found in the Irminger Sea. Mixing between LSW and Mediterranean Water in the Eastern Basin increases the LSW salinity eastward. In the Irminger Sea, Yashayaev et al. (2007) suggested interactions between LSW from the Iceland Basin, which crosses the Reykjanes Ridge and flows northeastward along its western flank, and LSW from the center of the Irminger Gyre. The LSW properties are thus asymmetric between the two sides of the Reykjanes Ridge with fresher LSW over the western flank of the ridge (Figure 1.7). Finally, the transport of LSW outside of the Labrador Sea is a good indicator of the variability of the subpolar gyre strength (Böning et al., 2006). Indeed, Hakkinen and Rhines (2004) suggested a link between the substantial decline of the subpolar gyre after 1994 and the depth of the convection in the Labrador Sea. More recently, Yashayaev and Loder (2017) showed strong time-variability of LSW formation in the Irminger Sea, and pointed out a progressive deepening of winter convection since 2012 that reaches 2100 m in 2016, possibly related to repeated positive North-Atlantic Oscillation (NAO) phases.

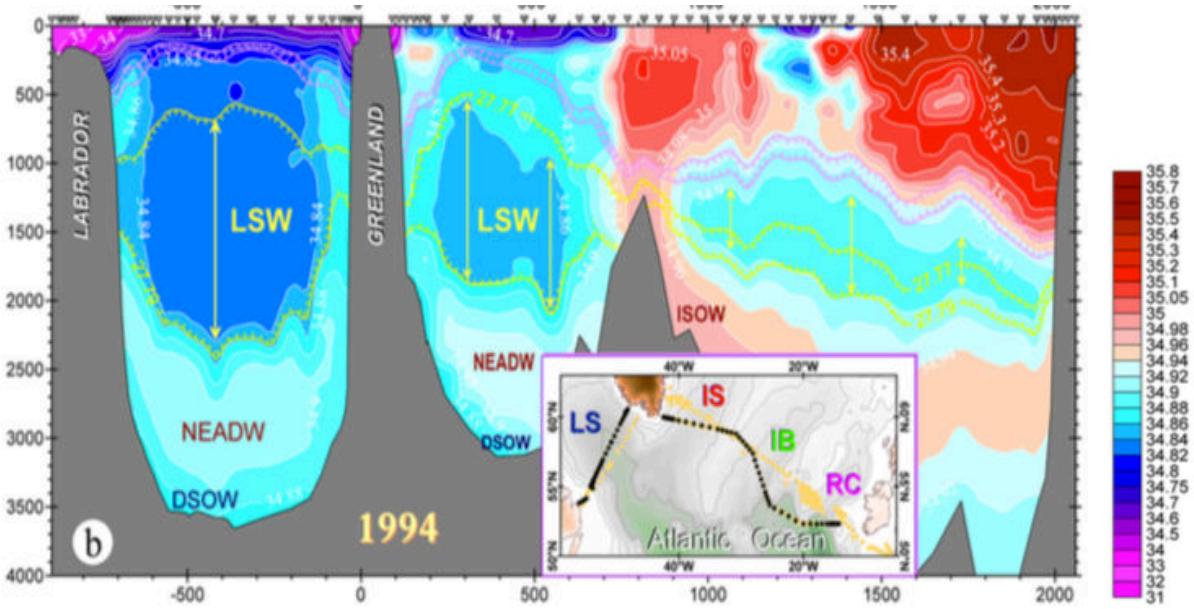

Figure 1.7: Salinity section along the trans-Atlantic section AR7 in 1994. The inserted map indicated the associated profiling sites. Hatched lines contour the potential density 24.72 and 24.74 (purple), 24.77 and 24.79 kg m $^{-3}$ (yellow). Source: Yashayaev et al. (2007).

1.3.4 Icelandic Slope Water

Between the two cores of LSW in Figure 1.3, another water mass is found above the crest of the Reykjanes Ridge along the Ovide line. The increase of salinity at 30 – 32°W indicates the presence of Icelandic Slope Water (ISW). ISW is formed close to the Iceland-Faroe Ridge by mixing between SPMW and overflow waters, and is further transformed by isopycnal mixing with LSW while flowing southward along the Reykjanes Ridge (Van Aken & De Boer, 1995; Van Aken et al., 2011; Read, 2001). ISW is thus formed in the Iceland Basin from water masses associated with both the upper and lower limbs of the MOC. Above the crest of the Reykjanes Ridge, ISW is identified by higher salinity and lower dissolved oxygen concentration than LSW. Above the Reykjanes Ridge at CONVEX-91 latitudes, Read (2001) specified that the ISW salinity and potential temperature were in the range 34.96 – 35.00 and 3 – 4°C, respectively.

1.3.5 Iceland-Scotland Overflow Water

At higher density over the Reykjanes Ridge, Iceland-Scotland Overflow Water (ISOW) largely composes the deep layers of the lower limb of the MOC. Formed by winter convection in the Greenland Sea and along the Arctic shelves (Eldevik et al., 2009), overflows join the eastern NASPG through the Iceland-Scotland sill. A large portion of overflow flows southward through the Feroe-Bank Channel, but overflow also crosses the shallower Iceland-Faroe Ridge. Immediately south of the Iceland-Scotland sill, ISOW is formed during entrainment of ambient water by the overflows, including upper waters. Indeed, at these latitudes, the overflow is shallow enough to entrain SPMW and LSW (Van Aken & De Boer, 1995; Dickson et al., 2002). ISOW is then carried southwestward along the Icelandic shelf and subsequently along the eastern flank of the Reykjanes Ridge. There, entrainment leads to the formation of new water masses such as ISW (Van Aken, 2000). Finally, ISOW spreads westward toward the Irminger Sea by crossing the Reykjanes Ridge through the BFZ and CGFZ (Saunders, 1994; Xu et al., 2010; Zou et al., 2017). In the northern part of the Irminger Sea, ISOW is joined by Denmark Strait Overflow Water (DSOW) that crosses the Denmark Strait from the Nordic Seas. On both sides of the Reykjanes Ridge (Figure 1.3), ISOW is identified by density higher than 27.8 kg m^{-3} and salinity higher than 34.94 (Saunders, 1994).

1.4 Impact of the topography on the North-Atlantic SubPolar Gyre: some key elements

1.4.1 Impact of topographic features on the flow

The ocean floor is a succession of ocean basins and seamounts that have a major influence on the oceanic circulation. For instance, it is well-known that ocean ridges block the spreading of water masses at depth (Holliday et al., 2015). At small-scales, the bottom roughness affects the deep circulation as well as the hydrological properties of the associated water masses through enhanced turbulent mixing and various other dynamical mechanisms (De Lavergne et al., 2017). In the northern North-Atlantic Ocean, such current-topography interactions affect the lower limb of the MOC. Originating from the Nordic Seas, the southward outflow of deep ISOW and DSOW are affected by major topographic features throughout the subpolar gyre. Firstly, the Greenland-Iceland-Scotland Ridge controls the overflows that cross the sill and

join the Iceland Basin and Irminger Sea (Swift, 1984). Then, the Hatton-Rockall Bank affects differently the water masses of the eastern North-Atlantic depending on their density (Holliday et al., 2015). Indeed, the northeastward NAC flow above 500 – 1000 dbar west of the Rockall Plateau and through the Rockall Trough to reach the Nordic Seas (Brambilla & Talley, 2008; Pollard et al., 2004), while recirculations of LSW within the Iceland Basin and the Rockall Trough were noted at intermediate depths (Holliday et al., 2000; Lankhorst & Zenk, 2006). Finally, ISOW are too dense to flow through the Hatton-Rockall Bank and continues southward through the Rockall Trough (Sherwin & Turrell, 2005) and along the Icelandic shelf and subsequently along the Reykjanes Ridge (Read, 2001; Saunders, 1994). Between the Iceland Basin and the Irminger Sea, the Reykjanes Ridge also strongly affects the circulation and water masses properties (Daniault et al., 2016).

1.4.2 The Reykjanes Ridge

The Reykjanes Ridge is a major topographic feature of the northern North-Atlantic Ocean that extends along a northeast/southwest line from the Icelandic shelf to 55°N, and then along a more meridional line to the CGFZ at 52.5°N (Figure 1.2). The summit of the Reykjanes Ridge is at about 300-m depth north of 63°N and deepens to more than 3000 m at the CGFZ. From its central position, the Reykjanes Ridge and associated fracture zones clearly influences the spatial pattern of the subpolar gyre circulation (Bower et al., 2002) and water masses (Thierry et al., 2008). Indeed, Figure 1.2 shows the general top-to-bottom anticyclonic circulation of the subpolar gyre around the Reykjanes Ridge. Located at the entrance of the Irminger Sea and Labrador Sea, the Reykjanes Ridge is also a gateway toward the deep convection areas. Desbruyères et al. (2013) showed that about 50% of light-to-dense conversion associated with the MOC occurs in the vicinity of the Reykjanes Ridge, which reinforce the importance of this region in the climate system.

From Greenland to Portugal, the historical repeated Ovide line (Figure 1.2) provides an averaged view of the top-to-bottom oceanic currents and water masses along the Reykjanes Ridge. There, the asymmetry of the structures and properties on both sides of the ridge shows that the Reykjanes Ridge acts as a barrier between the Iceland Basin and the Irminger Sea by constraining the exchange of volume and water mass transport (Figure 1.3 and Figure 1.8). Indeed, the Irminger Current on the western side of the Reykjanes Ridge is relatively

baroclinic, while the East Reykjanes Ridge Current on the eastern side of the ridge is composed of narrow and more barotropic flows (Figure 1.8). In term of water masses, the core of RRMW is not symmetric over the Reykjanes Ridge but is located over its eastern flank (Figure 1.3). Deeper, LSW composes the intermediate waters of the Iceland Basin and Irminger Sea, but is not observed over the crest of the Reykjanes Ridge. Along the Ovide line, ISW separates the two pools of LSW although the top of the Reykjanes Ridge is lower than the depths encompassing LSW. The topography of the ridge prevents the spreading of LSW and influences the formation of ISW at these depths. Finally, ISOW is found over the bottom topography of the Reykjanes Ridge, but is saltier (34.96 – 35) and deeper (below 1200 m) on the eastern side of the Reykjanes Ridge than on its western side (salinity of 34.94 – 34.96 below 1000-m depth). By crossing the Reykjanes Ridge, the deepest water masses should interact with the bathymetry of the ridge such that their hydrological properties evolve westward. Although these observations clearly outline the role of the Reykjanes Ridge on the circulation of the subpolar gyre, its impact on the flow and water masses remains unclear.

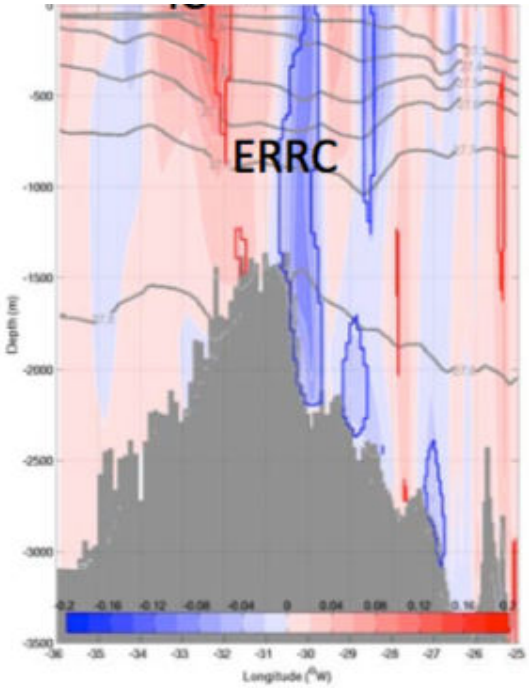

Figure 1.8: Mean 2002 – 2010 velocity section along part of the Ovide line and localized above the Reykjanes Ridge (Daniault et al., 2016). Positive (negative) values correspond to northward (southward) velocities. Red (blue) lines represent the limits of the region where the flow was northward (southward) during each Ovide cruise. The grey lines show isopycnals. East Reykjanes Ridge Current is labeled ERRC.

1.4.3 Cross-ridge flow

The formation of intermediate and deep waters in the Irminger and Labrador Seas is influenced by the amount of warm and salty water masses reaching these basins and thus by their pathways upstream through the Reykjanes Ridge (Cuny et al., 2002; Myers et al., 2007). Across the Reykjanes Ridge, RAFOS float trajectories drifting at σ_0 = 27.5 and 27.7 kg m^{-3} (Figure 1.9) preferentially join the Irminger Sea over the BFZ at 57°N (Bower et al., 2002). This westward pathway was also identified at 1000 dbar by Argo float trajectories (Ollitrault & Colin de Verdière, 2014). At higher density, ocean model outputs (Xu et al., 2010; Zou et al., 2017) and Lagrangian floats (Lankhorst & Zenk, 2006) showed that ISOW escapes the Iceland Basin mainly through the BFZ and CGFZ. More precisely, Xu et al. (2010) showed that the southward flow of ISOW along the Reykjanes Ridge is more complex than previously thought and is composed of several southward veins at around 60°N. They highlighted that the shallowest and westernmost vein of ISOW mainly feeds the flow across the BFZ. Although a cross-ridge flow of ISOW through the BFZ is consistent with the OVIDE data analysis of Daniault et al. (2016), no direct observation of ISOW through the BFZ allows us to quantify its transport. In the CGFZ however, the observations of Saunders (1994) as well as the model outputs of Xu et al. (2010) estimated an ISOW transport of 2.4 ± 0.5 Sv. More recently, both high-resolution models (Xu et al., 2010) and mooring observations (Bower & Furey, 2017) showed that the ISOW transport is strongly variable through the CGFZ (Figure 1.10) and is mainly correlated with the variability of the deep-reaching branches of the NAC.

At northern latitudes, other analyses suggested additional pathways across the Reykjanes Ridge. Based on measurements perpendicular to the ridge axis, the Ovide project provided indirect series of significant cross-ridge transports from Iceland to the Ovide line, even though no major fracture zones were identified there (Daniault et al., 2016; Lherminier et al., 2010). Lherminier et al. (2010) have estimated a cross-ridge transport ranging between 9.6 ± 2.1 Sv in 2002 and 13.8 ± 2.1 Sv in 2004. However, a westward pathway in the northern part of the Reykjanes Ridge has been subject to controversy in the literature. Chafik et al. (2014) and Childers et al. (2015), considering indirect measurements of roughly the same latitude band, estimated a very weak westward transport in the upper 400 m of the water column over the Reykjanes Ridge. Thus, the ocean circulation scheme of Chafik et al. (2014) in Figure 1.11 is different from that provided by Daniault et al. (2016) in Figure 1.2. Chafik et al. (2014) schemed that the westward cross-ridge flow only occurs south of 57°N.

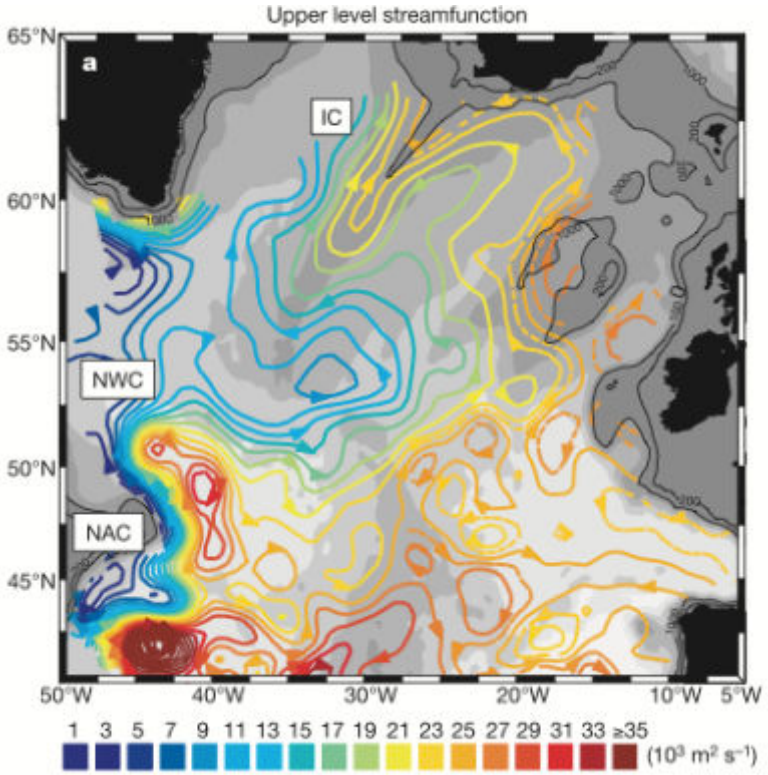

Figure 1.9: Mean streamfunction of the ocean circulation in the northern North-Atlantic Ocean from subsurface RAFOS float data at the density σ_0 = 27.5 kg m^{-3}. Main currents are indicated as follows: Irminger Current (IC), North-West Corner (NWC) and North-Atlantic Current (NAC). Source: Bower et al. (2002).

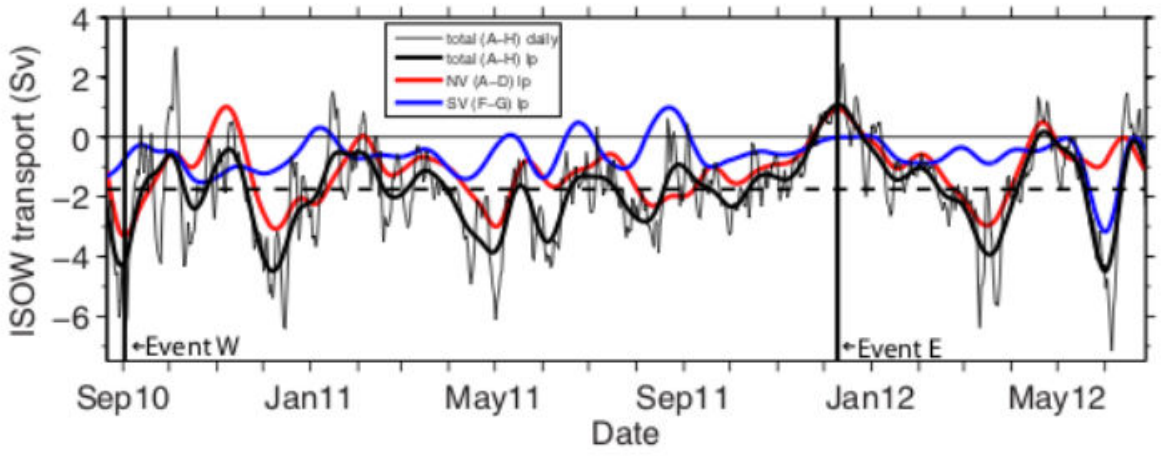

Figure 1.10: Time series of ISOW transport across the mooring array through the CGFZ. The thick black line shows the 30-day low-pass filtered transport values, the thin black line indicates daily mean total transport values. The dashed line indicates the mean transport over the time series. The red and blue lines show low-pass filtered transport in the northern valley and in the southern valley of the CGFZ, respectively. Source: Bower and Furey (2017).

Although the identification of these pathways across the Reykjanes Ridge was a step forward in our understanding of the subpolar gyre circulation, so far, direct observations along the Reykjanes Ridge were lacking to identify all the cross-ridge pathways and to quantify them. The vertical structure of the cross-ridge flow also remains unclear, as does the connection of the westward flow across the Reykjanes Ridge to the upstream NAC branches. Indeed, although the distribution and transport of the NAC water masses are well known in the Iceland Basin (Brambilla & Talley, 2008; Holliday et al., 2015; Pollard et al., 2004), their distributions along the Reykjanes Ridge related to the bathymetry of the ridge have never been documented, and the associated transports have only been quantified in an integral way (Daniault et al., 2016; García-Ibáñez et al., 2015). As a result, the intensity of the westward branch of the subpolar gyre had only been estimated on given densities (Bower et al., 2002), from proxies (Hakkinen & Rhines, 2004), or from general circulation models (Böning et al., 2006; Lohmann et al., 2009). However, a quantification of the water mass transport across the Reykjanes Ridge would provide benchmarks for the validation of these models that still present inconsistencies in the circulation and properties of the NASPG (Penduff et al., 2007; Rattan et al., 2010). For instance, the water masses are too salty in the vicinity of the Reykjanes Ridge (de Boisséson et al., 2012; Desbruyères et al., 2013). This shift in salinity is possibly related to a wrong representation of the circulation around the Reykjanes Ridge (Rattan et al., 2010) and, for instance, a too strong East Reykjanes Ridge Current along the eastern side of the ridge (Treguier et al., 2005).

At smaller scale, the impact of the bathymetry on the deep cross-ridge water masses deserves further investigations. Indeed, publications showed that the fracture zones are sites of large modifications of the water mass properties (Mercier et al., 1994). For instance, Heezen et al. (1964) showed that the sills of equatorial fracture zones (Romanche and Chain Fracture Zones) partly blocked the circulation of the densest water masses, which constrains the eastward evolution of their hydrological properties. Hogg et al. (1982) also showed that mixing and entrainments strongly change the Antarctic Bottom Water properties in the Vema Chanel at about 30°S. Although Bower et al. (2002) and Xu et al. (2010) identify the BFZ, deep and wide gap in the Reykjanes Ridge, as a major route for the exit of ISOW toward the Irminger Sea, no study investigated the westward pathways of ISOW through the complex bathymetry of the BFZ, or the westward evolution its hydrological properties. High-resolution data sets are thus needed to determine if the main sills of the BFZ channel the cross-ridge

flow (Bower et al., 2002) or if, for instance, other small-scale processes like eddy features are involved (Krauss, 1995).

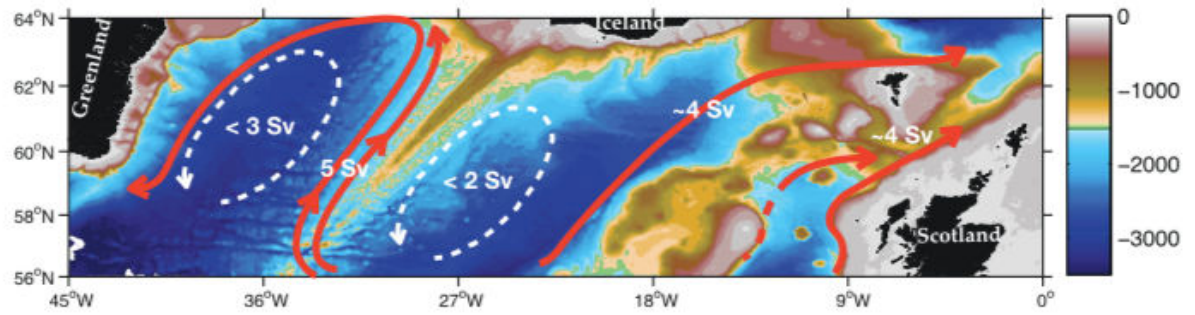

Figure 1.11: Ocean circulation of the upper 400 m across the northeast North-Atlantic Ocean. Transports are indicated in Sverdrup. Source: Chafik et al. (2014).

1.4.4 Along-ridge flow

From the top to the bottom, along-ridge currents follow the bathymetry of the Reykjanes Ridge: the East Reykjanes Ridge Current (ERRC) on the eastern side and the Irminger Current (IC) on the western side. At surface, sub-surface drifters (Otto & Van Aken, 1996; Valdimarsson & Malmberg, 1999), upper-ocean repeated transects (Chafik et al., 2014; Childers et al., 2015; Knutsen et al., 2005), and numerical models (Treguier et al., 2005) showed that the ERRC is a narrow southwestward flow of similar intensity than the IC (Daniault et al., 2016). However, the presence of a continuous and strong southward current on the eastern side of the Reykjanes Ridge is less clear from altimetric surface velocities (Jakobsen et al., 2003). In Figure 1.12, Jakobsen et al. (2003) showed that the southward velocities along the eastern side of the Reykjanes Ridge were weak at surface. Similarly, some surface drifters showed that the southward flow was not continuous along the Reykjanes Ridge but was strongly perturbed by small-scale features in the Iceland Basin (Flatau et al., 2003; Reverdin et al., 2003).

Along the Ovide line, Daniault et al. (2016) provided an averaged view of the top-to-bottom vertical structure of the ERRC. At about 58.8°N (Figure 1.8), the ERRC was composed of a main quasi-barotropic branch at 30.1°W and two surface and bottom intensified branches at 28.5°W and 29°W, respectively, which correspond altogether to a 200 km wide current east of the top of the Reykjanes Ridge. This top-to-bottom structure is similar to that previously

documented by Sarafanov et al. (2012) for 2002 – 2008 at 59.5°N. In addition, Figure 1.8 shows that the ERRC is bounded to the east by a narrow northeastward flow of 100 km width, which was also observed by previous studies (Knutsen et al., 2005). Overall, the top-to-bottom ERRC was thus only documented in a narrow band of latitudes (58.8 – 59.5°N) and was never directly observed south and north of it. As a consequence, little is known on the ERRC formation in the northern part of the Reykjanes Ridge, as well as on the southward evolution of its vertical and horizontal structure and of its hydrological properties. The seasonal to interannual variability of the ERRC is also unknown. For instance, Reverdin et al. (2003) suggested that the ERRC is more intense in winter than in summer, which should be taken into account in the estimation of the ERRC transport. Additional data are thus required to document the evolution of the ERRC along the Reykjanes Ridge, to better understand its formation mechanisms, and to describe its connections with the NAC in the Iceland Basin and with the IC across the Reykjanes Ridge.

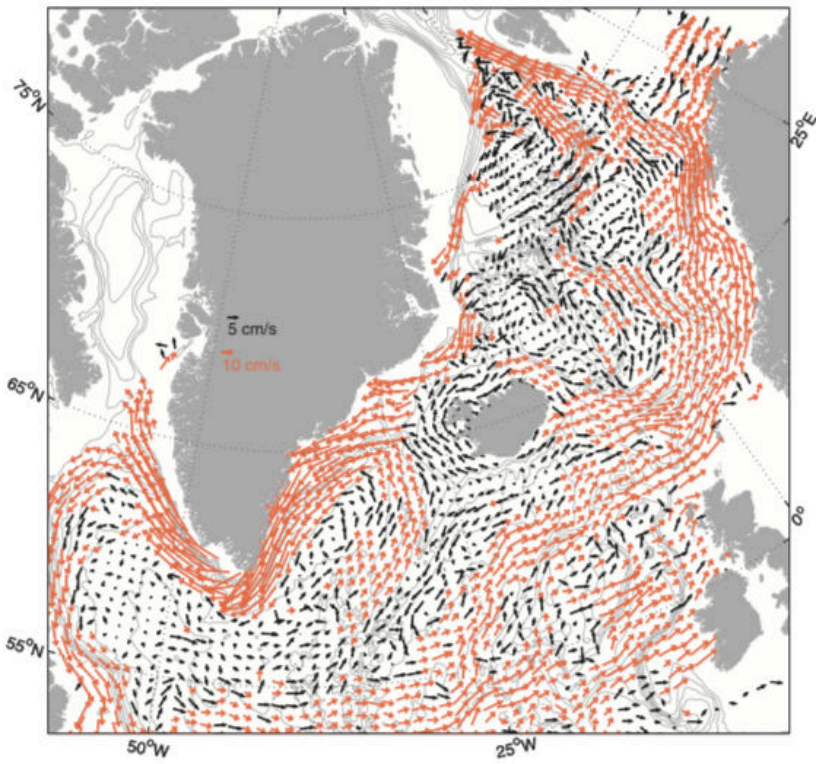

Figure 1.12: Quasi-Eulerian current vectors derived from altimetry with low-velocity in black and high-velocity in red arrows. Source: Jakobsen et al. (2003).

By crossing the Reykjanes Ridge, the westward branch of the subpolar gyre joins the IC located along the western flank of the ridge (Figure 1.2 and Figure 1.9). Våge et al. (2011) defined the IC as a two-branch surface-intensified northeastward flow of about 200 km wide west of the top of the ridge. Along the Reykjanes Ridge, the IC is schemed as a northward continuous flow without any connections with the northward branch of the Irminger Gyre (Figure 1.2). However, Yashayaev et al. (2007) suggested interactions between the Irminger Gyre and the IC along the repeated trans-Atlantic section AR7 (Figure 1.7), which is consistent with Sy et al. (1997) and Fan et al. (2013) that highlighted strong eddy activity in the center of the Irminger Sea that could favors such interactions.

The major source of IC water comes from the NAC that leaves the Iceland Basin after crossing the Reykjanes Ridge (Lavender et al., 2000; Ollitrault & Colin de Verdière, 2014; Våge et al., 2011). However, because of the southward deepening of the Reykjanes Ridge, the westward flows that cross the Reykjanes Ridge north of the CGFZ should differently affected the northward circulation and hydrological properties of the IC depending on the latitudes. For instance, the deep layers of the IC should be less affected by the top-to-bottom cross-ridge flow on the northern part of the ridge than on its southern part where deep waters are able to cross the ridge. Similarly, if large amount of deep waters indeed cross the Reykjanes Ridge through the BFZ (Bower et al., 2002; Xu et al., 2010), this deep circulation should locally affected the deep layers of the IC. Further investigations of the top-to-bottom IC structure are thus required to better understand the evolution of the IC north and south of the Ovide latitudes, as well as its interactions with the surrounded water masses from the Iceland Basin and from the Irminger Sea.

1.5 The Reykjanes Ridge Experiment Project

The aforementioned studies have revealed the importance of the Reykjanes Ridge on the circulation of the NASPG. Yet, the underlying impacts of the Reykjanes Ridge on the current structures and on the evolution of the water mass properties are not fully understood and need more localized observations over the ridge. The Reykjanes Ridge Experiment (RREX) project was developed to better understand the interactions between the ocean currents and the Reykjanes Ridge. As defined by the Principal Investigators (V. Thierry & H. Mercier, personal communication), the aims of the RREX project were to conduct an innovative study of (1) the circulation around and over the Reykjanes Ridge and to identify the processes

controlling the dynamical connections between the two sides of the ridge; (2) to quantify the water mass transformation in the vicinity of the Reykjanes Ridge; and (3) to identify key parameters that are critical for an adequate representation of the circulation and water mass properties in ocean models in order to improve the next generation of climate models.

More precisely, the (1) objective was to:

• O1.1: document the mean horizontal and vertical structure and the variability, from daily to seasonal and possibly interannual time scales, of the flow around the Reykjanes Ridge, and thus of the East Reykjanes Ridge Current and the Irminger Current;

• O1.2: identify the main pathways of ISOW near the Reykjanes Ridge and the corresponding transports, especially through the Bight Fracture Zone;

• O1.3: quantify the exchanges above the ridge such as determine the origin of the water entrained by the Irminger Current and the fate of the RRMW;

• O1.4: identify the dynamical flow regimes that prevail on both sides of the Reykjanes Ridge and the local and remote processes that control the horizontal and vertical structures of the currents and the exchanges above the ridge.

To achieve these objectives, the RREX project provided for the first time a synoptic high-resolution monitoring of the flow along and across the Reykjanes Ridge, as well as observations of turbulence to monitor the mixing processes enhanced by the bathymetry. The RREX project also seeks to quantify the variability of these currents at daily to seasonal time-scales. To do so, hydrographic, velocity and turbulent measurements were acquired during a first cruise in summer 2015 (RREX2015, Figure 1.13) and during a second cruise in summer 2017 (RREX2017, Figure 1.14). An array of 7 current meter moorings was also deployed during the first cruise and recovered during the second cruise in the BFZ area. Finally, Argo floats were deployed to complete the description of the seasonal variability of the currents. The RREX project is a French contribution to the OSNAP international project (Lozier et al., 2017) through moorings deployed over the Reykjanes Ridge and contributes to the international Argo program through the deployment of Deep-Arvor floats.

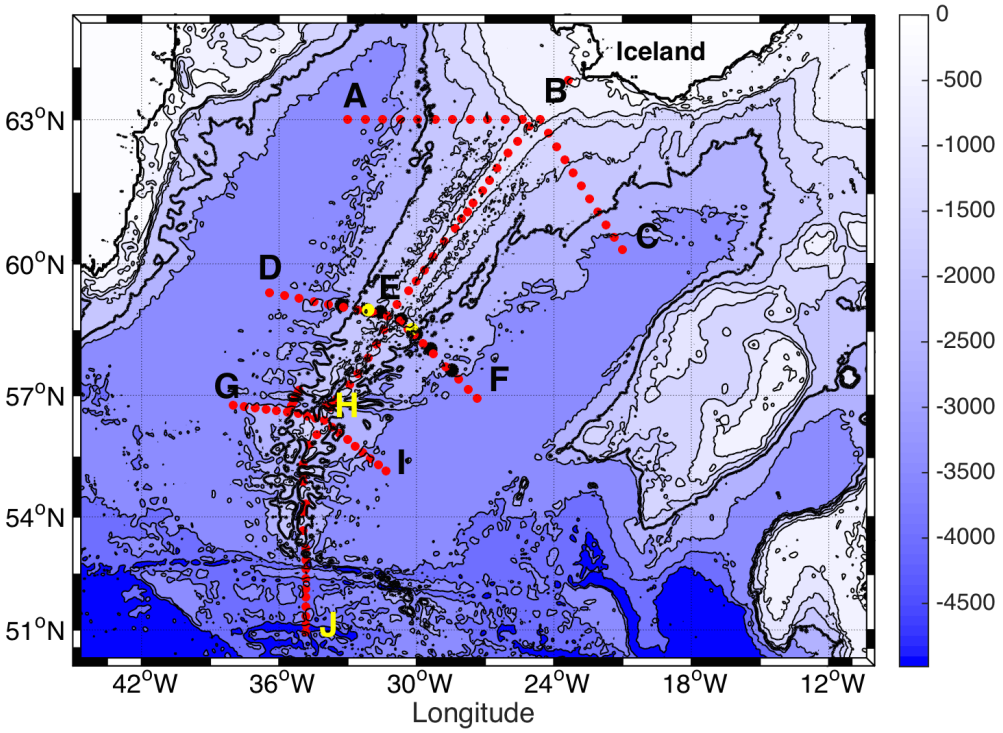

Figure 1.13: (Red dots) Hydrographic stations carried out during the RREX2015. The locations of moorings and ASFAR deployments are indicated by black and yellow dots, respectively. Blue contours show the bathymetry of the northern North-Atlantic Ocean.

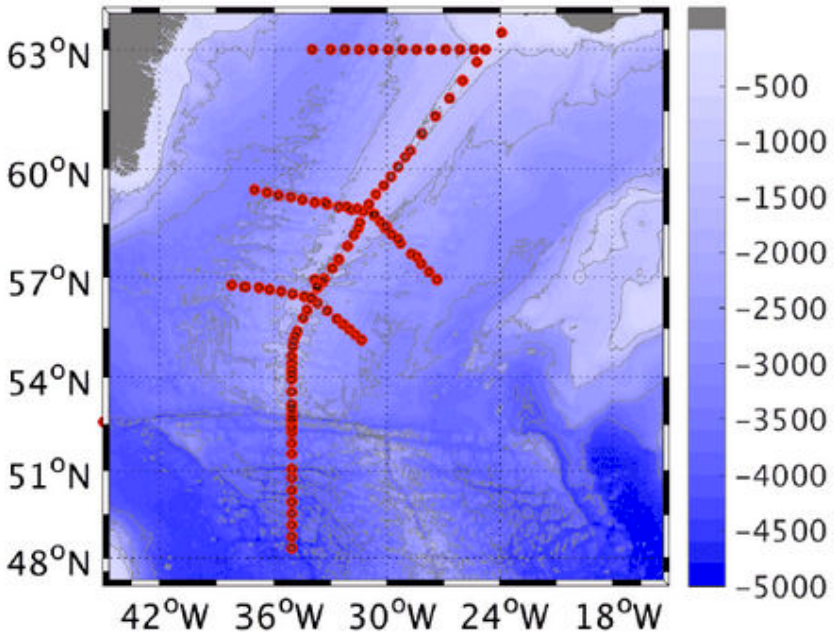

Figure 1.14: Location of the hydrographic stations carried out during the RREX2017 cruise. Blue contours show the bathymetry of the northern North-Atlantic Ocean.

1.6 Aims of the PhD thesis

Despite the clear influence of the Reykjanes Ridge on the subpolar gyre circulation, and subsequently on the climate system, the structure of the along-ridge and cross-ridge flows are still incompletely documented. The distribution and evolution of the water masses over the Reykjanes Ridge are also poorly understood, as well as their link with the distribution of the water masses in the Iceland Basin. The asymmetrical distribution of the currents and water mass distribution on both sides of the Reykjanes Ridge has thus not been explained yet (Figures 1.3 and 1.8).

As part of the RREX project, this PhD thesis focuses on the first and second objectives described in section 1.5. The goal of this PhD is to document the synoptic circulation around and over the Reykjanes Ridge and to better understand and quantify the water mass transformation in the vicinity of the ridge. The final aim of this PhD is to create a detailed and quantified scheme of the 3-D oceanic circulation along and over the Reykjanes Ridge from the top down to the bottom. Mainly based on hydrographic and velocity data recorded during the RREX2015 cruise in June – July 2015, but also on other tools described in chapter 2, we address important issues that are still unanswered. The five questions asked by this PhD thesis are:

Q1: What are the intensity and structure of the westward branch of the North-Atlantic Subpolar Gyre across the Reykjanes Ridge? By mainly using the section that follows the crest of the Reykjanes Ridge in June – July 2015, we will describe the effect of the bathymetry on the circulation of the subpolar gyre. Preferred pathways across the Reykjanes Ridge will be identified and quantified as the locations where the westward cross-ridge flow is intensified. The vertical structure of the cross-ridge flow will also be discussed in order to see if the impact of the bathymetry depends on the depth. This question is part of the RREX project O1.3 and will be addressed in chapter 3.

Q2: Is the distribution of the water masses along the Reykjanes Ridge linked to the large-scale circulation of the subpolar gyre or/and to other local processes? By mainly using the section that follows the crest of the Reykjanes Ridge in June – July 2015, we will be able to quantify the water mass transformation above the Reykjanes Ridge and to document their connections upstream with the cyclonic circulation of the NAC in the Iceland Basin. As a consequence of this large-scale circulation, particular attention will be paid to the densification of SPMW above the Reykjanes Ridge, which paves the way for further

densification occurring downstream in the Irminger Sea. Moreover, we will see that small-scale processes, such as isopycnal and diapycnal mixing, as well as local fracture in the bathymetry of the Reykjanes Ridge, shape the water mass distribution in the vicinity of the Reykjanes Ridge. This question is part of the RREX project O1.3 and will be addressed in chapter 3.

Q3: More precisely, how the westward Iceland-Scotland Overflow Water is influenced by the bathymetry of the Reykjanes Ridge? Is ISOW entirely constrained to join the Irminger Sea through the deepest fracture zones of the Reykjanes Ridge that was previously identified (the BFZ and the CGFZ), or is there additional pathways through other non-named areas? By mainly using the section that follows the crest of the Reykjanes Ridge in June – July 2015, we will first identify and quantify all the ISOW pathways across the Reykjanes Ridge. These questions are part of the RREX project O1.2 and will be addressed in chapter 3. Moreover, although the BFZ was previously identified as a preferred pathway of ISOW across the Reykjanes Ridge, nothing is known about how this narrow bathymetry affect the westward circulation of ISOW. How the ISOW properties evolve between the entrance and exit of the fracture zone? By combining high-resolution sections obtained in the BFZ during three cruises (RREX2015, RREX2017 and OVIDE2018), as well as Deep Argo float trajectories, we will then determine the deep circulation and dynamic in the BFZ, and the role of the mixing in the evolution of the ISOW properties. This question is part of the RREX project O1.2 and will be addressed in chapter 5.

Q4: How the East Reykjanes Ridge Current interacts with the North-Atlantic Current in the Iceland Basin and what are its connections to the cross-ridge flow? By mainly using the three zonal sections perpendicular to the crest of the Reykjanes Ridge in June – July 2015, we will explain the formation mechanisms of the ERRC as it was observed along the Ovide line. We will also document the southward evolution of its horizontal and vertical structures along the Reykjanes Ridge. In term of water masses, we will document the evolution of the associated water mass properties, and more importantly, we will link these evolutions with the distribution of the water masses upstream in the Iceland Basin and downstream over the Reykjanes Ridge. The origin and fate of the water masses in the vicinity of the Reykjanes Ridge will thus be investigated. This question is part of the RREX project O1.1 and will be addressed in chapter 4.

Q5: Does the northward Irminger Current affected by inflows from the Irminger Gyre and from the Iceland Basin? By mainly using the three zonal sections perpendicular to the crest of the Reykjanes Ridge in June – July 2015, we will investigate the top-to-bottom evolution of the horizontal and vertical structures and properties of the IC. From the CGFZ to Iceland, we will highlight connections between the IC and the northward branch of the Irminger Gyre, as well as with the westward cross-ridge flow, and we will see that these connections differently affect the circulation of the two branches of the IC at each density. Final schemes of the large-scale circulation in the vicinity of the Reykjanes Ridge will be provided for each water masses identified along the ridge. This question is part of the RREX project O1.1 and will be addressed in chapter 4.

To answer these questions, geostrophic velocities and associated integrated transports were computed along each hydrographic section carried out during the two cruises of the RREX project (RREX2105 and RREX2017) and during a third cruise realized in 2018 by the Ovide program (OVIDE2018). To estimate accurate geostrophic transports, a detailed treatment of the hydrographic and velocity measurements was required. Specifically, the treatment of the Shipboard-ADCP (Acoustic Doppler Current Profiler) measurements was deeply investigated. These methods of computation are addressed in chapter 2.

2 Data and methods

2.1 Data

The RREX2015 cruise, carried out from 5 June to 10 July 2015 on the R/V Thalassa, was the first of the two cruises carried by the RREX project (Thierry et al., 2018). Along three sections perpendicular to the ridge axis, and a fourth section that extended from the Iceland shelf to 50°N, $CTDO_2$ (Conductivity Temperature Depth Oxygen), nutrient, pH and total alkalinity measurements were acquired at one hundred and thirty-three (133) stations (Figure 2.1). Current measurements were also continuously acquired by two Shipboard-ADCPs (Acoustic Current Doppler Profiler) operating at 38 kHz and at 150 kHz. This section details the acquisition and processing of these data sets as well as additional data used in this PhD thesis. Section 2.1.3 is based on a report published on SEANOE (Petit et al., 2018a).

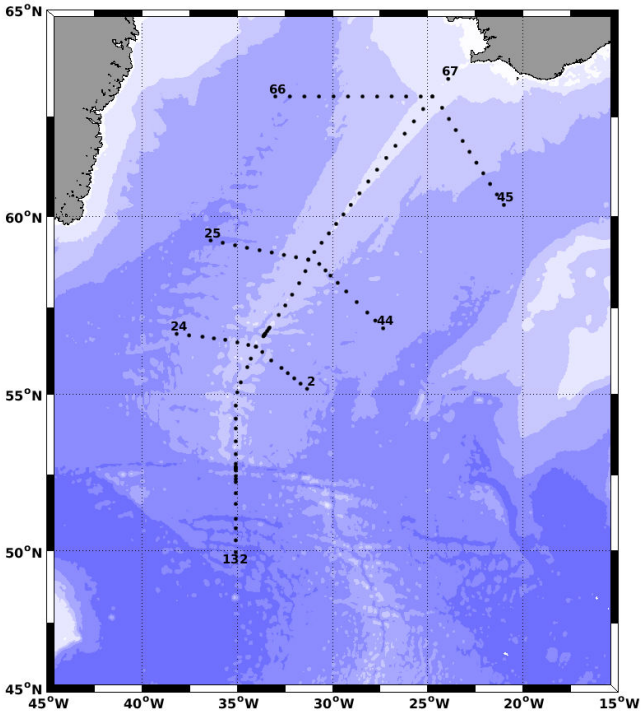

Figure 2.1: Locations of the hydrographic stations performed during the RREX2015 cruise (black dots). Bathymetry is plotted in color with color changes at 500 m, 1000 m and every 1000 m below 1000 m.

2.1.1 $CTDO_2$ data

The RREX2015 cruise was realized from 5 June 2015 to 10 July 2015 on the R/V Thalassa from Brest to Brest. During the cruise, $CTDO_2$ measurements were acquired at 133 hydrographic stations along four sections, including a test station off France (Figure 2.1). These four sections were carried out between the Irminger Sea and the Iceland Basin. The first section to be occupied was the southernmost zonal section, defined between stations 2 to 24, and referred to as the South Section in the following. The intermediate zonal section is a reoccupation, from 27.2°W to 36.4°W, of the hydrographic line carried out in the framework of the Ovide program (Daniault et al., 2016). It is defined between stations 25 to 44 and referred to as the Ovide Section. The northernmost zonal section is defined between stations 45 to 66 and is referred to as the North Section. The three zonal sections intersect the top of the Reykjanes Ridge at 34°W/56.4°N, 31.3°W/58.8°N and 24.7°W/63°N, respectively. Finally, a meridional section was carried out along the crest of the Reykjanes Ridge from the Icelandic continental shelf to 53°N, while its southern part from 53°N to 50°N retraces Saunders (1994)'s hydrographic line along 35°W. It is defined between stations 67 to 132 and referred to as the Ridge Section. During the cruise, the nominal station spacing was 30 km, which corresponds to less than 4 hours between two stations. The spacing was reduced to 2 km at the BFZ and CGFZ at about 57°N and 52.5°N, respectively. High spatial resolution of $CTDO_2$ measurements were also carried out west of the BFZ main sill between stations 102 and 107. The sections were interrupted by mooring deployments after station 9, station 18 and station 83. Details on the locations of the stations are summarized in Annex A.

At all hydrographic stations, conductivity, temperature and dissolved oxygen of seawater were measured as a function of pressure. The Seabird Electronics 911+ $CTDO_2$ probe was composed of 2 sets of sensors and was mounted on a rosette of 28 bottles. For $CTDO_2$ calibration purposes, seawater samples were analyzed on board for salinity and dissolved oxygen concentration. Temperature and pressure sensors were calibrated at the laboratory before and after the cruise and no sensor drift was detected. The accuracies of the $CTDO_2$ measurements were found to be 1 dbar for pressure, 0.001°C for temperature, 0.0025 for salinity and 1 μmol kg^{-1} for dissolved oxygen (Branellec & Thierry, 2016).

2.1.2 Lowered-ADCP data

Mounted on the rosette, Lowered-ADCPs (Acoustic Doppler Current Profiler) measurements were acquired at all hydrographic stations. The inverse method from Visbeck (2002) was used to process and combine data from upward and downward looking 300 kHz L-ADCPs . The horizontal velocity profiles at each station were thus compared and constrained by averaged Shipboard-ADCP profiles (see section 2.1.3) in order to improve the L-ADCP profiles near the sea surface. The vertical cell size was set at 16 m and the overall velocity error was estimated at 0.03 m s^{-1}.

2.1.3 Shipboard-ADCP data

We first recall ADCP measurement principle. An ADCP emits pulses of acoustic energy, called pings, in four directions from 4 beams positioned at 90° of each other. As these emitted pulses travel, they are reflected back to the ADCP by suspended particles moving with the flow (Figure 2.2). Due to Doppler effect, the reflected acoustic pulses are shifted in frequency. This shift depends on the flow velocity and allows measurements of velocity amplitude. By combining the shifts measured by the 4 beams, the ADCP provides three-dimensional velocities and a measurement error.

The Shipboard-ADCP (S-ADCP) does not measure the absolute flow velocity, but the flow velocity in the ocean with respect to the ship velocity. The latter is in general larger than the absolute flow velocity. To estimate the absolute flow velocity (V_{flow}), the ship velocity relative to the bottom (V_{ship}) must be subtracted from the relative flow velocity measured by the S-ADCP (V_{ADCP}):

$$V_{flow} = V_{ADCP} - V_{ship} \quad (1.1)$$

Three different errors affect the S-ADCP measurements. Firstly, the S-ADCP axis may be misaligned with the ship axis as shown in Figure 2.3. This mounting angle can be known by the users, but may be uncertain. To minimize this source of error, which will be referred to hereinafter as the misalignment error, a calibration procedure needs to be applied to determine the misalignment angle α. Secondly, an error is related to the amplitude of the velocity measured by the S-ADCP (Figure 2.3). Indeed, in addition to calibration issues, the plastic window separating the S-ADCP from the seawater can modify the acoustic signal and induce

an error for the velocity amplitude. Finally, the attitude of the ship during the cruise has to be corrected because it affects both measuring depth and vertical velocities.

Configurations of the two S-ADCPs used during the RREX2015 cruise are described in section 2.1.3.1. Section 2.1.3.2 describes the S-ADCP data processing done with CASCADE software to provide the best estimate of V_{flow}. It presents in particular the attitude, amplitude and misalignment corrections applied to the S-ADCP data to take into account errors due to the S-ADCP installation on the ship. Errors associated with V_{ADCP} and V_{ship} are discussed in section 2.1.3.3. A conclusion on the S-ADCP processing is provided in section 2.1.3.4.

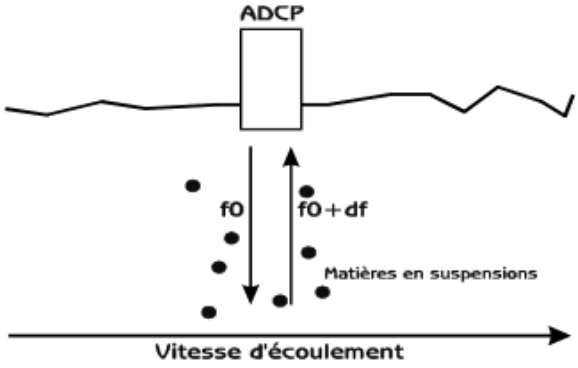

Figure 2.2: S-ADCP system (*www.eaufrance.fr/IMG/pdf/Charte-fr.pdf*).

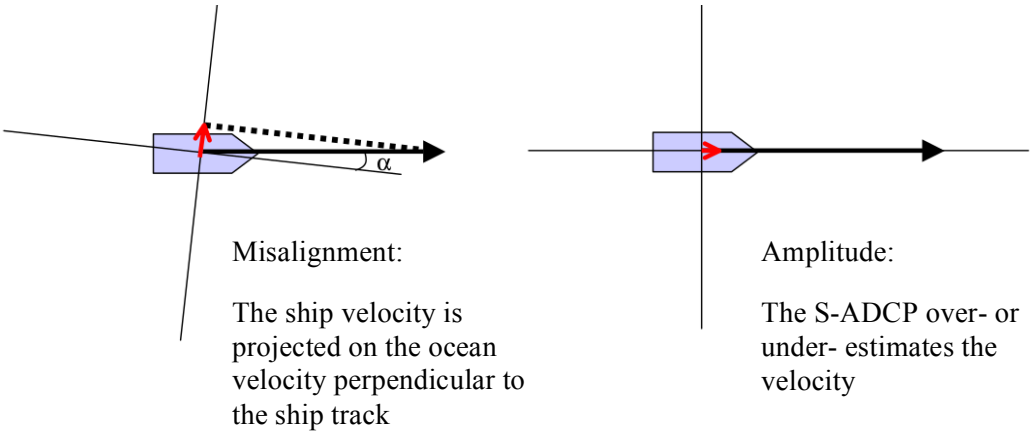

Figure 2.3: Scheme of the misalignment and amplitude errors.

2.1.3.1 S-ADCPs configuration during RREX2015 cruise

V_{ADCP} were measured during the RREX2015 cruise from two S-ADCPs operating at 38 kHz (OS38) and at 150 kHz (OS150). As shown in Figure 2.4, the maximum depth reached by the pulses was 1300 – 1400 m for the OS38 and 200 – 250 m for the OS150.

Data Acquisition System VMDAS is used to configure S-ADCP data. The configuration parameters are specified in Table 2.1. The number of vertical cells (called bins) was set to 85 for OS38 and 38 for OS150. The vertical sizes of bins were 24 m for OS38 with the middle of the first bin at 47.06 m, and 8 m for OS150 with the middle of the first bin at 20.28 m. No data is available in the first 35 m for OS38, and the first 16 m for OS150, because of the delay between emission and reception. To avoid interferences, the two S-ADCP emissions were synchronized. The resulting ping rate was 4.27 seconds for both instruments. Pings were averaged by VMDAS over 2-minute periods referred hereinafter as 2-minute ensembles.

The two instruments can operate in unmodulated Narrow Band mode (NB) or in modulated Broad Band mode (BB). The NB mode allows long-range emission while BB mode allows higher precision velocity measurement at the expense of the range. For a given accuracy, the vertical resolution in BB mode is better than in NB mode. A drawback of the BB mode is its strong sensitivity to ambient acoustic noise and interference with other sonars (Firing & Hummon, 2010), but this was dealt with on board by synchronizing acoustic emissions. As seen in Table 2.1, OS38 was used in NB mode for maximal range. Because OS150 only reaches 200 – 300 m, high precision was preferred over depth range and the BB mode was used. The BB mode was also used for OS38 during Bottom-Tracking (BT) in shallow waters. In BT, one ping over two is used to measure the ship velocity with respect to ocean bottom, which allows estimation of S-ADCP misalignment.

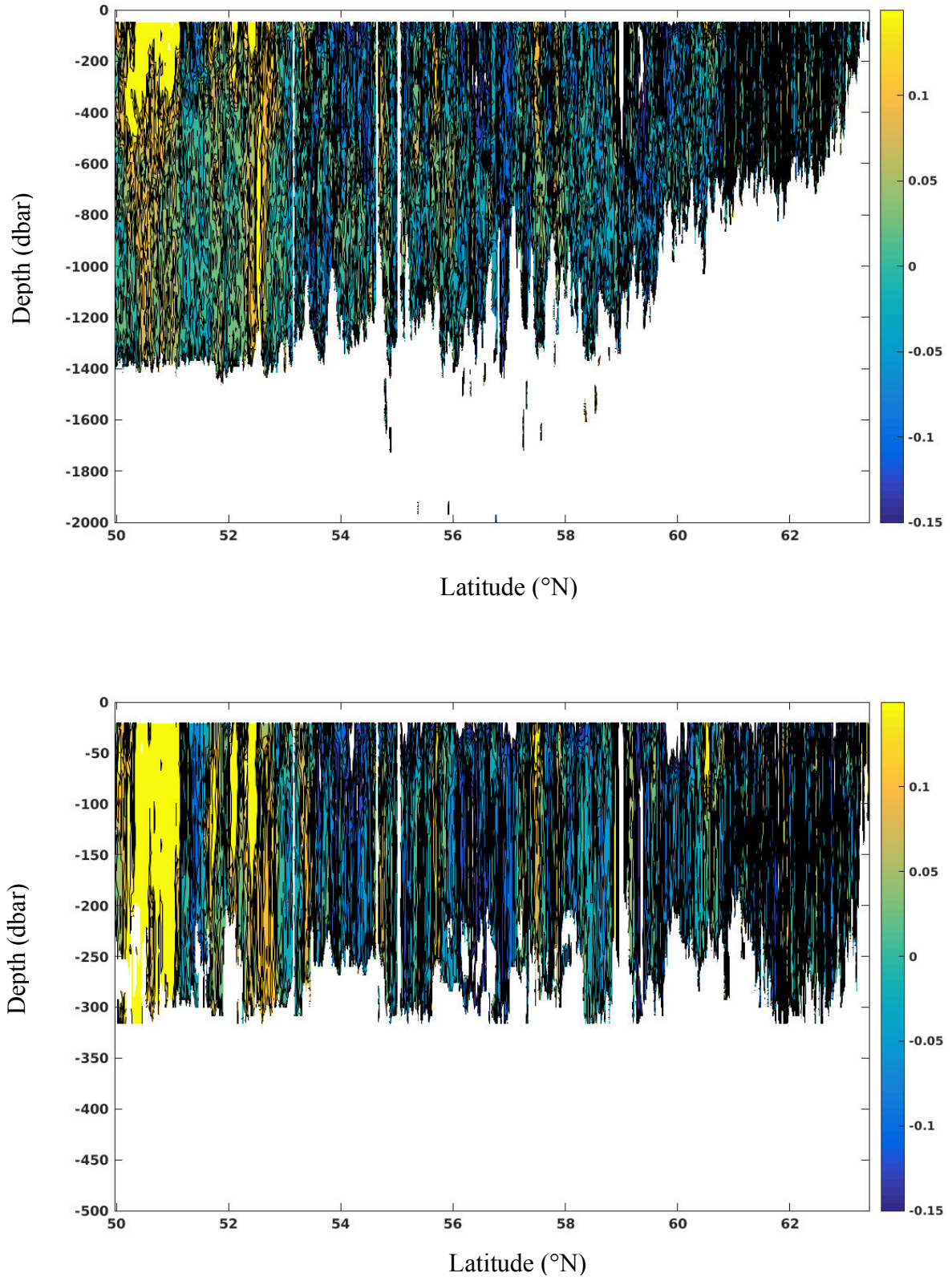

Figure 2.4: Velocity profile along the Ridge Section estimated by the two S-ADCPs mounted on the French R/V Thalassa. Amplitude (cm s^{-1}) of the component perpendicular to the section is shown for OS38 (upper panel) and OS150 (lower panel). Note the different vertical scales.

Table 2.1: Configuration of S-ADCP (OS38/OS150). Bin size is in meters.

Section	Parameterization	Number of bin	Bin size	BT mode on
1 to 2	BB/BB	85/38	24/8	1/1
3 to 21	NB/BB	85/38	24/8	0/0
22 to 24	BB/BB	85/38	24/8	1/1
25 to 37	NB/BB	85/38	24/8	0/0
38 to 39	BB/BB	85/38	24/8	1/1

2.1.3.2 S-ADCP data processing

S-ADCP data acquired during the RREX2015 cruise were processed with Cascade Version 7.0 software (« Chaine Automatisée de Suivi des Courantomètres Acoustiques Doppler Embarqués », http://www.umr-lops.fr/en/Technology/Software/Cascade-V7.1-a-matlab-software-to-process-Vessel-Mounted-ADCP-data) developed by LOPS (Laboratoire d'Océanographie Physique et Spatiale, Brest, France) since 1998. This software is designed to qualify, correct, fill gaps in, filter, and select final S-ADCP data acquired by VMDAS (file.STA).

The S-ADCP data processing was done in two stages summarized in Table 2.2 (Le Bot et al., 2011). The processing is done on the absolute flow velocity of 2-minute ensemble data points. In first stage, ETOPO1 bathymetry (Amante & Eakins, 2009) was used with statistical tests to detect doubtful or bad data. Then barotropic tides were removed based on tidal currents generated by the OSU tidal prediction software tpxo8.0 (Egbert & Erofeeva, 2002). The model resolution is 1/6° for the open ocean and it resolves the tidal components M2, S2, N2, K2, K1, O1, P1, Q1, M4, MS4, MN4, MM and MF. Finally, attitude, amplitude and misalignment corrections were estimated. The same steps were followed in a second stage except that the latter corrections were applied before data qualification and removal of the barotropic tides. At the end, filters were applied to the data and the gaps were filled in.

Table 2.2: Treatment steps of Cascade.

Step 1: New file ➔ Remove ship velocity ➔ Add bathymetry ➔ Quality control ➔ Compute the barotropic tides ➔ Determination of the corrections to apply (attitude, amplitude, misalignment)
Step 2: New file ➔ Remove ship velocity ➔ Add bathymetry ➔ Correction applied ➔ Quality control ➔ Compute the barotropic tides ➔ Filtering and gap filling

2.1.3.2..1 Quality control of the data

The aim of the quality control was to detect doubtful or bad data. First, bins below ocean bottom were removed by Cascade using ETOPO1 bathymetry. Then, series of tests were applied based on parameters defined in Table 2.3. These parameters were default values proposed by Cascade and were appropriate to the OS38 and OS150 of the RREX2015 cruise. The data was rejected if:

- The horizontal velocity (U,V) was greater than 200 cm s^{-1}
- The correlation between emitted and received pings averaged over 2 minutes was less than 0.60.
- The velocity error, which was computed as the difference between the two estimates of vertical velocity, was greater than 20 cm s^{-1}.
- The percentage of good pings for a given 2-minute ensemble (PGOOD) is smaller than 10%.
- The vertical shear of horizontal velocities was larger than 0.2 s^{-1}.
- The value is larger than ± 2.7 times the standard deviation computed over 30 ensembles of 2 minutes

Depending on the test result, a specific flag is attributed to the data and the failed data points are rejected (Table 2.4).

Table 2.3: Statistical test parameters use to quality control S-ADCP data in Cascade. Data that are rejected by statistical tests are flagged as bad.

Threshold of the vertical speed error (cm s^{-1})	20
Maximum of the vertical shear of horizontal velocity (s^{-1})	0.2
Number of ensembles to be considered before/after every profile	30
Number of STD from the median	2.7
Bottom depth detection	Bathy ETOPO1
Maximal speed (cm s^{-1})	200
Correlation threshold	0.60
Minimum % of good ensemble	10

Table 2.4: Definition of the flags.

Flags	Statistical Tests
Flag 2: suspicious data	
Flag 3: bad data	Moving median test
Flag 4: bad data	Vertical shear > 0.2 s^{-1}
Flag 5: bad data	Error velocity > 20 cm s^{-1} ; correlation < 60 ; PGOOD < 10%
Flag 6: bad data	Horizontal velocity > 2 m s^{-1}
Flag 7: no data	
Flag 8: below the bottom	
Flag 9: manual invalidation	

2.1.3.2..2 Attitude correction

The pitch and roll given by the ship navigation system were used by VMDAS for real time correction of S-ADCP measurements. We thus considered that the remaining attitude error, which depends on the position of the S-ADCP on the ship, was constant during the cruise. Cascade computed the remaining attitude angle between ship and S-ADCP from the mean vertical velocity averaged over the cruise. Indeed, vertical velocities should be of the order of 10^{-3} m s^{-1} and not affected by the ship motion. Without attitude correction, vertical velocities estimated from OS38 are positively biased (yellow zones in Figure 2.5, upper panel), with large value of mean vertical velocities averaged over the cruise (0.026 m s^{-1}) and with a root-mean-square (RMS) of 5.4 10^{-3} m s^{-1}. Assuming that the mean vertical velocity was induced by a projection of ship horizontal velocity onto the vertical, the attitude correction was obtained by dividing S-ADCP vertical velocity by the ship horizontal velocity. Indeed, for low angle values, the sinus of the angle can be considered as being a good approximation of the angle. The corrections are 0.3° for OS38 and 0.1° for OS150. The correction removes the bias of vertical velocities and was applied to our data set. For instance, once the OS38 data were corrected, the mean vertical velocity averaged over the cruise was 10-fold lower (−0.0048 m s^{-1}) and the RMS (4.5 10^{-3} m s^{-1}) was barely changed (Figure 2.5, lower panel).

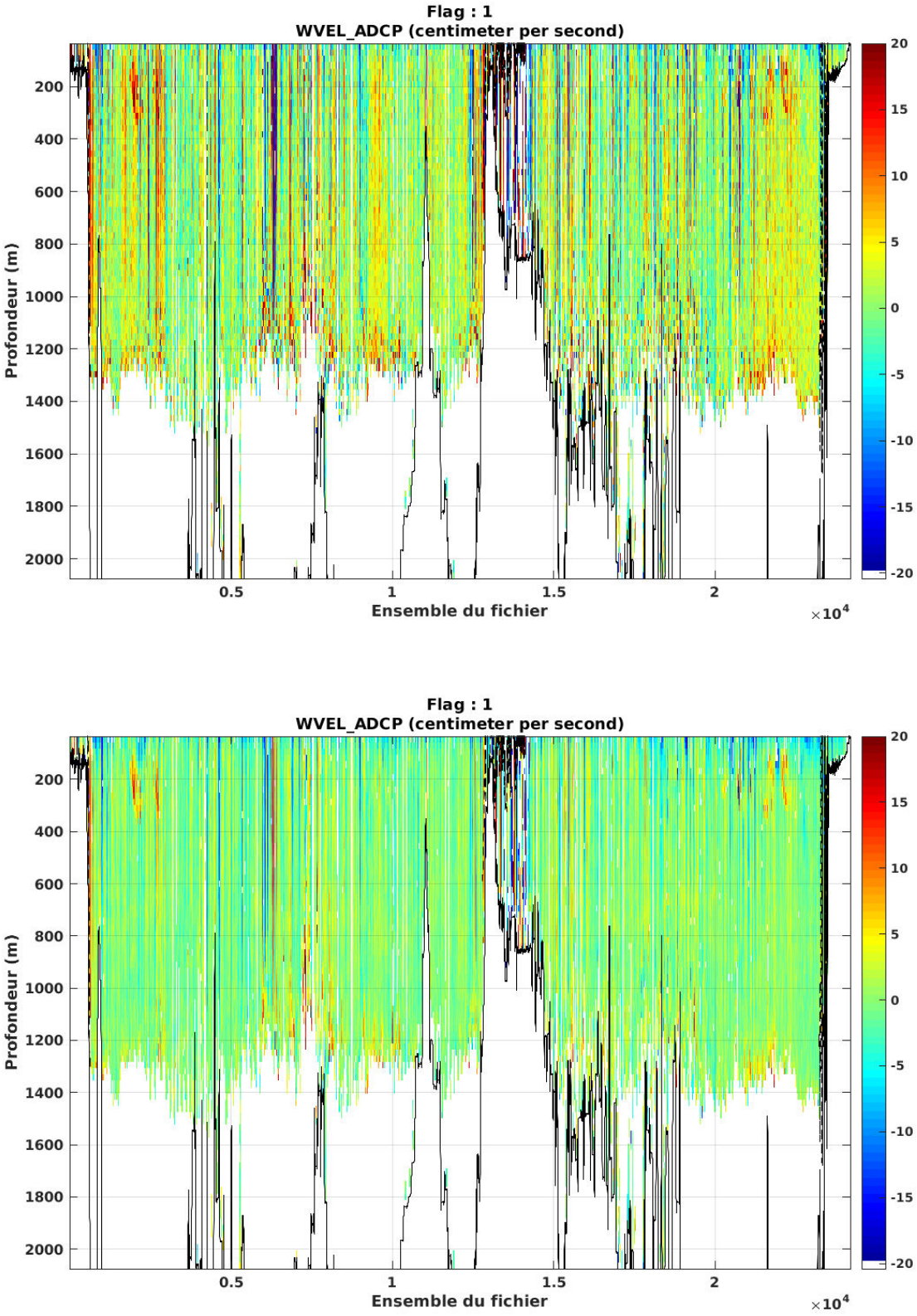

Figure 2.5: Vertical velocity of OS38 (cm s^{-1}) without attitude correction (upper panel) and with attitude correction of 0.3° (lower panel). Figures are from Cascade.

2.1.3.2..3 Amplitude and misalignment correction

To correct misalignment and amplitude errors, S-ADCP data should be calibrated using a Water-Tracking (WT) method or a Bottom-Tracking (BT) method. The WT calibration minimizes the root-mean-square differences between ocean velocities estimated by S-ADCP and by GPS during ship accelerations and decelerations, assuming a constant ocean current in a reference layer during these periods. The BT calibration compares the ship velocity estimated by GPS, to the ship velocity estimated from the S-ADCP bottom ping. The latter calibration is most reliable even though it requires specific conditions. Indeed, the BT calibration must be realized in shallow water (the acoustic pulse has to reach the bottom), which was the case at the beginning and end of the cruise, as well as on the northern part of the Reykjanes Ridge.

An amplitude and misalignment correction was thus estimated using Bottom-Tracking (BT) data in Cascade. Coefficients of amplitude and misalignment corrections were respectively associated with the difference of amplitude and direction between GPS and BT ship velocities for rectilinear motion and uniform speed of the ship. These computations should only take into account data recorded while the ship was moving (ship velocities > 2.5 m s^{-1}). Indeed, linear regression of BT versus GPS ship velocities used for the determination of amplitude correction in Figure 2.6 highlights the outliers at low ship speed. Statistical tests were implemented in Cascade to remove outliers. We considered data for which C_{ship}> 2.5 m s^{-1} and data for which the amplitude differences between BT and GPS ship velocities were less than 2.7 times the standard deviation. By following this procedure, we obtained a correlation coefficient of 0.99 between the BT and GPS ship velocity estimates. The amplitude correction was estimated as the slope of the linear regression between the two estimates (Figure 2.7, Table 2.5). Similar statistical tests were implemented for the misalignment computation (Figure 2.8, Table 2.5).

To refine the misalignment correction, OS38 data were compared with OS150 data for several corrections (Table 2.6). The aim was to determine whether these two data sets were compatible and if varying the misalignment correction within the confidence interval minimized a possible bias between these two data sets.

Without misalignment correction (0/0 in Table 2.6), there is a negative bias of -0.0099 cm s^{-1} between the two S-ADCP ocean velocity estimates averaged between the surface and 250 m.

The OS38 alignment has then a positive trigonometric angle α with OS150, which means that OS38 orthogonal velocities are on the left side of OS150 orthogonal velocities.

Table 2.5: Misalignment and amplitude corrections for OS38 and OS150.

OS38	Misalignment α (°)	Amplitude a (cm s^{-1})
Bottom Tracking	0.07 ± 0.03	1.0067 ± 0.0001

OS150	Misalignment α (°)	Amplitude a (cm s^{-1})
Bottom Tracking	-0.06 ± 0.03	1.0027 ± 0.0001

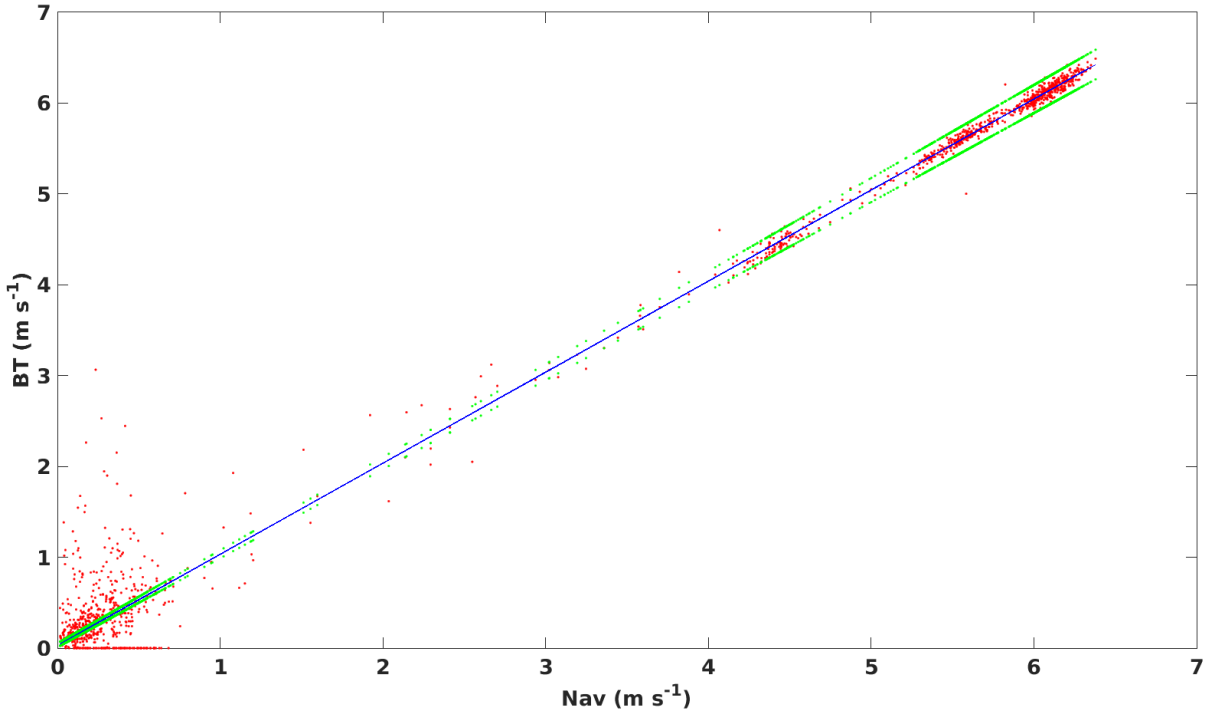

Figure 2.6: Linear regression (blue line) of BT versus NAV (GPS) velocities above Reykjanes Ridge (red dots) with the 99% confidence interval (green lines) for OS38. All data acquired above Reykjanes Ridge were used for the determination of amplitude correction ($R^2 = 0.98$).

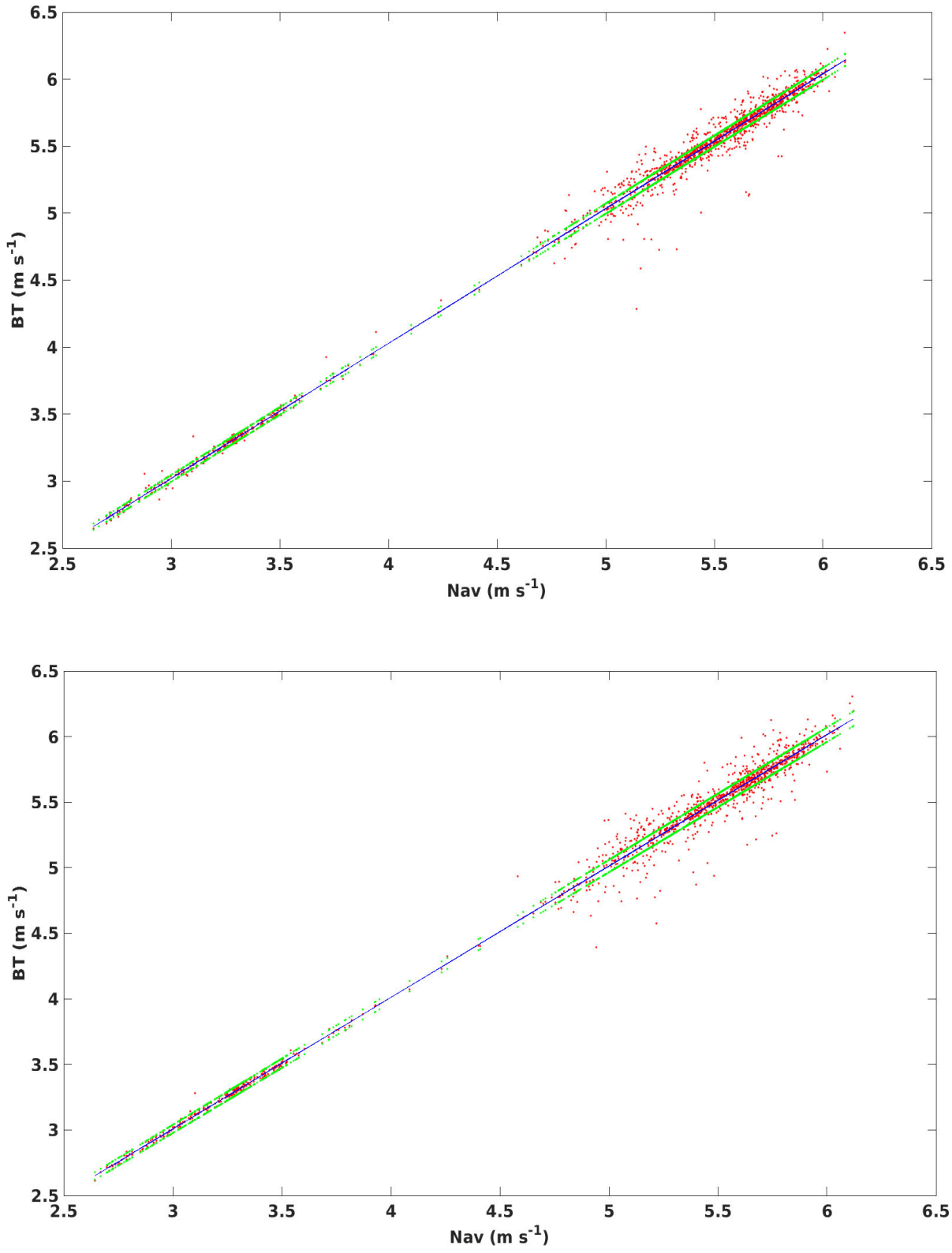

Figure 2.7: Linear regressions (blue line) of BT versus NAV (GPS) velocities (red dots) with the 99% confidence interval (green lines) for OS38 (upper panel) and OS150 (lower panel). Data used for the determination of amplitude correction were taken at the beginning and end of the cruise (R^2 = 0.99). The correction factor applied was a = 1.0067 cm s^{-1} for OS38 and a = 1.0027 cm s^{-1} for OS150.

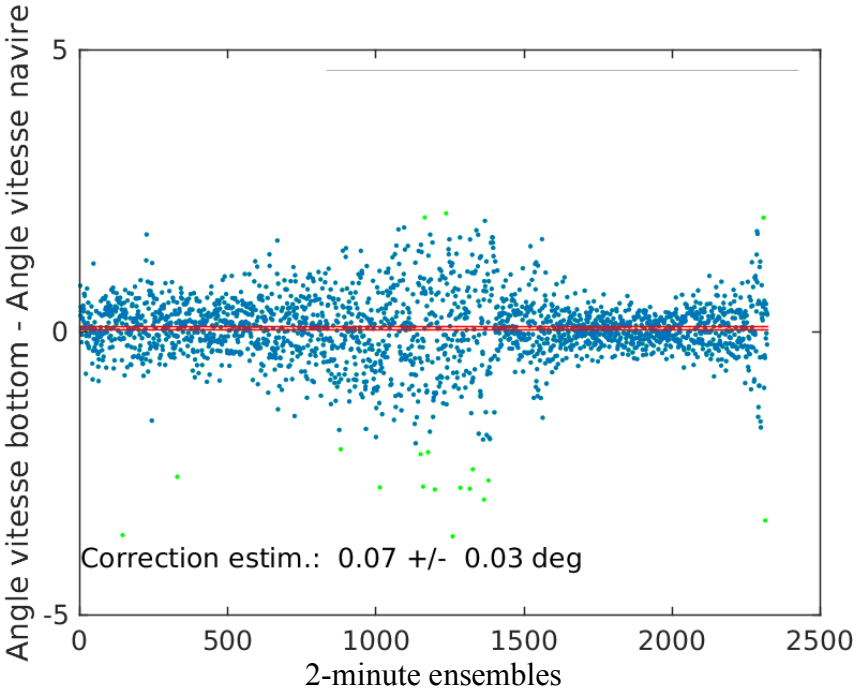

Figure 2.8: Difference of direction between Bottom-Tracking and GPS ship velocities for each 2-minute ensembles of OS38. The misalignment correction coefficient is the difference averaged on the whole data set and was estimated by Cascade as 0.07 ± 0.03°. Blue dots are data taken into account for the computation while green dots were excluded by the statistical tests of Cascade. Red lines delimit the confidence interval of 95%. Figure from Cascade.

Applying the misalignment corrections provided by Cascade (0.07 for OS38 and -0.06 for OS150 in Table 2.6) divides the bias between OS38 and OS150 by three. Nevertheless, velocities perpendicular to the ship track still have a positive bias of 0.0032 m s^{-1}. By varying the misalignment corrections of OS38 and OS150 within their respective confidence intervals, we found that the smallest biases (10^{-3} m s^{-1}) were obtained with corrections 0.05/-0.04, 0.06/-0.04 and 0.05/-0.05. For these 3 pairs of corrections, bias values are very close. Figure 2.9 shows that the vertical average of cumulated differences is similar whatever the choice. The maximum difference is 0.00073 m s^{-1} for the Ridge Section, 0.00017 m s^{-1} for the North Section, 0.001 m s^{-1} for the South Section and 0.0001 m s^{-1} for the Ovide Section. Figure 2.9 shows the rapid convergence of these differences after averaging over about 100 km. Because the misalignment correction 0.05° for OS38 and -0.04° for OS150 are among the best choices for the full RREX2015 cruise, we applied these corrections to our data sets.

Table 2.6: Statistical studies of the misalignment correction for the Ridge Section. Among the coefficients proposed by Cascade, bias and standard deviation were computed between OS38 and OS150 orthogonal velocities (cm s^{-1}).

Misalignment corrections OS38/OS150 (degree)	Bias (cm s^{-1})	Standard deviation (cm s^{-1})
0/0	-0.0099	0.018
0.07/-0.06	0.0032	0.017
0.06/-0.05	0.0011	0.017
0.05/-0.04	-0.00081	0.017
0.04/-0.03	-0.0028	0.017
0.04/-0.04	-0.0018	0.017
0.06/-0.04	0.00020	0.017
0.07/-0.04	0.0012	0.017
0.05/-0.03	-0.0018	0.017
0.05/-0.05	0.00014	0.017
0.05/-0.06	0.0011	0.017

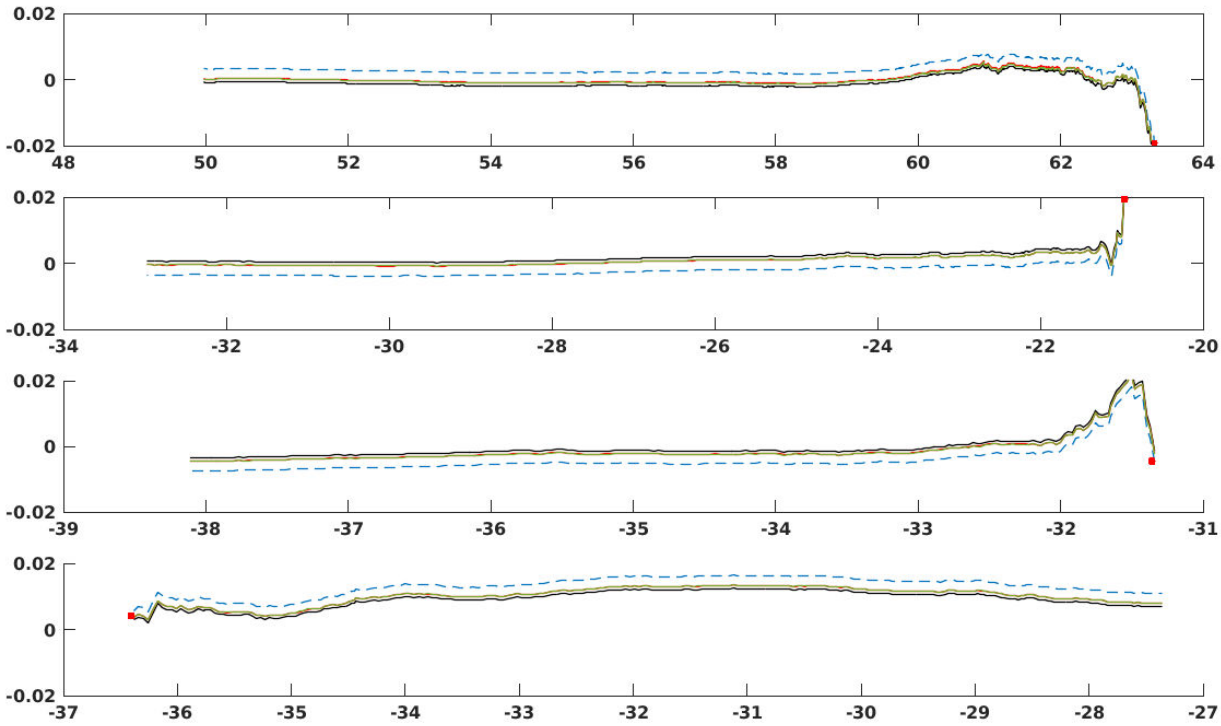

Figure 2.9: X-axis: Latitude / Longitude (°N / °W); Y-axis: Vertical top-to-bottom average of cumulated differences of orthogonal velocities (m s^{-1}) between OS38 and OS150 for various misalignment corrections along the Ridge (top), North (mid top), South (mid bottom) and Ovide (bottom) Sections. The blue dash line is for the initial misalignment correction 0.07/-0.06; the black line is for 0.05/-0.04; the red line is for 0.06/-0.04; and the green line is for 0.05/-0.05. Red point indicates the beginning of the accumulation.

2.1.3.2..4 Filtering and gap filling

As described in Table 2.2, the corrections previously determined (attitude, misalignment and amplitude) are applied before filtering and gap filling the data.

To filter the data, a running average is used on 3 horizontal and vertical points following the [¼ ½ ¼] rule. Note that when the average includes more than 2 suspicious data (flag = 2), the resulting data is flagged as suspicious (Table 2.4). Missing data (white areas of the raw data in Figure 2.10, upper panel) are replaced by the average of two surrounded good data and are flagged as suspicious (flag = 2). Figure 2.10 (bottom panel) shows the filtering and gap filling of the OS38 data proposed by Cascade. Because the averaged velocity only changed by 10^{-4} m s^{-1} before and after this stage, the interpolation does not impact the final result and was applied to our data set.

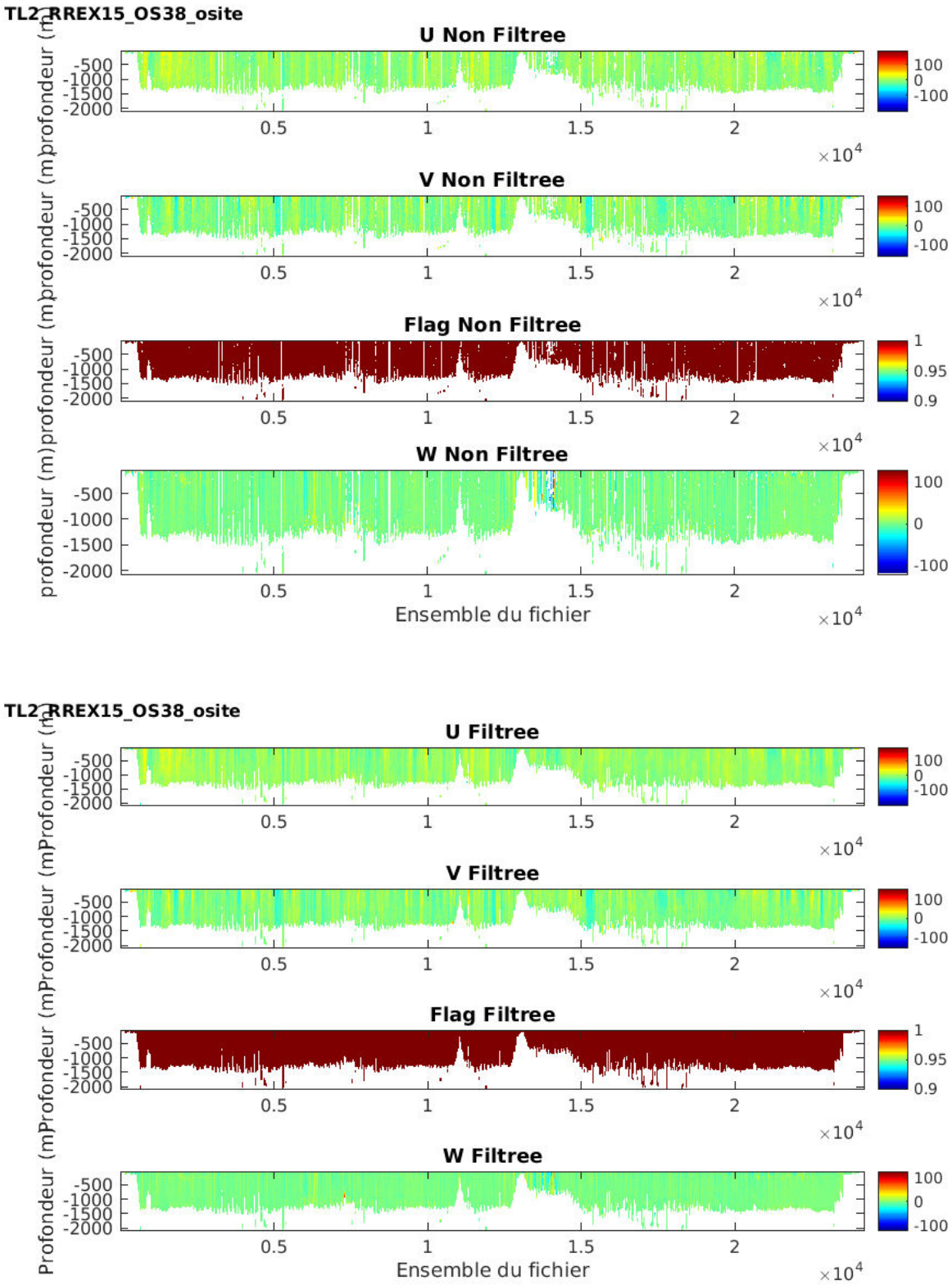

Figure 2.10: OS38 velocities and flag before (top) and after (bottom) filtering and gap filling. Figures are from Cascade.

2.1.3.3 Instrumental errors

Main instrumental errors come from the S-ADCP and GPS, which affect V_{ADCP} and V_{Ship}, respectively. Firstly, the S-ADCP error depends on the S-ADCP frequency, calibration, and configuration (such as the BT, bin size...) reported in Table 2.1. For OS38, profiles were mainly acquired in NB mode with a bin size of 24 m. As stated by the manufacturer, the measurement error on a single ping velocity is 23 cm s^{-1}. By averaging the velocity profiles over 2-minute ensemble of 29 pings, the velocity error decreases to $\varepsilon_{OS38} = 23/\sqrt{29} = 4.27$ cm s^{-1}. In BT, 2-minute ensemble was associated with 17 pings resulting in a larger velocity error of 5.58 cm s^{-1}. The OS150 was configured in BB mode with a bin size of 8 meters, which is associated with a velocity error of 9 cm s^{-1} per ping. For a 2-minute ensemble of 29 pings, the velocity error decreases to $\varepsilon_{OS150} = 1.67$ cm s^{-1}. In BT, 2-minute ensemble was associated with 17 pings resulting in a velocity error of 2.18 cm s^{-1}.

The second main instrumental error comes from the GPS. As shown by King & Cooper (1993), a 0.5° error in the ship heading affects the ship velocity of about 1%. For a ship moving at 5 m s^{-1} the induced error is 5 cm s^{-1}. During the RREX2015 cruise, GPS HDS800 gave geographical coordinates of the ship. Because the GPS system is identical to Chafik et al. (2014), its accuracy was estimated by using the same calculation, which show a standard error of $\varepsilon_{GPS} = 1$ cm s^{-1} for 2-minute averaged GPS derived ship velocity.

In NB mode, the total instrumental error on absolute ocean velocity, caused by S-ADCP and GPS, is then $\sqrt{(4.27^2 + 1^2)} = 4.39$ cm s^{-1} for OS38. In BB mode, the total instrumental error is 2.40 cm s^{-1} for OS150. All these instrumental errors are random and decrease to zero for a large number of data.

2.1.3.4 Conclusion

We processed and qualified S-ADCP data acquired during the RREX2015 cruise on the R/V Thalassa using the software Cascade. The processing consisted in validating, correcting, filling gaps in, filtering, and selecting final S-ADCP data. Considering the mean vertical velocity averaged over the cruise, we estimated an attitude corrections of 0.3° for OS38 and 0.1° for OS150. We also estimated the misalignment (α) and amplitude (a) corrections by comparing ship velocity determined by GPS, to ship velocity estimated from the S-ADCP

bottom ping in shallow water. Minimizing the bias between OS38 and OS150 further refined the misalignment correction. For the OS38, we found $\alpha = 0.05°$ and $a = 1.0067$ cm s^{-1}. For the OS150, we found $\alpha = -0.04°$ and $a = 1.0027$ cm s^{-1}. After correction, the agreement between OS38 and OS150 is remarkable and reveals the overall quality of these data sets (difference RMS of about 0.0001 m s^{-1}).

We also estimated the total instrumental error on the absolute ocean velocity calculated from errors on both V_{ADCP}, the flow velocity relative to the ship velocity estimated by the S-ADCP, and V_{ship}, the ship velocity relative to the bottom measured by GPS. For OS38 in Narrow Band mode, the total instrumental error on the absolute ocean velocity is 4.39 cm s^{-1}. For OS150 in Broad Band mode, the total instrumental error is 2.40 cm s^{-1}.

2.1.4 The AVISO data set

Merged-Absolute Dynamic Topography (MADT) from the Ssalto/Duacs AVISO (Archiving, Validation and Interpretation of Satellite Oceanographic data center) altimeter products distributed by CMEMS (Copernicus Marine Environment Monitoring Service) on a 1/3° grid was used to compute time-averaged surface geostrophic velocities over the period from 5 June to 10 July 2015.

2.1.5 Atmospheric reanalysis

Wind stress data from the two global atmospheric reanalysis, ERA-Interim reanalysis (Dee et al., 2011) and NCEP/NCAR reanalysis (Kalnay et al., 1996) were used to compute the Ekman transport at the location and time of measurements at each hydrographic station.

2.2 Computation of geostrophic transports

2.2.1 General Principle

Derived from the thermal wind equation, Equation 2.2 allows us to compute geostrophic velocities at each pair of hydrographic stations. Using the dynamical height difference between two adjacent stations, relative geostrophic velocities orthogonal to the axis of the two stations are computed as:

$$V_{geo}{}^{rel}\,(x, z) = V_{geo}\,(x, z) - V_{geo}\,(x, Z_0) = \frac{dH(x,z)}{f\,.\,l(x)} \qquad (2.2)$$

Where V_{geo} (x, z) is the absolute geostrophic velocity at the depth z and at the middle horizontal position x between the two stations, V_{geo} (x, Z_0) is the referenced velocity at a reference depth (Z_0 = 0 m), f is Coriolis parameter, l is the distance between $CTDO_2$ stations, and dH is the difference between two adjacent stations of the dynamical heights relative to the surface at each depth. The dynamical height was computed relative to the surface with potential temperature, salinity and pressure of $CTDO_2$ data from the surface to the bottom. Over sloping topography, the treatment of bottom triangles requires a specific procedure, which is discussed in section 2.2.2.

To obtain an absolute geostrophic field, the geostrophic field referenced to the surface has to be adjusted to an absolute reference velocity at the absolute reference layer L_{ref}. The absolute geostrophic profile was computed by adding a constant velocity correction to the geostrophic velocity profile referenced to the surface. For a long time, this reference velocity was not directly measured. Then, it was estimated from climatological values (Álvarez et al., 2004), from floats and more recently from Lowered or Shipboard ADCP (Joyce et al., 2001). Ganachaud (2003) also showed the possibility of using altimetry data, although the altimetric uncertainties are larger along boundary currents and over topographic ridge due to larger geoid errors at small horizontal scales. Studies along the historic Ovide line (Lherminier et al., 2007, 2010) have shown the good accuracy of absolute geostrophic fluid constrained by S-ADCP reference velocity. For this study, the S-ADCP data were thus used to estimate the reference velocity at the absolute reference level. OS38 was preferred over OS150 because the measurements reached deeper depths associated with less energetic ageostrophic motions (Figure 2.3).

Finally, the absolute geostrophic velocity was used to compute geostrophic transports along the four hydrographic sections. These transports are the sum of geostrophic and Ekman transports. To compute geostrophic transport, each geostrophic velocity was assigned to a surface equal to the distance between the stations of each pair multiplied by the vertical resolution of the geostrophic velocity profile. Then, the transport for a region limited by the hydrographic stations in the horizontal, and constant depths, isopycnals, or bathymetry in the vertical, was computed as the sum of the products of the geostrophic velocities by the associated surfaces over the region considered.

2.2.2 Bottom triangles

In presence of sloping topography, especially over the rough bathymetry of the Reykjanes Ridge, the geostrophic velocity referenced to the surface can only be computed down to the deepest common level (DCL) and do not reach the bottom as shown in Figure 2.11. For computing velocities in the triangle localized below the DCL of a pair of hydrographic stations, it is recommended to extrapolate the hydrographic data of the shallow station (white dots) from the measured deeper station (black dots). The dynamical height at the shallow station was extrapolated below the DCL by using the deepest station potential temperature and salinity. The geostrophic reference level should not be below the DCL to avoid the propagation of errors. Four methods of extrapolation, considered as robust by Ganachaud (2003), were compared:

- « Plane fit » computes a linear function by using the least-squares method such as: $P_{extrapolate} = P_1X + P_2Z + P_3$ where X is the distance between the two stations of the pair, Z is the depth relative to the DCL, P_i are the linear coefficients computed from the dynamical height at the DCL of the shallowest station and below the DCL of the deepest station, and $P_{extrapolate}$ is the dynamical heights computed below the DCL of the shallowest station (white dots) by linear interpolation from the DCL point of the shallow station.

- « Polynomial fit » uses a higher order polynomial than the « plane fit » such as: $P_{extrapolate} = P_1X + P_2Z + P_3 + P_4Z^2$. The higher order is in Z because data are localized

vertically below the DCL of the deepest station. Non-linear variations near the bottom are thus taken into account.

- « Constant slope » computes the slope of dynamical height between the two stations of the pair at the DCL level by using the last point of the shallowest station and the two last points of the deepest station. This slope is then applied from the measured data below the DCL of the deepest station. This is the least reliable method because only three measured points are used to interpolate the profile.

- « Horizontal extrapolation » uses a linear horizontal extrapolation below the DCL from data of the deepest station and these next to it. The method is able to compute the velocity shear in a triangle. However, the maximal extrapolated depth of the shallow profile is limited to the common depth of the two deepest stations.

To apply the most appropriate method, absolute geostrophic velocities were estimated in the bottom triangles by using these four methods of extrapolation. Table 2.7 compares the associated cumulated transports along the Ridge Section. These transports were computed as the sum of the products of the absolute geostrophic velocities by the associated surfaces of the bottom triangles, which is between the DCL and the bottom vertically, and between the two stations of the pair horizontally. The bottom triangles were adjusted to the bottom depth given by the ship sounder. Table 2.7 shows low cumulated transports in the bottom triangles (< 2 Sv), and that the « plane fit » method is associated with a higher transport than the « polynomial fit » method. As specified by Ganachaud (2003), the « plane fit » does not reproduce the nonlinear variability near the bottom. A second order polynomial is thus preferred in regions of nonlinear variability such as in the vicinity of the Reykjanes Ridge. On the contrary, the « constant slope » method is associated with lower transports than the « polynomial fit » method. The « constant slope » method is the least reliable method because only three measured points are used to extrapolate the dynamical height of the shallower station. Finally, we note that the « horizontal extrapolation » method is associated with an identical transport than that computed with the « polynomial fit » method. Although Ganachaud (2003) considered the « horizontal extrapolation » as more reliable, it cannot be used systematically along the Ridge Section because of a large number of seamounts. Indeed, the dynamical height differences may be computed between two stations that are localized on each side of a seamount where the dynamic is different. The vertical variability measured by

the deepest hydrographic station cannot be applied to the shallower station on the other side of the seamount. Therefore, the second-order « polynomial fit » method is considered as the most appropriate method and was applied along the four sections of the RREX2015 cruise.

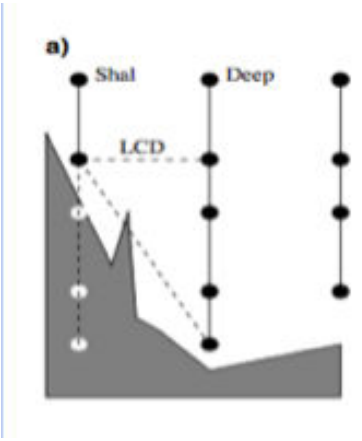

Figure 2.11: This figure from Ganachaud (1999) illustrates the bottom triangle problem. The first line corresponds to the shallow station, the second line to the deep station. The black dots indicate $CTDO_2$ measurements while the white dots indicate the extrapolated data. The DCL stands for the Deepest Common Level. The topography is shaded.

Table 2.7: Cumulated transports (Sv) in the bottom triangles of the Ridge Section for the four methods of extrapolation, and RMS of the differences between these methods and the « polynomial fit » method.

	Plane fit	Polynomial fit	Constant Slope	Horizontal Extrapolation
Accumulated Transports (Sv)	-1.14	-0.9	-0.63	-0.9
RMS ($m\ s^{-1}$)	$1.9\ 10^{-5}$	X	$1.2\ 10^{-5}$	$3.7\ 10^{-5}$

2.2.3 Computation of the absolute reference velocities

The absolute geostrophic field was computed by adjusting the geostrophic field referenced to the surface to an absolute reference velocity, which was fitted to OS38 measurements between the two stations of the pair (Gourcuff et al., 2011; Lherminier et al., 2007). After having projected S-ADCP velocities perpendicularly to the axis of the station pair, the S-ADCP velocities were averaged in a layer called the absolute reference layer L_{ref} and constrained the geostrophic profile in this layer. The determination of the absolute reference layer is discussed in section 2.2.5. Equation 2.3 shows the computation of the absolute geostrophic field.

$$V_{abs}(x, z) = V_{geo}^{rel}(x, z) - \langle V_{geo}^{rel}(x, z) \rangle_{Lref} + \langle V_{ADCP}(x, z) \rangle_{Lref} \quad (2.3)$$

Where $V_{geo}^{rel}(x, z)$ is the relative geostrophic velocity computed with the Equation 2.2, $\langle V_{geo}^{rel}(x, z) \rangle_{Lref}$ is the relative geostrophic velocity averaged in the absolute reference layer L_{ref}, $\langle V_{ADCP}(x, z) \rangle_{Lref}$ is the S-ADCP reference velocity averaged in the absolute reference layer L_{ref}, and z is the depth (m).

Two methods can be used to estimate the S-ADCP reference velocities $\langle V_{ADCP}(x, z) \rangle_{Lref}$. The « averaging » method, used by Lherminier et al. (2007), horizontally averages S-ADCP velocities between two hydrographic stations and provides mean velocities at the middle geostrophic point. The « filtering » method filters out small scales from S-ADCP data between two hydrographic stations such as the absolute reference velocity is the S-ADCP velocity found at the geostrophic point. In this study, the S-ADCP reference velocities were estimated by combining these two methods: the S-ADCP data were first horizontally filtered and then averaged between two hydrographic stations. The aim was to filter out the small-scale perturbations that perturb the averaged S-ADCP data, without loosing information over the station pair. Indeed, mesoscale features can locally perturb S-ADCP velocities averaged between two stations of tens of kilometers, but as shown by Lherminier et al. (2007), these side effects tend to be smoothed by filtering the data. Lanczos filter was preferred in order to minimize Gibbs phenomenon in the vicinity of the cutoff frequency in the function of transfer. By applying various cutoff frequency between [1/L : 1/2Δx] with Δx = 2 km, it appears that cutoff frequency smaller than $1.3\ 10^{-4}\ s^{-1}$, equivalent to 8 km, was appropriate along the Ridge Section. A filter with a cutoff frequency of $1.3\ 10^{-4}\ s^{-1}$ was thus applied on the OS38 velocities.

2.2.4 Determination of the absolute reference layer

One difficulty was to choose an absolute reference layer L_{ref}. To satisfy the geostrophic hypothesis, the layer should not be too close to the surface nor the bottom, which are affected by strong ageostrophic motions caused by energetic bottom and wind frictions, interaction of tides with bathymetry (internal waves), inertial oscillations, or cyclogeostrophic terms at surface (Ganachaud, 1999). S-ADCP velocities at depths shallower than 50 – 100 m are thus not geostrophic and should not be taken into account (Gourcuff et al., 2011). However, even when considering layers deeper than 100 m, the resulting absolute geostrophic velocities V_{abs} varied depending on the absolute reference layer that was applied. Figure 2.12 shows the impact of the absolute reference layer on the cumulated transport curves computed from the associated absolute geostrophic velocities along the Ridge Section and fitted to OS38. The difference between these cumulated transport curves could reach over 15 Sv and occurs mainly at the BFZ (56.7°N), at pair 113 (54.5°N) and at the CGFZ (52.5°N). To select an appropriate layer, it is thus useful to inspect the velocity profiles at these locations separately.

To analyze the differences between the OS38 and absolute geostrophic velocities and better understand their origin, the two velocity profiles were compared at each station pair. At station pair 110 (Figure 2.13), which is associated with a typical station pair of our data set, the profiles are parallel. This means that the two data sets have the same physical content, even though small-scale features perturb OS38 velocities. A Lanczos filter was used vertically to smooth these small-scale perturbations. At station pair 110, the noise was reasonably reduced with a filtering on 400 m, which indicates that the absolute reference layer should be vertically filtered on 400 m and preferentially defined with a minimum thickness of 400 m. At station pair 113 (Figure 2.14), which is associated with large differences in the cumulated transport curves (Figure 2.12), the OS38 profile shows larger vertical variations than at station pair 110. These variations are not observed in the geostrophic profile, probably because these small-scales variations were associated with inertial waves that twisted the filtered velocity profile above 500 m. The absolute reference layer should thus be vertically filtered on 400 m and preferentially defined with a minimum thickness of 400 m as well as deeper than 500-m depth.

In some cases, it may be hard to select an appropriate absolute reference layer. Figure 2.15 (upper panel) shows strong vertical shears that perturbed geostrophic profiles at the BFZ and CGFZ. These features are related to the reduced spacing of the hydrographic stations at these

locations (Figure 2.1). Indeed, geostrophic profiles computed between closely spaced hydrographic stations are more affected by internal waves. However, the ageostrophic perturbations vanish when a unique averaged OS38 velocity is applied to these geostrophic profiles (Figure 2.15, lower panel). For each fracture zone, each geostrophic profile was thus adjusted to the same OS38 reference velocity that was averaged between pairs 96 – 101 for the BFZ and 119 – 122 for the CGFZ.

To conclude, the strong differences between the cumulated transport curves showed in Figure 2.12 are mainly explained by ageostrophic motions localized above 500 m at about 54.5°N and by the high horizontal resolution above the BFZ and CGFZ. Figure 2.16 shows the cumulated transport curves computed with an absolute reference layer deeper than 500 m, vertically filtered, and with the specific computation applied at the BFZ and CGFZ. There, the cumulated transport curves are close. The maximum difference between the two furthest curves is under 2 Sv. Finally, selecting L_{ref} = 600 – 1000 m of 400-m thick led to the best agreement between the geostrophic and OS38 profiles and was applied in our computation.

2.2.5 Conclusion

In section 2.2, we computed top-to-bottom absolute geostrophic velocities along the four sections of the RREX2015 cruise. These velocities allowed us to quantify the first exchange of volume and water mass transports above the Reykjanes Ridge and to better understand the role of the Reykjanes Ridge on the dynamic and water mass transformation in the subpolar gyre. A major difficulty in the vicinity of the Reykjanes Ridge was to compute geostrophic velocities over its sloping and rough bathymetry. To estimate accurate geostrophic transports across the deepest fracture zones, we used a second-order polynomial fit in the bottom triangles of the four hydrographic sections. In order to minimize the impact of ageostrophic motions, we adjust the geostrophic profiles with OS38 velocities that were horizontally and vertically filtered by 2-km × 16-m using Lanczos filters with respective cutoff wave numbers of 1/8 km^{-1} and 1/400 m^{-1}. Finally, we showed that the absolute geostrophic velocities strongly depend on the depth and thickness of the absolute reference layer due to ageostrophic perturbations in the OS38 velocities. At the BFZ and CGFZ, the high horizontal resolution also causes ageostrophic motions in the geostrophic velocity profiles. By studying the OS38

and geostrophic profiles separately, we choose to apply the absolute reference layer L_{ref} = 600 – 1000 m, with a unique averaged absolute reference velocity at the BFZ and CGFZ.

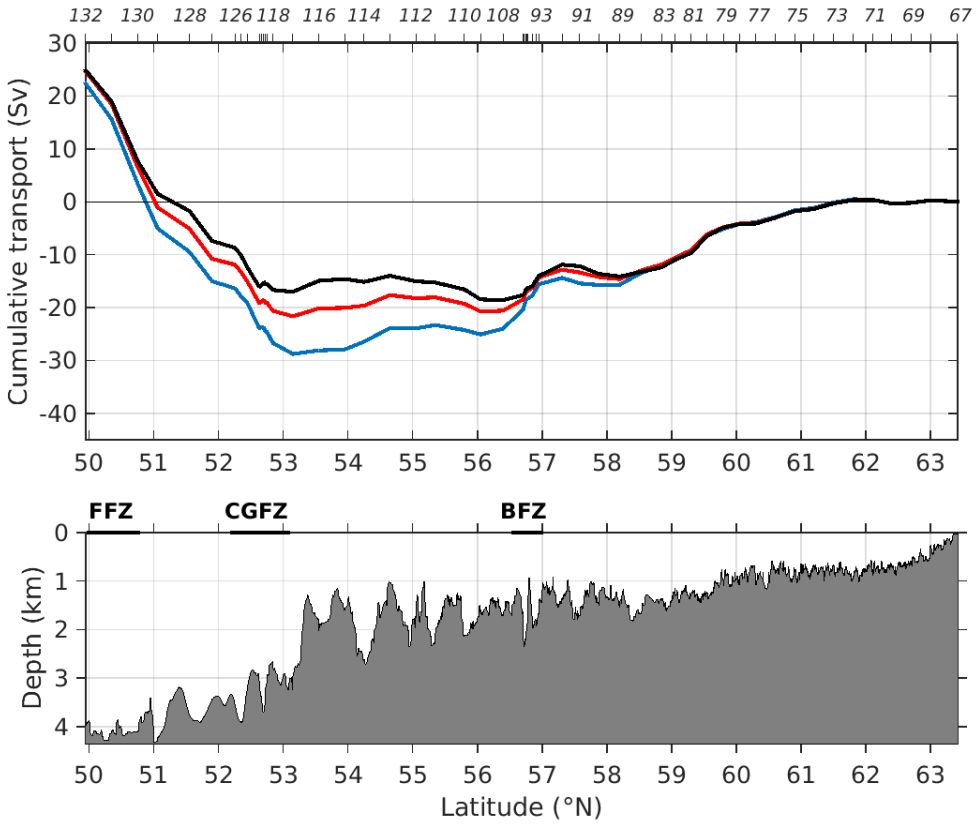

Figure 2.12: Cumulated transport curves (Sv) fitted to OS38 with various absolute reference layers (deeper than 100 m): L_{ref} = 400 – 500 m (blue line), L_{ref} = 500 – 600 m (red line), L_{ref} = 600 – 700 m (black line). The locations of the hydrographic stations are shown on the top axis. Lower panel: Bathymetry along the Ridge Section. CGFZ stands for Charlie Gibbs Fracture Zone, BFZ for Bight Fracture Zone, and FFZ for Faraday Fracture Zone.

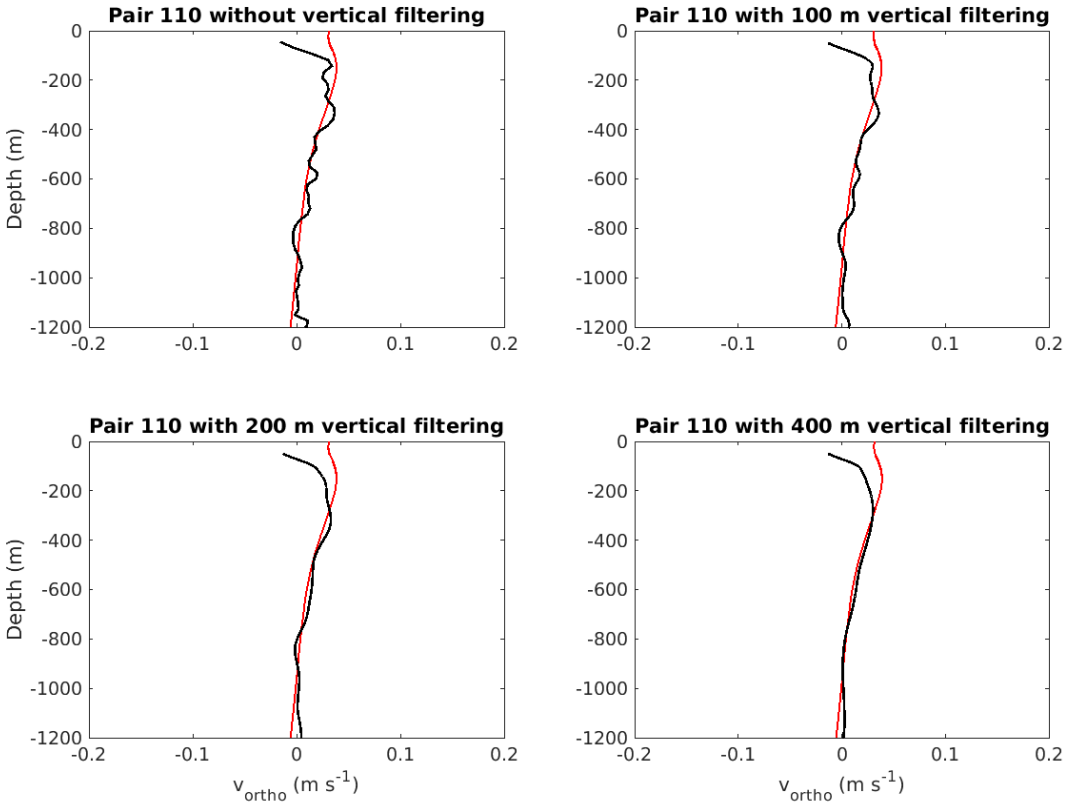

Figure 2.13: Velocity profiles of pair 110. Red lines are the absolute geostrophic velocities fitted to OS38 with L_{ref} = 500 – 1000 m; Black dash lines are the vertically filtered velocities from OS38.

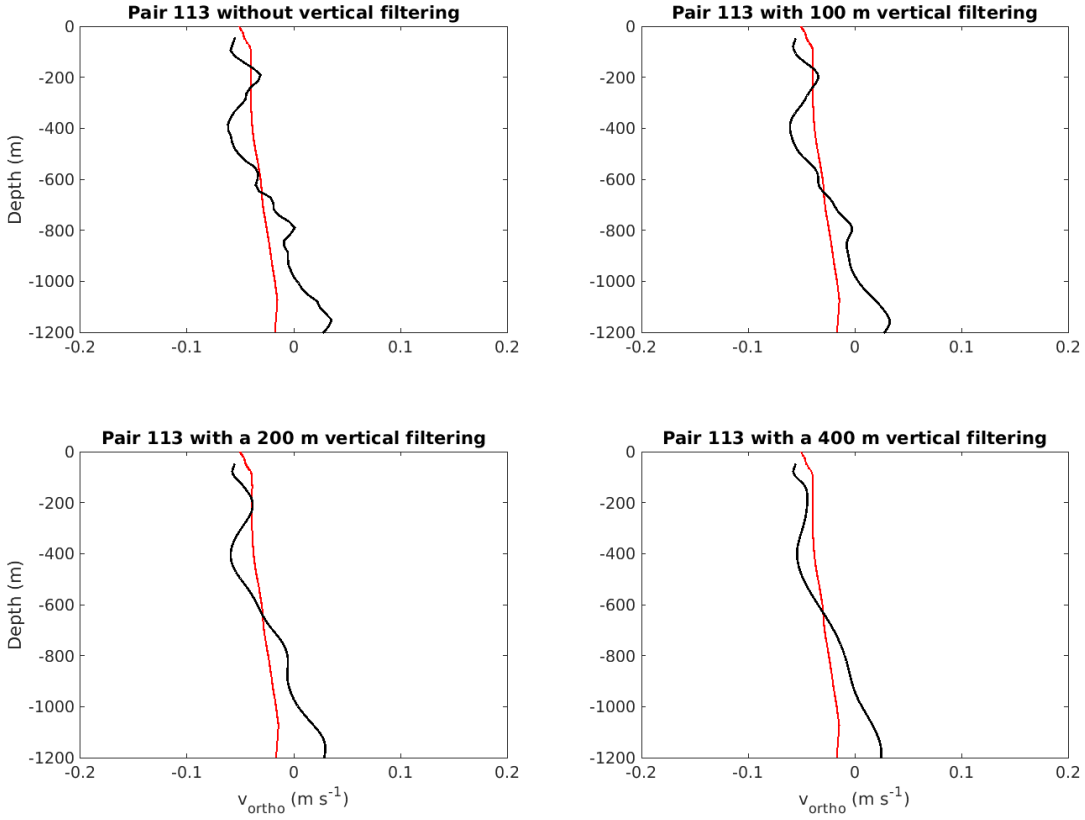

Figure 2.14: Same as Figure 2.13 for pair 113.

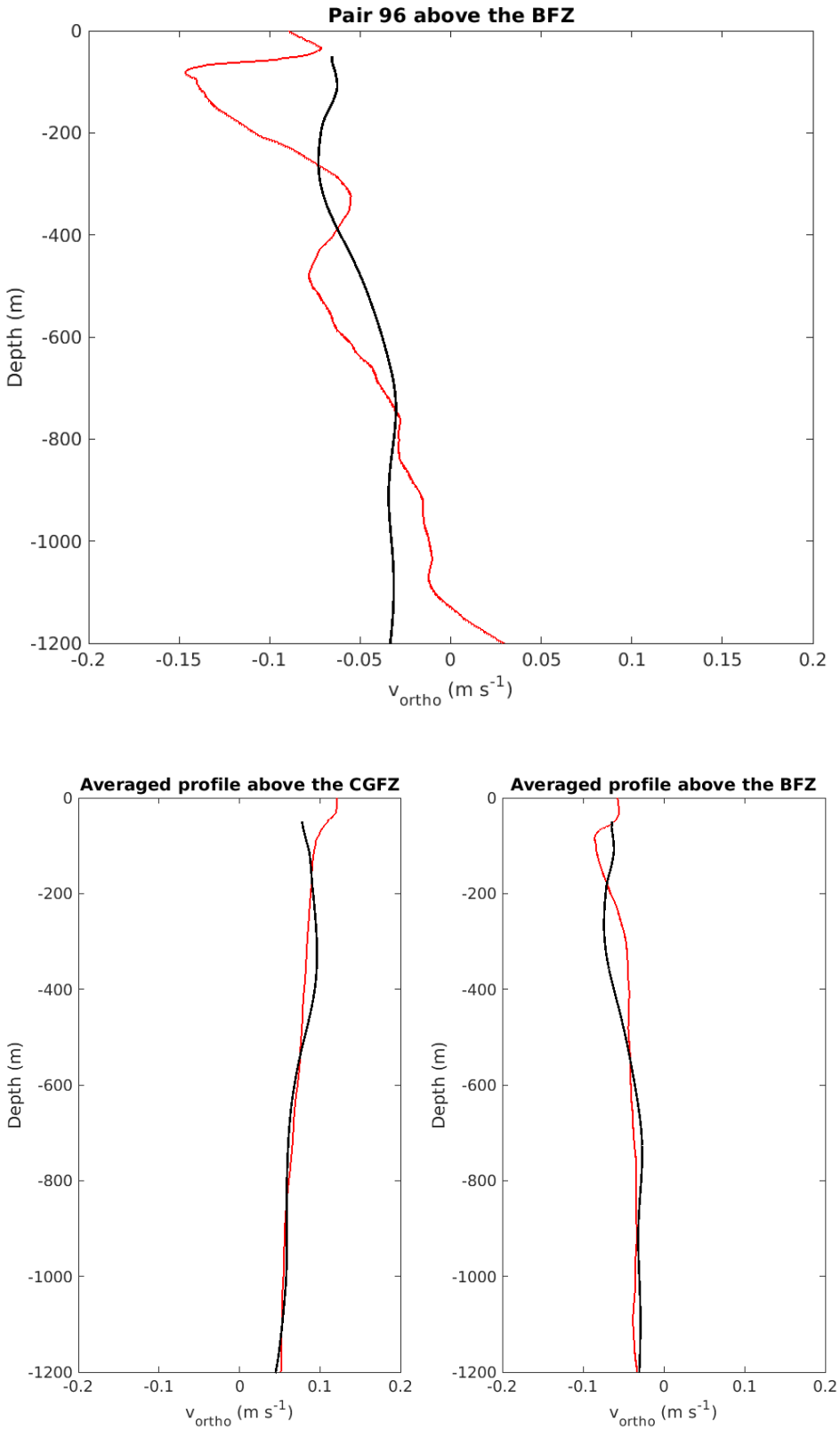

Figure 2.15: Velocity profiles of pair 96 (upper panel) and of the averaged velocities above the BFZ and CGFZ (lower panels). Red lines are the absolute geostrophic velocities fitted to OS38 and with L_{ref} = 500 – 1000 m; Black dash lines are the vertically filtered velocities from OS38; Black plain lines indicate the location of the absolute reference layer.

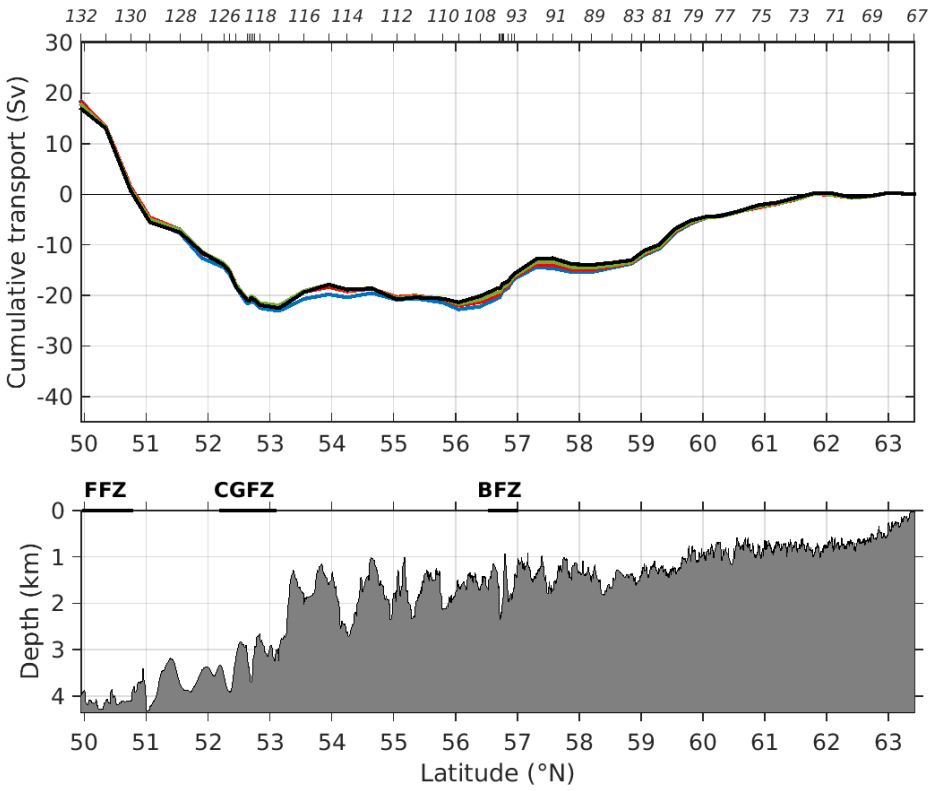

Figure 2.16: Cumulated transport curves (Sv) fitted to OS38 with various absolute reference layers (deeper than 500 m): L_{ref} = 500 – 1000 m (blue line), L_{ref} = 600 – 1000 m (red line), L_{ref} = 700 – 1000 m (green line), L_{ref} = 800 – 1000 m (black line). A specific computation was applied at the BFZ and CGFZ. The locations of the hydrographic stations are shown on the top axis. Lower panel: Bathymetry along the Ridge Section. CGFZ stands for Charlie Gibbs Fracture Zone, BFZ for Bight Fracture Zone, and FFZ for Faraday Fracture Zone.

3 First direct estimates of volume and water mass transports across the Reykjanes Ridge

Based on chapter 2, we describe and quantify the top-to-bottom transport of the subpolar gyre that crossed the Reykjanes Ridge during the summer 2015, and thus we investigate the questions Q1, Q2 and Q3 given in Introduction. This chapter is based on an article published in *Journal of Geophysical Research: Ocean* (Petit et al., 2018b).

Abstract

The Reykjanes Ridge is a major topographic feature located south of Iceland in the North-Atlantic Ocean that strongly influences the subpolar gyre (SPG) circulation. Based on velocity and hydrographic measurements carried out along the crest of the Reykjanes Ridge from the Icelandic continental shelf to 50°N during the RREX cruise in June – July 2015, we derived the first direct estimates of volume and water mass transports over the Reykjanes Ridge. North of 53.15°N, circulation was mainly westward; south of this latitude it was mainly eastward. The westward transport was estimated at 21.9 ± 2.5 Sv (Sv = 10^6 m^3 s^{-1}) and represents the SPG intensity. The westward flows followed two main pathways at 57°N near the Bight Fracture Zone and at 59 – 62°N. We argue that those pathways were connected to the northern branch of the North Atlantic Current and to the Sub-Arctic Front respectively, which were both intersected by the southern part of the section. In addition to this horizontal circulation, mixing and bathymetry shaped the water mass distribution. Water mass transformations in the Iceland Basin lead to the formation of weakly stratified SubPolar Mode Water (SPMW). We explain why SPMW, the main water mass contributing to the westward flow, was denser at 57°N than at 59 – 62°N. At higher densities, both Intermediate Water and Icelandic Slope Water contributed more to the westward transport across the Reykjanes Ridge than the sum of Labrador Sea Water and Iceland-Scotland Overflow Water.

3.1 Introduction

The Reykjanes Ridge, which is located at the northern part of the Mid-Atlantic Ridge (MAR), is a major topographic feature of the northern North-Atlantic. Located between the Iceland Basin, to the east, and the Irminger Sea, to the west, the Reykjanes Ridge extends along a northeast/southwest line from Iceland to 55°N, south of the Bight Fracture Zone (BFZ), and then along a more meridional line to the Charlie Gibbs Fracture Zone (CGFZ) at 52.5°N (Figure 3.1). At the CGFZ, the MAR shifts eastward. The summit of the Reykjanes Ridge is at about 300 m depth at 63°N and deepens to more than 3000 m at the CGFZ. Between 60°N and the CGFZ, the Reykjanes Ridge is cut by many fracture zones of increasing bottom depths towards the south while summits constantly reach 1100 – 1300 m (Figure 3.2). Lying at the heart of the subpolar gyre and located on the pathways of the North-Atlantic Current

(NAC) and overflow waters toward the Irminger and Labrador Seas, the Reykjanes Ridge is a major obstacle for North-Atlantic circulation (Figure 3.1) and a gateway to deep convection areas (Piron et al., 2017). Most likely, its sea floor roughness constrains deep circulation through mixing (De Lavergne et al., 2017).

The cyclonic circulation of the subpolar gyre extends roughly from 50 to 65°N (Figure 3.1). The eastward flowing NAC bounds the subpolar gyre to the south. At the MAR, three branches of the NAC are dynamically constrained by deep fracture zones: Maxwell Fracture Zone at 48°N, Faraday Fracture Zone (FFZ) at 50.5°N and CGFZ at 52.5°N (Bower & von Appen, 2008; Bower & Furey, 2017; Roessler et al., 2015; Schott et al., 1999). The central NAC branch flowing near 50.5°N is characterized by a sharp salinity front and is generally referred to in the literature as the Sub-Arctic Front (SAF) (Daniault et al., 2016). Above the Reykjanes Ridge, the westward flow of the subpolar gyre is fed by the NAC branches that flow cyclonically in the Iceland Basin and by deep flows from the Nordic Seas (Figure 3.1). RAFOS float trajectories showed that the westward branch of the subpolar gyre preferentially follows the BFZ at 57°N (Bower et al., 2002). Likewise, models showed that deep overflows from Iceland-Scotland Ridge preferentially join the Irminger Sea through the BFZ and CGFZ (Xu et al., 2010; Zou et al., 2017). Although the identification of those pathways through the fracture zones was a major step forward in our understanding of the subpolar gyre circulation, other analyses based on measurements perpendicular to the ridge axis suggested that the subpolar gyre takes additional pathways across the Reykjanes Ridge. For instance, the Ovide project provided series of indirect transport estimates showing significant westward transport north of the BFZ, although no specific fracture zones were identified there (Daniault et al., 2016; Lherminier et al., 2010). Chafik et al. (2014) and Childers et al. (2015) suggested that this westward transport is very weak between 0 and 400 m depth. The preferred pathways across the Reykjanes Ridge and the vertical structure of the flow thus remain unclear, as does the connection of the westward flows across the Reykjanes Ridge to the upstream NAC branches. Finally, most of the water masses crossing the Reykjanes Ridge westward (see section 3.2.5 for water mass description) undergo modifications in the Iceland Basin by air-sea exchange in the mixed layer, isopycnal and diapycnal mixing at intermediate depths, or entrainment in the deep overflows. Although the distribution and transport of these water masses by the subpolar gyre are known in the Iceland Basin, their distributions along the Reykjanes Ridge related to the circulation and the bathymetry have never been documented,

and the associated transports have only been quantified in an integral way (Daniault et al., 2016; García-Ibáñez et al., 2015).

Until now, direct observations along the Reykjanes Ridge were lacking. As a result, no detailed view of volume and water mass transports was available for this area and subpolar gyre intensity had only been estimated on given densities (Bower et al., 2002), from proxies (Hakkinen & Rhines, 2004), or from general circulation models (Böning et al., 2006; Lohmann et al., 2009). A quantification of the water mass transports across the Reykjanes Ridge would provide benchmarks for the validation of ocean general circulation models, which are presently inadequate for representing the cross-ridge flows in the area (Penduff et al., 2007; Rattan et al., 2010).

This study aims to quantify the full water column transport above the Reykjanes Ridge, from Iceland to 50°N. It is based on a synoptic data set collected as part of the RREX project along the crest of the Reykjanes Ridge during June-July 2015. The effect of the bathymetry on the transport will be investigated by identifying the preferred pathways across the Reykjanes Ridge and by characterizing the vertical structure of the circulation.

This paper is organized as follows. Section 3.2 presents the data and method used for this study. The currents and associated transports across the Reykjanes Ridge are presented in section 3.3, including a description of the water mass transports. In section 3.4, results are compared to previous findings and are discussed in a context of larger scale circulation and water mass transformation. Finally, results are summarized in section 3.5.

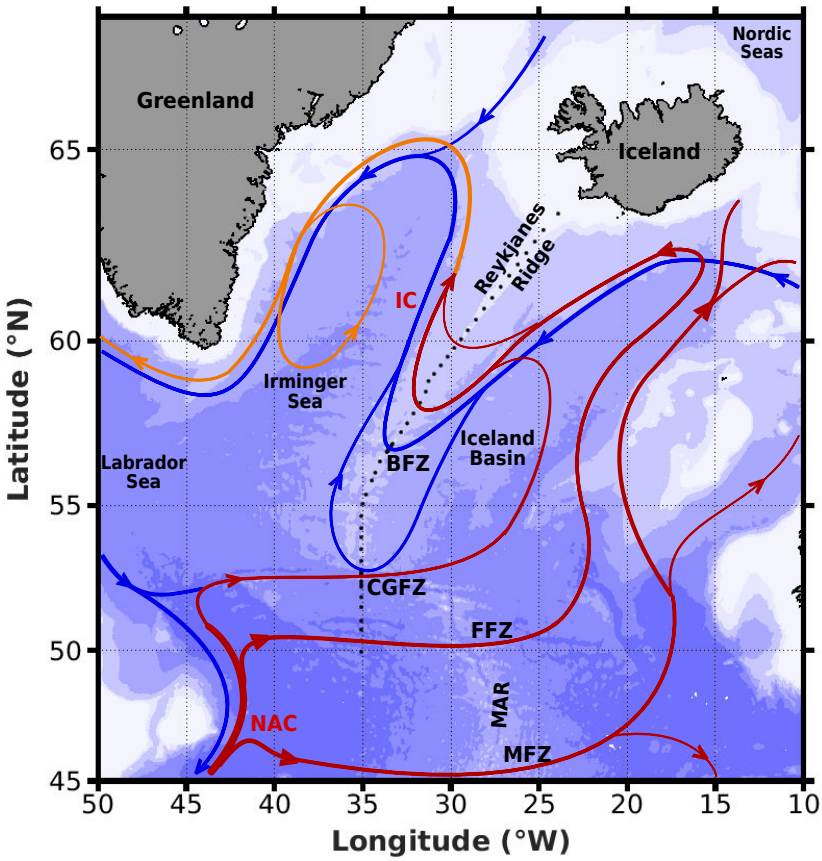

Figure 3.1: Schematic of large-scale circulation in the northern North Atlantic based on Daniault et al. (2016). Locations of the hydrographic stations where measurements were performed during the RREX2015 cruise along the Ridge Section are shown by black dots. Bathymetry is plotted in color with color changes at 500 m, 1000 m and every 1000 m below 1000 m. Topographical features and currents of the North Atlantic are indicated as follows: Bight Fracture Zone (BFZ), Charlie-Gibbs Fracture Zone (CGFZ), Faraday Fracture Zone (FFZ), Maxwell Fracture Zone (MFZ), Mid-Atlantic Ridge (MAR), North-Atlantic Current (NAC), and Irminger Current (IC).

3.2 Data and Methods

3.2.1 Description of the cruise

The RREX2015 cruise was carried out from June 5 to July 10 2015 on the N/O Thalassa. $CTDO_2$ (Conductivity Temperature Depth Oxygen), nutrient, pH and total alkalinity measurements were acquired at 56 stations along a section that extended from Iceland to 50°N (Figure 3.1). Referred to hereinafter as the Ridge Section, this section was designed to study the exchanges of volume and properties between the Iceland Basin and the Irminger Sea above the Reykjanes Ridge, and constitutes the main data source for this study. The Ridge Section follows the crest of the Reykjanes Ridge from the Icelandic continental shelf to 53°N, while its southern part from 53°N to 50°N retraces Saunders (1994)'s hydrographic line along

35°W. Between 57.3 and 56.1°N, the section cuts the BFZ east of its main sill (Figure 3.2, inset). The nominal station spacing of 30 km was reduced to 2 km at the BFZ and CGFZ, at about 57°N and 52.5°N respectively (Figure 3.2). The collection of measurements along the Ridge Section was interrupted twice: a first time after station 83 to deploy moorings and a second time after station 101 to carry out hydrographic measurements west of the BFZ main sill. As a result, the time elapsed between station 83 and the following station along the section (station 88) was 34 hours. Similarly, the time elapsed between measurements at station 101 and the following station along the section (station 107) was 22 hours. Otherwise, the time between measurements at successive stations was less than 4 hours.

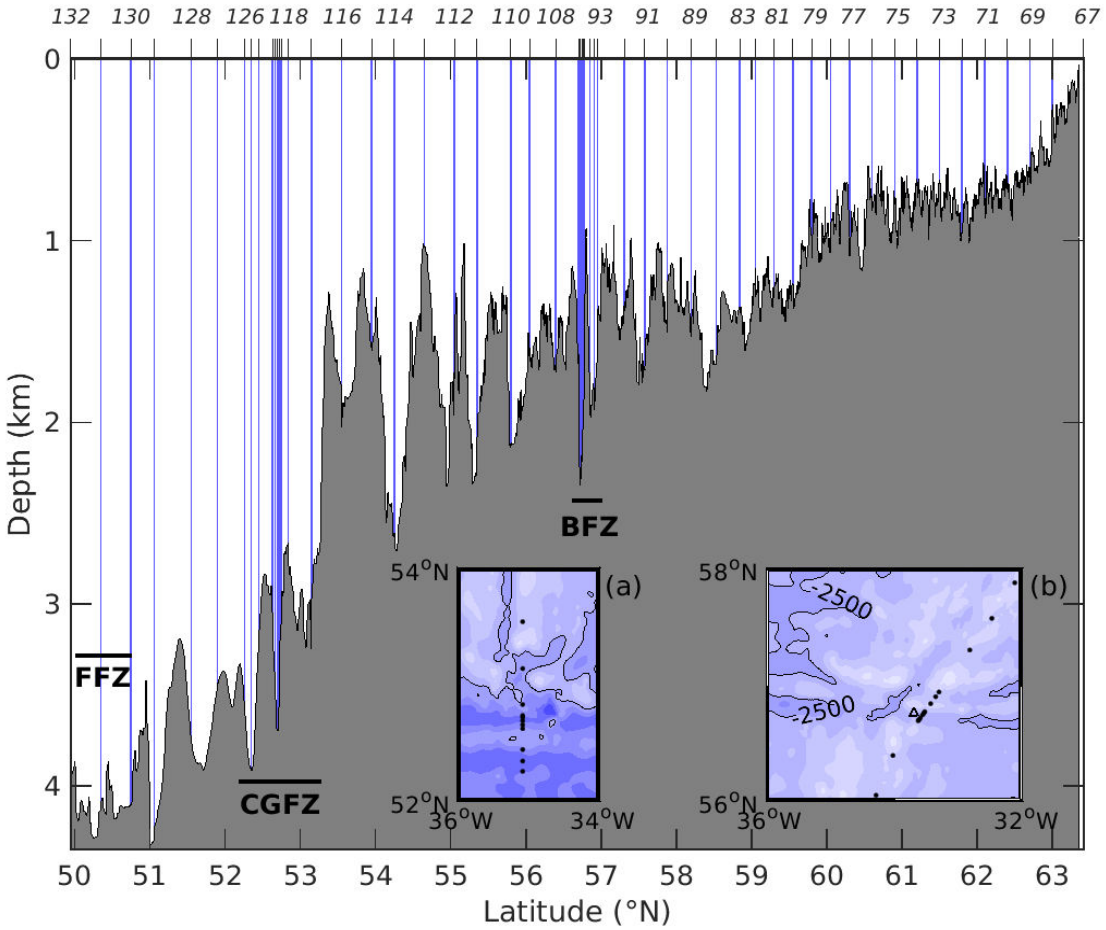

Figure 3.2: Locations of the hydrographic stations carried out along the top of the Reykjanes Ridge during the RREX2015 cruise (blue vertical lines). The bathymetry (grey shading) was recorded by the ship echo-sounder. Hydrographic station spacing was reduced in the Bight Fracture Zone (BFZ) and Charlie Gibbs Fracture Zone (CGFZ). The BFZ, CGFZ and Faraday Fracture Zone (FFZ) are indicated. Inserted maps: (a) Bathymetry in the CGFZ area with 500-m isobath spacing. The black line outlines the -2500-m isobath. Locations of stations 116 to 126 (black dots) are indicated; (b) Bathymetry in the BFZ area with 500-m isobath spacing. Locations of stations 92 to 101 and 107 to 109 (black dots) and of the main sill of the BFZ (black triangle) are indicated. The deepest bathymetries are represented with the darkest blue.

3.2.2 Data sets

Temperature, conductivity and dissolved oxygen were measured as a function of pressure at all hydrographic stations (Thierry et al., 2018), using a Seabird Electronics 911+ $CTDO_2$ probe mounted on a rosette equipped with 28 bottles. The rosette was stopped 15 meters above the bottom. For $CTDO_2$ calibration purposes, seawater samples were analyzed on board for salinity and dissolved oxygen concentration. Temperature and pressure sensors were calibrated at the laboratory before and after the cruise and no sensor drift was detected. The accuracies of the $CTDO_2$ measurements were found to be 1dbar for pressure, 0.001°C for temperature, 0.0025 for salinity and 1μmol kg^{-1} for dissolved oxygen (Branellec & Thierry, 2016). Figure 3.3 and Figure 3.4 show vertical sections of hydrographic properties along the Ridge Section and their distribution in the θ-S space.

The rosette was equipped with both upward and downward looking 300 kHz L-ADCPs (Lowered Acoustic Doppler Current Profiler, RD Instruments). The inverse method from Visbeck (2002) was used to process and combine these two data sets and to estimate the horizontal velocity profiles. The vertical cell size was set at 16 m and the overall velocity error was estimated at 0.03 m s^{-1}. More details on the L-ADCP processing can be found in Lherminier et al. (2007).

Upper layer current velocity components were measured from the ship using two S-ADCPs (Shipboard Acoustic Doppler Current Profiler, RD Instruments) operating at 38 kHz (OS38) and 150 kHz (OS150) (Thierry et al., 2018). In this study, we used the OS38 data only. The OS150 data were used to verify the OS38 calibration corrections (Petit et al., 2018a). The bin size was set at 24 m and the pinging rate was 3 s. The OS38 operated in narrowband mode and the maximum depth reached was 1300 m. Velocity profiles were averaged over 2-minute ensembles by the acquisition software to decrease the measurement error. These ensembles were then processed using Cascade Version 7.0 (“Chaine Automatisée de Suivi des Courantomètres Acoustiques Doppler Embarqués”) (Le Bot et al., 2011). Details of the processing are given in Petit et al. (2018a). The mean departure of the ADCP from the horizontal was estimated at 0.3° by minimizing the vertical velocity. Misalignment and amplitude corrections were estimated at 0.05° and 1.0067 cm s^{-1}, respectively, using the bottom track procedure (Firing & Hummon, 2010). The barotropic tidal currents were removed from the 2-minute averaged velocity data using TPXO8.0 OSU tidal prediction

software based on the Tidal Data Inversion (Egbert & Erofeeva, 2002). Finally, S-ADCP data were averaged over 2-km segments along the Ridge Section.

Bathymetry was measured every 30 s along the ship track using a 12 kHz echo-sounder (Figure 3.2). The bathymetric model ETOPO1 (Amante & Eakins, 2009) was used to fill few gaps in the recorded bathymetry at around 52°N and 60.5°N.

Merged-Absolute Dynamic Topography (MADT) from the Ssalto/Duacs AVISO (Archiving, Validation and Interpretation of Satellite Oceanographic data center) altimeter products distributed by CMEMS (Copernicus Marine Environment Monitoring Service) on a 1/3° grid was used to compute time-averaged surface geostrophic velocities over the period from 5 June to 10 July 2015.

Wind stress data from the two global atmospheric reanalysis, ERA-Interim reanalysis (Dee et al., 2011) and NCEP/NCAR reanalysis (Kalnay et al., 1996), were used to compute the Ekman transport at the location and time of measurements at each hydrographic station.

3.2.3 S-ADCP referenced geostrophic velocities

Dynamic height referenced to the surface was computed from temperature, salinity and pressure at all $CTDO_2$ stations. Their horizontal gradients were then computed between two adjacent stations and used in the thermal wind equation to compute geostrophic velocities referenced to the surface. In presence of a sloping topography, the geostrophic velocity between two $CTDO_2$ stations cannot be computed in the bottom triangle, which is to say below the deepest common level (DCL) of a pair of stations. To estimate the geostrophic flow in the bottom triangle, Ganachaud (2003) recommended the interpolation of hydrographic properties at the shallowest station from adjacent data. We used a second-order polynomial fit suggested by Ganachaud (2003) and computed hydrographic properties below the DCL at the shallowest station by second-order interpolation of the hydrographic properties at the DCL and below. Geostrophic velocities were computed in the bottom triangle of each pair of stations based on the interpolated dynamic heights. Because the interpolation led to unrealistic velocity at the station pair 114 – 115, the geostrophic velocity in the bottom triangle was computed as decreasing to zero at the bottom.

An absolute geostrophic field was estimated by adjusting the geostrophic field referenced to the surface to S-ADCP absolute velocity measurements following Lherminier et al. (2007) and Gourcuff et al. (2011). The absolute geostrophic profile was computed by adding a constant velocity correction to the geostrophic velocity profile referenced to the surface. The correction is the difference in a reference layer L_{ref} between the S-ADCP velocities horizontally averaged between the two stations of the pair and the geostrophic velocities referenced to the surface. To do this, it is best that the physical contents of the geostrophic and S-ADCP velocities in layer L_{ref} be as similar as possible. This means that we should avoid depths where ageostrophic motions, caused by bottom and wind frictions, interactions of tides with bathymetry, inertial oscillations, or cyclogeostrophic terms are the most intense (Ganachaud, 1999). Selecting L_{ref} = 600 – 1000 m led to the best agreement between the geostrophic and S-ADCP profiles. In order to remove "small scale side effects" when averaging S-ADCP data over limited horizontal and vertical distances, we filtered the original 2-km × 16-m gridded S-ADCP velocities horizontally and vertically using Lanczos filters with respective cutoff wave numbers of 1/8 km^{-1} and 1/400 m^{-1} applied consecutively. The cutoff frequencies are of the order of magnitude of the Rossby radius horizontally and of L_{ref} thickness vertically. The filtering decreased significantly the root-mean-square (RMS) difference between the geostrophic velocities and the S-ADCP velocities. Above the BFZ and CGFZ, strong ageostrophic motions prevented robust determination of the reference velocity at the 2-km resolution allowed by the CTD sampling. A single reference velocity was thus estimated over the BFZ and CGFZ (stations 96 – 101 and 119 – 122 respectively). Figure 3.5 shows the resulting absolute geostrophic velocity section along the Reykjanes Ridge.

3.2.4 Transport estimates and errors

Transport across the Ridge Section is the sum of geostrophic and Ekman transports. To compute the geostrophic transport, each geostrophic velocity was assigned to a surface equal to the distance between the stations of each pair multiplied by the vertical resolution of the geostrophic velocity profile. Then, the transport for a region limited by the hydrographic stations in the horizontal, and constant depths, isopycnals, or bathymetry in the vertical, was computed as the sum of the products of the geostrophic velocities by the associated surfaces over the region considered. Figure 3.6 shows the resulting top-to-bottom integrated transport along the Ridge Section cumulated from Iceland to 50°N.

Errors for the total transports were computed as follows. The main source of error in the geostrophic transports comes from errors in the determination of the reference velocity, which are the sum of errors due to S-ADCP instrumental noise E_{inst_noise}, S-ADCP calibration error E_{inst_bias} and errors due to the presence of ageostrophic motions in the S-ADCP velocities E_{ageo}. An additional error E_{bott} comes from the extrapolation of the hydrographic properties in the bottom triangles (Ganachaud, 2003). The Ekman transport error E_{Ekman} mainly comes from the uncertainty in the wind stress data. Accounting for all contributions, the error in the total transports for a given region $E_{transport}$ can be written as:

$$E_{transport} = \sqrt{\left([\ \delta_{layer}^{surface}\ E_{Ekman}^2 + S.E_{ageo}^2 + S.E_{inst\_noise}^{\ 2} + \delta_{layer}^{bottom}\ E_{bott}^2\ ]\right)} + S.E_{inst\_bias} \qquad (3.1)$$

Where S is the surface of the area over which the transport is computed. $\delta_{layer}^{surface}$ and δ_{layer}^{bottom} are Kronecker deltas, indicating that those errors are taken into account only when the surface or bottom layers are included in the region. The errors are considered as random, except for the S-ADCP calibration error, which is a systematic error.

The instrumental error was estimated as the mono-ping standard deviation (0.23 m s^{-1}), given by the manufacturer, divided by the number of S-ADCP measurements used to calculate the referenced velocity. To obtain an error for the transport, E_{inst_noise} was multiplied by the surface S of the considered region. Over a horizontal distance of 30 km and a layer thickness of 1500 m, E_{inst_noise} is equal to 0.01 Sv. Its contribution to the error on the top-to-bottom integrated transport along the Ridge Section was estimated at 0.7 Sv.

To estimate the error for the absolute geostrophic velocity due to ageostrophic motions, we followed Lherminier et al. (2007) and considered the length scale Lg, set at half the Rossby radius, below which ageostrophic motions dominate. About half of the variance associated with these scales was removed by filtering the S-ADCP data as described above. We computed the variance of the S-ADCP signal in the layer L_{ref} for each Lg segment along the Ridge Section. Then, assuming a decorrelation between ageostrophic signals for one Lg segment to the other, we computed an averaged ageostrophic variance for the region considered. At the first order, this variance is due to the sum of the ageostrophic signal and instrumental noise. We thus removed the instrument noise variance from the small-scale variance to obtain an estimate of the variance of the ageostrophic motions. This variance was then divided by N, with N the number of segments Lg in the horizontal for the area considered. The square root of this value, multiplied by the surface of the considered region, gives the ageostrophic transport error $S.E_{ageo}$. Typically, for a 30-km distance and a layer

thickness of 1500 m, the error was ~ 0.06 Sv. On the top-to-bottom integrated transport along the Ridge Section, this error was estimated at 1 Sv.

The error E_{bott} due to the extrapolation of the hydrographic data in the bottom triangle was estimated by computing the RMS difference between the polynomial fit method used in this study with three other extrapolation methods proposed by Ganachaud (2003). The maximum value equal to 0.4 Sv was found at the station pair 124 – 125. The error, cumulated along the Ridge Section, was estimated at 0.7 Sv.

The error in the Ekman transport (E_{Ekman}) was estimated as the RMS difference between EraInterim and NCEP Ekman transports. This error, cumulated along the Ridge Section, was estimated at 0.04 Sv.

The instrumental bias E_{inst_bias} due to error in the S-ADCP misalignment correction was computed as the difference between the OS38 transports and OS150 (both corrected for misalignment) in the part of the water column where the signals overlapped. The bias was estimated at 8 10^{-4} m s^{-1}, which corresponds to a 2.7-Sv bias for the top-to-bottom transport once cumulated along the Ridge Section.

Finally, because it took ten days to carry out the measurements along the Ridge Section, the data are not fully synoptic. To evaluate this asynopticity, we computed the RMS difference in AVISO surface velocities between the beginning (24 June 2015) and the end (5 July 2015) of the section. This RMS difference is equal to 0.015 m s^{-1}, which is marginally significant given the 0.03-m s^{-1} error for AVISO velocities (Gourcuff et al., 2011). Although this asynopticity error may be underestimated because of the smoothing used for generating AVISO products, this result suggests that the asynopticity error is negligible.

3.2.5 Water mass characterization

By referring to the literature and to properties observed along the Ridge Section (Figure 3.3, Figure 3.4), we identified four layers delimited by isopycnals that encompass nine main water masses. Layer 1, defined by σ_0 < 27.52 kg m^{-3}, contains North Atlantic Central Water (NACW) of subtropical origin (Iselin, 1936) and Sub-Arctic Water (SAW) of subpolar origin (Dickson et al., 1988). These water masses are separated by a sharp salinity front defined by approximately 34.94 at station 130 and separating NACW to the south from SAW to the north.

Further north, a weaker salinity front near station 91 separates SAW to the south from NACW to the north. There, NACW properties differ from those observed south of station 130 due to air-sea heat loss in the Iceland Basin (Figure 3.4).

Layer 2, defined by $27.52 < \sigma_0 < 27.71$ kg m^{-3}, contains Sub-Arctic Intermediate Water (SAIW) of subpolar origin and is characterized by salinity below 34.94 (Arhan, 1990), and Subpolar Mode Water (SPMW) with salinity above 34.94 and relatively low potential vorticity ($q < 6.10^{-11}$ m^{-1} s^{-1}). The potential vorticity was computed as $q = \frac{-f}{\rho_0}\frac{\partial \rho}{\partial z}$, where f is the Coriolis parameter, ρ_0 is the reference density and ρ is the potential density referenced to the mid-depth interval over which the vertical gradient of density is computed. The homogeneous SPMW is formed in the winter mixed layer and may also be fed by underlying intermediate waters when the winter mixed layer is deep enough (de Boisséson et al., 2012; Brambilla & Talley, 2008; Thierry et al., 2008). Layer 2 also contains Intermediate Water (IW) associated with patches of low oxygen concentration ($O_2 < 272$ µmol kg^{-1}) and high salinity ($S > 34.94$), and lies just above the isopycnal 27.71 in the northern part of the Reykjanes Ridge and in the NAC. Carried by the Gulf Stream and subsequently by the NAC, the aged IW is biogeochemically defined by minima of O_2 and maxima of NO_3 (Van Aken & De Boer, 1995).

Layer 3, defined by $27.71 < \sigma_0 < 27.8$ kg m^{-3}, encompasses Labrador Sea Water (LSW) that is formed by deep convection in the Irminger and Labrador Seas and has a relative minimum in salinity ($S < 34.94$) (Van Aken et al., 2011; Sy et al., 1997). The layer also contains Icelandic Slope Water (ISW) of higher salinity and lower dissolved oxygen concentration than LSW. ISW is formed close to the Iceland-Faroe Ridge by mixing between SPMW and overflow waters and is further transformed by isopycnal mixing with LSW while flowing southward along the Reykjanes Ridge (Read, 2001).

Finally, Layer 4, defined by $\sigma_0 > 27.8$ kg m^{-3}, contains Iceland-Scotland Overflow Water (ISOW), which flows along the eastern flank of the Reykjanes Ridge from the Iceland-Scotland Ridge and is characterized by salinity above 34.94 (Kanzow & Zenk, 2014; Saunders, 1994). Transported by the subtropical branch of the NAC, layer 4 also encompasses Lower Deep Water (LDW) characterized by salinity below 34.94, potential temperature below 3°C, and a relative high concentration of dissolved oxygen ($O_2 > 278$ µmol kg^{-1}) and dissolved silicic acid ($Si(OH)_4 > 18$ µmol kg^{-1}, not shown). LDW is formed by mixing of diluted overflow waters from the north and diluted Antarctic Bottom Water from the south (McCartney, 1992).

Criteria for the identification of each water mass based on the above description are given in Table 3.1 (see also Figure 3.4). These criteria will be used below to determine the spatial distribution of each water mass along the Ridge Section and the associated transports. The transport for a given station pair was computed by integrating the velocity field over the surface occupied by the water mass at this station pair.

Table 3.1: Criteria based on limits and ranges of potential density (σ_0), salinity (S), dissolved oxygen concentration (O_2) and potential vorticity (q) for the identification of the water masses along the Ridge Section. These limits and ranges are shown in Figure 3.3. NACW stands for North Atlantic Central Water; SAW for Sub-Arctic Water; SAIW for Sub-Arctic Intermediate Water; IW for Intermediate Water; SPMW for SubPolar Mode Water; LSW for Labrador Sea Water; ISW for Icelandic Slope Water; LDW for Lower Deep Water; ISOW for Iceland-Scotland Overflow Water.

Water masses	Potential density ($kg\ m^{-3}$)	Salinity	Oxygen ($\mu mol\ kg^{-1}$)	Potential Vorticity ($m^{-1}s^{-1}$)
NACW	$\sigma_0 < 27.52$	$S > 34.94$		
SAW	$\sigma_0 < 27.52$	$S < 34.94$		
SAIW	$27.52 < \sigma_0 < 27.71$	$S < 34.94$		
IW	$27.52 < \sigma_0 < 27.71$	$S > 34.94$	$O_2 < 272$	
SPMW	$27.52 < \sigma_0 < 27.71$	$S > 34.94$	$O_2 > 272$	$q < 6\ 10^{-11}$
LSW	$27.71 < \sigma_0 < 27.8$	$S < 34.94$		
ISW	$27.71 < \sigma_0 < 27.8$	$S > 34.94$		
LDW	$\sigma_0 > 27.8$	$S < 34.94$		
ISOW	$\sigma_0 > 27.8$	$S > 34.94$		

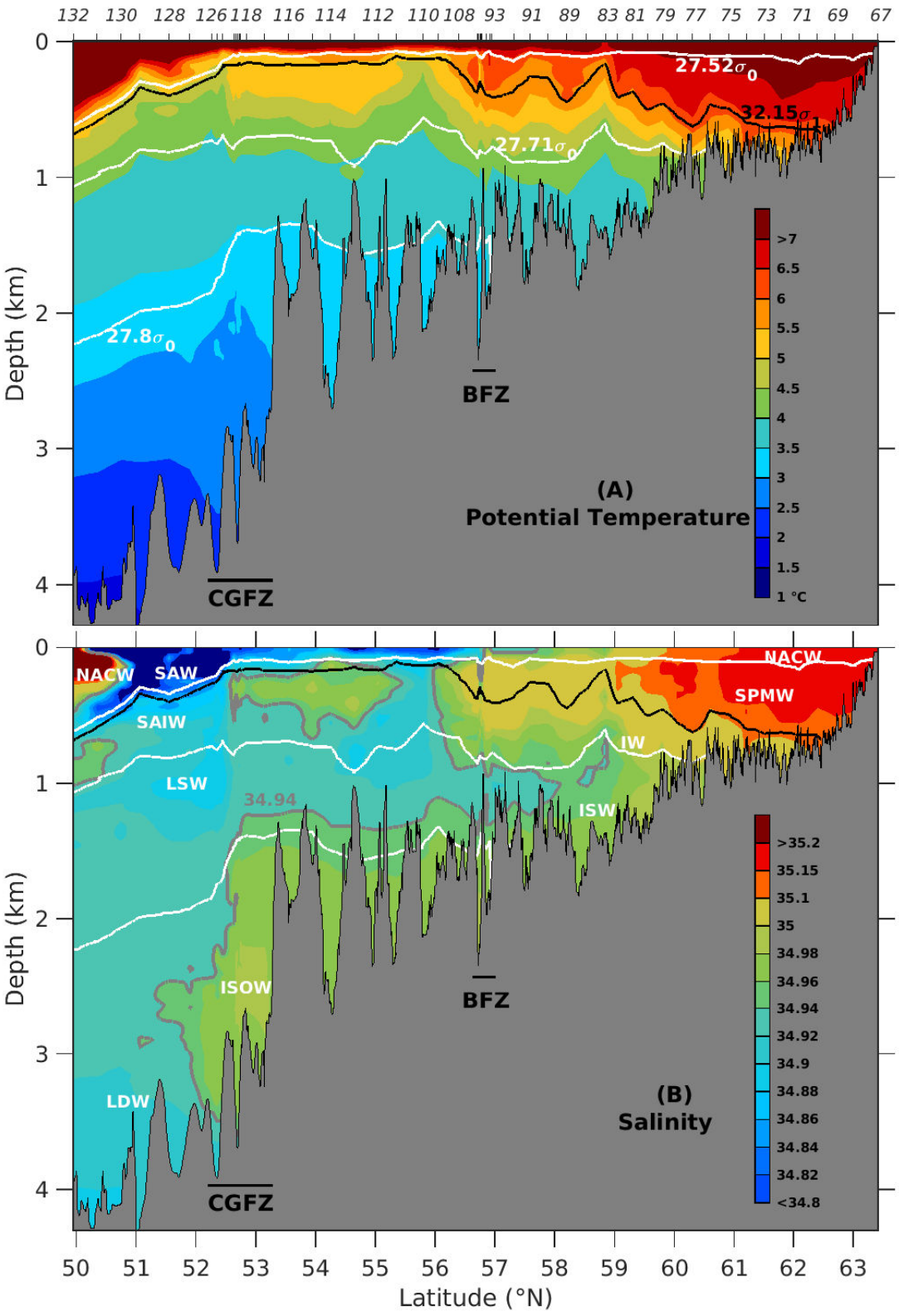
132 130 128 126 118 116 114 112 110 108 93 91 89 83 81 79 77 75 73 71 69 67
Depth (km)
27.52σ0
32.15σ1
27.71σ0
27.8σ0
BFZ
CGFZ
(A)
Potential Temperature
>7
6.5
6
5.5
5
4.5
4
3.5
3
2.5
2
1.5
1 °C
NACW
SAW
SAIW
LSW
34.94
NACW
SPMW
IW
ISW
ISOW
LDW
BFZ
CGFZ
(B)
Salinity
>35.2
35.15
35.1
35
34.98
34.96
34.94
34.92
34.9
34.88
34.86
34.84
34.82
<34.8
50 51 52 53 54 55 56 57 58 59 60 61 62 63
Latitude (°N)

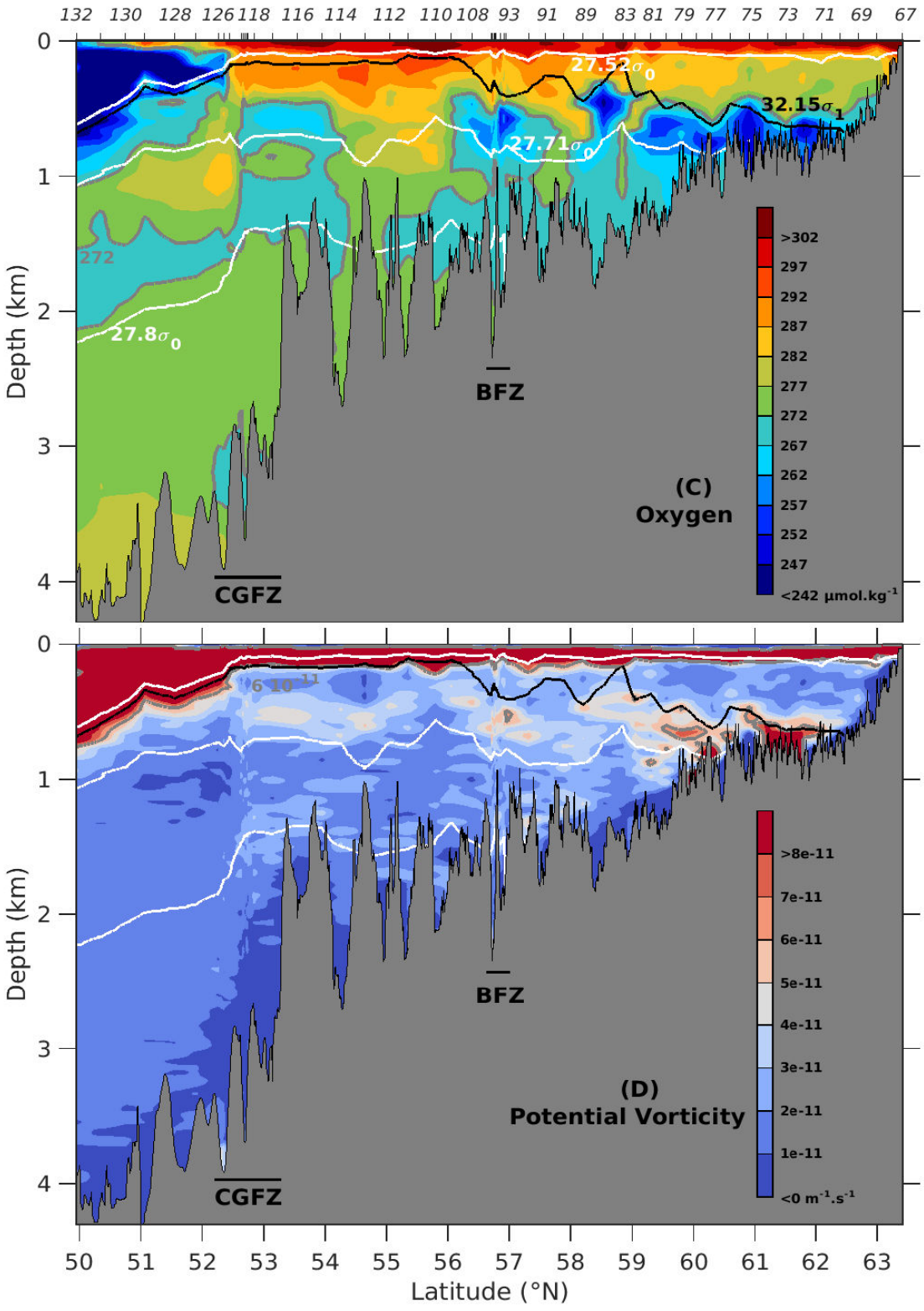

Figure 3.3: Hydrographic sections along the Ridge Section based on $CTDO_2$ data: (A) Potential temperature in °C; (B) Salinity; (C) Dissolved oxygen concentration in µmol kg^{-1}; (D) Potential vorticity in m^{-1} s^{-1}. The bold black lines represent the potential density anomaly σ_1 = 32.15 kg m^{-3}. The bold grey lines show the isohaline 34.94 in panel (B), isoline 272 µmol kg^{-1} in panel (C) and isoline 6 10^{-11} $m^{-1}s^{-1}$ in panel (D). In all panels, the bold white lines show the potential density anomalies σ_0 = 27.52, 27.71 and 27.8 kg m^{-3} that are used to delimit the identified water masses (see Table 3.1). Bathymetry in grey is from the ship survey. The BFZ and CGFZ are indicated.

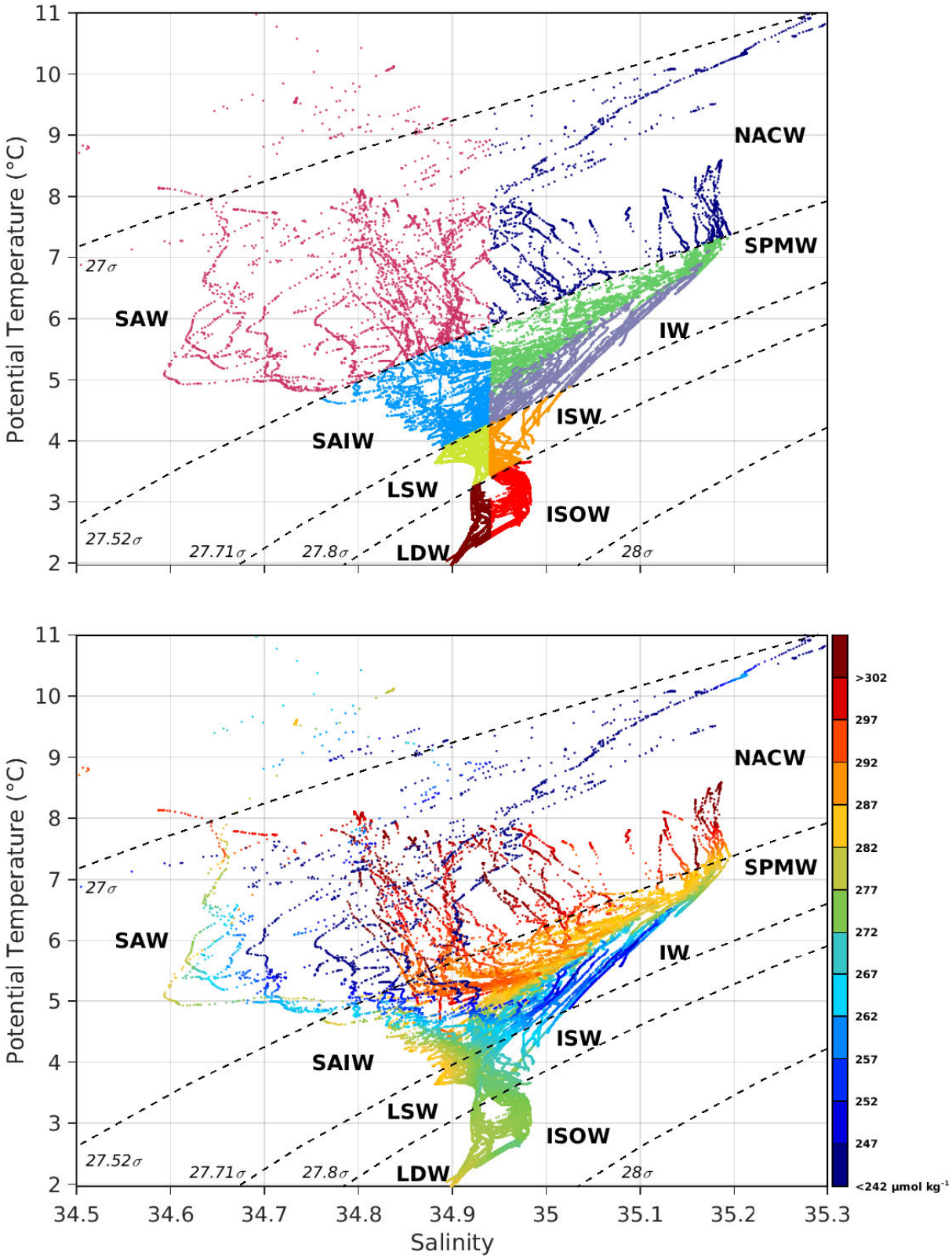

Figure 3.4: Potential Temperature θ/S diagrams displaying all hydrographic profiles along the Ridge Section. (Upper panel) Each water mass indicated in Table 3.1 is represented by a different color. (Lower panel) The colors correspond to oxygen concentration (µmol kg^{-1}). In the two panels, dashed black lines indicate the isopycnals σ_0 = 27, 27.52, 27.71, 27.8 and 28 kg m^{-3}. The water masses indicated by their abbreviations are listed in Table .

3.3 Results: transports across the Reykjanes Ridge

3.3.1 The top-to-bottom cross-ridge flow

We computed the top-to-bottom vertically integrated transports, cumulated southward from Iceland (Figure 3.6), from the absolute geostrophic velocities (Figure 3.5). Positive values correspond to eastward velocities. Starting from Iceland, the cumulative transport decreases until 56.1°N, indicating a westward flow. This flow is intensified between 62 and 59°N and above the BFZ, between 57.3 and 56.1°N, revealing two main cross-ridge flows. Between 56.1 and 53.15°N, the cumulative transport reaches a plateau, indicating weak flows of opposite direction. South of 53.15°N, the transport sharply increases corresponding to an eastward flow.

A first quantification of the cross-ridge transports was obtained by considering the cumulative transports in four regions (Figure 3.6). Region 1 (south of 53.15°N) delimits the eastward flowing NAC, but also encompasses some of the westward flow of ISOW at the CGFZ. In region 1, the top-to-bottom integrated transport was estimated at 40.2 ± 2.3 Sv. As revealed by the absolute geostrophic velocity section (Figure 3.5), the NAC divides in two branches that are respectively aligned with the FFZ, centered at 50.5°N, and the CGFZ, centered at 52.5°N. The top-to-bottom transports of the two NAC branches over the FFZ and CGFZ were estimated at 22.8 ± 1.1 Sv and 17.4 ± 1.7 Sv, respectively. From the northern boundary of region 1 to the Icelandic slope, relatively intense westward flows alternate with relatively weak eastward flows (Figure 3.5). Region 2 (between 53.15 and 56.1°N) is located south of the BFZ and is characterized by no net flow (0 ± 1.4 Sv, Figure 3.6). The top-to-bottom transports in the two main pathways at the BFZ (region 3 between 56.1 and 57.3°N) and at 59 – 62°N were estimated at -8.0 ± 0.5 Sv and -13.6 ± 0.8 Sv, respectively. The overall transport in regions 2 – 4, which corresponds to the intensity of the subpolar gyre, was estimated at -21.9 ± 2.5 Sv.

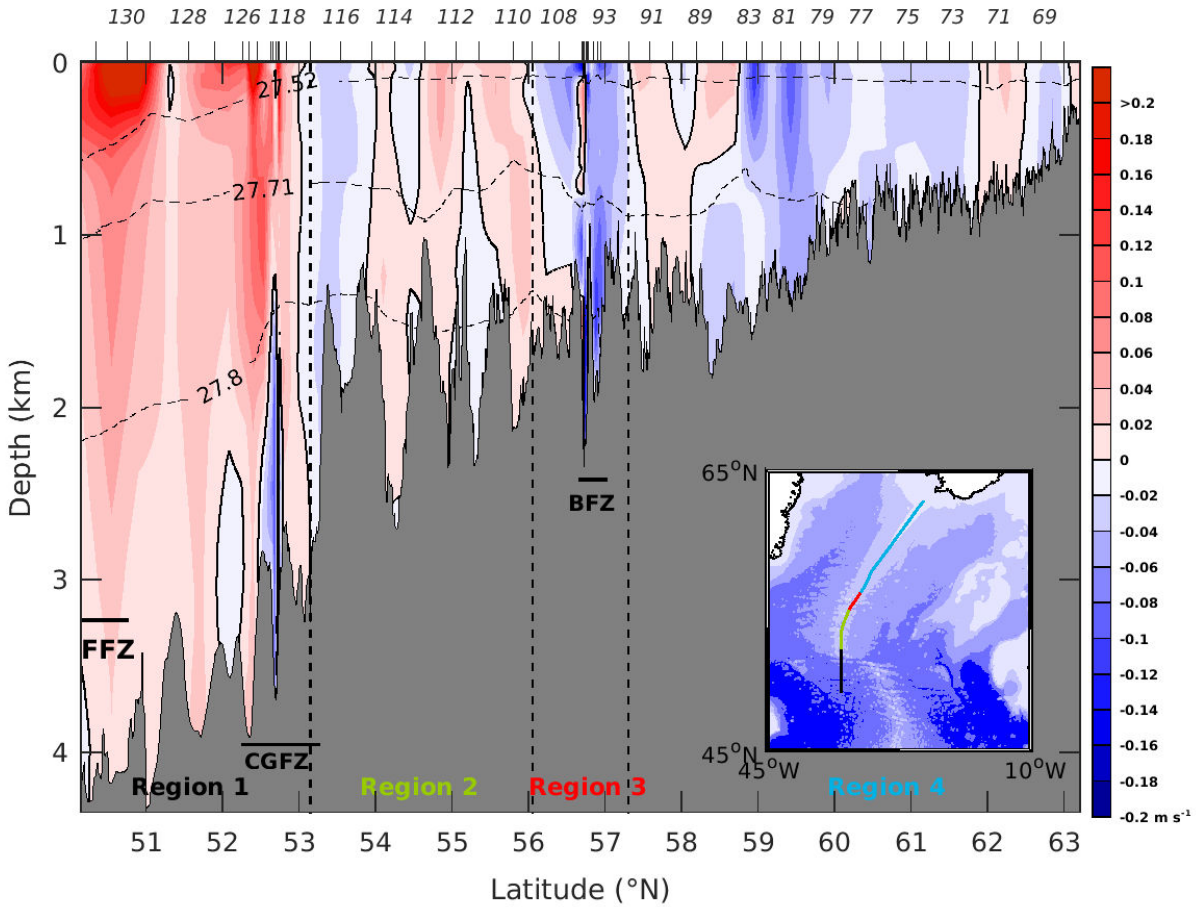

Figure 3.5: Velocity section along the Ridge Section (m s^{-1}). Positive values correspond to eastward velocities. The dashed black lines indicate the potential density σ_0 = 27.52, 27.71 and 27.8 kg m^{-3}. Bathymetry is shown in grey. Dashed vertical black lines divide the section into four regions (see text). The locations of the hydrographic stations are indicated on the top axis. Insert: Map of the bathymetry of the North-Atlantic with a 1000-m spacing. The deepest bathymetries are represented with the darkest blue. The four regions along the Ridge Section are shown with different colors.

3.3.2 Water mass transports across the Reykjanes Ridge

To quantify the contributions of the water masses to the cross-ridge flow, we computed their transport according to the water mass definition (Table 3.1) in the density layers they belong to. We then cumulated these transports from Iceland to 50°N (Figure 3.7) and in the four regions (Figure 3.8).

Layer 1 thickness varies strongly with latitude, from ~ 600 m at 50°N to ~ 200 m north of 53°N (Figure 3.3). Accordingly, the bulk of the transport in this layer occurs to the south of the section in the NAC (region 1). Here, the eastward transports of SAW and NACW were estimated at 8.0 ± 0.2 Sv and 4.1 ± 0.2 Sv, respectively (Figure 3.7, Figure 3.8). No NACW was transported in region 2, but a westward flow of NACW was also observed in regions 3 and 4 (-2.0 ± 0.1 Sv).

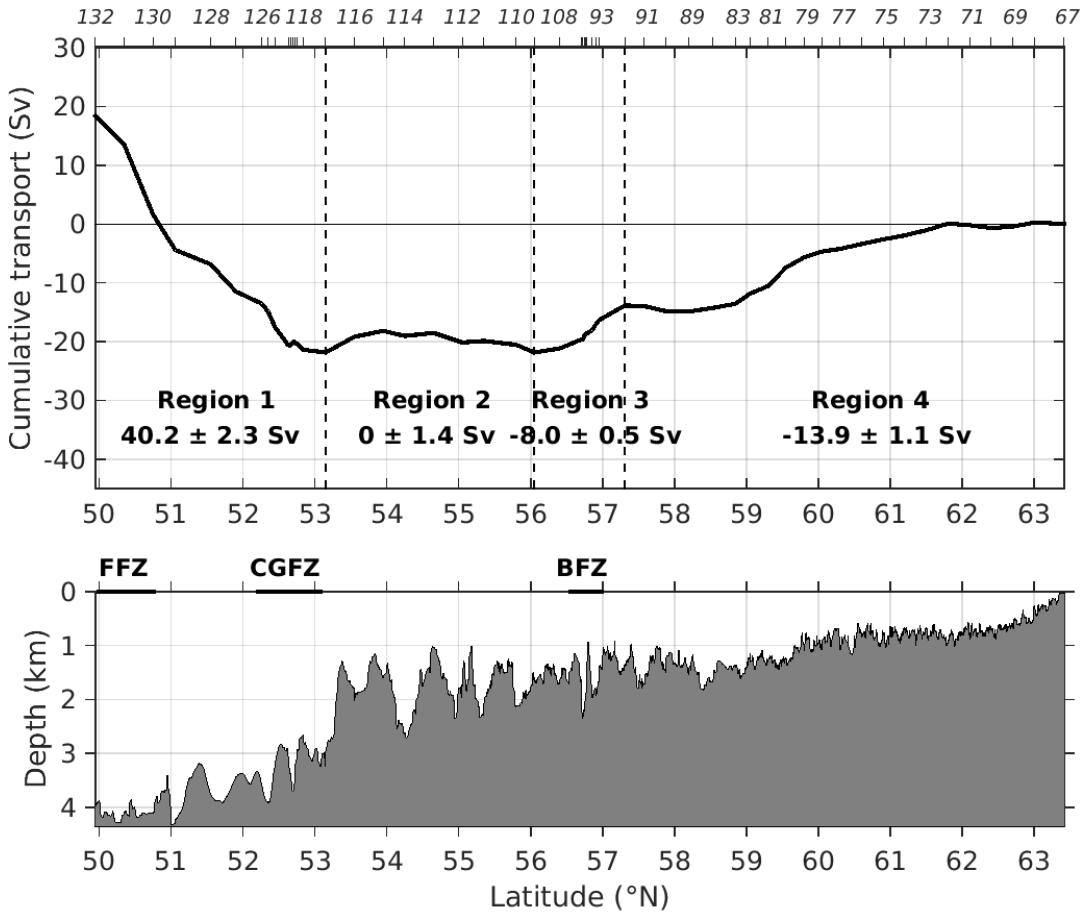

Figure 3.6: Upper panel: Top-to-bottom vertically integrated transport (Sv) along the Ridge Section cumulated from Iceland to 50°N. Increasing (decreasing) cumulative transport corresponds to eastward (westward) transport. The dashed lines divide the section into four regions (see text). The locations of the hydrographic stations are shown on the top axis. Lower panel: Bathymetry along the Ridge Section. CGFZ stands for Charlie Gibbs Fracture Zone, BFZ for Bight Fracture Zone, and FFZ for Faraday Fracture Zone.

In layer 2 (Figure 3.7, Figure 3.8), SAIW was transported eastward by the NAC in region 1 (7.3 ± 0.6 Sv). A weak eastward flow of IW was also observed in the southern part of region 1 (0.8 ± 0.1 Sv). The residual transport (-1.2 ± 0.2 Sv) is associated with a stratified (potential vorticity > 6 10^{-11} m^{-1} s^{-1}) water mass, observed in the upper part of this layer, with the same salinity and oxygen characteristics as SPMW (S > 34.94 and O_2 > 272 µmol kg^{-1}). In regions 2 – 4, the SPMW transport was estimated at -6.5 ± 0.9 Sv and intensified at the BFZ (-2.1 ± 0.1 Sv) and 59 – 62°N (-5.2 ± 0.4 Sv). Similarly, the IW transport was estimated at -4.8 ± 0.4 Sv in regions 2 – 4 and intensified at the BFZ (-1.7 ± 0.1 Sv) and 59 – 62°N (-3.2 ± 0.4 Sv).

In layer 3, LSW of relatively high oxygen concentration (O_2 > 272 µmol kg^{-1} in Figure 3.3) flows eastward in region 1 and between 54 and 56.1°N in region 2 with transports of 13.2 ± 0.5 Sv and 0.9 ± 0.6 Sv, respectively (Figure 3.7). In between these eastward flows as well as at the BFZ, relative low oxygen concentration and high salinity indicate modified LSW flowing westward with a transport of -0.9 ± 0.1 Sv between 53.15 and 54°N in region 2 and -1.3 ± 0.2 Sv at the BFZ. The cross-ridge flow of ISW (-4.8 ± 0.5 Sv) occurs mainly between 58.3°N and 60°N in region 4. Further north, the Reykjanes Ridge is not deep enough to allow the crossing of ISW that lies deeper than 800 m.

In layer 4, no deep waters cross the Ridge Section north of the BFZ (Figure 3.7, Figure 3.8). LDW flows eastward south of and through the southern valley of the CGFZ (south of 52.5°N). The net LDW transport was estimated at 6.7 ± 1.3 Sv. ISOW crosses the Reykjanes Ridge at the BFZ and CGFZ (stations 116 – 126) with transports of -0.8 ± 0.8 Sv and -1.1 ± 0.7 Sv, respectively, while a net ISOW transport of 0 ± 0.4 Sv was estimated between the BFZ and CGFZ.

3.4 Discussion

In this section, we first discuss the circulation observed across the Reykjanes Ridge in the wider context of the subpolar circulation based on an AVISO altimetry map (Figure 3.9). We then discuss the distribution and evolution of all the water masses along the Reykjanes Ridge, focusing in more detail on SPMW and IW, and then on ISOW. Finally, by comparing the inflow with the outflow across the section, we discuss the water mass transformation occurring in the Iceland Basin.

3.4.1 Circulation across the Reykjanes Ridge

The AVISO altimetry map (Figure 3.9) provides a view of circulation in the Subpolar North Atlantic at the time of the cruise. It shows complex structures at the ocean surface with multiple eddies and meanders associated with the NAC as well as the cyclonic circulation in the Iceland Basin and the anticyclonic circulation around the Reykjanes Ridge fed by the NAC. The AVISO altimetry map reveals that, at the time of the cruise, the NAC was composed of three different branches at 46 – 47°N, 50 – 51°N and 52 – 53°N. The latter two branches were sampled by our data set north of 50°N (Figure 3.5). These are the northern

NAC branch and the SAF reported in Daniault et al. (2016), the latter being associated with a sharp salinity front. The top-to-bottom integrated transport of the NAC was estimated at 40.2 ± 2.3 Sv in region 1. Although this synoptic estimate is high compared to the 2002 – 2012 mean transport (24.2 ± 5 Sv) reported by Daniault et al. (2016), it lies within the observed range of variability (see Figure 2 in Daniault et al., 2016). During the cruise, the strong intensity of the NAC could be due either to eddies or meanders, as shown by Roessler et al. (2015) and Bower and von Appen (2008), or to time variability at a longer time scale. Indeed, Roessler et al. (2015) and Breckenfelder et al. (2017) demonstrated a link between the intensity of the NAC and the NAO, with a more vigorous NAC during a positive NAO state, which was the case in 2015 (Piron et al., 2017).

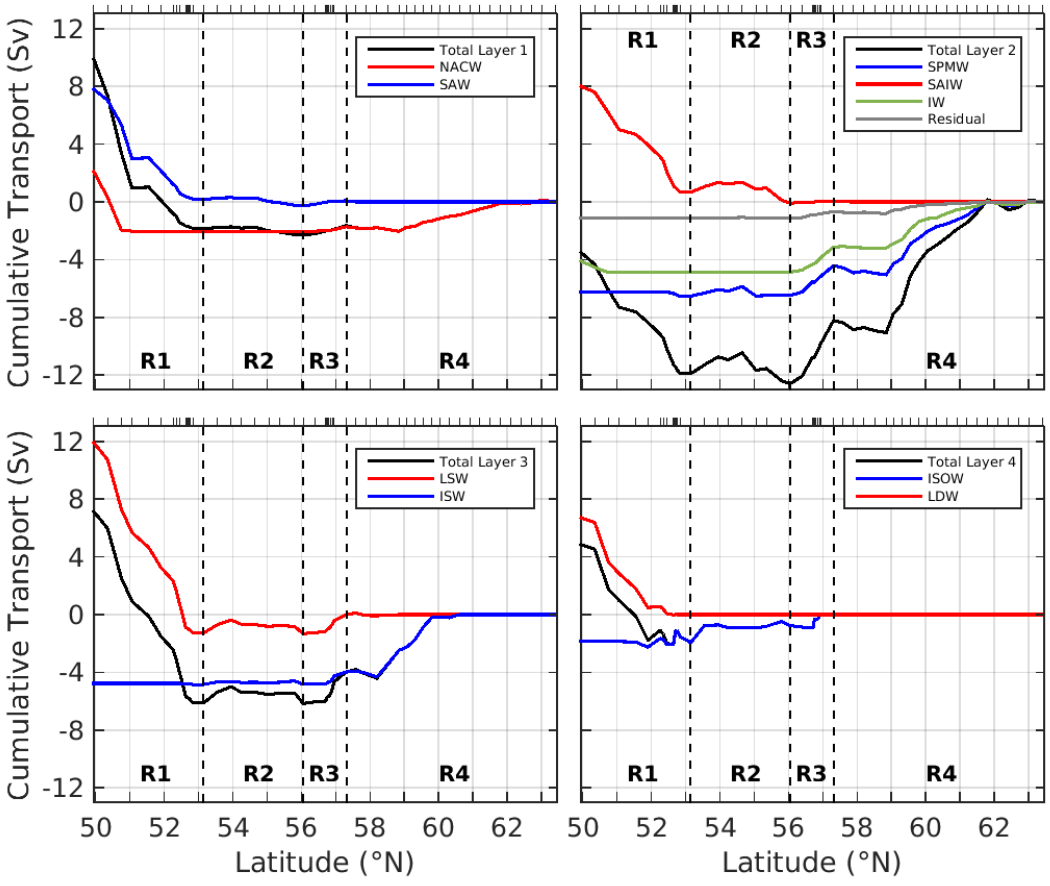

Figure 3.7: Transports (Sv) across the Ridge Section (black lines) cumulated from Iceland to 50°N and integrated into: Layer 1 in the upper-left panel; Layer 2 in the upper-right panel; Layer 3 in the lower-left panel; Layer 4 in the lower-right panel. Blue lines indicate the transports for SAW (upper-left panel), SPMW (upper-right panel), ISW (lower-left panel) and ISOW (lower-right panel). Red lines indicate the transports for NACW (upper-left panel), SAIW (upper-right panel), LSW (lower-left panel) and LDW (lower-right panel). Green line indicates the transports for IW and grey line indicates the residual transport (upper-right panel). These transports are integrated as defined in Table . Locations of the hydrographic stations are given at the top of the upper panels (black ticks).

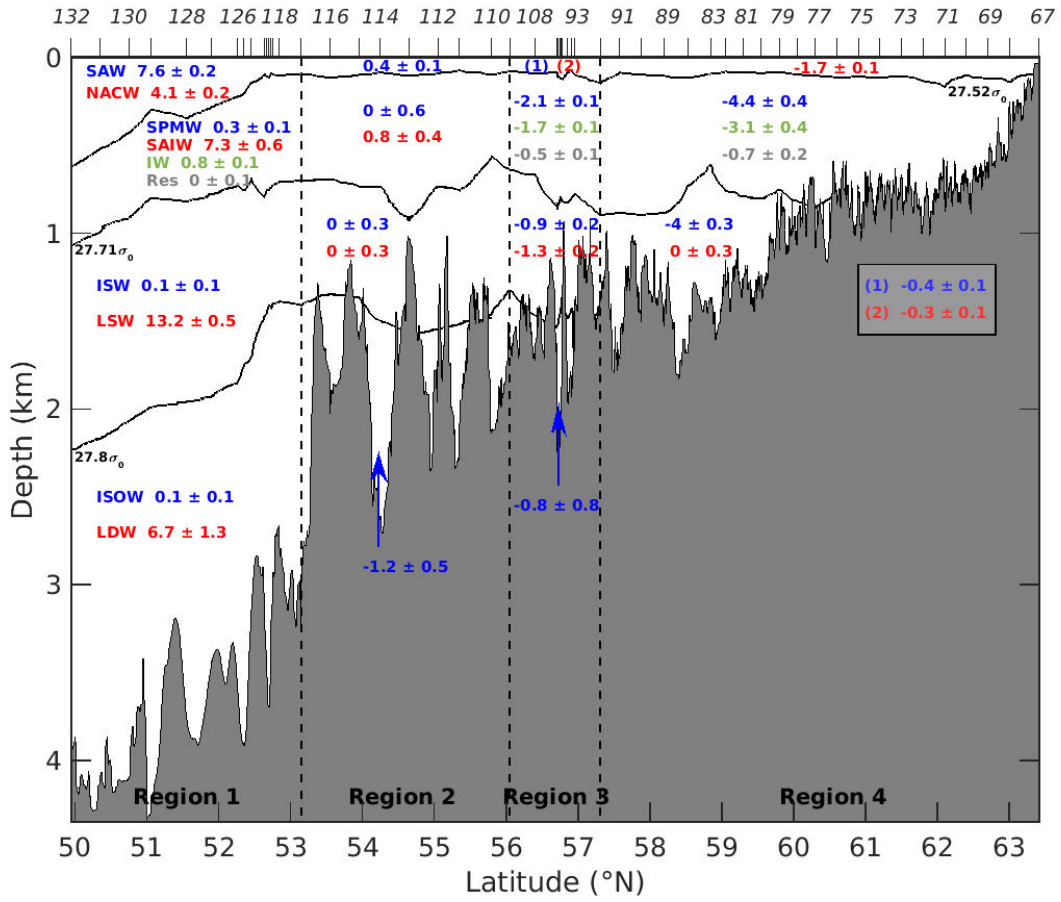

Figure 3.8: Transports (Sv) of each water mass (as identified in Table) integrated over each box encompassed by the isopycnals σ_0 = 27.52, 27.71 and 27.8 kg m^{-3} (solid black lines) and by the four regions (dashed black lines). The colors in regions 2 to 4 relate to the water mass acronyms shown in region 1.

The westward flow of the subpolar gyre occurs in two main branches: at the BFZ and at 59 – 62°N (Figure 3.5). The BFZ pathway is consistent with Bower et al. (2002) who showed, based on an analysis of acoustically tracked floats drifting at σ_0 = 27.5 and 27.7 kg m^{-3}, that cross-ridge flows occur preferentially over fracture zones. The westward pathway at the BFZ is also seen at 1000 dbar on the mean current map derived from Argo float trajectories (see Figure 7 in Ollitrault & Colin de Verdière, 2014). Our data set provides the first direct estimate of the cross-ridge flow magnitude in the surroundings of the BFZ (-8.0 ± 0.5 Sv) and shows that its minimum is at mid-depth, with similar amplitudes at the ocean surface and ocean bottom (Figure 3.5).

The presence of a westward pathway in the northern part of the Reykjanes Ridge (north of the BFZ) has been subject to controversy in the literature. Using S-ADCP sections averaged over 1999 – 2002, Chafik et al. (2014) found almost no transport in the upper 400 m of the water

column above the Reykjanes Ridge between Iceland and 59.5°N. In contrast, using an inverse box model, Lherminier et al. (2010) estimated westward top-to-bottom cross-ridge transports of 9.6 ± 2.1 Sv in 2002 and 13.8 ± 2.1 Sv in 2004 between Iceland and 58.5°N. Using an extended data set spanning 2002 – 2010, García-Ibáñez et al. (2015) computed a westward mean transport of 9.4 ± 4.7 Sv at the same location. Our top-to-bottom integrated westward transport of 14.3 ± 0.8 Sv between Iceland and 58.5°N is consistent with the latter results, showing a significant cross-ridge flow north of 58.5°N.

As pointed out by Daniault et al. (2016), the difference between the results of Chafik et al. (2014) and those of Lherminier et al. (2010) and García-Ibáñez et al. (2015) could be related to the difference in latitude between their data sets as well as to the difference in the vertical range used for the transport computations. We used our data set to check these hypotheses. The transport of the upper 400 m was estimated at -6.5 ± 0.5 Sv between Iceland and 58.5°N and at -3.9 ± 0.4 Sv between Iceland and 59.5°N, which is much lower than our top-to-bottom transport estimates. These results show some dependence on the southern latitude limit used for the transport computations and confirm that the major factor was the limited layer (0 – 400 m) used by Chafik et al. (2014). Additional differences from Chafik et al. (2014) might be caused by time variability and the spread of the locations of the S-ADCP sections averaged by Chafik et al. (2014), which spanned a large latitudinal band around the 59 – 62°N pathway (Figure 3.5). This makes the interpretation of Chafik et al. (2014)'s results somehow difficult, given the sensitivity of transport estimates to the choice of the southern latitude limit. Interestingly, the westward pathway north of 58.5°N is also followed by the Argo floats at 1000 dbar, suggesting that this could be a permanent feature (see Figure 7 in Ollitrault & Colin de Verdière, 2014). The bathymetry shows a sharp deepening between 60 and 58.3°N, which might be the reason for the location of the intensified westward flow there (Figure 3.6). Indeed, 67% of the top-to-bottom transport in region 4 occurs between 60 and 58.3°N.

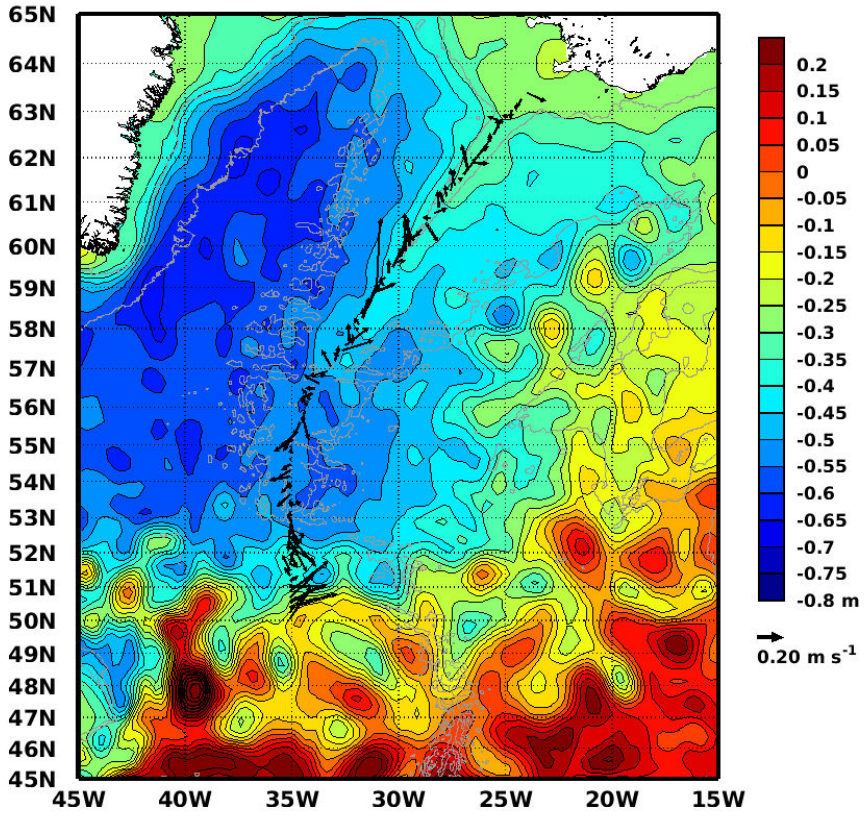

Figure 3.9: Absolute dynamic topography (m) of the subpolar gyre averaged between 24 June and 5 July 2015. Black vectors indicate the surface velocities (m s^{-1}) along the Ridge Section during the cruise. Bathymetries of -1500 m and -2500 m are outlined in grey.

3.4.2 NAC water masses

In region 1, which encompasses the entire northern branch and most of the middle branch of the NAC, the NAC water masses are of subtropical origin (NACW, IW and LDW) and subpolar origin (SAW, SAIW, LSW and ISOW) (Figure 3.7 and Figure 3.8). Recalling that the NAC is both the eastward limb of the subpolar gyre carrying subpolar waters and the upper limb of the Meridional Overturning Circulation (MOC) carrying subtropical waters, the respective intensities of subtropical and subpolar origin waters in the NAC gives us some insight into the relative strengths of each circulation branch. We estimated these intensities as the ratio of subpolar or subtropical water transports divided by the overall eastward flow (40.2 ± 2.3 Sv). In total, the NAC transported a larger proportion of subpolar waters (71.1%). Indeed, the three main water masses contributing to the NAC, LSW (32.8%), SAW (18.9%) and SAIW (18.2%), are of subpolar origin. The proportion of subpolar waters was greater in

the northern branch (83.6%) than in the SAF (61.4%). The larger influence of subpolar water masses compared to subtropical ones reflects a stronger contribution of the subpolar gyre than the MOC to these branches.

3.4.3 Subpolar Mode Water and Intermediate Water

SPMW and IW were seen to be major components of the westward branch of the subpolar gyre, representing 29.7% and 21.9% of the westward transport in regions 2 – 4, respectively.

In two areas along the Reykjanes Ridge, SPMW shows nearly homogeneous densities around σ_0 = 27.56 kg m^{-3} from 59 to 63°N, and σ_0 = 27.61 kg m^{-3} from 53 to 55.5°N (Figure 3.10). The transition between these two pools occurs at the BFZ. SPMW salinity and potential temperature varies progressively from 35.17-7.1°C at 63°N to 34.95-5.2°C at 53°N, but the temperature/salinity variations are density-compensated in each pool. In a similar way to our results, de Boisséson (2010; see Figure 2.10 therein) found a southward increase in SPMW density over the Reykjanes Ridge that he attributed to the circulation and water mass composition of the NAC branches in the Iceland Basin. The model showed that SPMW transported by the westward flow north of 59°N was fed by the SAF, while that transported by the flow at the BFZ was fed by the northern branch of the NAC. As the northern branch carries colder water masses than the SAF (Figure 3.3), SPMW found at the BFZ was denser than that observed further north. In our data, the connection of the SAF with the westward flow at 59 – 62°N is supported by the distribution of the NACW along the Ridge Section. This water mass, which was only present in the SAF (south of 51°N), was observed north of 59°N but not above the BFZ. This is further confirmed by the AVISO sea surface height map shown in Figure 3.9. Isolines suggest that, after looping in the Iceland Basin, the northern branch of the NAC and the SAF are connected to the westward flows at the BFZ and 59 – 62°N, respectively.

Although the cumulated transport of SPMW is low in region 2 (Figure 3.8), the patch of SPMW seen at 53 – 55.5°N is associated with an eastward transport (Figure 3.7). This patch of dense (σ_0 = 27.61 kg m^{-3}, Figure 3.10) SPMW does not seem to be related to a branch of the NAC. It suggests a different formation mechanism from that discussed by de Boisséson et al. (2012). In Brambilla and Talley (2008), the dense variety of SPMW found at 53 – 55.5°N belongs to a tongue of SPMW extending eastward to the Irminger Sea at the center of the

cyclonic gyre, as indicated by the temperature distribution on the 27.5σ_0 isopycnal (see Figures 4 and 7 in Brambilla & Talley, 2008). This cyclonic circulation associated with weaker stratification at its center, also shown by Bower et al. (2002), could favor localized formation of dense SPMW close to its center.

IW, characterized by the lowest oxygen, was found in the SAF with an eastward transport of 0.8 ± 0.1 Sv and at the BFZ and 59 – 62°N with westward transports of 3.2 ± 0.4 Sv and 1.7 ± 0.1 Sv, respectively (Figure 3.3, Figure 3.7 and Figure 3.8). The NAC northern branch contains only SAIW in the layer 2. In the SAF, the IW properties (34.94-4.5°C) are similar to those of Antarctic Intermediate Water (AAIW) observed by Harvey and Arhan (1988; see Figure 11 therein). IW observed at 59 – 62°N is characterized by salinity and temperature of 35.1 and 6.5°C, respectively. The fresher and colder IW at the BFZ (34.9-4.8°C) could be more influenced by SAIW.

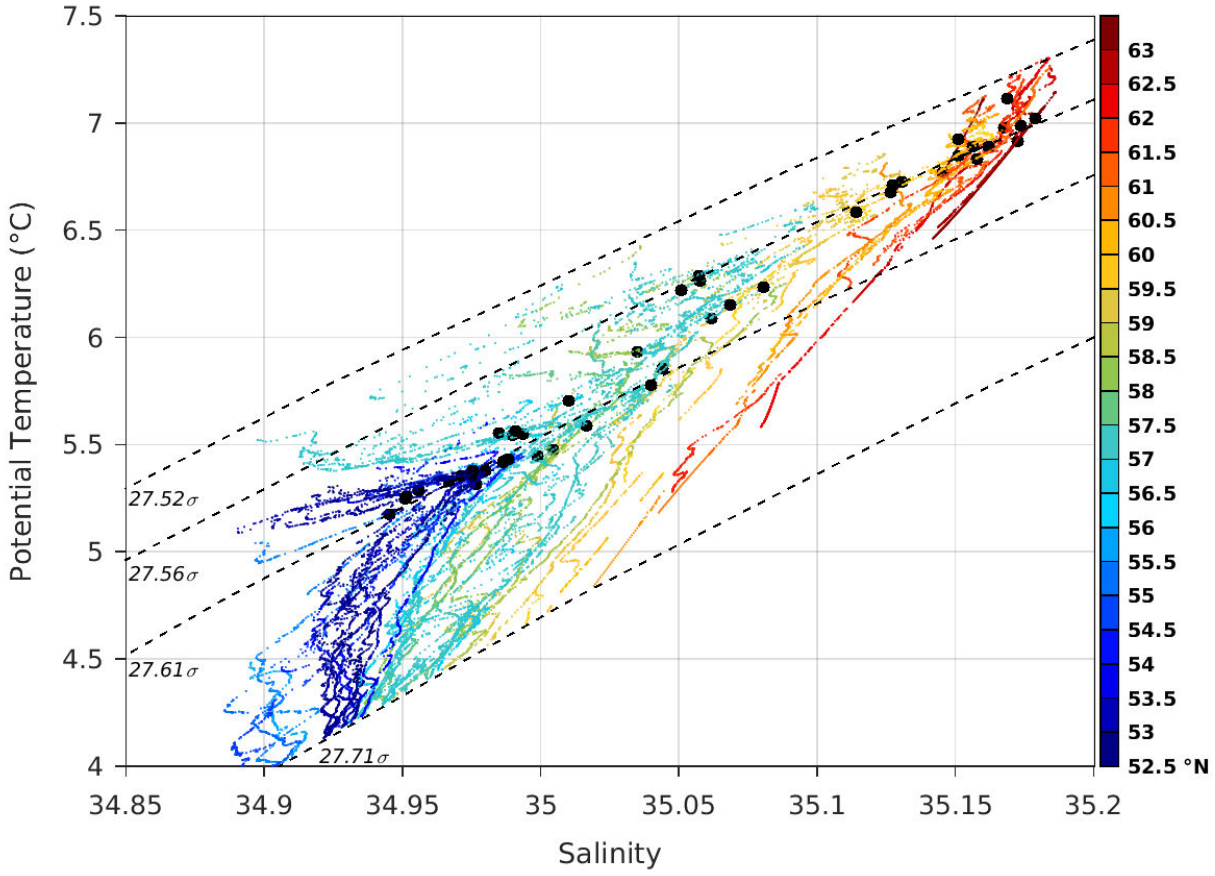

Figure 3.10: Potential Temperature θ/S diagram displaying all hydrographic profiles of SPMW as defined in Table 3.1. The locations of the profiles along the Ridge Section (°N) are shown in color. For all profiles, black dots mark the hydrologic properties at the minimum of potential vorticity in the SPMW layer. Dashed black lines indicate the isopycnals σ_0 = 27.52, 27.56, 27.61 and 27.71 kg m^{-3}.

3.4.4 Iceland-Scotland Overflow Water

In the CGFZ, the westward flow of ISOW through the northern valley is almost entirely compensated by an eastward flow of ISOW through the southern valley (Figure 3.7). Analyzing high-resolution ocean circulation models, Xu et al. (2010) found an ISOW flow over the Reykjanes Ridge occurring through the BFZ and CGFZ, but also north of the BFZ. This latter pathway, which is not observed in our data set, could be related to the fact that ISOW density was lower in the model than in the observations. Despite these limitations, Xu et al. (2010) and Zou et al. (2017) estimated a mean transport of -1.2 ± 0.1 Sv north of the CGFZ, consistent with our observations.

Our estimate of ISOW transport through the CGFZ during the cruise is weaker than that found in past studies. Xu et al. (2010) and Saunders (1994) found an ISOW transport of -2.4 ± 0.5 Sv through the CGFZ. More recently, Bower and Furey (2017) studied the evolution of ISOW transport through the CGFZ using an array of eight moorings deployed between 2010 and 2012. They estimated an ISOW time-averaged transport of -1.7 ± 0.5 Sv, but showed that the ISOW flow varied strongly between intense westward events and weaker westward or even eastward events. The low-frequency variability of ISOW transport through the CGFZ is mainly correlated with the variability of the deep-reaching branches of the NAC. During eastward events, the northern branch of the NAC is localized over the northern valley and the westward ISOW flow is limited to the northern wall of the CGFZ.

In Figure 3.11, we show the profiles of geostrophic and L-ADCP velocities in the CGFZ (52.35°N-52.9°N). L-ADCP measurements provide local velocities at each station while geostrophic velocities are average velocities between stations (Lherminier et al., 2007), so we cannot expect a perfect agreement between the two data sets. Nevertheless, the dynamical structures were in good agreement in the strong eastward currents associated with the northern branch of the NAC that occupied the northern and southern valleys of the CGFZ from the surface down to the bottom. In the northern valley, the flow of ISOW was split in two at 52.72°N by a top-to-bottom eastward vein of the NAC or a deep reaching eddy.

Based on Bower and Furey (2017), the velocity profiles recorded in the period 3 – 5 July 2015 were not typical of extreme eastward events, characterized by maximum NAC surface velocities located over the northern valley. The deep-reaching branch of the NAC was instead localized above the southern valley with a surface speed of 0.23 m s^{-1}. Bower and von Appen (2008) specified that a minimum surface speed of 0.15 m s^{-1} is required to disturb the ISOW

flow. During the 2015 RREX cruise, the NAC was thus to the north and strong enough to disturb the flow of ISOW, but not sufficiently far north to block or reverse it in the CGFZ.

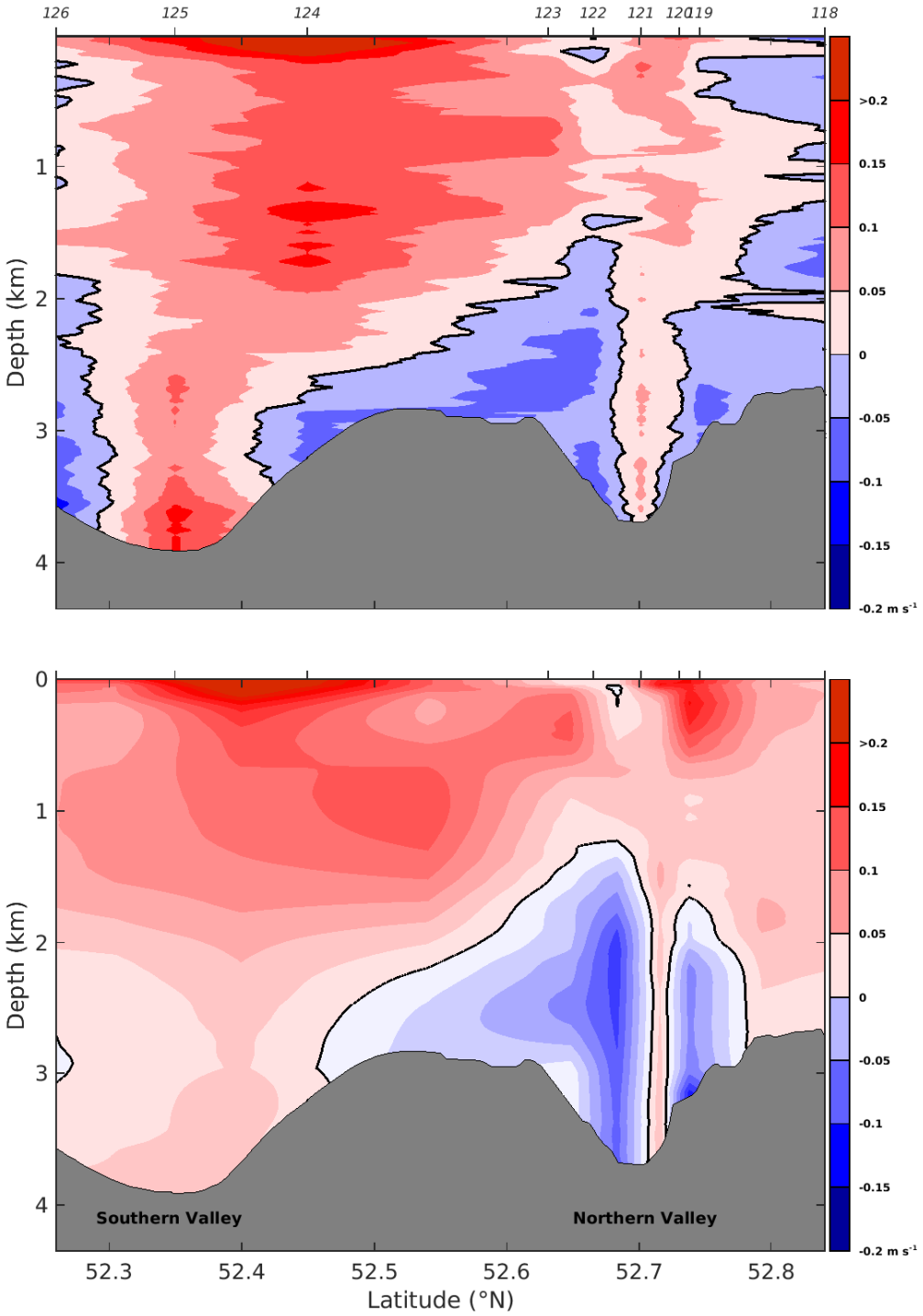

Figure 3.11: L-ADCP (upper panel) and geostrophic (lower panel) velocity sections in the CGFZ (m s^{-1}). Positive values correspond to eastward velocities. The bathymetry from the ship is shown in grey with the locations of the two valleys. The locations of the hydrographic stations are given on the top axis.

3.4.5 Water mass transformations

We will now consider the contributions of the water masses to the MOC. We base our discussion on Figure 3.12, which shows the transports integrated by region and plotted as a function of density appropriately showing the water mass transformations. Note that our interpretation of Figure 3.12 is made in terms of water mass transformations along pathways connecting the northern NAC branch and the SAF to the westward flow over the Reykjanes Ridge, and mixing of the Iceland-Scotland overflows. Following Mercier et al. (2015), we consider the water masses that are less dense (denser) than σ_1 = 32.15 kg m^{-3} (or σ_0 = 27.6 kg m^{-3}) to belong to the upper (lower) limb of the MOC (Figure 3.3). In region 1, the MOC upper limb is composed of NACW, SAW and some SAIW (Figure 3.12), which flow eastward towards the Iceland Basin at a rate of 12.9 ± 0.2 Sv. In regions 2 – 4, the MOC upper limb is mainly composed of weakly stratified SPMW in regions 3 and 4, and NACW in region 4, with hardly any contribution of SAW or SAIW. These water masses flow westward at a rate of 8.8 ± 0.6 Sv. The NACW transport in the westward flow is maximal at σ_0 = 27.38 kg m^{-3} (region 4, Figure 3.12), while it occurs at lower density in the SAF (σ_0 = 27 – 27.25 kg m^{-3}, Figure). SPMW shows maximum transport at σ_0 = 27.56 kg m^{-3} in region 4 and weaker transport at σ_0 = 27.6 kg m^{-3} in the BFZ (region 3). The stratified NACW and SAW transported by the NAC are thus transformed into denser and less stratified SPMW by air-sea buoyancy loss (de Boisséson et al., 2012). This densification mostly occurs within the upper limb of the MOC and paves the way for further densification occurring downstream in the Irminger Sea and feeding of the lower limb of the MOC (Sarafanov et al., 2012).

In the MOC lower limb (σ_1 > 32.15 kg m^{-3}), the maximum transport in the NAC is associated with an eastward transport of LSW at σ_0 = 27.72 kg m^{-3}, while weaker westward transport of LSW is found at σ_0 = 27.73 kg m^{-3} in the BFZ and at 27.75 kg m^{-3} in region 4 (Figure 3.12). In regions 2 – 4, both ISW (-4.9 ± 0.3 Sv) and IW (-4.8 ± 0.4 Sv) contribute more to the westward transport across the Reykjanes Ridge than does the sum of LSW (-1.3 ± 0.7 Sv) and ISOW (-2.0 ± 0.9 Sv) (Figure 3.8). The maximum transport of ISW around σ_0 = 27.78 kg m^{-3} in region 4 reveals the modal characteristic of this water mass. ISW is formed by local entrainment and mixing of SPMW and ISOW, but also incorporates LSW by isopycnal mixing, which partly explains the small cross-ridge transport associated with LSW in our diagnostic.

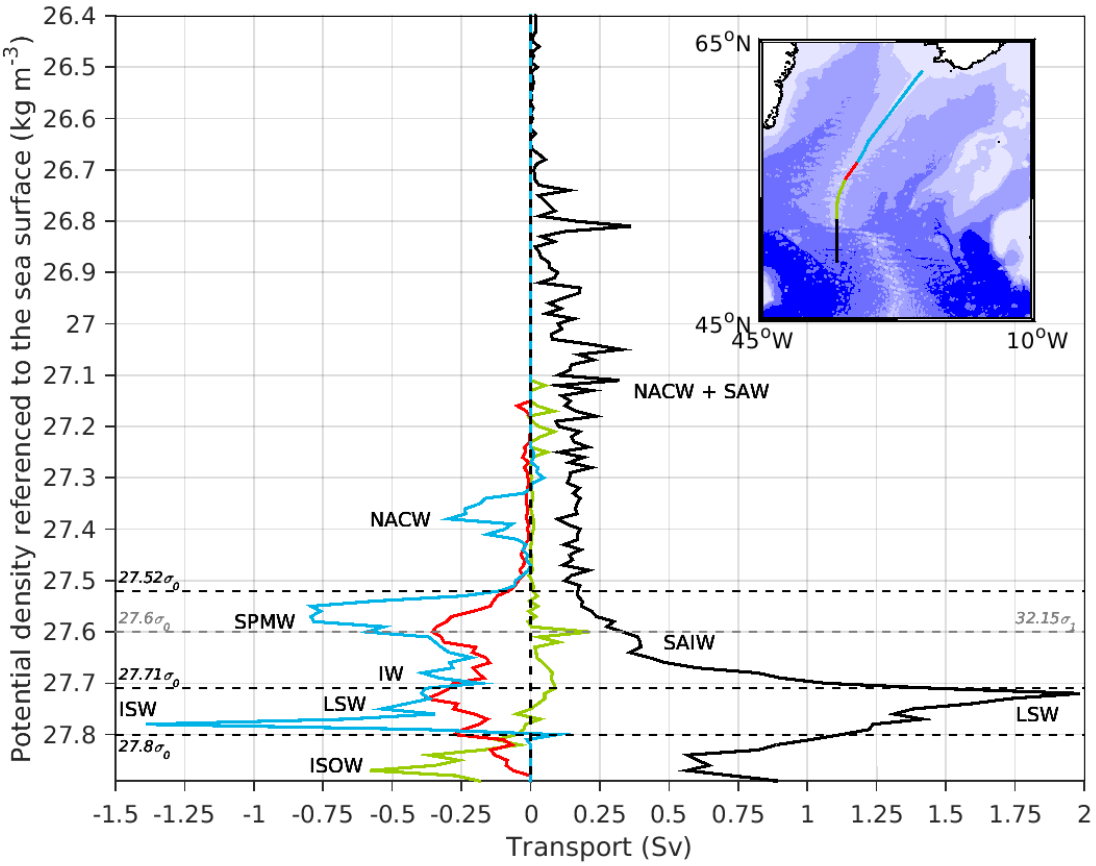

Figure 3.12: Transport integrated in 0.01 bins of density σ_0 for the four regions identified in Figure 3.6: region 1 is shown in black (50 – 53.15°N), region 2 in green (53.15 – 56.1°N), region 3 in red (56.1 – 57.3°N) and region 4 in blue (57.3°N – Iceland). Horizontal dashed black lines indicate the potential density σ_0 = 27.52, 27.71 and 27.8 kg m^{-3}. Dashed grey line indicates the potential density σ_1 = 32.15 kg m^{-3}. Some water masses listed in Table are associated with a peak of maximum transport.

3.5 Conclusion

During June – July 2015, the circulation and hydrography was recorded by 2 S-ADCPs and at 56 CTDO$_2$ stations along the crest of the Reykjanes Ridge, from the Icelandic continental shelf south to 50°N. The associated geostrophic transports were estimated by combining S-ADCP and hydrographic data. These observations provide the first direct estimates of exchanges of volume and properties between the Iceland Basin and the Irminger Sea across the Reykjanes Ridge.

Before entering the Iceland Basin, the NAC crosses the MAR following deep fractures zones. During June – July 2015, the NAC was in a northern position, such that we identified two surface-intensified branches north of 50°N that followed the CGFZ and FFZ. These branches

correspond to the northern branch of the NAC and to the SAF as identified in the literature (Daniault et al., 2016) and were associated with top-to-bottom transports of 17.4 ± 1.7 Sv and 22.8 ± 1.1 Sv, respectively. Compared to the portion of the SAF measured in this study, which contains 61.4% of subpolar waters and 38.6% of subtropical waters, the northern branch contains a larger proportion of subpolar waters, representing 83.6% of its top-to-bottom transport. In the surface layers, the NAC transported highly stratified water masses, while at deeper levels it transported LSW at a density of σ_0 = 27.72 kg m^{-3}. This latter water mass was the main contributor to the NAC and represented 32.8% of its top-to-bottom integrated transport.

The westward flow across the Reykjanes Ridge was estimated at -21.9 ± 2.5 Sv and represents the first direct estimate of subpolar gyre intensity. This flow follows two main passages: at 59 – 62°N with a transport of -13.6 ± 0.8 Sv and through the BFZ with a transport of -8.0 ± 0.5 Sv. As these pathways are already present in other data sets, they are likely permanent features related to the bottom topography. The flows at the BFZ (Bower & von Appen, 2008) and at about 60°N were associated with a sharp deepening of the crest of the Reykjanes Ridge. In terms of water masses, the three main contributors to the top-to-bottom westward flow were SPMW (29.7%), ISW (22.3%), and IW (21.9%), while the contributions of ISOW and LSW were only 9.1% and 5.9%, respectively. SPMW found at and south of the BFZ (σ_0 = 27.61 kg m^{-3}) was denser than SPMW found at 59 – 62°N (σ_0 = 27.56 kg m^{-3}) as a result of cyclonic circulation in the Iceland Basin connecting the SAF to 59 – 62°N and the northern NAC branch to the BFZ. At greater depths, IW and ISW also crossed the Reykjanes Ridge following these two pathways. However, the westward flow of ISW was strictly localized south of 60°N because the Reykjanes Ridge is not deep enough to allow the transport of ISW north of this latitude.

ISOW crossed the Reykjanes Ridge between 52°N and 57.3°N; no sign of ISOW was recorded north of the BFZ. Through the BFZ and south of it, ISOW transports were estimated at -0.8 ± 0.8 Sv and -1.1 ± 0.7 Sv, respectively. These results compare favorably with those from numerical models (Xu et al., 2010; Zou et al., 2017), although the ISOW transport through the CGFZ was weak, as a consequence of the position and strength of the northern branch of the NAC in summer 2015 that disturbed the ISOW flow in the CGFZ (Bower & Furey, 2017).

Finally, our data set shows that large water mass transformations and densifications occurred in the Iceland Basin. Densification did not lead to a significant light-to-dense conversion of the water masses from the upper to the lower limb of the MOC, but it preconditioned the water column by forming weakly stratified water masses, especially SPMW, that favor the downstream overturning occurring in the Irminger Sea.

4 Formation and evolution of the East Reykjanes Ridge Current and Irminger Current

In this chapter, we provide a 3-D analysis of the circulation around and above the Reykjanes Ridge during the summer 2015, and thus we investigate the questions Q3, Q4 and Q5 given in Introduction. To quantify this circulation, geostrophic transports were estimated across the four sections carried out during the RREX2015 cruise.

4.1 Introduction

The topography of the northern North-Atlantic Ocean comprises a succession of basins and ridges that constrain the horizontal circulation of the subpolar gyre. Among them, the Reykjanes Ridge, which is located between the Iceland Basin and the Irminger Sea, composes the northern part of the Mid-Atlantic Ridge. This major topographic feature extends southwest of Iceland and terminates at the Charlie Gibbs Fracture Zone (CGFZ) at 35°W/52.5°N (Figure 4.1).

The circulation scheme in Figure 4.1 is an overall view of the mean circulation in the northern North-Atlantic Ocean adapted from Daniault et al. (2016). The northeastward North-Atlantic Current (NAC) is an extension of the Gulf Stream and bounds the cyclonic circulation of the subpolar gyre to the south. Divided into three main branches, the NAC is dynamically constrained to cross the Mid-Atlantic Ridge eastward above deep fracture zones (Bower & von Appen, 2008; Bower & Furey, 2017; Roessler et al., 2015; Schott et al., 1999). The northern branch of the NAC follows the Charlie Gibbs Fracture Zone (CGFZ) at 35°W/52.5°N, the Sub-Arctic Front follows the Faraday Fracture Zone (FFZ) at 35°W/50.5°N, and the southern branch of the NAC follows the Maxwell Fracture Zone at 35°W/48°N. Part of these branches flows cyclonically in the Iceland Basin and reaches the eastern flank of the Reykjanes Ridge. There, influenced by the bathymetry of the Reykjanes Ridge, the top-to-bottom current is constrained to flow anticyclonically around the ridge to join the Irminger Sea (Bower et al., 2002). Along the eastern flank of the Reykjanes Ridge, the southwestward current feeds the westward branch of the subpolar gyre and is called the East Reykjanes Ridge Current (ERRC) (Treguier et al., 2005). In the Irminger Sea, the cyclonic circulation flows primarily northeastward along the western flank of the Reykjanes Ridge as the Irminger Current (IC), and then southwestward along the eastern flank of Greenland as the East-Greenland Irminger Current (Lherminier et al., 2007). At the southern tip of Greenland, a narrow cyclonic recirculation of the East-Greenland Irminger Current forms the Irminger Gyre in the western part of the Irminger Sea (Våge et al., 2011).

The ERRC was observed mostly at surface and sub-surface and appears in high-resolution numerical simulations. Studies based on sub-surface drifters (Otto & Van Aken, 1996; Reverdin et al., 2003; Valdimarsson & Malmberg, 1999), upper-ocean repeated transects (Chafik et al., 2014; Childers et al., 2015; Knutsen et al., 2005), and numerical models (Treguier et al., 2005) described the ERRC as a narrow southwestward flow east of the

Reykjanes Ridge. However, maps of surface velocities derived from satellite altimetry showed low-velocity chaotic southward flow east of the Reykjanes Ridge, which could hardly be associated with a continuous steady current (Jakobsen et al., 2003). This discrepancy could be nevertheless due to the coarse horizontal resolution of altimetry maps. Along the repeated Ovide transect, Daniault et al. (2016) provided an averaged view of the top-to-bottom vertical structure of the ERRC. At about 58.8°N, the ERRC was composed of a main quasi-barotropic branch at 30.1°W and two surface and bottom intensified branches at 28.5°W and 29°W, respectively, which correspond altogether to a 200-km wide current east of the top of the Reykjanes Ridge. This averaged structure of the ERRC is similar to that previously documented by Sarafanov et al. (2012) in 2002 – 2008 at 59.5°N. However, the top-to-bottom structure and hydrological properties of the ERRC was only documented in a narrow band of latitudes (58.8 – 59.5°N) and was never observed south and north of it. Documenting the evolution of the ERRC along the Reykjanes Ridge, better understanding its formation mechanisms, and describing its connections with the IC, would greatly improve our knowledge on the water mass pathways from the eastern part of the subpolar gyre to the Irminger Sea and the impact of the Reykjanes Ridge on the ocean circulation as well.

By crossing the Reykjanes Ridge, the westward branch of the subpolar gyre joins the IC on the western flank of the ridge (Figure 4.1). Våge et al. (2011) defined the IC as a two-branch surface-intensified northeastward flow of about 200-km wide west of the top of the Reykjanes Ridge. Flowing northward along the Reykjanes Ridge, the IC is schemed as a continuous flow without connections with the Irminger Gyre in Figure 4.1. However, Yashayaev et al. (2007) showed exchanges of Labrador Sea Water (LSW) between the Irminger Gyre and the IC along the repeated trans-Atlantic section (AR7), suggesting interactions between them. Moreover, Sy et al. (1997) and Fan et al. (2013) highlighted strong eddy activity in the center of the Irminger Sea that should favor such interactions. Those are selected examples that the circulation and interactions between the main currents in the Irminger Sea remains unclear and deserves further investigations.

The major source of IC water comes from the NAC that quickly leaves the Iceland Basin after crossing the Reykjanes Ridge (Lavender et al., 2000; Ollitrault & Colin de Verdière, 2014; Våge et al., 2011). Across the Reykjanes Ridge, Bower et al. (2002) pointed out the Bight Fracture Zone (BFZ) at 57°N as a preferential cross-ridge pathway from RAFOS float trajectories. Likewise, models showed that deep overflows from the Nordic Seas preferentially join the Irminger Sea through the BFZ and CGFZ (Xu et al., 2010; Zou et al.,

2017). Additional pathways across the Reykjanes Ridge were suggested north of the BFZ, although no specific fracture zones were identified there (Daniault et al., 2016; Lherminier et al., 2010). It is more recently that exchanges of volume and properties between the Iceland Basin and the Irminger Sea were directly estimated. Based on data from the Reykjanes Ridge Experiment (RREX) project, Petit et al. (2018b) showed that the north – south deepening of the Reykjanes Ridge crest resulted in a westward flow that preferentially crossed the ridge at the BFZ and at 59 – 62°N. The Subpolar Mode Water (SPMW) and intermediate waters crossed the Reykjanes Ridge by following these two pathways. Above the Reykjanes Ridge, they showed that SPMW found at BFZ was denser than SPMW found at 59 – 62°N, which was related to their connections to the northern branch of the NAC and to the SAF, respectively, through the cyclonic circulation in the Iceland Basin. For density higher than 27.8 kg m^{-3}, Iceland-Scotland Overflow Water (ISOW) from the Nordic Seas crossed the Reykjanes Ridge between 52°N and 57.3°N, with a major part going through the BFZ, but no sign of ISOW was recorded further north. Overall, 21.9 ± 2.5 Sv crossed the Reykjanes Ridge toward the Irminger Sea between Iceland and 53.15°N. This cross-ridge flow should affect the circulation and properties of the IC between Iceland to 53.15°N, but this has not been documented yet. Further investigations of the top-to-bottom IC structure are required to better understand the evolution of the IC north and south of the Ovide latitudes, as well as its interactions with the surrounded water masses from the Iceland Basin and the Irminger Sea. Documenting the evolution of the along-ridge currents based on the top-to-bottom transects at three different latitudes across the Reykjanes Ridge conducted as part of the RREX project in 2015 will complete and correct our view of the ocean circulation near the Reykjanes Ridge.

In this paper, section 4.2 presents the data and method used for this study. Then, the horizontal and vertical structures of the along-ridge flows as well as their latitudinal evolution along the Reykjanes Ridge are described in section 4.3. The latitudinal evolution of the hydrological properties of the along-ridge flows are also analyzed and compared to the properties of the cross-ridge flows. Section 4.4 discusses the circulation scheme deduced from our results and its comparison to previous findings. Finally, results are summarized in section 4.5.

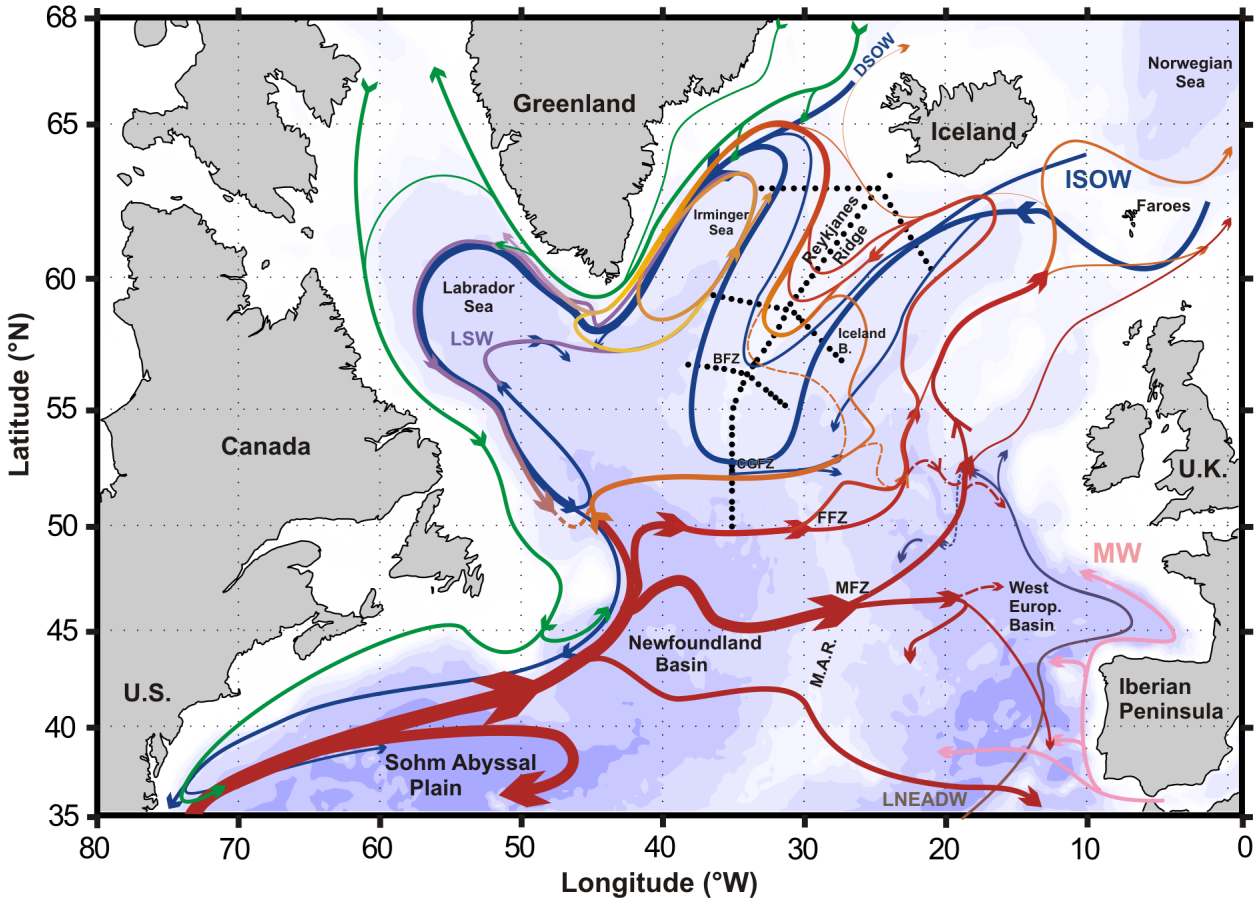

Figure 4.1: Schematic of the large-scale circulation in the northern North Atlantic adapted from Daniault et al. (2016). Locations of the hydrographic stations carried out during the RREX2015 cruise along four sections are overlaid (black dots). Bathymetry is plotted in color with color changes at 100 m, 1000 m and every 1000 m below 1000 m. Topographical features of North Atlantic are labeled: Bight Fracture Zone (BFZ), Charlie-Gibbs Fracture Zone (CGFZ), Faraday Fracture Zone (FFZ), Maxwell Fracture Zone (MFZ), Mid-Atlantic Ridge (MAR). The main associated water masses are indicated: Denmark Strait Overflow Water (DSOW), Iceland-Scotland Overflow Water (ISOW), Labrador Sea Water (LSW), Mediterranean Water (MW) and Lower North East Atlantic Deep Water (LNEADW), which is called Lower Deep Water (LDW) in the following.

4.2 Data and Methods

4.2.1 Data sets

The RREX2015 cruise was carried out from 5 June to 10 July 2015 on the French N/O Thalassa. A total of one hundred and thirty-two (132) CTDO_2 (Conductivity Temperature Depth Oxygen) stations were occupied during the RREX2015 cruise (Figure 4.1). Three sections were conducted perpendicular to the ridge axis and a fourth section extended from the Iceland shelf to 50°N. The three zonal sections intersect the top of the Reykjanes Ridge at 24.7°W/63°N, 31.3°W/58.8°N and 34°W/56.4°N, and are referred to hereinafter as the North

Section (NS), Ovide Section (OS) and South Section (SS) respectively. The OS is a reoccupation, from 27.2°W to 36.4°W, of the hydrographic line carried out in the framework of the Ovide program (Daniault et al., 2016). These sections were designed to study the meridional evolution of the IC and ERRC on the sides of the Reykjanes Ridge. The meridional section, called Ridge Section (RS), was used by Petit et al. (2018b) to document and quantify cross-ridge flows. The nominal station spacing was of 30 km along the four sections and was reduced to 2 km at the BFZ (57°N) and CGFZ (52.5°N). To deploy moorings along the vessel track, the SS was interrupted for 25 hours after station 9, the OS was interrupted for 18 hours after station 38, and the RS was interrupted for 34 hours after station 83. The RS was also interrupted for 22 hours after station 101 to carry out hydrographic measurements west of the BFZ main sill. These interruptions were not significant in comparison with the time spent to record each hydrographic station (about four hours). Nevertheless, the weak asynopticity related to the time spent during the entire cruise was taken into account in the computation of error transports as showed by Petit et al. (2018b). At each hydrographic station, temperature, conductivity and dissolved oxygen were measured as a function of pressure using a Seabird Electronics 911+ $CTDO_2$ probe mounted on a rosette of 28 bottles. The $CTDO_2$ accuracies were 1dbar in pressure, 0.001°C in temperature, 0.0025 in salinity and 1μmol kg^{-1} in dissolved oxygen (Branellec & Thierry, 2016). Along the ship track, a 12 kHz echo-sounder measured the bathymetry every 30 s.

Velocity measurements were obtained using two S-ADCPs (Shipboard Acoustic Doppler Current Profiler, RD Instrument) operating at 38 kHz (OS38) and 150 kHz (OS150). In this study, we only used the OS38 data. The bin size was set to 24 m, the maximum depth range was 1300 m and the pinging rate 3 s. Details about calibration of OS38 velocities can be found in Petit et al. (2018a).

Surface geostrophic velocities were computed from the Merged-Absolute Dynamic Topography (MADT) of the Ssalto/Duacs AVISO (Archiving, Validation and Interpretation of Satellite Oceanographic data center) altimeter products distributed by CMEMS (Copernicus Marine Environment Monitoring Service) on a 1/3° grid. These velocities were averaged over 10 June to 23 June 2015, which corresponds to the time required to record the three zonal sections during the RREX2015 cruise.

Finally, Ekman transports were calculated at the location and time of each hydrographic station from the wind stress data of two global atmospheric reanalysis, ERA-Interim reanalysis (Dee et al., 2011) and NCEP/NCAR reanalysis (Kalnay et al., 1996).

4.2.2 S-ADCP referenced geostrophic velocities and transport estimates

Geostrophic velocities between two adjacent $CTDO_2$ stations were computed using the thermal wind equation and a reference level arbitrarily set to the surface. Dynamical heights needed for the thermal wind computation were computed from temperature, salinity and pressure. An absolute geostrophic field was then estimated by adjusting the geostrophic field to S-ADCP velocity measurements by adding a constant velocity correction to the geostrophic profile referenced to the surface (Gourcuff et al., 2011; Lherminier et al., 2007; Petit et al., 2018b). As in Petit et al. (2018b), the correction is the difference between the S-ADCP velocities horizontally averaged between two stations and the geostrophic velocities in a reference layer L_{ref} = 600 – 1000 m. At the RS, a unique reference velocity was used over the BFZ and CGFZ (stations 96 – 101 and 119 – 122 respectively) to cop with strong ageostrophic motions (see Petit et al., 2018b). Geostrophic flow in the bottom triangles of the sloping topography was computed following Petit et al. (2018b).

Transports across each section were computed as the sum of geostrophic and Ekman transports. The geostrophic transport was estimated by integrating geostrophic velocity over the horizontal distance of the pair of stations and over the vertical resolution (1 m) of the geostrophic velocity profile. This computation was applied for regions limited by isopycnals or bathymetry in the vertical and for the surface to bottom integrated transport as well. Readers are invited to refer to Petit et al. (2018b) for a presentation of the method used to compute errors for the transports.

In an attempt to close the volume budgets of the ERRC and IC, which horizontal extensions are estimated in section 4.3 below, we divided the area into four boxes. Two boxes were delimited by the NS, OS, RS between the NS and OS, and were closed by lines joining the stations of the eastern limit of the ERRC (stations 49 and 41) and western limit of the IC (stations 28 and 62) (see Figure 4.7). Two other boxes were delimited by the OS, SS, RS between the OS and SS, and were closed by lines joining the stations of the eastern limit of the ERRC (stations 41 and 2) and the western limit of the IC (stations 23 and 28). The volume

budgets of these four boxes were estimated from the transports across the sections and by computing transports between the eastern limits of the ERRC and the western limits of the IC. For the latter, horizontal gradients of dynamical heights referenced to the surface were computed between the ERRC endpoint stations and IC endpoint stations. The geostrophic velocities derived from these gradients were adjusted at surface to the geostrophic velocities from AVISO that were averaged between the two endpoint stations. Transports were estimated by integrating these absolute geostrophic velocities over the distance between stations and depth.

4.2.3 Water mass characterization

In this section, we define nine water masses in the vicinity of the Reykjanes Ridge by referring to Petit et al. (2018b). Defined by $\sigma_0 < 27.52$ kg m^{-3}, Layer 1 encompasses North Atlantic Central Water (NACW) with salinity higher than 34.94 and Sub-Arctic Water (SAW) with salinity lower than 34.94 (Figure 4.2a). Defined by $27.52 < \sigma_0 < 27.71$ kg m^{-3}, Layer 2 contains Subpolar Mode Water (SPMW) with salinity and dissolved oxygen concentration (Figure 4.2c) higher than 34.94 and 272 µmol kg^{-1}, respectively, and potential vorticity (Figure 4.2d) lower than 6 10^{-11} $m^{-1}s^{-1}$. It also contains Intermediate Water (IW) with salinity higher than 34.94 and dissolved oxygen concentration lower than 272 µmol kg^{-1}, and Sub-Arctic Intermediate Water (SAIW) with salinity lower than 34.94. Defined by $27.71 < \sigma_0 < 27.8$ kg m^{-3}, Layer 3 contains Labrador Sea Water (LSW) with salinity lower than 34.94 and Icelandic Slope Water (ISW) with salinity higher than 34.94. Finally defined by $\sigma_0 > 27.8$ kg m^{-3}, Layer 4 encompasses Iceland-Scotland Overflow Water (ISOW) with salinity higher than 34.94 and Denmark Strait Overflow Water (DSOW) in the Irminger Sea with salinity lower than 34.94 (Sarafanov et al., 2012). Criteria for the identification of these water masses are reported in Table 4.1 and outlined along the hydrographic sections in Figure 4.2. Readers are invited to refer to Figure 4.3 of Petit et al. (2018b) for the identification of these water masses along the Ridge Section.

Along the three zonal sections, we identify three varieties of SPMW all satisfying PV < 6 10^{-11} but with different salinity in Figure 4.2a and potential temperature in Figure 4.2b: $SPMW_5$ is defined by salinity less than 35.1 and potential temperature range of 5 – 5.5°C. It is centered above the ridge at the SS and is also found on its western side at the OS. Salinity and

potential temperature of $SPMW_6$ are in the range 35.1 – 35.15 and 6.5 – 7°C, respectively. $SPMW_6$ is located on the eastern side of the ridge at the OS and is also found on its western side at the NS. Finally, $SPMW_7$ is defined by salinity higher than 35.15 and potential temperature in the range 7 – 7.5°C. It is observed on the eastern and western flank of the Reykjanes Ridge at the NS.

Table 4.1: Criteria used for the identification of the water masses along the sections. They are based on limits in potential density (σ_0), salinity (S), dissolved oxygen concentration (O_2) and potential vorticity (PV), computed as $f/\rho = \partial\rho/\partial z$, where f is the Coriolis parameter and ρ is the potential density referenced to the mid-depth interval over which the vertical gradient of density is computed. Potential density limits are reported on Figure 4.2a as well. NACW stands for North Atlantic Central Water; SAW for Sub-Arctic Water; SAIW for Sub-Arctic Intermediate Water; IW: Intermediate Water; SPMW for SubPolar Mode Water; LSW for Labrador Sea Water; ISW for Icelandic Slope Water; DSOW for Denmark Strait Overflow Water; ISOW for Iceland-Scotland Overflow Water.

Water Masses	Potential density (kg m^{-3})	Salinity	Oxygen (μmol kg^{-1})	Potential Vorticity (m^{-1} s^{-1})
NACW	$\sigma_0 < 27.52$	S > 34.94		
SAW	$\sigma_0 < 27.52$	S < 34.94		
SAIW	$27.52 < \sigma_0 < 27.71$	S < 34.94		
IW	$27.52 < \sigma_0 < 27.71$	S > 34.94	$O_2 < 272$	
SPMW	$27.52 < \sigma_0 < 27.71$	S > 34.94	$O_2 > 272$	$PV < 6\ 10^{-11}$
LSW	$27.71 < \sigma_0 < 27.8$	S < 34.94		
ISW	$27.71 < \sigma_0 < 27.8$	S > 34.94		
DSOW	$\sigma_0 > 27.8$	S < 34.94		
ISOW	$\sigma_0 > 27.8$	S > 34.94		

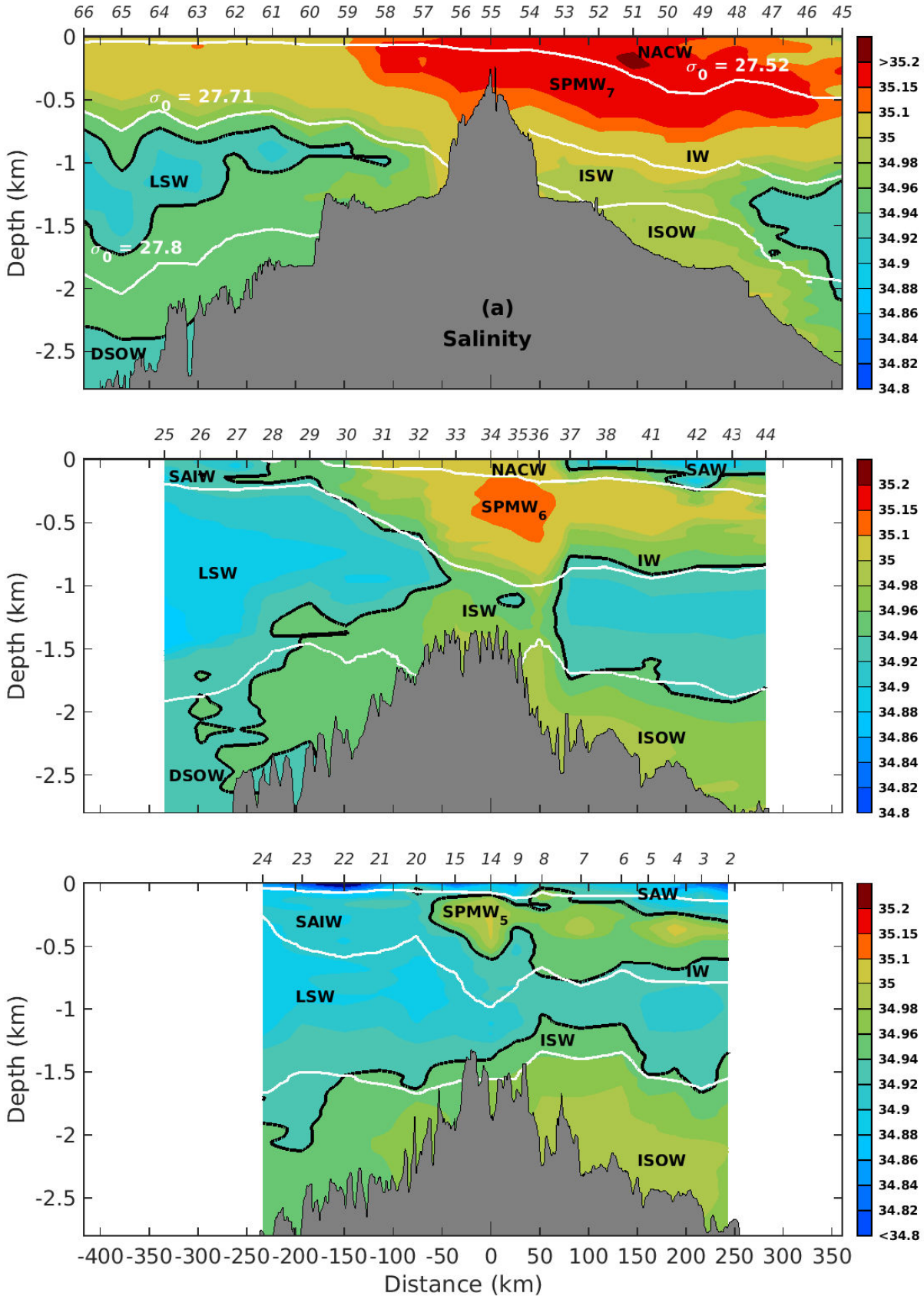
66 65 64 63 62 61 60 59 58 57 56 55 54 53 52 51 50 49 48 47 46 45
NACW
σ_0 = 27.52
SPMW$_7$
σ_0 = 27.71
IW
ISW
LSW
ISOW
σ_0 = 27.8
(a)
Salinity
DSOW
Depth (km)
25 26 27 28 29 30 31 32 33 34 35 36 37 38 41 42 43 44
SAIW
NACW
SAW
SPMW$_6$
IW
LSW
ISW
ISOW
DSOW
24 23 22 21 20 15 14 9 8 7 6 5 4 3 2
SAW
SPMW$_5$
SAIW
IW
LSW
ISW
ISOW
-400 -350 -300 -250 -200 -150 -100 -50 0 50 100 150 200 250 300 350
Distance (km)
>35.2
35.15
35.1
35
34.98
34.96
34.94
34.92
34.9
34.88
34.86
34.84
34.82
34.8
<34.8

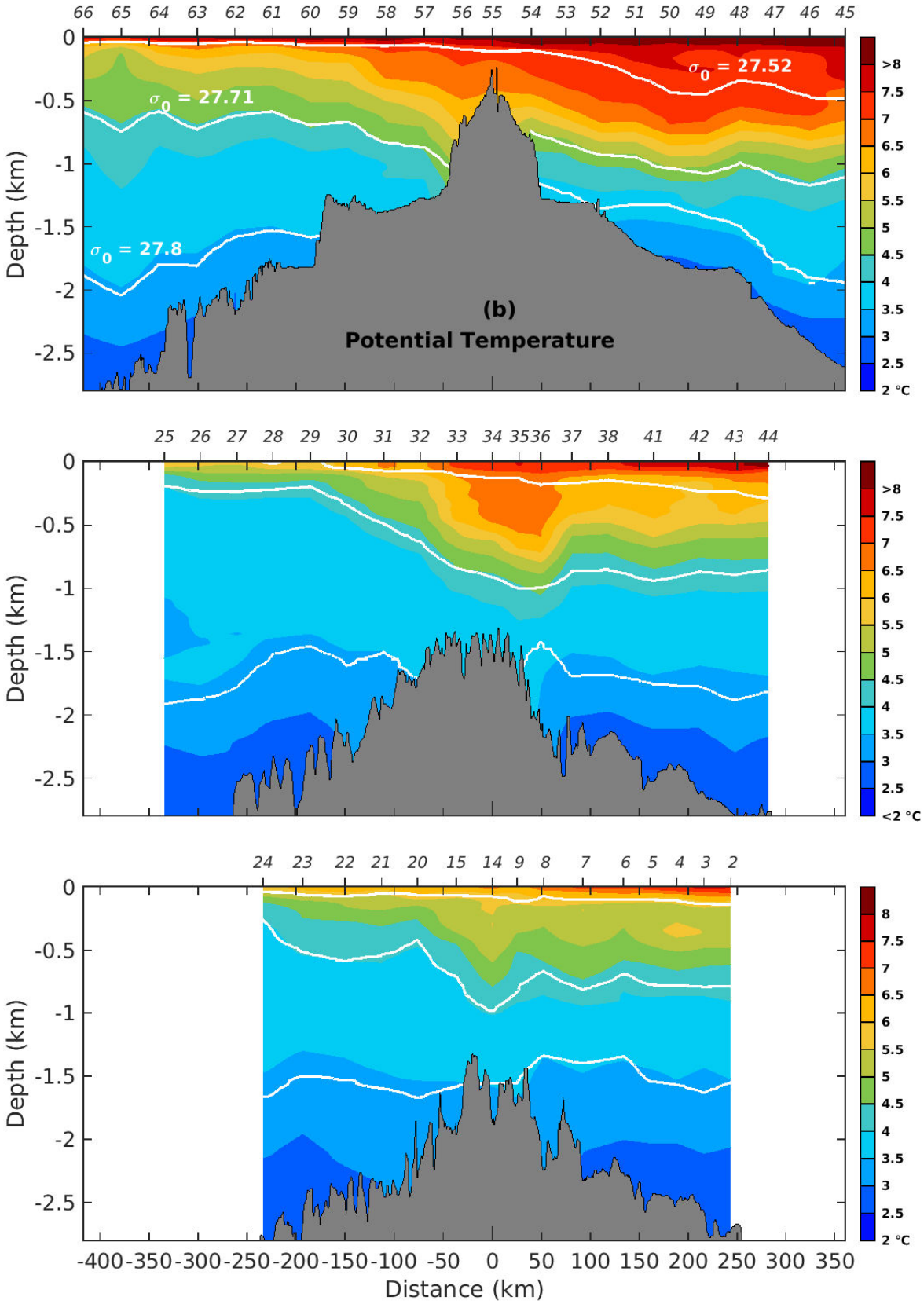
66 65 64 63 62 61 60 59 58 57 56 55 54 53 52 51 50 49 48 47 46 45
Depth (km)
0
-0.5
-1
-1.5
-2
-2.5
σ_0 = 27.52
σ_0 = 27.71
σ_0 = 27.8
(b)
Potential Temperature
>8
7.5
7
6.5
6
5.5
5
4.5
4
3.5
3
2.5
2 °C
25 26 27 28 29 30 31 32 33 34 35 36 37 38 41 42 43 44
Depth (km)
<2 °C
24 23 22 21 20 15 14 9 8 7 6 5 4 3 2
Depth (km)
8
-400 -350 -300 -250 -200 -150 -100 -50 0 50 100 150 200 250 300 350
Distance (km)

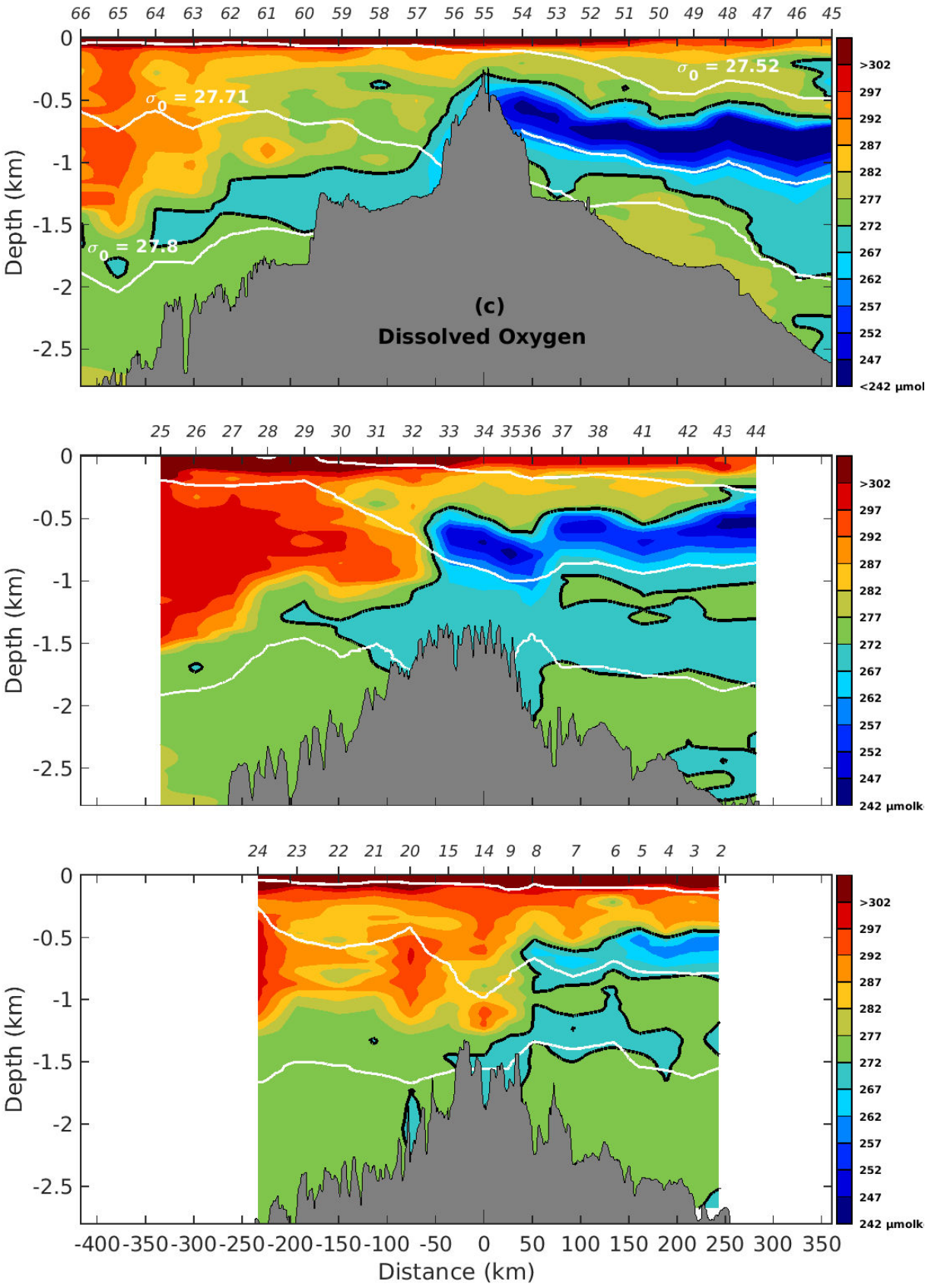
66 65 64 63 62 61 60 59 58 57 56 55 54 53 52 51 50 49 48 47 46 45
σ_0 = 27.71
σ_0 = 27.52
σ_0 = 27.8
(c)
Dissolved Oxygen
Depth (km)
0
-0.5
-1
-1.5
-2
-2.5
>302
297
292
287
282
277
272
267
262
257
252
247
<242 µmol
25 26 27 28 29 30 31 32 33 34 35 36 37 38 41 42 43 44
242 µmolk
24 23 22 21 20 15 14 9 8 7 6 5 4 3 2
-400 -350 -300 -250 -200 -150 -100 -50 0 50 100 150 200 250 300 350
Distance (km)

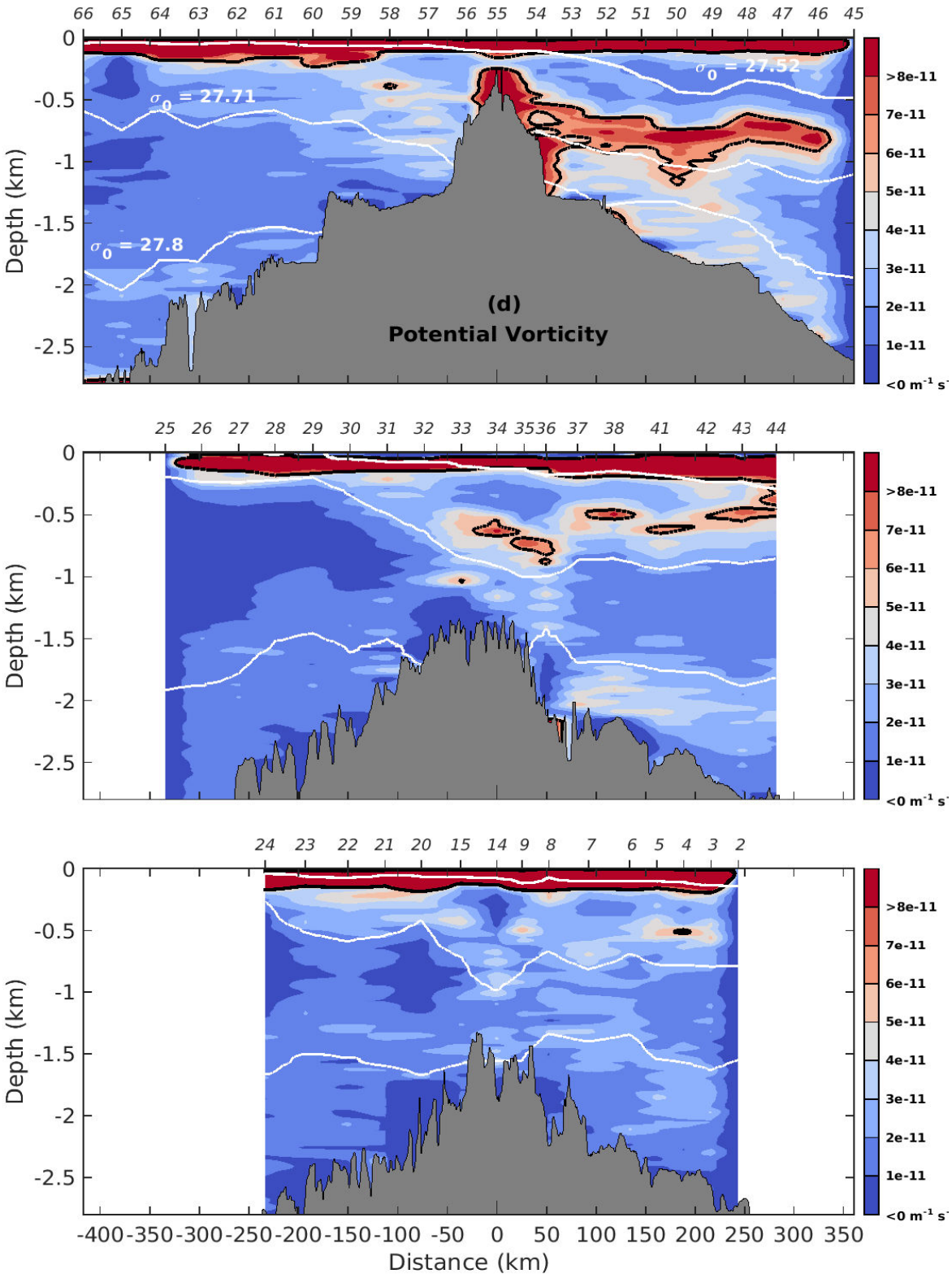

Figure 4.2: (a, b, c, d) Hydrological properties along the North (upper panels), Ovide (middle panels) and South (lower panels) sections based on CTDO$_2$ data. The potential vorticity was computed as $q = \frac{-f}{\rho_0}\frac{\partial \rho}{\partial z}$, where f is the Coriolis parameter, ρ_0 is the reference density and ρ is the potential density referenced to the mid-depth interval over which the vertical gradient of density was computed. The white lines show the potential density anomalies σ_0 = 27.52, 27.71 and 27.8 kg m^{-3}. Bathymetry from the ship survey is shown in grey. Locations of the hydrographic stations are indicated on the top axis. The black bold lines outline the criteria used for the identification of water masses in Table 4.1.

4.3 Results: Connections between the Iceland Basin and the Irminger Sea

4.3.1 Horizontal and vertical structures of the along-ridge currents

Figure 4.3 shows absolute geostrophic velocities across the SS, OS and NS. Across the NS, the southward flow east of the Reykjanes Ridge is divided in three bottom-intensified branches localized, from west to east, at 0 – 75 km, +100 – 240 km, and +250 – 300 km. The latter lies only in Layers 3 and 4. Northward flows are observed between these branches and at the eastern end of the section. Across the OS, the southward flow is also divided in three branches. The western branch is surface-intensified (> 0.1 m s^{-1}) and localized at 0 – 100 km, the middle branch is bottom-intensified and localized at +110 – 175 km, and the eastern branch is bottom-intensified with a core at +225 km and is separated from the middle branch by a weak northward flow at +180 km (< 0.02 m s^{-1}). Across the SS, the southward flow is also divided in three main branches: a surface-intensified western branch at 0 – 50 km that contains no southward core in its Layer 4, a bottom-intensified middle branch with a core at +150 km that only lies in Layers 3 and 4, and a bottom-intensified eastern branch at +200–250 km. At +50 – 125 km, the symmetry of the hydrological properties and isopycnals (Figure 4.2) shows that the flow is perturbed by a coherent structure in Layers 1 and 2. To sum-up, two southward bottom-intensified branches are found east of +100 km at the three sections, while the vertical structure of the western branches, localized west of +100 km, varies between the three sections. This western branch is bottom-intensified at the NS and surface-intensified at the OS and at the SS.

West of the Reykjanes Ridge, the flow is divided in two northward surface-intensified branches bounded to the west by southward surface-intensified flows at the three sections, even though the southward flow was not completely sampled at the SS (Figure 4.3). The two northward branches are localized at -250 – 0 km at the NS, with similar surface velocities in both branches (0.08 m s^{-1}). At the OS, the two northward branches are localized at -200 – 0 km, with larger surface velocities in the eastern branch (0.21 m s^{-1}) than in the western branch (0.11 m s^{-1}). Finally, the two northward branches are localized at -50 – 0 km and at -200 – 100 km at the SS and are separated by a southward bottom-intensified flow at -100 – 50 km. Two northward surface-intensified branches are thus found directly west of the top of the Reykjanes Ridge at the three zonal sections, even though they are separated by a southward flow at the SS. They will be referred hereinafter as the western and eastern IC branches.

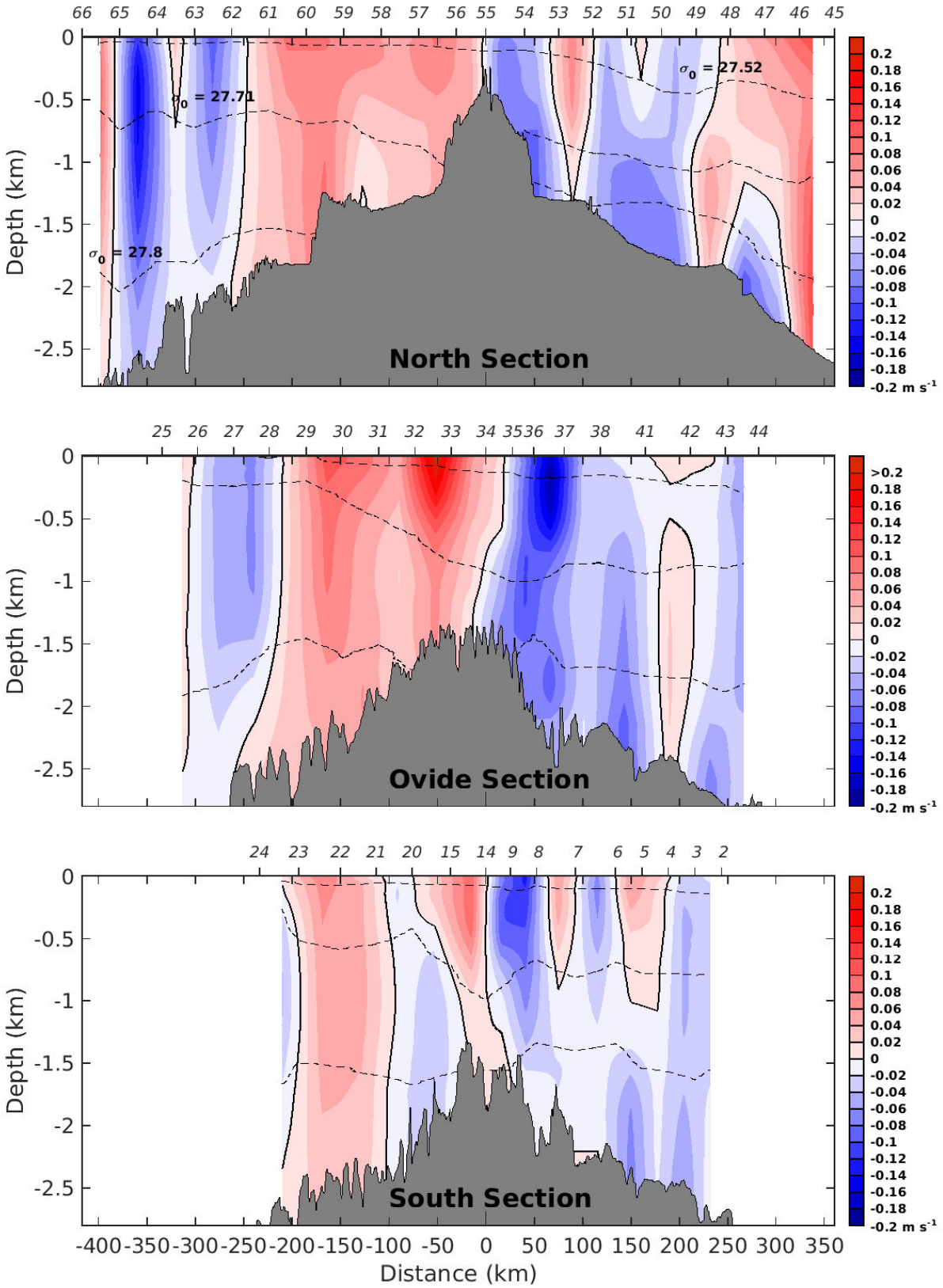

Figure 4.3: Geostrophic velocity along the North (upper panel), Ovide (middle panel) and South (lower panel) Sections (m s^{-1}). Positive values correspond to northward velocities. The black bold line outlines the 0 isotach. The dashed black lines indicate the potential density σ_0 = 27.52, 27.71 and 27.8 kg m^{-3}. Bathymetry from the ship survey is added in grey. Locations of the hydrographic stations are indicated on the top axis.

According to Daniault et al. (2016), the time-averaged ERRC comprises southward flows of about 200-km wide east of the top of the Reykjanes Ridge. Likewise, Våge et al. (2011) showed that the time-averaged IC comprises two surface-intensified northward flows within about 200 km west of the top of the Reykjanes Ridge. To characterize the ERRC and IC transports in our data set, we first computed vertically integrated top-to-bottom transports from the geostrophic velocities in Figure 4.3, and cumulated these transports from the top of the Reykjanes Ridge in Figure 4.4 (upper panel). The ERRC and IC transports were defined as the respective minimum and maximum of the cumulative transport curves at about 200 km east and west of the top of the Reykjanes Ridge. Beyond the outer edges of these currents, the flows were linked to the large-scale circulation in the Iceland Basin and Irminger Sea by comparing the top-to-bottom transports with absolute dynamic topography velocities from AVISO in Figure 4.5.

In Figure 4.4, the cumulative transport curves on the eastern side of the ridge reach a minimum at +220 km (station 49) for the NS, +165 km (station 41) for the OS, and +245 km (station 2) for the SS. These minimums bound the main southward along-ridge flows that constitute the ERRC. East of these limits, variations of the cumulative transport curves are caused by eddies or meanders, such that the northward flow at stations 45 – 46 of the NS (Figure 4.3) is associated with an eddy at 20 – 22°W/59 – 60.5°N (Figure 4.5), and the northward/southward flows at stations 41 – 44 of the OS is associated with a meander of the NAC at 28°W/57°N. With these limits, the ERRC transports were estimated at -10.6 ± 0.9 Sv at the NS, -20.0 ± 0.6 Sv at the OS, and -13.0 ± 1.2 Sv at the SS.

On the western side of the ridge, the cumulative transport curves reach a maximum at -260 km (station 62) for the NS, -225 km (station 28) for the OS, and -195 km (station 23) for the SS. These maximums bound the main northward along-ridge flow that belongs to the IC. West of these limits, variations in the cumulated transport curves are caused by eddies and meanders in the Irminger Sea. Indeed, the northward and following southward flows at stations 64 – 66 of the NS (Figure 4.3) are associated with a large eddy at 32.5°W/63°N (Figure 4.5), while the southward flow east of this eddy at stations 62 – 63 is associated with a meander of the IC at 30 – 32°W/62.5 – 63°N. Similarly, Figure 4.6 shows that the southward flow at the western edge of the OS (-300 – 200 km in Figure 4.3) is associated with a recirculation of the northward branch of the Irminger Gyre at 36°W/59.5°N. Given the above limits, the IC transports were estimated at 15.7 ± 0.9 Sv at the NS, 23.5 ± 0.6 Sv at the OS, and 9.8 ± 1 Sv at the SS.

Table 4.2: Transports (Sv) of the ERRC and IC of each zonal section (SS: South Section; OS: Ovide Section; NS: North Section) and into each layer (Layer 1: $\sigma_0 < 27.52$; Layer 2: $27.52 < \sigma_0 < 27.71$; Layer 3: $27.71 < \sigma_0 < 27.8$; Layer 4: $\sigma_0 > 27.8$).

	SS		OS		NS	
	IC (st. 14–23)	ERRC (st. 2–14)	IC (st. 28–34)	ERRC (st. 34–41)	IC (st. 55–62)	ERRC (st. 49–55)
Layer 1	0.6	-0.7	1.6	-1.3	1.1	-1.2
Layer 2	4.1	-4.6	7.6	-7.4	8.4	-4
Layer 3	2.6	-3.5	10.3	-6.4	5.2	-2.6
Layer 4	2.5	-4.2	4	-4.9	1	-2.8

The ERRC and IC transports vary in latitude. The ERRC and IC transports peak at the OS where they are twice as large as their transports at the NS and SS. This is also true for their four layers, as shown in Table 4.2, except for Layer 2 where the IC transport peaks at the NS. Considering that the NAC waters join the ERRC and that ERRC waters join the IC, the latitudinal variations of the ERRC and IC transports are necessarily explained by meridional inflows (outflow) that locally join (leave) these along-ridge currents. To quantify these inflows and outflows, and to close the circulation of the ERRC and IC, we built a volume budget by combining the along-ridge transports with the cross-ridge transports estimated between the NS and OS (RS4), the OS and SS (RS3), and the SS and the northern boundary of the NAC located at 53.15°N (RS2). The NAC northern boundary was defined following Petit et al. (2018b) as the minimum of cumulated transport across the Ridge Section (Figure 4.4). Estimates of the amount of water joining or leaving the IC and ERRC were first obtained as residuals of the sum of the volume transports across the three sections forming each of the four boxes and for which we had direct transport estimates. In Figure 4.7, the budget residual shows that an input of 23.2 Sv from the Iceland Basin is necessary to close the volume budget of the ERRC between the NS and the OS (red box). Another quantification of this input was obtained by computing the geostrophic transport between the eastern limit of the ERRC at the NS and at the OS (see section 4.2.2). It was estimated at 22.6 Sv. Both estimates are in good agreement. Similarly, the volume budget shows that an input from the Irminger Sea of 6.1 Sv

is required to feed the IC between the SS and the OS (blue box), while an output of 21.6 Sv toward the Irminger Sea is necessary to explain the decrease in the IC transport between the OS and the NS (orange box). These estimates are also in good agreement with the geostrophic estimates. However, note that the two transport estimates significantly differ (-3.1 Sv versus 6.5 Sv) when considering the ERRC evolution between the OS and SS (green box). Thin coherent structures not resolved by AVISO but observed in Layers 1 and 2 of the SS (Figure 4.3) may explain the discrepancy between the two estimates at that location.

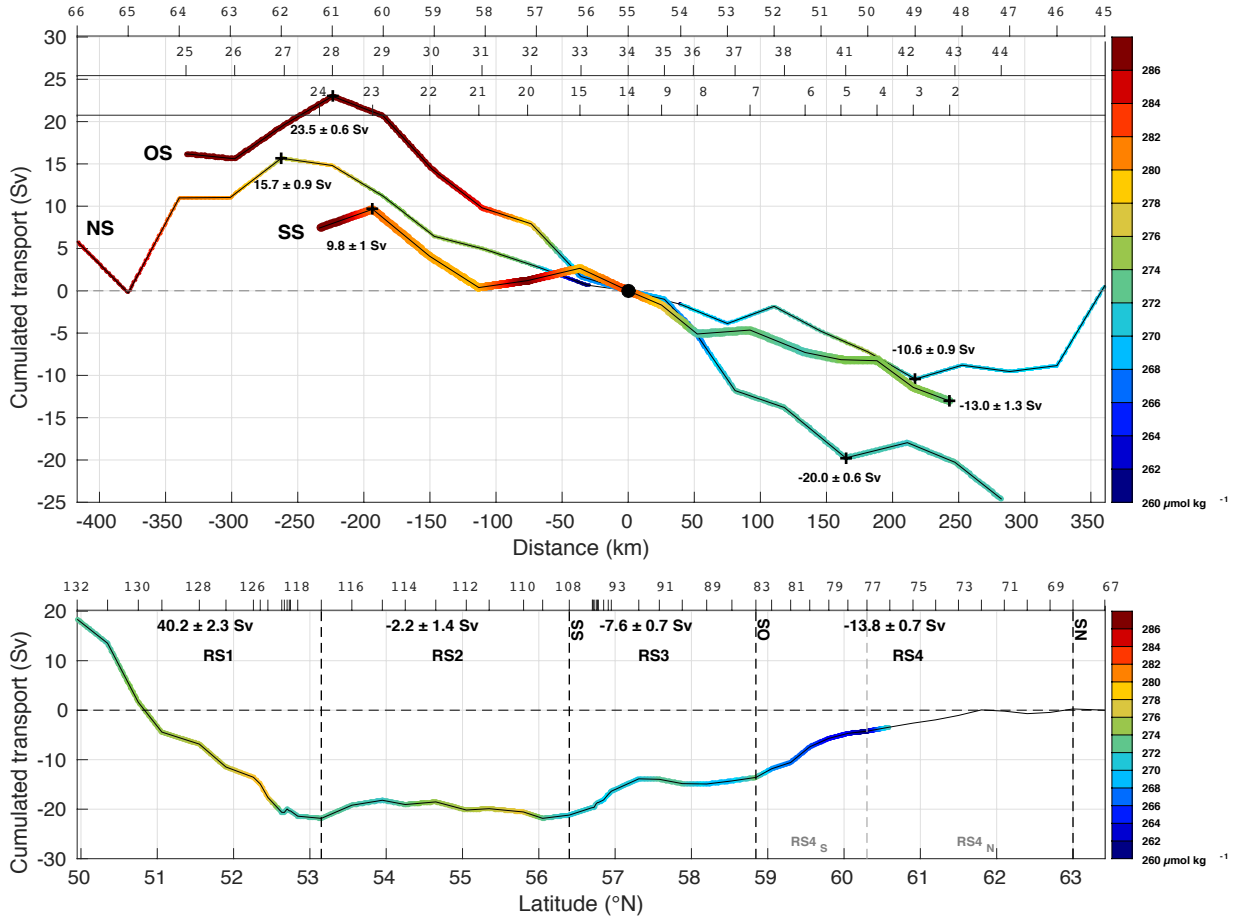

Figure 4.4: (Upper panel) Top-to-bottom vertically integrated transport (Sv) along the North (stations 45 to 66), Ovide (stations 25 to 44) and South (stations 2 to 24) sections cumulated from the top of the Reykjanes Ridge (black point at 0 km) toward the Iceland basin eastward and Irminger Sea westward. (Lower panel) Top-to-bottom vertically integrated transport (Sv) along the Ridge Section from Petit et al. (2018b). Each zonal section (NS, OS, SS) is delimited in the lower panel as vertical black and gray lines, such as the limits of regions RS2, RS3 and RS4 are different from that taken by Petit et al. (2018b). In each panel, locations of the hydrographic stations are shown on the top axis. The dissolved oxygen concentrations are averaged between 27.71 and 27.8 kg m^{-3} and are indicated in color on the transport curves when the water masses are observed along the section. Northward and eastward (southward and westward) transports are positive (negative).

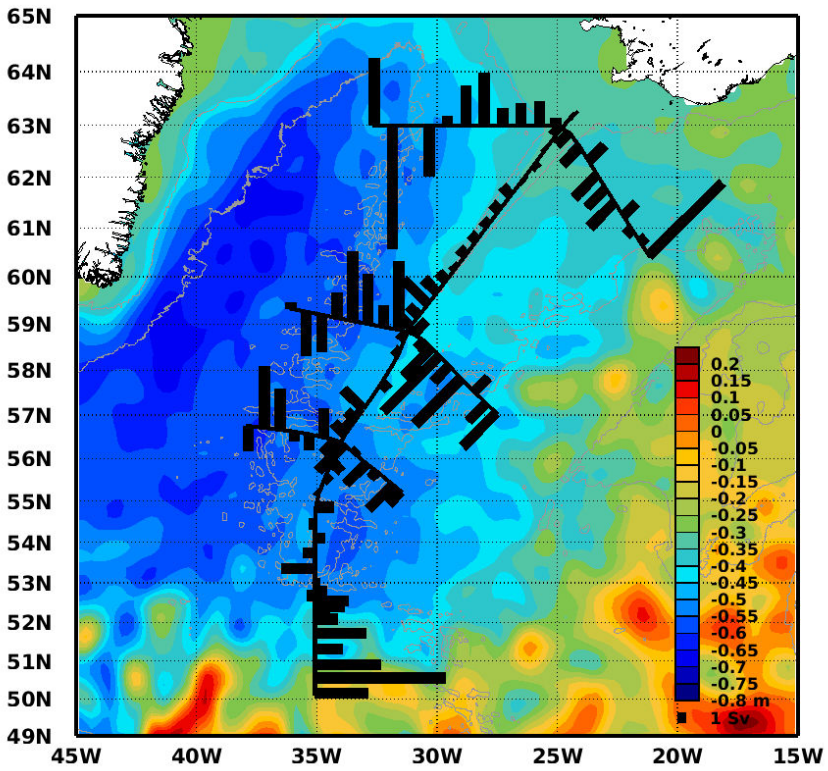

Figure 4.5: Absolute Dynamic Topography (m) of the subpolar gyre from AVISO that were time-averaged during the cruise between 10 to 23 June 2015. Black bars represent the top-to-bottom vertically integrated transports (Sv) at each pair of station perpendicular to the four sections. Bathymetries -1000 m and -2500 m are plotted in grey.

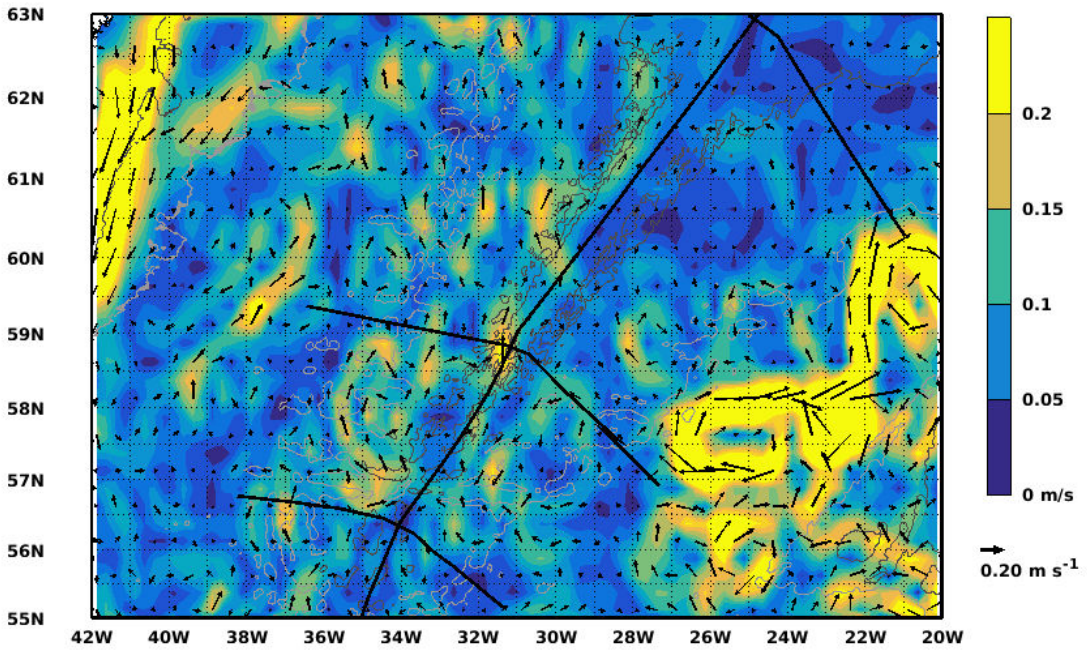

Figure 4.6: Contours and color shading indicate the amplitude of the surface velocity vectors from AVISO and time-averaged between 15 to 19 June 2015, time during which the Ovide Section was carried out. Black lines indicate the position of the sections.

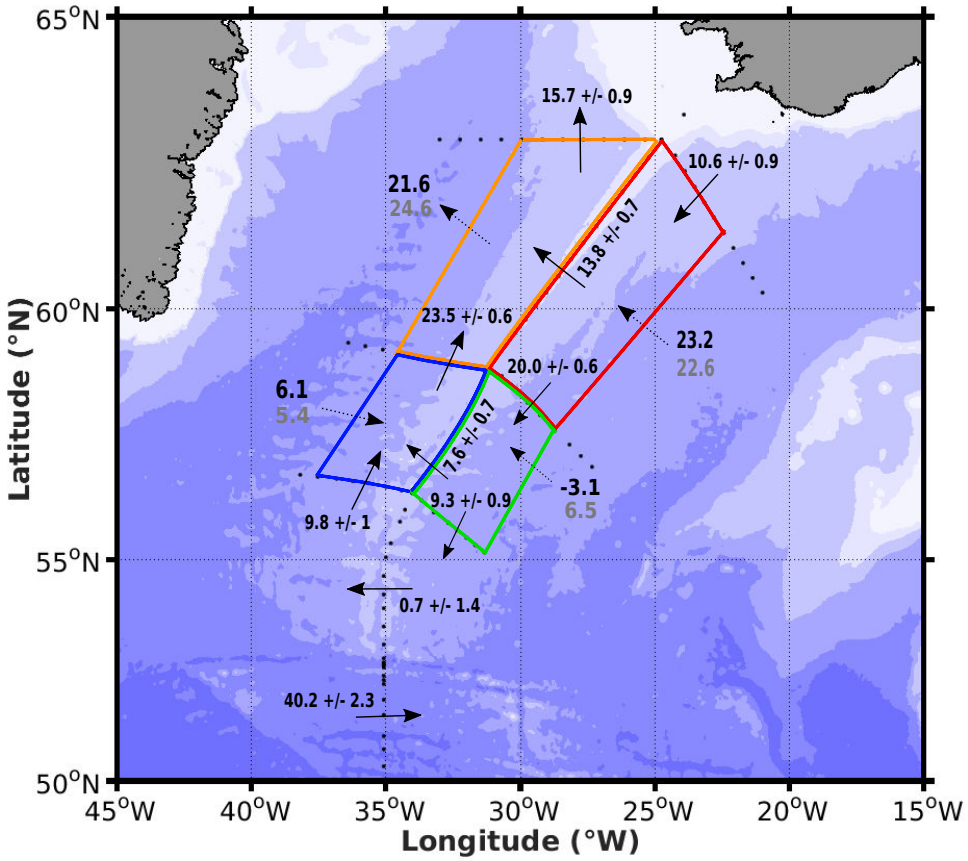

Figure 4.7: Scheme showing the top-to-bottom vertically integrated transports (Sv) of the ERRC and IC in each box delimited by the North Section, Ovide Section, South Section and Ridge Section (plain arrows). In each box are indicated the associated input/output transports estimated to offset the box (dashed arrows). In grey are the effective input/output transports computed between the eastern and western last hydrographic stations of the ERRC and IC, respectively.

4.3.2 Hydrography of the eastern flank of the Reykjanes Ridge

In section 4.3.1, we showed that the ERRC and IC structures and transports vary in latitude due to flows joining or leaving the currents. Now we will study the evolution of their hydrological properties in order to better understand the connections between the along-ridge currents and the inflowing and outflowing branches. We compare in this section the southward hydrological evolution of the ERRC with the outflowing branches of the cross-ridge flow, and in section 4.3.3, we link these variations with the northward hydrological evolution of the IC. We will thus be able to discuss their interactions and mixing. Study of the property evolution will also reveal connections between the along-ridge currents and the circulation at the centers of the Iceland Basin and Irminger Sea that were not sampled during the RREX2015 cruise.

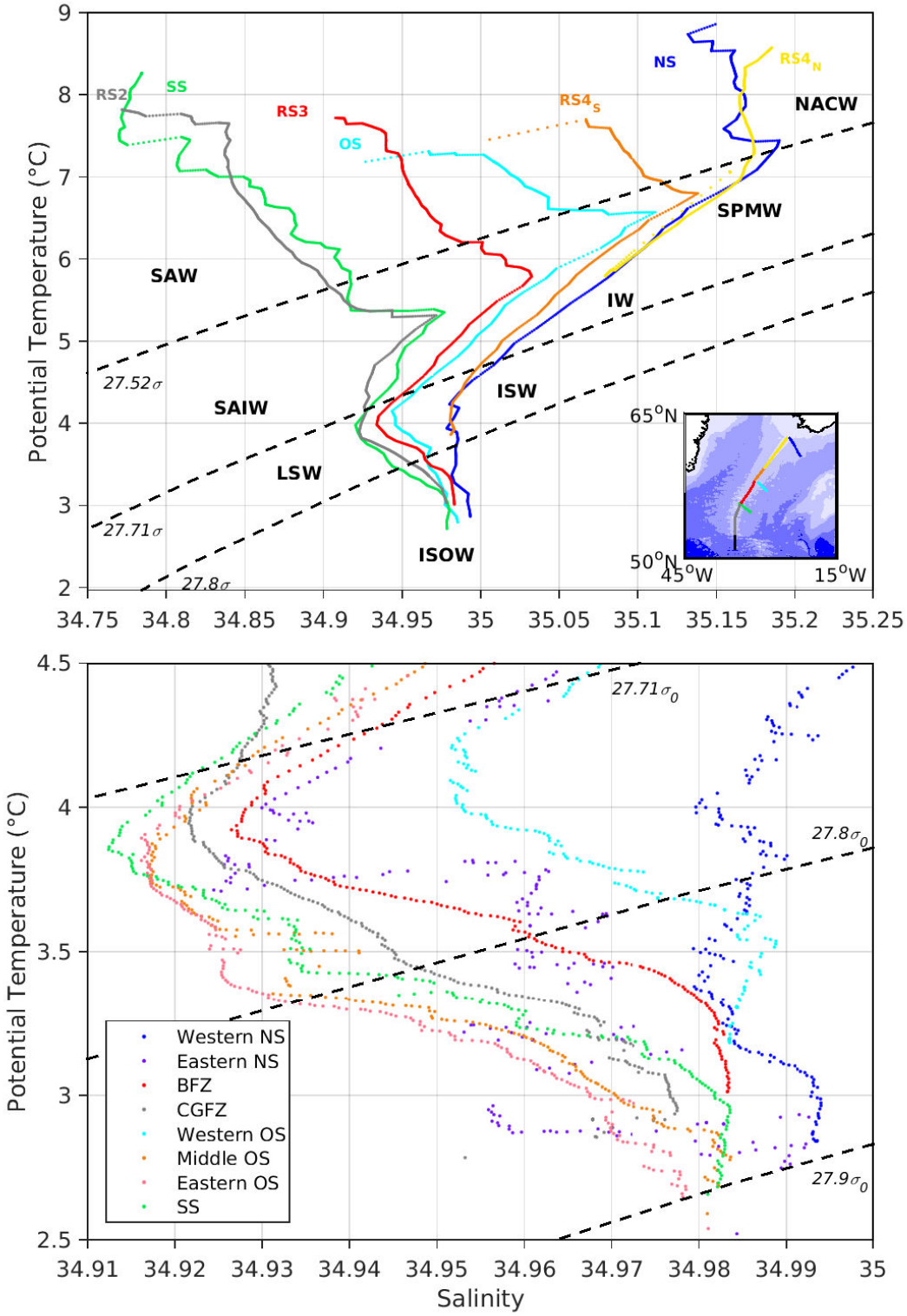

Figure 4.8: (upper panel) θ/S diagram displaying the hydrographic profiles averaged along isopycnals of the ERRC at the North (NS, blue line), Ovide (OS, cyan line), and South (SS, green line) Sections and across the Ridge Section at Region 1 (RS1, black line), Region 2 (RS2, grey line), Region 3 (RS3, red line), at 58.8–60.3°N ($RS4_S$, orange line) and at 60–63°N ($RS4_N$, yellow line). Water masses defined in Table 4.1 are indicated. Insert: Map of the bathymetry of the North-Atlantic with a 1000 m spacing (darkest blue are deeper) on which the sections are shown with different colors. (lower panel) θ/S diagram displaying the hydrographic profiles averaged along isopycnals of the southward cores of ISOW east of the Reykjanes Ridge and at the BFZ and CGFZ. The dashed black lines indicate isopycnals σ_0 = 27.52, 27.71 and 27.8 kg m^{-3} that along with surface and bottom are the limits of Layers 1 to 4.

Figure 4.8 (upper panel) shows averaged θ/S profiles of the ERRC at the NS, OS and SS. These profiles are compared to the averaged θ/S profiles of the westward cross-ridge flows for RS4, RS3 and RS2. The RS4 segment was divided in two sub-segments at 58.8 – 60.3°N ($RS4_S$) and at 60.3 – 63°N ($RS4_N$) in order to precisely resolve the cross-ridge flow of ISW that mainly occurs at 58.8 – 60°N (Petit et al., 2018b). Temperature and salinity in Layers 1 and 2 (σ_0 < 27.71 kg m^{-3}) decrease southward from the NS to the SS. Along 27.52σ_0, this decrease amounts to more than 1.7°C in temperature and 0.3 in salinity. A similar evolution is observed above the ridge from $RS4_N$ to RS2 due to the similarity of the hydrographic profiles at the NS and $RS4_N$ and at the SS and RS2. In between, the sub-segment $RS4_S$ is fresher by about 0.05 than the sub-segment $RS4_N$ along 27.52σ_0. The same difference is observed between the sub-segment $RS4_S$ and the OS, the OS and the RS3, as well as between the RS3 and the SS. This evolution is fully consistent with the three varieties of SPMW identified in Figure 4.2, with temperature decreasing from 7°C at the NS to 5°C at the SS. In Layer 3 (27.71 < σ_0 < 27.8 kg m^{-3}), temperature and salinity decrease southward from the NS to SS of almost 0.07 and 0.5°C along 27.71σ_0, respectively. The same evolution is observed above the ridge from $RS4_S$ to RS2. The ISW properties are similar at the NS and at $RS4_S$, which is the northernmost region for the cross-ridge flow of intermediate waters (Petit et al., 2018b). Similarly, the LSW properties are similar at the SS and at RS2. Note that the largest difference between two successive regions occurs between $RS4_S$ and OS. ISW in region $RS4_S$ is saltier by up to 0.05 along 27.71σ_0 than at OS. In summary, a general isopycnal freshening and cooling encompasses the water masses of Layers 1 to 3 from north to south.

Figure 4.8 (lower panel) shows the averaged θ/S profiles for the southward flowing ISOW layers east of the Reykjanes Ridge (Figure 4.3, σ_0 > 27.8 kg m^{-3}), as well as at the BFZ and at the CGFZ, which are preferential pathways of ISOW across the Reykjanes Ridge (Petit et al., 2018b). At each section, we averaged together profiles having similar properties. At the NS, we averaged the two western most branches at 0 – 75 km and +100 – 240 km to get the western NS profile in Figure 4.8. At the SS, we averaged the southward branches localized at +125 – 250 km to get the SS profile in Figure 4.8. The ISOW properties of the western NS core are similar to the western core of ISOW found at the OS, as well as to that at the BFZ (salinity higher than 34.98 for σ_0 > 27.83). At the SS, the hydrological profile has an intermediate position between the western and eastern OS profiles, and is identical to the CGFZ profile. Note that the ISOW density at the BFZ reaches lower values than at the CGFZ due to the shallower depth of the BFZ.

These results show that the southward hydrological evolution of the ERRC is similar to the southward hydrological evolution of the westward cross-ridge flow, which shows direct links between them. Moreover, the north to south cooling and freshening of Layers 1 – 3 is driven by the characteristics of the water masses joining continuously the ERRC from the Iceland Basin. Detailed circulation schemes were deduced from these results and were drawn for Layers 1 to 4 in Figures 4.11 to 4.14. Consistent with the transport budget in Figure 4.7 that shows a significant inflow from the Iceland Basin in the red box, we present here a new vision of the circulation along the eastern side of the Reykjanes Ridge. From the north to the south of the Reykjanes Ridge, water joins continuously the ERRC from the Iceland Basin, and water leaves continuously the ERRC toward the Irminger Sea via westward cross-ridge flow permitted by the southward deepening of the Reykjanes Ridge and the fracture zones as shown by Petit et al. (2018b). Layers 1 and 2 (Figures 4.11 and 4.12) can cross the ridge in its northernmost part ($RS4_N$), while ISW (Figure 4.13) can cross the ridge further south ($RS4_S$) only. Finally, the lightest variety of ISOW crosses the ridge through the BFZ and the densest variety of ISOW joins the Irminger Sea further south (Figure 4.14).

4.3.3 Hydrography of the western flank of the Reykjanes Ridge

Figure 4.9 (left panel) compares averaged θ/S profiles of the eastern and western IC branches at the SS (SS_E and SS_W, respectively) with the northern branch of the NAC ($RS1_N$) and the westward cross-ridge flow (RS2). Even though the surface waters ($\sigma_0 < 27.52$ kg m^{-3}) are similar in the two IC branches, the sub-surface waters ($27.52 < \sigma_0 < 27.71$ kg m^{-3}) of the eastern branch are 0.03 saltier and 0.2°C warmer than the western branch along $27.6\sigma_0$. For $27.6 < \sigma_0 < 27.71$ kg m^{-3}, the eastern profile is identical to the cross-ridge profile RS2, while the western profile is identical to the NAC profile $RS1_N$.

The middle panel (Figure 4.9) compares averaged θ/S profiles of the IC branches at the SS (SS_E and SS_W) and at the OS (OS_E and OS_W). These profiles are also compared to the averaged θ/S profiles of the southward branch across the OS at -300 – 200 km, which was associated with a recirculation of the Irminger Gyre (IG), and to the westward cross-ridge flow at the BFZ ($RS3_{BFZ}$), which is a main pathway of the water masses in Layers 1 and 2 according to Petit et al. (2018b). At the OS, the water masses of the eastern branch are 0.06 saltier than that of the western branch along $27.6\sigma_0$. At 27.6 – 27.71 kg m^{-3}, the IW properties

of the eastern OS branch are identical to that at the BFZ ($RS3_{BFZ}$), and the OS_W profile is in an intermediate position between the $RS3_{BFZ}$, IG, SS_E and SS_W profiles.

The right panel (Figure 4.9) compares the averaged θ/S profiles of the IC branches at the OS (OS_E and OS_W) and at the NS (NS_E and NS_W), as well as with the cross-ridge flows between the two sections at $RS4_S$ and $RS4_N$. At the NS, the water masses of the eastern branch are 0.05 saltier than the western branch along $27.52\sigma_0$. The eastern profile is identical to the cross-ridge profile $RS4_N$, while the western profile is identical to the cross-ridge profile $RS4_S$. Both significantly differ from the hydrological properties of the IC at the OS.

At denser level (Layer 3, $27.71 < \sigma_0 < 27.8$ kg m^{-3}), the LSW properties of the eastern SS branch (Figure 4.9, left panel) are identical to that at the $RS1_N$ and RS2 but are 0.1°C warmer and 0.02 saltier along the isopycnal $27.73\sigma_0$ than the western SS branch. At the OS (middle panel), the hydrological properties of the two IC branches are similar. In the θ/S diagram, these properties lie in between those observed at the SS, $RS3_{BFZ}$ and IG. The water masses observed in the two branches of the IC at the OS thus result from a complex mixing between Irminger and Iceland waters. At the NS, along $27.73\sigma_0$, water masses are in an intermediate position between LSW from the OS and ISW from the cross-ridge flow $RS4_S$. Able to cross the Reykjanes Ridge at these latitudes, intermediate ISW joins and mixes with the IC between the OS and NS.

Finally for Layer 4 ($\sigma_0 > 27.8$ kg m^{-3}), the ISOW properties of the western SS branch are similar to that at the CGFZ (Figure 4.9, left panel). At the OS (middle panel), the ISOW properties of the two branches are similar to those at the SS, except for the properties of the densest ISOW that are identical to those from the IG. At the NS (right panel), the ISOW properties of the western branch are similar to that at the OS.

To conclude, the IC branches are fed by westward cross-ridge flows in the southern part of the Reykjanes Ridge, called hereinafter as Iceland inflow, and associated with the ERRC branches discussed in section 4.3.2 (Figure 4.9, left and middle panels). However at the SS and OS, the IC branches are also fed by fresher and colder flows than that coming from the Iceland Basin. Indeed, Figure 4.4 shows the averaged dissolved oxygen concentrations of the Layer 3 along the cumulated transport curves. The oxygen concentration varies along the western side of the sections from 268 to 286 μmol kg^{-1}, and shows overall more oxygenated contents along the OS and SS than the westward cross-ridge flow RS2 and RS3 (~ 270 μmol kg^{-1}). The IC is thus also fed by more oxygenated intermediate flows than those transported

by the cross-ridge flow from the Iceland Basin. According to the volume budget in Figure 4.7, which shows eastward inflows between the SS and OS, this inflow comes from the Irminger Sea and is called hereinafter as Irminger inflow. At the SS, the similarity between the properties of this inflow and those of the northern NAC branch for $27.6 < \sigma_0 < 27.71$ kg m^{-3} suggests that part of this inflow comes from the NAC that join the IC at the SS without entering the Iceland Basin. At the NS however, both IC waters from the OS and Iceland inflows feed the IC branches, consistent with the volume budget in Figure 4.7. The circulation of the IC in Figures 4.11 – 4.14 highlights new interactions between the IC and the interior of the Irminger Sea and outlines its effect on the northward circulation and the evolution of the IC layers.

4.3.4 Circulation in density layers

We will now discuss the inflows (outflows) that join (leave) the ERRC and IC in each class of density. Figure 4.10 shows transports of the ERRC and IC (as defined in section 4.3.1) and plotted as a function of density. In this section, we only discuss the inflow and outflow generated by horizontal circulation and do not consider diapycnal exchanges. At the NS, the ERRC transport is relatively constant as a function of density in Layers 2, 3 and 4 but very weak in Layer 1. At the OS, the ERRC transport is higher at $\sigma_0 = 27.56$ kg m^{-3}, between $\sigma_0 = 27.71$ kg m^{-3} and $\sigma_0 = 27.8$ kg m^{-3} and at $\sigma_0 = 27.83$ kg m^{-3} than at the NS. At these densities, between the NS and OS, Iceland inflows are not balanced by cross-ridge outflows. Because there is no horizontal inflow of ISOW from the interior of the Iceland Basin between the NS and OS, the increase at $\sigma_0 = 27.83$ kg m^{-3} should be related to vertical mixing with the above water masses. On the contrary, the ERRC transport is weaker at the SS than at the OS in Layers 3 and 4. This indicates stronger cross-ridge outflows than Iceland inflows at these densities between the OS and the SS. South of the OS, Layers 3 and 4 are no longer blocked by the bathymetry of the Reykjanes Ridge and can cross the ridge toward the Irminger Sea. Note the densification of maximum transport in Layer 2 that is localized at $\sigma_0 = 27.62$ kg m^{-3} at the SS.

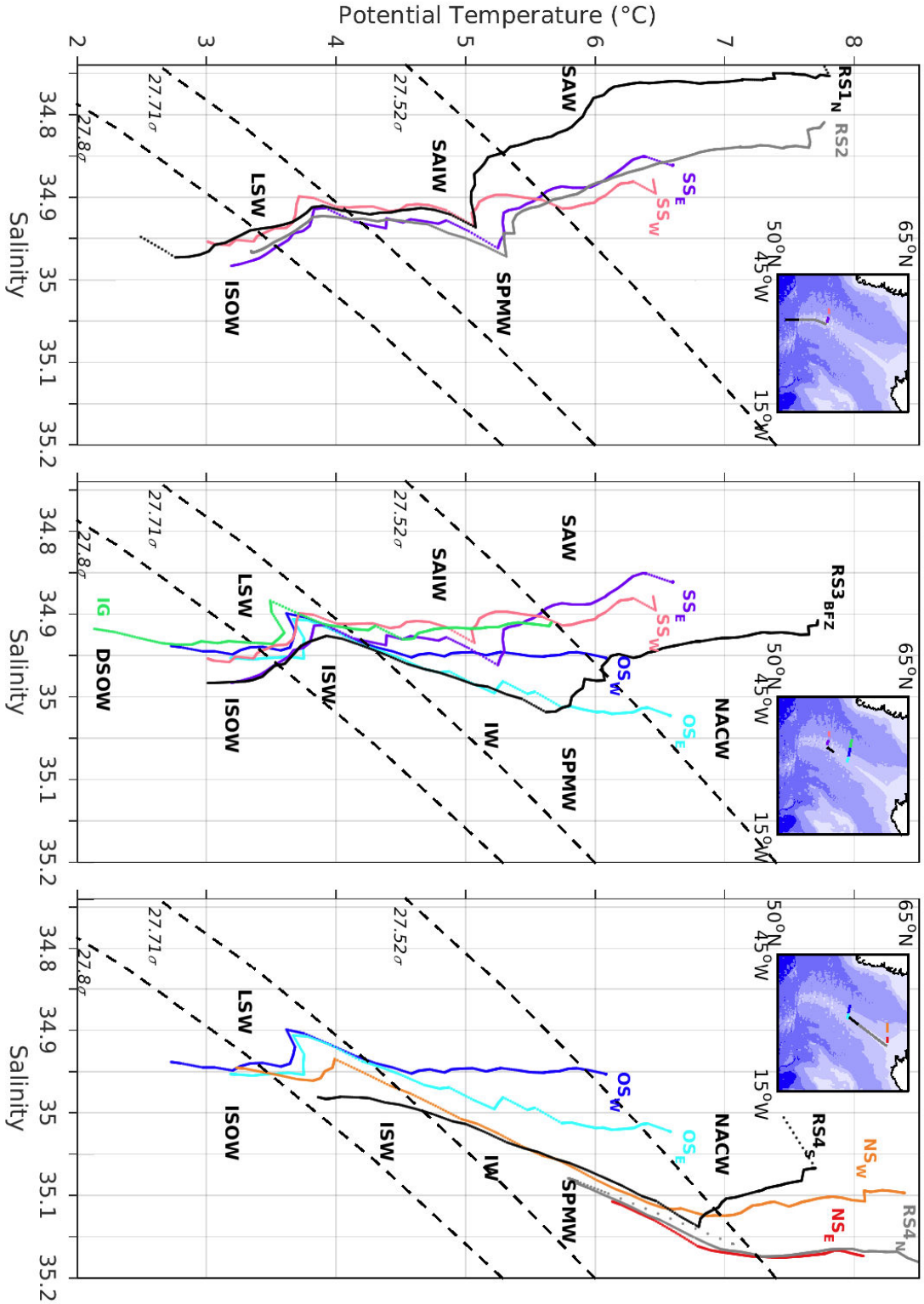

Figure 4.9: Potential Temperature θ/S diagram displaying the hydrographic profiles averaged along isopycnals for the eastern and western branches of the IC at the South (left panel), Ovide (middle panel), and North (right panel) Sections and for cross-ridge flows at the Ridge Section. The tilted-black lines indicate the isopycnals σ_0 in kg m^{-3} from 27.52, 27.71 and 27.8. Water masses are added as defined in Table 4.1.

From south to north of the Reykjanes Ridge, the northward IC transport is maximum at σ_0 = 27.62 kg m^{-3}, σ_0 = 27.73 kg m^{-3} and σ_0 = 27.86 kg m^{-3} at the SS. Note the maximum transport of about 0.75 Sv at σ_0 = 27.62 kg m^{-3} for both current at the SS. At σ_0 = 27.73 kg m^{-3} and σ_0 = 27.79 kg m^{-3}, the IC transport at the OS (about 2 Sv and 1.5 Sv, respectively) is more than threefold the IC transport at the SS (about 0.5 Sv and 0.25 Sv, respectively). This is consistent with the multiple inflows in Layer 3 discussed in section 4.3.3, both from the Iceland Basin and the Irminger Sea. However at the NS, the IC transport decreases in Layer 3 compared to the IC transport at the OS. This shows outflow from the IC in Layer 3. Finally from the SS to the NS, note the similar intensity but the associated progressive decreases of ISOW density in the IC.

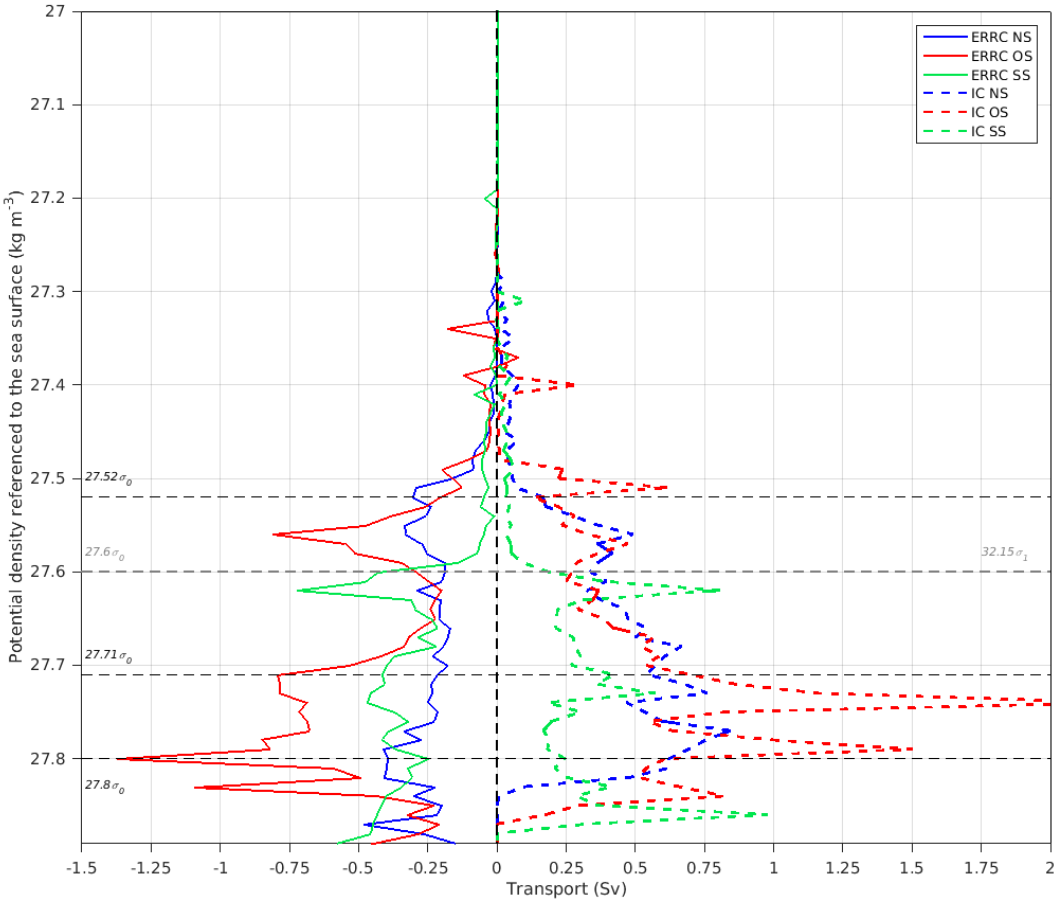

Figure 4.10: Transport integrated in 0.01 bins of density σ_0 for the ERRC (negative transports, plain lines) and IC (positive transports, dashed lines) across the three zonal sections. Horizontal dashed black lines indicate the potential density σ_0 = 27.52, 27.71 and 27.8 kg m^{-3}. Dashed grey line indicates the potential density σ_1 = 32.15 kg m^{-3}.

4.4 Discussion

In this section, we summarize and discuss the large-scale circulation of the ERRC and IC based on their hydrological and structural latitudinal evolution along the flanks of the Reykjanes Ridge. This ocean circulation will be compare to previous findings and to the cross-ridge flows recently documented by Petit et al. (2018b).

4.4.1 Large-scale circulation of the ERRC

Along the eastern side of the Reykjanes Ridge, we showed that the horizontal and vertical structures of the southward flow strongly change from the NS to the SS, with a bottom-intensified western branch at 0 – 75 km of the NS, and a surface-intensified western branch at 0 – 100 km of the OS and at 0 – 50 km of the SS (Figure 4.3). Across the Reykjanes Ridge, Petit et al. (2018b) showed that the bathymetry shapes the water mass transports across the Reykjanes Ridge such as Layers 1 to 3 preferentially cross the ridge at 59 – 62°N and at the BFZ, while the overflow (Layer 4) does not cross the ridge north of the BFZ. Here, we link these two results to show that the different layers of the southward along-ridge flow do not flow continuously into one top-to-bottom current from the NS to the SS (Figures 4.11 – 4.14). On Figures 4.7 and 4.8, we identified salty surface flows from the Iceland Basin and fresh overflow from the Nordic Seas at the NS. Between the NS and the OS, the southward flow entrains fresher surface flows than north of the NS, which over-compensates in Layers 1 and 2 the westward cross-ridge flow at 59 – 62°N. At the OS, this strong Iceland inflow locally form a more barotropic branch of 100-km wide compared to the NS at the same location (Figure 4.3). Between the OS and SS, the western branch of light ISOW is detrained toward the Irminger Sea by crossing the Reykjanes Ridge through the BFZ (Figure 4.8). At the SS, this outflow locally forms a surface-intensified southward flow with no core of ISOW at 1500 – 2000-m depth (Figure 4.3). Finally, the densest ISOW, mainly localized beyond +100 km from the top of the ridge, crosses the ridge through deepest fracture zones south of the BFZ (Figure 4.8). By constraining the westward cross-ridge flow, the Reykjanes Ridge thus forms cores of ISOW along its eastern flank that locally converge with surface inflows from the NAC into one top-to-bottom current at the OS, called ERRC.

At the OS, the ERRC transport is estimated at -20.0 ± 0.6 Sv. There, Sarafanov et al. (2012) and Daniault et al. (2016) estimated averaged ERRC transports of -9.4 ± 1.7 Sv (2002 – 2008)

and -12.1 ± 1.1 Sv (2002 – 2012), respectively, weaker than our estimates. To explain the differences between their averaged estimates and our snapshot, we decompose the ERRC transport in several layers. Sarafanov et al. (2012) computed a mean transport of -4.5 ± 1.4 Sv for densities of $27.55 < \sigma_0 < 27.8$ kg m^{-3}, while we obtain an ERRC transport of -12.9 ± 0.2 Sv at these densities. Likewise, Daniault et al. (2016) computed a mean transport of -4.8 ± 0.3 Sv for densities of $\sigma_1 > 32.15$ and $\sigma_0 < 27.8$ kg m^{-3}, while we obtain an ERRC transport of -10.2 ± 0.2 Sv at these densities. At denser level ($\sigma_0 < 27.8$ kg m^{-3}), Sarafanov et al. (2012) and Daniault et al. (2016) computed a mean transport of -4 ± 0.4 Sv and -3.2 ± 0.4 Sv, respectively. At these densities, we obtain a transport of -4.9 ± 0.3 Sv (Table 4.2), close to their estimates. Mainly composed of SPMW and LSW in the Iceland Basin, the ERRC variability seems dominantly associated with the variability of its intermediate layers (Layers 2 and 3).

In the northern part of the Iceland Basin (between 60 – 64°N/22°W), Kanzow and Zenk (2014) reported that the southward flow was intensified at depth, which was supported by Childers et al. (2015) who noted a weak surface flow (< 0.05 m s^{-1}) above 400-m depth at these latitudes. Composed by a southward plume of three cores of ISOW, Kanzow and Zenk (2014) estimated a mean ISOW transport of -3.8 ± 0.6 Sv (2000 – 2002) for $\sigma_0 > 27.8$ kg m^{-3}, and showed strong variability from -6.5 to -1.5 Sv on less than seven months. From numerical models, Xu et al. (2010) and Zou et al. (2017) also estimated an ISOW transport of -3.3 Sv and -3.8 Sv, respectively. Across the NS and from the top of the ridge to +325 km (station 46), we estimated an ISOW transport of -4.1 ± 0.6 Sv at these densities. Similarly to that at the OS, the ISOW transport at the NS compares favorably with previous results showing stability over time.

In their work, Kanzow and Zenk (2014) showed large difference of hydrological properties in the ISOW plume (see Figure 9, therein). The offshore core of the plume at 21.5°W had salinity range of 34.94 – 34.98 for density higher than $27.84\sigma_0$, while the inshore core of the plume at 22.1°W had salinity higher than 34.98 at these densities. Across the NS, we also show that the western branch at 0 – 240 km was 0.03 saltier than the eastern branch at +250 – 300 km along $27.87\sigma_0$ (Figure 4.8, lower panel). With salinity higher than 34.98, our western branch is thus associated with the inshore core of Kanzow and Zenk (2014), while our eastern branch is associated with their offshore core. In their plume of ISOW, Kanzow and Zenk (2014) showed that the eastern offshore core had larger intraseasonal fluctuations in both flow and salinity, and assumed that it was due to meander and recirculation that enhanced lateral

water mass exchange between the ambient water and the eastern core of the plume. Here, we confirm that such fluctuations should be linked to the activity of the NAC because we observed a strong eddy immediately east of the eastern vein of ISOW at the NS (at 20 – 22°W/59 – 60.5°N in Figure 4.5) that influence its properties southward (Figure 4.8).

Finally, Jakobsen et al. (2003) showed that the IC was stronger at sub-surface than the ERRC (see Figures 3 and 5, therein). However, we show that the strength of these two currents has the same order of magnitude in the top 1000 m of the OS and SS (0.21 m s^{-1} and 0.1 m s^{-1}, respectively). Maps of surface and sub-surface velocities from drifters and satellite altimetry used by Jakobsen et al. (2003) average their velocities on large distance horizontally, which may not properly reproduce the strength of narrow southward along-ridge flow that appeared weak along the eastern side of the ridge.

4.4.2 Large-scale circulation of the IC

At about 59°N, Våge et al. (2011) showed that the western and eastern branches of the IC have different properties, the western branch containing more subpolar water than the eastern branch. In their study, Våge et al. (2011) explained that the western branch was associated with the northern branch of the NAC, which quickly leaved the Iceland Basin by crossing the ridge, while the eastern branch was associated with the saltier and warmer Sub-Arctic Front. Here, we precise that the hydrological differences between the two IC branches are higher in Layers 1 and 2 (Figure 4.9), with an eastern branch about 0.05 saltier along 27.52σ_0 than the western branch at each section. By comparing the cross-ridge flow with the along-ridge flow, we show in Figures 4.11 – 4.14 that the water leaving the ERRC feeds the IC and that this inflow occurs from Iceland to 53.15°N, strongly constrained by the bathymetry of the Reykjanes Ridge (Petit et al., 2018b). As a consequence, the different layers of the northward IC do not flow continuously into one top-to-bottom current from the SS to the NS, as discussed in the following paragraph.

Inflows and outflows along the Reykjanes Ridge locally change the hydrological properties of the IC branches, which affects their local densities. Because the density field controls the intensity of the IC, westward outflows from the IC toward the Irminger Sea are highlighted by the slope of its isopycnals σ_0 = 27.52 and 27.71 kg m^{-3} in Figure 4.3, which are steeper at the OS than at the NS. Between the OS and the NS, Layers 1 and 2 of the IC are largely detrained

toward the Irminger Gyre, such that new IC branches are formed by cross-ridge inflows from RS4 (Figure 4.9). At the NS, the eastern branch is thus fed by cross-ridge flow from the northern part of the region RS4 while the western branch is fed by colder and fresher cross-ridge flow from the southern part of the region RS4. The presence of strong outflows from the IC at these latitudes is consistent with Reverdin et al. (2003) who showed sub-surface drifters joining the Irminger Gyre from the Irminger Current (Reverdin et al., 2003, their Figure 12). However, Layers 3 and 4 of the IC at the NS are mostly connected to the IC from the south due to the bathymetry of the Reykjanes Ridge that prevents the densest water masses to cross the ridge north of the BFZ. Indeed, ISW is the lighter water mass of these layers able to cross the ridge at 58.3 – 60°N (Petit et al., 2018b), which mixes with LSW from the IC.

Between the SS and the OS, we show another source of fresh and cold water (Figure 4.9). Even though the two branches of the IC entrain cross-ridge flows, the western branch also incorporates fresher and colder water from the Irminger Sea. An eastward inflow into the IC from the Irminger Gyre is consistent with Reverdin et al. (2003) and Lazarevich et al. (2004) who showed sub-surface drifters and RAFOS floats joining the IC from the Irminger Gyre (Lazarevich et al., 2004, their Figure 2; Reverdin et al., 2003, their Figure 12). From repeated trans-Atlantic section (AR7), Yashayaev et al. (2007) also showed exchanges of LSW between the Irminger Gyre and the IC. The strong eddy activity in the Irminger Sea (Fan et al., 2013; Sy et al., 1997) could favor the mixing between the Irminger Gyre and the IC water masses, as well as the southward meander of the Irminger Gyre localized west of the IC at the OS (Figure 4.3). Although this meander was often observed at this location (Daniault et al., 2016; Sarafanov et al., 2012; Våge et al., 2011), its direct impact on the IC and the Irminger Gyre was nevertheless never documented, and the cause of its regular formation west of the IC was neither explained as well.

South of the SS, publications showed that the IC is only formed by the NAC that enters in the Iceland Basin by crossing eastward the MAR, and re-enters in the Irminger Sea by crossing back westward the ridge (Bower et al., 2002; Lavender et al., 2000; Ollitrault & Colin de Verdière, 2014; Våge et al., 2011). However, we showed that the western branch of the IC is 0.03 fresher and 0.2°C colder along $27.6\sigma_0$ than its eastern branch and than the westward cross-ridge flow south of the SS (Figure 4.9, left panel), but is identical to the northern branch of the NAC. At these densities, we argue that the western branch is largely connected to northeastward flow that bifurcates from the NAC system before entering in the Iceland Basin. This latter branch is outlined by the dynamic topography -0.55 m on Figure 4.5. In the

literature, such pathway is found at sub-surface and intermediate depth. Using drifter data, Jakobsen et al. (2003) showed surface pathways that directly link the NAC to the Irminger Current without entering the Iceland Basin (Jakobsen et al., 2003, their Figure 5). Using data from synoptic hydrographic surveys, Pollard et al. (2004) estimated the baroclinic transport of this Irminger inflow at 8 Sv in the top 1400 m. In the western branch of the SS, we estimated a baroclinic transport of 7 ± 1 Sv, which is in good agreement with their results.

At Ovide latitudes, Sarafanov et al. (2012) and Daniault et al. (2016) estimated an averaged IC transport of 13.0 ± 1.9 Sv (2002 – 2008) and 9.5 ± 3.4 Sv (2002 – 2012) respectively, which included the southward meander of the Irminger Gyre west of the IC. For the same limits, we computed a higher IC transport of 15.6 ± 0.8 Sv (Figure 4.4). Likewise, Rossby et al. (2017) found an IC transport of 14.66 Sv at 59.5°N, between the surface and 1900 m, while we computed a higher IC transport of 21.6 – 15.6 Sv at the OS – NS above 1900 m. As for the ERRC (see section 4.4.1), the IC transport is higher than the previous estimates although it remains within the range of high interannual variability reported by Våge et al. (2011) over 16 years (1991 – 2007). Higher transports were also observed in the northern branch of the NAC and in the SAF in 2015. There, Petit et al. (2018b) estimated a NAC transport of 40.2 ± 2.3 Sv in 2015, while Daniault et al. (2016) estimated an averaged transport of 24.2 ± 5 Sv in 2002 – 2012. These results suggest that the subpolar gyre was stronger in June – July 2015 than the average circulation at the beginning of 2000s. In addition, these previous estimations of the IC transports include the southward meander of the Irminger Gyre, which is by definition instable. Daniault et al. (2016) showed that the intensity of this southward flow at about 34 – 35°W strongly varies over 6 years. Not always observed, its intensity might reach 10.5 Sv southward (Daniault et al., 2016, their Figure 2). To estimate an accurate IC transport, it is thus advisable to not include the southward meander of the Irminger Gyre in the computation.

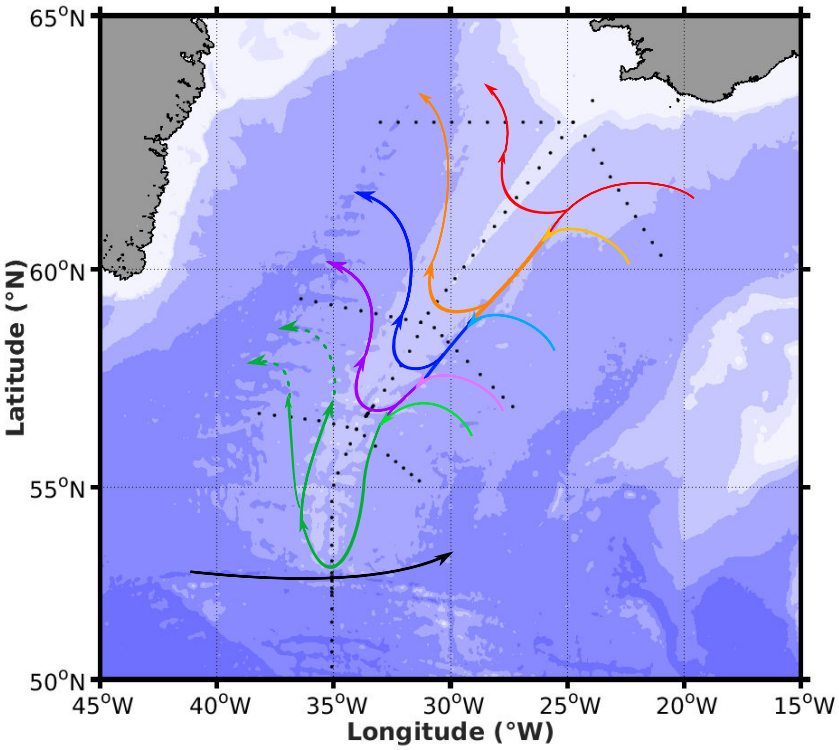

Figure 4.11: Schematic ocean circulation in the vicinity of the Reykjanes Ridge in Layer 1. Color code follows the evolutions of hydrological properties of the water masses. Dashed arrows are uncertain pathways.

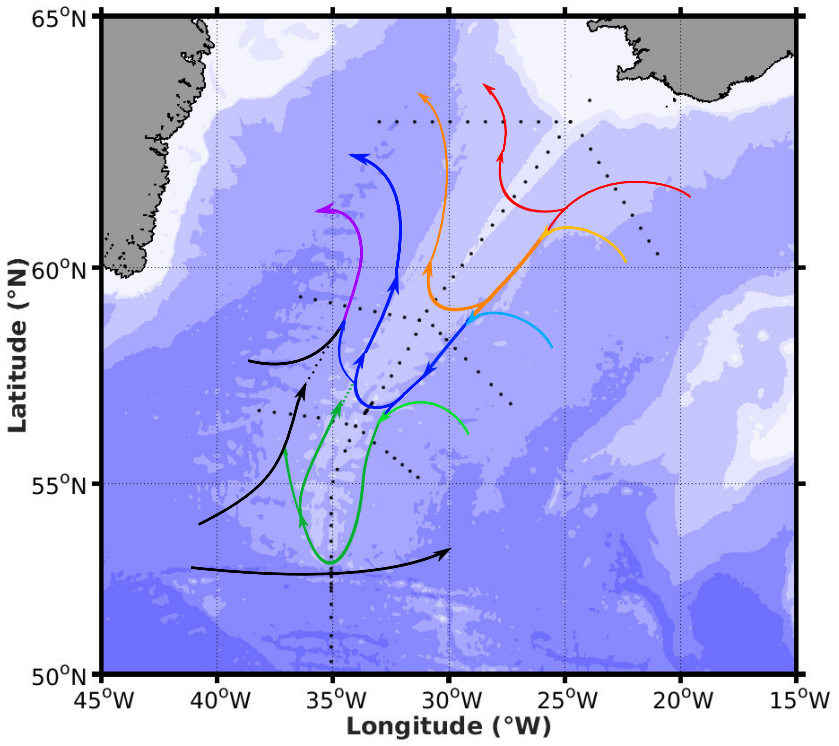

Figure 4.12: Same as Figure 4.11 for Layer 2.

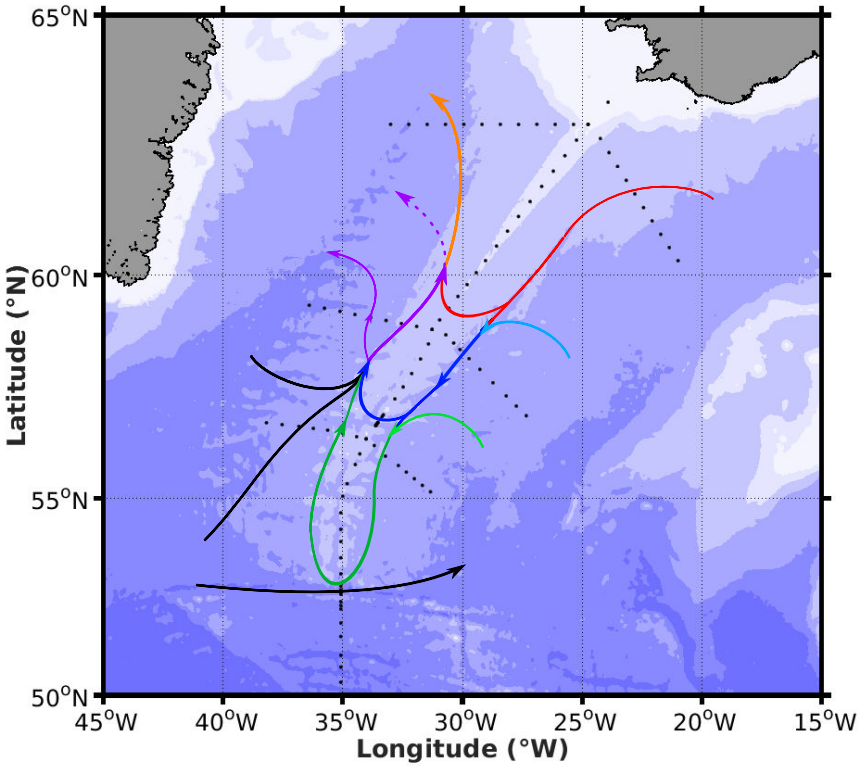

Figure 4.13: Same as Figure 4.11 for Layer 3.

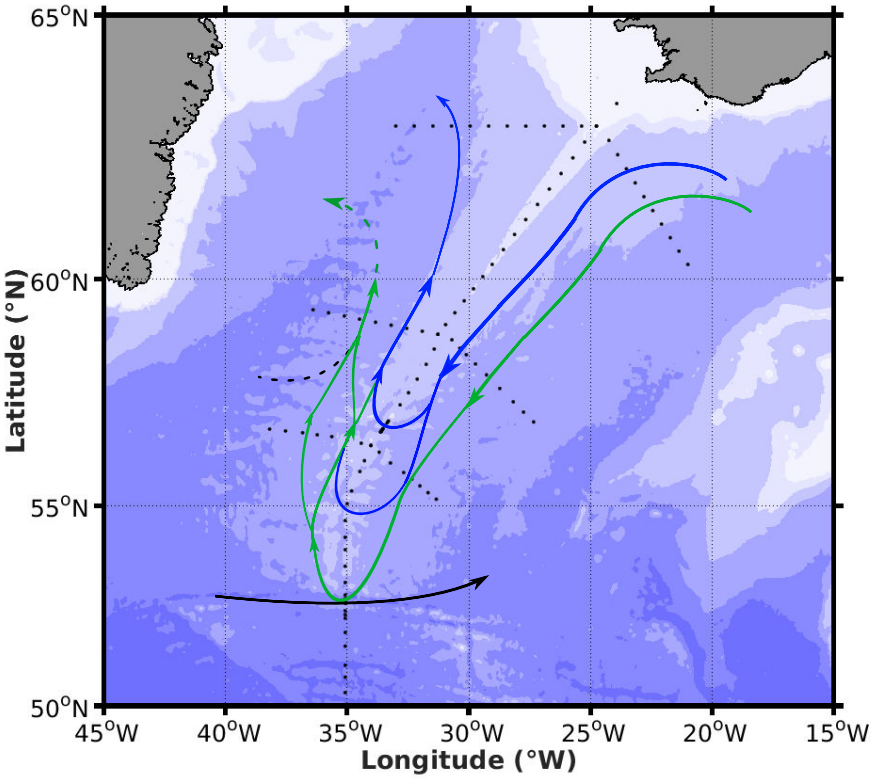

Figure 4.14: Same as Figure 4.11 for Layer 4.

4.5 Conclusion

The Reykjanes Ridge Experiment (RREX) data set allowed an in-depth investigation of the circulation around and over the Reykjanes Ridge. By computed geostrophic and Ekman transports along four sections across and along the top of the Reykjanes Ridge, we were able to better understand the evolution and formation of the ERRC and IC on both sides of the ridge, and to better explain the effect of the bathymetry on their connections.

Based on the literature, the ERRC was defined by southward flows of about 200 km wide east of the top of the Reykjanes Ridge (Daniault et al., 2016), and was estimated in our study at -10.6 ± 0.9 Sv across the North Section (NS), -20.0 ± 0.6 Sv across the Ovide Section (OS), and -13.0 ± 1.2 Sv across the South Section (SS). Likewise, the IC was defined by two surface-intensified northward flows within about 200 km west of the top of the Reykjanes Ridge (Våge et al., 2011), and was estimated at 15.7 ± 0.9 Sv across the NS, 23.5 ± 0.6 Sv across the OS, and 9.8 ± 1 Sv across the SS. At Ovide latitudes, the IC and ERRC transports are thus higher than at other latitudes due to zonal flows joining or leaving the currents.

The southward evolution of the horizontal and vertical structures of the ERRC showed for the first time that this current does not have identical characteristics north and south of the Ovide latitudes. The southward current did not continuously flow along the Reykjanes Ridge into one top-to-bottom barotropic current. The study of its hydrological evolution highlighted that water leaves the current toward the Irminger Sea via westward cross-ridge flows as soon as they are no longer blocked by the bathymetry of the Reykjanes Ridge. From its eastern edge, this current is also joined by westward inflows of NAC water from the Iceland Basin, which locally compensate the detrainments of ERRC water across the Reykjanes Ridge. The top-to-bottom barotropic ERRC observed at the Ovide latitudes by Daniault et al. (2016) is thus formed by a local convergence of southward flows, which combine inflows of the NAC at surface and southward flows blocked by the Reykjanes Ridge at depth.

Between the two sides of the Reykjanes Ridge, water leaving the ERRC via cross-ridge flow feeds the IC. Partly blocked by the bathymetry of the Reykjanes Ridge, this inflow depends on the density of their water masses, which affects differently the layers of the IC. South of the Ovide latitudes, Layers 2 and 3 of the western IC branch also incorporate NAC water that joins the IC before entering in the Iceland Basin as part of a Labrador – Irminger Sea cyclonic circulation. There, the two IC branches are thus differently influenced by inflows of NAC waters from the Iceland Basin (eastern branch) and the Irminger Sea (western branch). North

of the Ovide latitudes, Layers 1 and 2 of the IC branches are largely detrained toward the center of the Irminger Sea, while the lower Layers 3 and 4 are more constrained by the bathymetry of the ridge to stay at constant depth and to flow northward.

This study is a step towards a better understanding of the subpolar gyre circulation, by connecting more clearly two major currents linking the ocean circulations of the Iceland Basin and Irminger Sea. However, this work gives rise to new questions. Firstly, we showed that the connection between the two sides of the Reykjanes Ridge are constrained by the bathymetry and strongly depends on the density of the water masses. However, we could not investigate the diapycnal exchange of waters between the layers of the ERRC and IC. How the outflows from the ERRC mix with the IC waters? Are light-to-dense conversions enhanced by these flows across the Reykjanes Ridge? Finally, the comparison of the two IC branches showed that inflows from the Irminger Sea affect more the western branch than the eastern branch. Such inflows could be related to intrusions from the Irminger Gyre, possibly by eddies or meanders formed between the northward branch of the Irminger Gyre and the IC. However, to our knowledge, very few studies have examined their interactions. How are formed such eddies and what are their consequences on the circulation and properties of the Irminger Gyre and IC?

5 Deep through-flow in the Bight Fracture Zone

In this chapter, we investigate the circulation and evolution of Iceland-Scotland Overflow Water through the BFZ and provide elements of dynamical processes induced by the bathymetry on the deep water. The associated time variability is also analyzed from hydrographic sections and Deep-Arvor floats. Thus, this chapter focuses on the second part of the question Q3 given in Introduction.

5.1 Introduction

Iceland-Scotland Overflow Water (ISOW) is a major component of the lower limb of the Meridional Overturning Circulation (MOC). ISOW is formed by mixing between overflows from the Nordic Seas, Atlantic Water and Labrador Sea Water (LSW) after crossing the Iceland-Scotland-Faeroe Ridge. In the northern part of the Iceland Basin, ISOW is characterized by potential density higher than 27.8 kg m^{-3} and salinity higher than 34.94 (Saunders, 1994). ISOW is then carried southwestward along the Icelandic shelf and subsequently along the eastern flank of the Reykjanes Ridge. There, Xu et al. (2010) showed that the southward flow of ISOW is composed of several veins and identified the Bight Fracture Zone (BFZ), a deep and wide gap of the Reykjanes Ridge, as a major route for ISOW toward the Irminger Sea. By analyzing hydrographic and velocity measurements along and across the Reykjanes Ridge, we detailed the circulation along the eastern side of the Reykjanes Ridge in chapter 4, and we connected these veins to the westward cross-ridge flow of ISOW and subsequently to the northward Irminger Current (IC). There, we showed that only the lightest variety of ISOW crosses the Reykjanes Ridge through the BFZ, while denser ISOW joins the Irminger Sea through deeper gaps, such as the Charlie Gibbs Fracture Zone (CGFZ). The circulation in the CGFZ has been widely investigated. In the CGFZ, both observations (Bower & Furey, 2017) and models (Xu et al., 2018) showed that the time evolution of the deep-reaching eastward branches of the NAC are correlated to the time evolution of the ISOW transport at depth. Moreover, Bower and Furey (2017) showed that the westward evolution of the ISOW properties in the CGFZ is explained by mixing between ISOW and surrounding water masses such as Lower Deep Water (LDW) and LSW.

At about 58.8°N, Daniault et al. (2016) showed a strong asymmetry of the ISOW properties between the eastern and western flanks of the Reykjanes Ridge, and we outlined in chapter 4 that this asymmetry is also observed south and north of these latitudes. Moreover, we showed that the northward flow of ISOW along the western side of the Reykjanes Ridge is connected to the southward flow of ISOW along the eastern side of the ridge by westward flows across the BFZ at about 57°N (see Figure 4.14). The asymmetry at depth is thus mainly related to the evolution of ISOW properties as it crosses the Reykjanes Ridge. Indeed, fracture zones are sites of large modifications of the water mass properties (Mercier et al., 1994). However, no study ever investigated the westward pathways of ISOW through the complex bathymetry of the BFZ, the westward evolution of its hydrological properties, or the mechanisms responsible for this evolution. Yet, ISOW feed the lower limb of the MOC, and better understanding its

evolution between the Iceland Basin and the Irminger Sea is crucial to characterize the North-Atlantic Subpolar Gyre. High-resolution data sets are thus needed to determine the pathways of the cross-ridge flows through the BFZ and the evolution of the ISOW properties along this path.

Section 5.2 presents the data and methods used for this study. In Section 5.3, the westward evolution of the ISOW transport and properties through the BFZ are investigated and their variations over time are documented. Finally, Section 5.4 summarizes the results and provides a first description of the ISOW circulation in the BFZ. There, we also discuss the mechanisms at the origin of the westward evolution of the ISOW properties.

5.2 Data and Methods

5.2.1 Bathymetry of the Bight Fracture Zone

The deepening of the Reykjanes Ridge southward from Iceland is associated with several fracture zones, including the Bight Fracture Zone (BFZ) at 57°N. In this section, we present the bathymetry of the BFZ (Figure 5.1). The BFZ axis extends quasi-zonally from the Iceland Basin to the Irminger Sea and intersects the rift valley of the Reykjanes Ridge at 56.75°N/34.17°W. A first sill is located on the eastern side of the rift valley at 56.73°N/33.72°W and is referred hereinafter as the eastern sill. The bottom depth at the eastern sill is at about 2150 m according to the bathymetry recorded during the RREX2015 cruise. This sill is deeper than the other sills found north of the BFZ at about 1500 – 2000 m. On the eastern side of the rift valley, the eastern sill is also the narrowest sill of the BFZ (8.7 km), the width of the fracture zone being measured here as the distance between the 2000-m isobaths. Immediately west of the eastern sill, the axis of the BFZ intersects the rift valley of the Reykjanes Ridge that is oriented northeast – southwest and reaches bottom depths larger than 2500 m. A second sill is located on the western side of the rift valley at 56.75°N/35.55°W and is referred hereinafter as the western sill. The depth of the western sill is similar to that of the eastern sill but its width is larger than that of the eastern sill when considering the 2000-m isobaths (11.3 km). At the approach of the Irminger Sea, the BFZ connects to two basins deeper than 2500 m and separated by a seamount with a summit that lies at about 1700 m. These two basins are referred hereinafter as the two western basins.

5.2.2 Hydrographic sections

This study is based on high-resolution measurements obtained during three different cruises at key locations of the BFZ. Twenty-one (21) $CTDO_2$ (Conductivity Temperature Depth Oxygen) stations were first carried out on 13 June (stations 16 – 20) and 30 June (stations 93 – 107) 2015 on the French N/O Thalassa during the RREX2015 cruise (Figure 5.1). Two sections were localized into the BFZ, and a third section was localized at the junction between the BFZ and the Irminger Sea. The first hydrographic section, called East Section, was carried out east of the eastern sill and encompasses a deep valley north of the eastern sill as well. The second hydrographic section, called Middle Section, was carried out across the rift valley of the Reykjanes Ridge. The third section was carried out through the western basins and is referred hereinafter as the West Section. These hydrographic sections were designed to study the deep circulation of ISOW that enters the BFZ from the Iceland Basin, circulates in the rift valley of the Reykjanes Ridge, and exits the BFZ toward the Irminger Sea. The nominal station spacing was less than 2 km along the East and Middle Sections and less than 10 km along the West Section. In addition, seven (7) $CTDO_2$ stations were carried out on 6 August 2017 on the French N/O l'Atalante during the RREX2017 cruise (stations 84 – 91, chapter 1.5). These stations were located close to the East Section recorded in 2015. The southern part of the East Section carried out in 2017 was localized slightly west of that carried out in 2015 in order to perfectly matched with the location of the eastern sill. Finally, six (6) $CTDO_2$ stations were carried out on 8 July 2018 on the French N/O Thalassa during the OVIDE2018 cruise (stations 103 – 108) and followed exactly the Middle Section recorded in 2015. The accuracies of the $CTDO_2$ measurements were identical during the three cruises and are described in chapter 2.1, except in 2018 where the $CTDO_2$ probe presented bias in dissolved oxygen concentration (only pre-calibrated data of the OVIDE2018 cruise were available for this thesis). This bias was estimated by comparing the dissolved oxygen concentration of the sensor with the dissolved oxygen concentration of the bottles mounted on the rosette. The dissolved oxygen concentration was thus less accurate in 2018 than for the other years and was estimated at 2 $\mu mol\ kg^{-1}$.

During each of the three cruises, the rosette was equipped with both upward and downward looking 300 kHz L-ADCPs (Lowered Acoustic Doppler Current Profiler, RD Instruments), and the upper layer current velocity components were measured by two S-ADCPs (Shipboard Acoustic Doppler Current Profiler, RD Instruments) operating at 38 kHz (OS38) and 150 kHz (OS150). The calibrations and processes of these measurements were identical during the

three cruises and are described in chapter 2.1. Methods used to compute geostrophic velocities and associated geostrophic transports across the hydrographic sections were also identical and the readers are invited to refer to chapter 2.2 for more details, as well as to Petit et al. (2018b) for a presentation of the method used to compute errors for the transports.

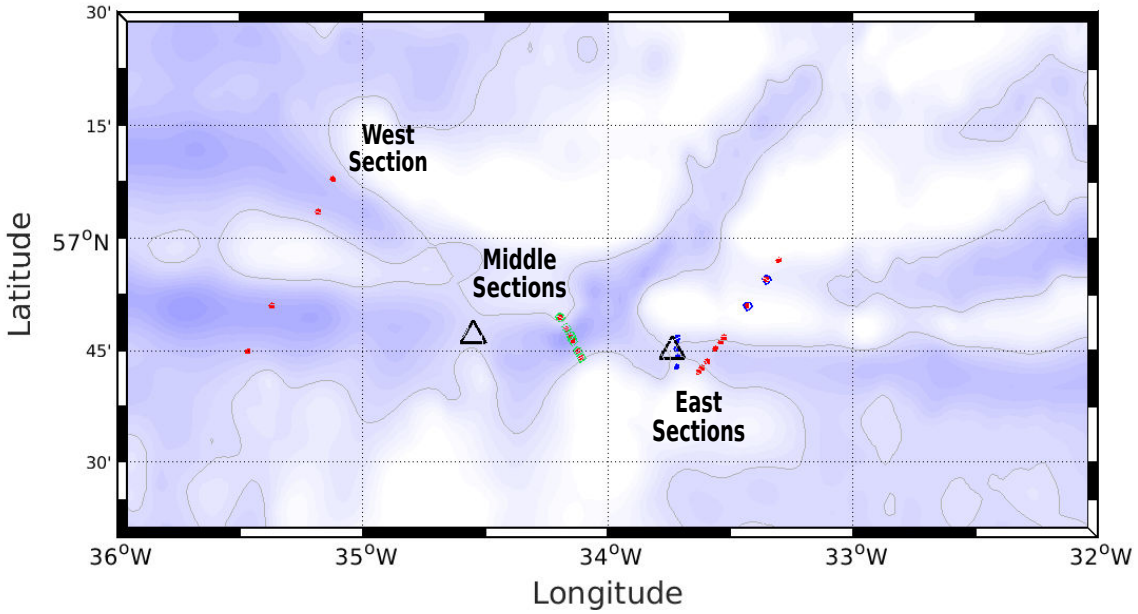

Figure 5.1: Bathymetry in the region of the Bight Fracture Zone obtained by contouring the ETOPO1 data set with 100-m isobaths spacing. The grey line outlines the 2100-m isobaths. The deepest bathymetries are represented with the darkest blue. Red dots indicate the locations of the hydrographic stations carried out during the RREX2015 cruise. Blue dots and circles indicate the locations of the hydrographic stations carried out during the RREX2017 cruise. Green circles indicate the locations of the hydrographic stations carried out during the OVIDE2018 cruise. Black triangles show the main sills of the BFZ.

5.2.3 Deep-Arvor floats

During the RREX2017 cruise, one Deep-Arvor float (WMO#6901603) was deployed at 56.73°N/33.72°W (station 89) along the East Section. In addition, two Deep-Arvor floats (WMO#6902881, 6902882) were deployed simultaneously during the OVIDE2018 cruise at 56.80°N/34.17°W along the Middle Section. The Deep-Arvor floats are Argo floats profiling down to 4000 m (Le Reste et al., 2016) and returning every 10 days top-to-bottom profiles of temperature, salinity and dissolved oxygen concentration as a function of pressure. An Iridium antenna transmits these data while the float surfaces. The #6901603 float completed 12 cycles before it died on 26 November 2017 (Table 5.1), and the #6902881 and #6902882

floats completed 6 cycles so far (28 August 2018). Because the floats take off directly after reaching their parking depth during their first cycles, with a delay of 4 hours between the #6902881 and #6902882 floats, the ISOW trajectories will be considered from cycle 2.

Temperature, conductivity and dissolved oxygen were measured as a function of pressure at each cycle using a Seabird SBE41CP CTD sensor with an accuracy of 0.01°C, 0.01 and 2.5 µmol kg^{-1}, respectively. For the #6901603 float, the bias in salinity was estimated following the Cabanes et al. (2016) method, and a correction of 0.003 was applied to each salinity profiles (Cabanes et al., 2018). For the two other floats, #6902881 and #6902882, a visual verification of the salinity profiles showed that no correction was required. Indeed, the first ascending profiles of the floats perfectly match with the reference profiles acquire during the float deployment below 1000-m depth (Figure 5.2).

Table 5.1: Details on the deployment and parking depth of the three Deep-Arvor floats.

Float WMO	**6901603**	**6902881**	**6902882**
Date of deployment	6 August 2007	8 July 2018	8 July 2018
Cruise	RREX2017	OVIDE2018	OVIDE2018
Number of cycle	12	6	6
Parking depths	Cycle 2: 1200 m Cycle 3 – 10: 2100m Cycle 11: 1100 m Cycle 12: 1500 m	Cycle 2 – 6: 2100 m	Cycle 2 – 3: 2100m Cycle 4: 1900 m Cycle 5 – 6: 2100 m

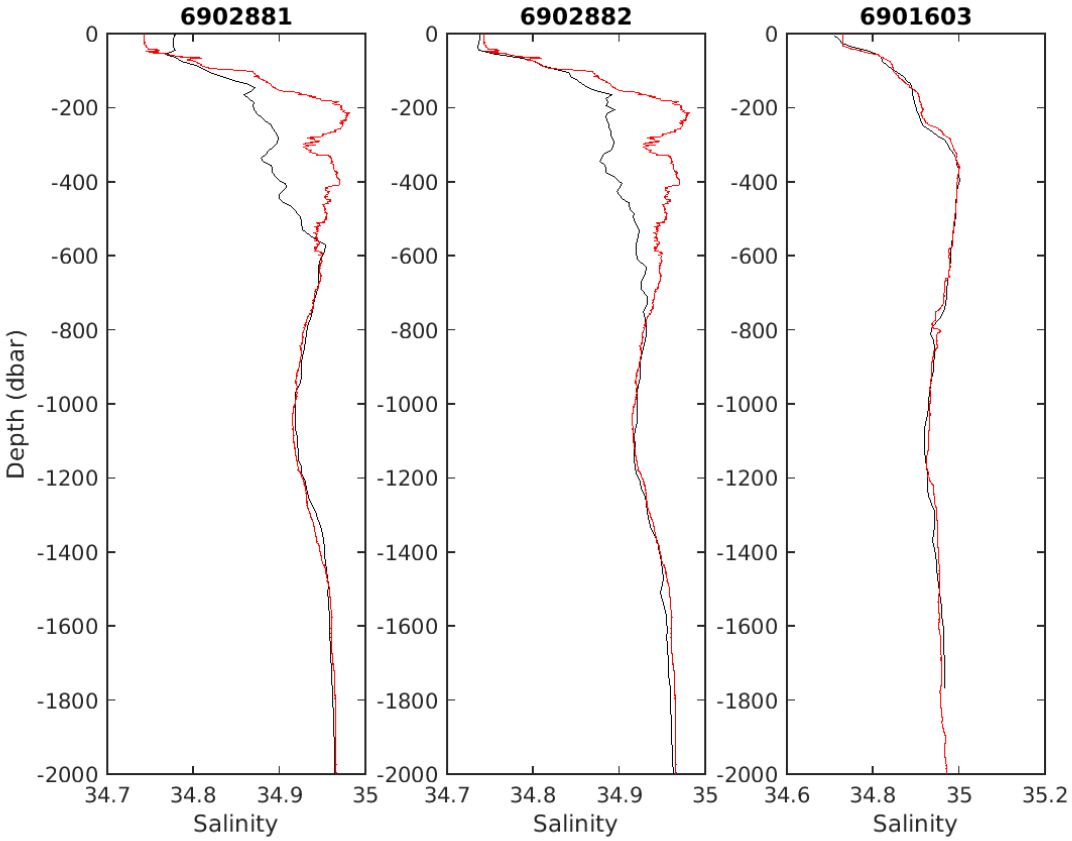

Figure 5.2: Salinity profiles of the first ascending profiles of the three Deep-Arvor floats (black lines) compared with the reference salinity profiles carried out during the float deployments (red lines). The #6901603 float was corrected in salinity by Cabanes et al. (2018), while the #6902881 and #6902882 floats was not corrected.

5.3 Results: Through-flow in the Bight-Fracture Zone

In the following sections, we study the ISOW pathways, transport and property evolution through the BFZ from the Iceland Basin to the Irminger Sea and document its variations over time. We first compare the flow across the East Section in 2015 and 2017 (section 5.3.1), and then across the Middle Section in 2015 and 2018 (section 5.3.2). Section 5.3.3 focuses on the outflow of ISOW across the West Section and on its connections with inflows from the Irminger Sea. Finally, the hydrological properties observed at the three sections (section 5.3.4) as well as the evolution of the ISOW properties along the float trajectories (section 5.3.5) are used to describe the circulation of ISOW through the BFZ.

5.3.1 The eastern sill of the Bight Fracture Zone

Figures 5.3 and 5.4 show the salinity, potential temperature, dissolved oxygen concentration and potential vorticity of the East Sections obtained in 2015 and 2017 that are 5.5 km apart. Defined by density higher than σ_0 = 27.8 kg m^{-3} and salinity higher than 34.94, ISOW is found below 1500 – 1600 m at the eastern sill and in the valley north of the sill. At the eastern sill, the ISOW salinity exceeded 34.98 in 2015 while it was less than 34.98 in 2017. Thus, ISOW reaches higher density (σ_0 > 27.85 kg m^{-3}) in 2015 than in 2017. Moreover, oxygen concentration (> 272 µmol kg^{-1}) and potential vorticity (> 1 10^{-11} m^{-1} s^{-1}) are higher along the southern wall of the sill in 2015 below isopycnal σ_0 = 27.85 kg m^{-3} than at the northern wall, while salinity and potential vorticity show higher values along the northern wall in 2017.

Figure 5.5 compares the geostrophic and L-ADCP velocities of the East Sections obtained in 2015 and 2017. Note that L-ADCP measurements provide local velocities at each hydrographic station while geostrophic velocities are average velocities between two successive stations (Lherminier et al., 2007), so we cannot expect a perfect agreement between the two data sets. Nevertheless, the main structures of the geostrophic and L-ADCP flows are in good agreement for the two years. In 2015, westward flows are intensified at the center of the sill (56.74°N) and in the valley north of the sill at 56.89°N, while an eastward flow is intensified along the northern wall of the sill at 56.77°N. On the contrary in 2017, an intense westward flow is localized along the northern wall of the sill at 56.77°N. There, note the stronger intensity of the geostrophic velocities (-0.36 m s^{-1}) compared with the L-ADCP velocities (-0.14 m s^{-1}). Westward flow of ISOW was thus intensified in the middle of the sill in 2015 while it was intensified along the northern wall of the sill in 2017. These differences could be related to the different locations of the East Sections (Figure 5.1). In 2015, the East Section was localized east of the eastern sill such that the flow was channeled by the narrow bathymetry found downstream of the eastern sill, while in 2017, the East Section was exactly at the eastern sill.

To quantify the contribution of ISOW to the top-to-bottom flow through the eastern sill of the BFZ, we computed the top-to-bottom vertically integrated transports across the East Sections in 2015 and 2017 from the geostrophic velocities in Figure 5.5, and then we integrated the transport according to the ISOW definition (Table 5.2). At the main sill of the East Sections (stations 96 – 101 in 2015 and stations 86 – 91 in 2017), the ISOW transports were estimated at -0.66 ± 0.1 Sv in 2015 and -0.54 ± 0.2 Sv in 2017, which represent 55.5 % and 48.6 % of

the top-to-bottom transports, respectively. Similar amount of ISOW was thus transported westward through the BFZ in 2015 than in 2017. Finally, the L-ADCP transports of ISOW were slightly weaker but still similar to the geostrophic transports of ISOW across the East Sections 2015 and 2017, except for the top-to-bottom transport across the East Section 2017 where the L-ADCP transport was positive and the geostrophic transport was negative (Table 5.3).

Table 5.2: Geostrophic top-to-bottom and ISOW transports (Sv) across the East and Middle Sections. ISOW is defined by $\sigma_0 > 27.8$ kg m^{-3} and salinity higher than 34.94. Transports in parenthesis indicate the transports integrated both over the main sill and the valley north of the sill (stations 93 – 101 in 2015 and stations 84 – 91 in 2017) during the RREX2015 and RREX2017 cruises.

	East S. 2015	**East S. 2017**	**Middle S. 2015**	**Middle S. 2018**
Top-to-bottom transports	-1.19 ± 0.2 (-3.47 ± 0.3)	-1.11 ± 0.2 (-1.14 ± 0.2)	-2.93 ± 0.2	-0.59 ± 0.1
ISOW transports	-0.66 ± 0.1 (-0.96 ± 0.1)	-0.54 ± 0.2 (-0.59 ± 0.2)	-1.25 ± 0.1	-0.26 ± 0.1

Table 5.3: L-ADCP top-to-bottom and ISOW transports (Sv) across the East and Middle Sections. ISOW is defined by $\sigma_0 > 27.8$ kg m^{-3} and salinity higher than 34.94. Transports in parenthesis indicate the transports integrated both over the main sill and the valley north of the sill (stations 93 – 101 in 2015 and stations 84 – 91 in 2017) during the RREX2015 and RREX2017 cruises.

	East S. 2015	**East S. 2017**	**Middle S. 2015**	**Middle S. 2018**
Top-to-bottom transports	-0.67 ± 0.2 (-2.27 ± 0.2)	+0.14 ± 0.1 (+0.37 ± 0.1)	-1.99 ± 0.1	-0.48 ± 0.1
ISOW transports	-0.16 ± 0.1 (-0.34 ± 0.1)	-0.17 ± 0.1 (-0.16 ± 0.1)	-0.81 ± 0.1	-0.21 ± 0.1

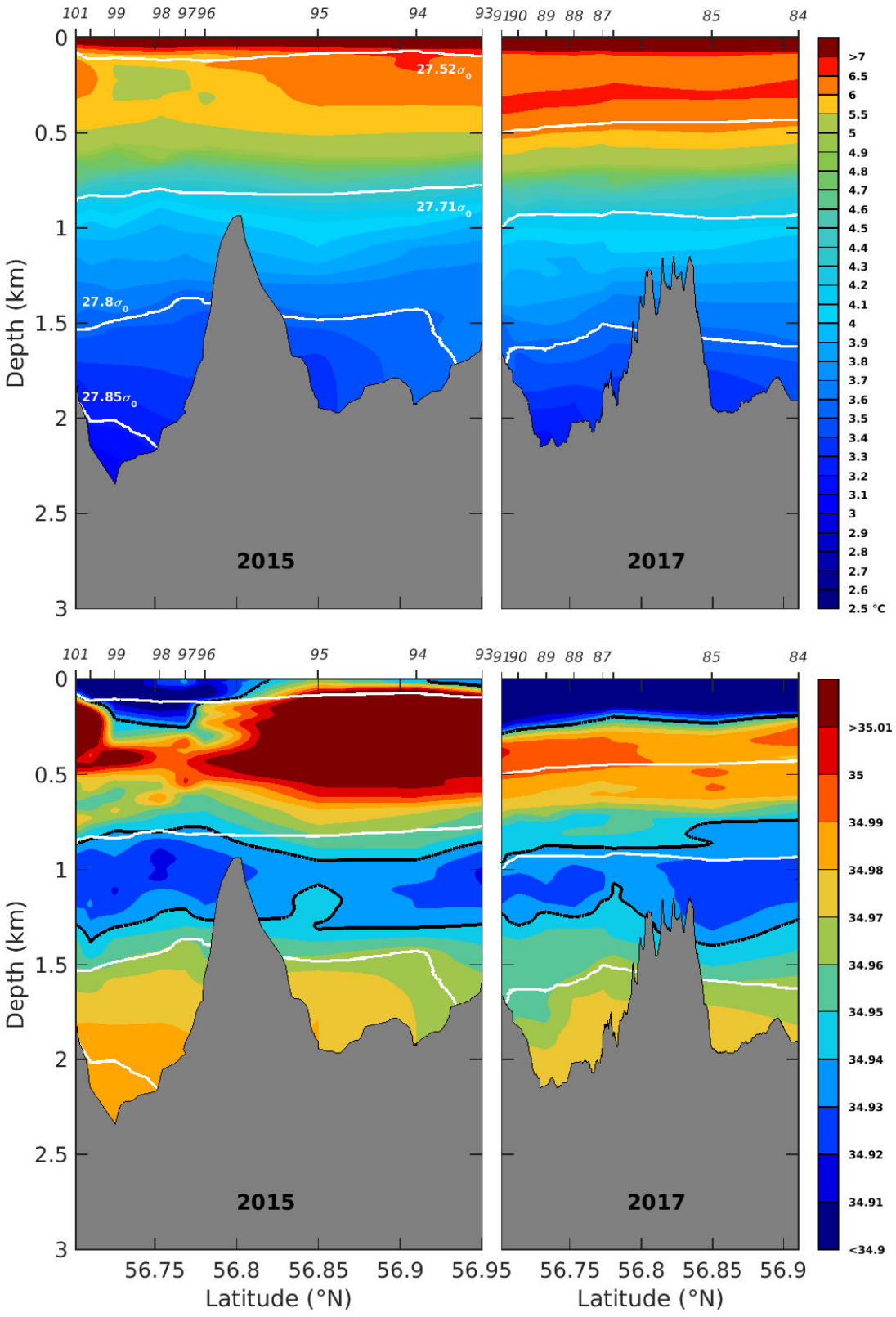

Figure 5.3: Hydrographic sections along the East Sections 2015 and 2017 based on CTDO2 data for (upper panels) potential temperature in °C and (lower panels) salinity. The bold black lines represent isohaline 34.94 for the lower panels. In all panels, the bold white lines show the potential density anomalies σ_0 = 27.52, 27.71, 27.8 and 27.85 kg m^{-3}. Bathymetries in grey are from the ship surveys. Locations and numbers of the hydrographic stations are indicated on the top axis.

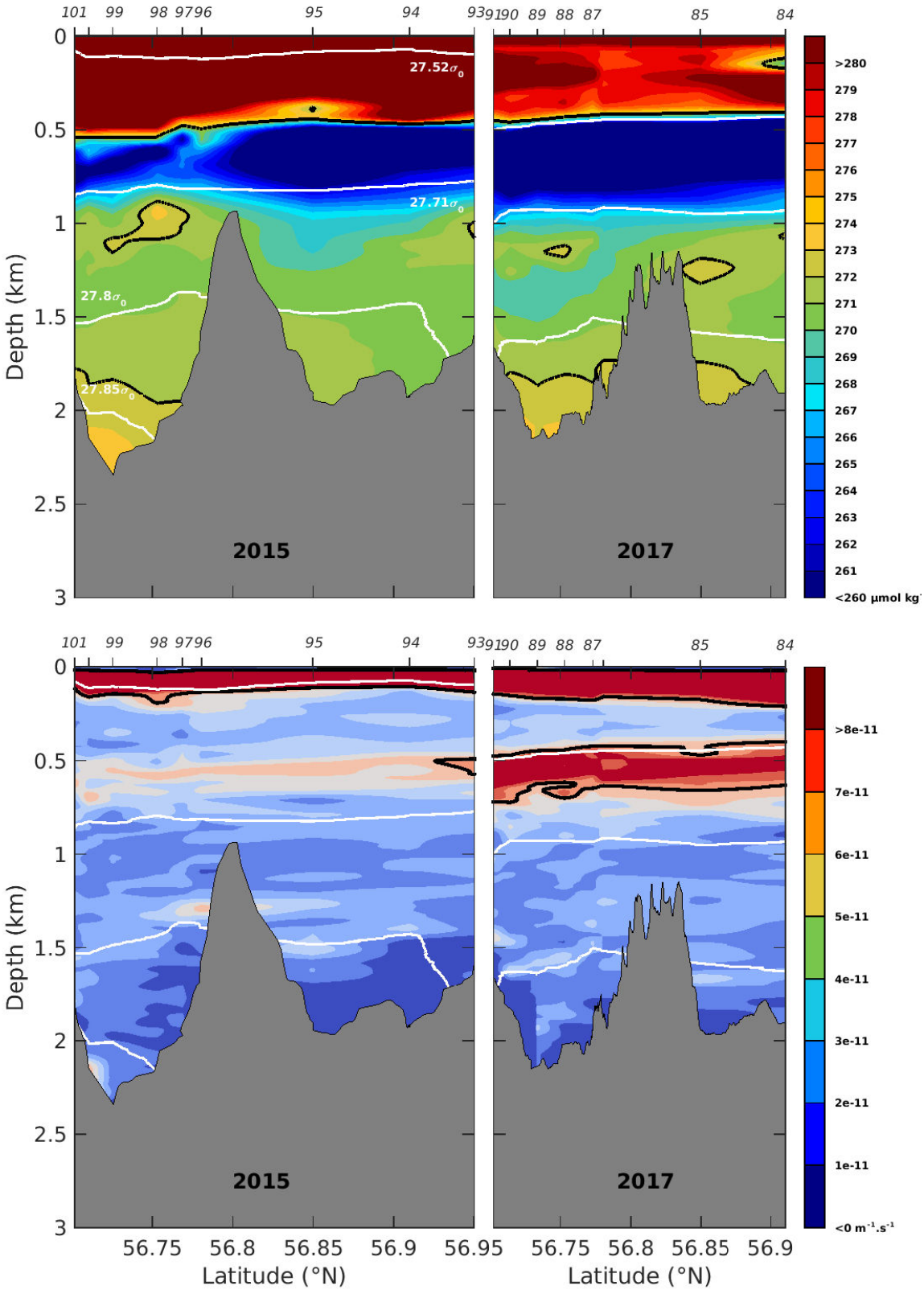

Figure 5.4: Hydrographic sections along the East Sections 2015 and 2017 based on CTDO2 data for (upper panels) dissolved oxygen concentration in µmol kg^{-1} and (lower panels) potential vorticity in m^{-1} s^{-1}. The bold black lines represent isoline 272 µmol kg^{-1} for the upper panels and isoline 6 10^{-11} m^{-1} s^{-1} for the lower panels. In all panels, the bold white lines show the potential density anomalies σ_0 = 27.52, 27.71, 27.8 and 27.85 kg m^{-3}. Bathymetries in grey are from the ship surveys. Locations of the hydrographic stations are indicated on the top axis.

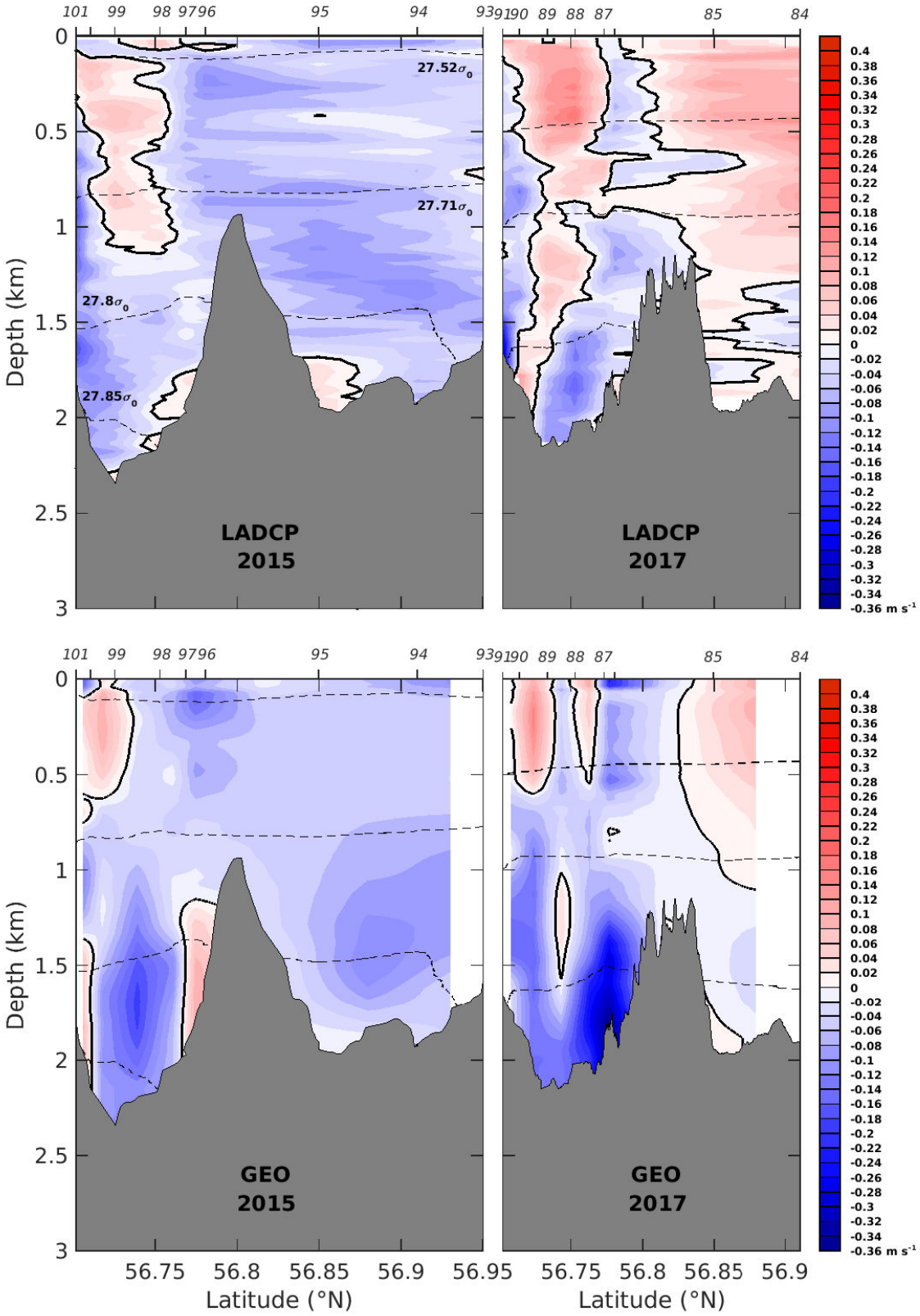

Figure 5.5: (upper panels) L-ADCP and (lower panels) Geostrophic velocity sections along the East Sections 2015 and 2017 (m s^{-1}). Positive values correspond to eastward velocities. The black bold line outlines the 0 isotach. The dashed black lines indicate the potential density σ_0 = 27.52, 27.71, 27.8 and 27.85 kg m^{-3}. Bathymetries from the ship surveys are added in grey. Locations of the hydrographic stations are indicated on the top axis.

5.3.2 The rift valley of the Reykjanes Ridge

Figures 5.6 and 5.7 compare the salinity, potential temperature, dissolved oxygen concentration and potential vorticity of the Middle Sections obtained in 2015 and 2018 in the rift valley of the Reykjanes Ridge. ISOW is found below 1400 – 1500 m and reaches higher salinity in 2015 (> 34.98) than in 2018 (< 34.98) at the bottom. Moreover, its salinity and oxygen concentration show higher values along the southern wall of the rift valley below isopycnal $\sigma_0 = 27.85$ kg m^{-3}.

Figure 5.8 compares the geostrophic and L-ADCP velocities of the Middle Sections obtained in 2015 and 2018. The main structures of the geostrophic and L-ADCP flows are in good agreement for the two years. In 2015 as well as in 2018, the westward flow of ISOW is intensified along the northern wall of the rift valley at 56.8°N, while eastward flows are localized along the southern wall. The eastward branch found along the southern wall of the rift valley, of similar properties than the westward branch found along the northern wall of the rift valley, is probably a local cyclonic recirculation caused by the bathymetry. In 2018, the deep eastward flow is intensified in two cores at 56.75°N and 56.78°N, while in 2015 the deep eastward flow is intensified in one core at 56.75°N. Moreover, the eastward flow of ISOW at 56.75°N is more intense in 2018 (0.14 m s^{-1}) than in 2015 (0.08 m s^{-1}). Note that the eastward branch reaches the surface in 2018 while it remains localized in the ISOW layer in 2015. To sum up, ISOW flows eastward along the southern wall of the rift valley and westward along the northern wall of the rift, and their intensity and vertical structure vary over time.

As for the East Sections, we computed the top-to-bottom and ISOW transports across the Middle Sections in 2015 and 2018 from the geostrophic velocities in Figure 5.8 (Table 5.2). The top-to-bottom transport as well as the ISOW transport was five times weaker in 2018 than in 2015, but for the two years, the ISOW transport represents the same proportion of the top-to-bottom transport (42.7 % in 2015 and 44.1 % in 2017). From the surface down to the bottom, the eastward flow localized along the southern wall of the rift valley was stronger in 2018 than in 2015 and should partly blocked westward flow of ISOW along the northern wall of the rift. Finally, we note that, at the Middle Sections 2015 and 2018, the L-ADCP transports were very close to the geostrophic transports (Table 5.3).

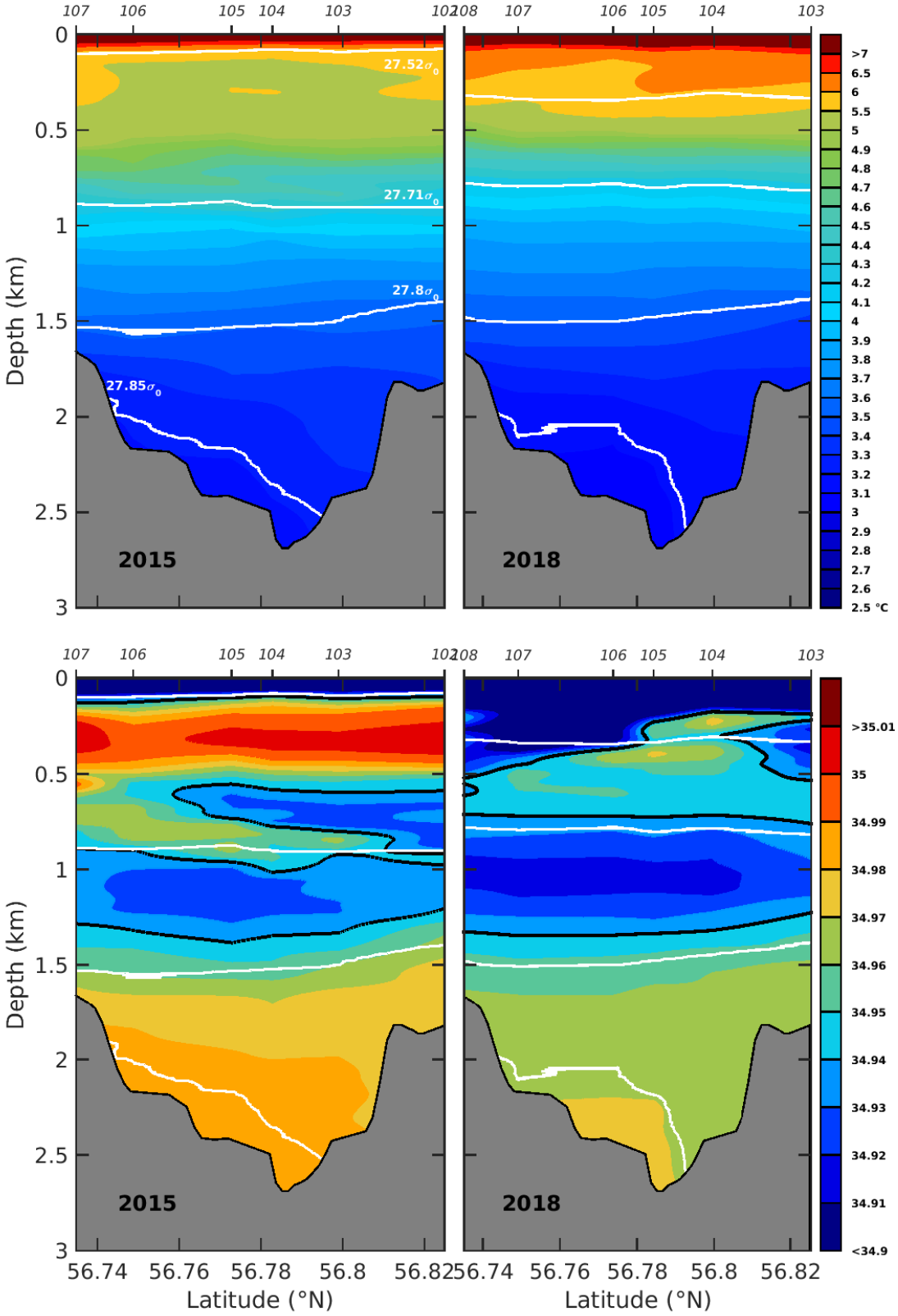

Figure 5.6: Hydrographic sections along the Middle Sections 2015 and 2018 based on CTDO2 data for (upper panels) potential temperature in °C and (lower panels) salinity. The bold black lines represent isohaline 34.94 for the lower panels. In all panels, the bold white lines show the potential density anomalies σ_0 = 27.52, 27.71, 27.8 and 27.85 kg m^{-3}. Bathymetry in grey is from the ship surveys. Locations of the hydrographic stations are indicated on the top axis.

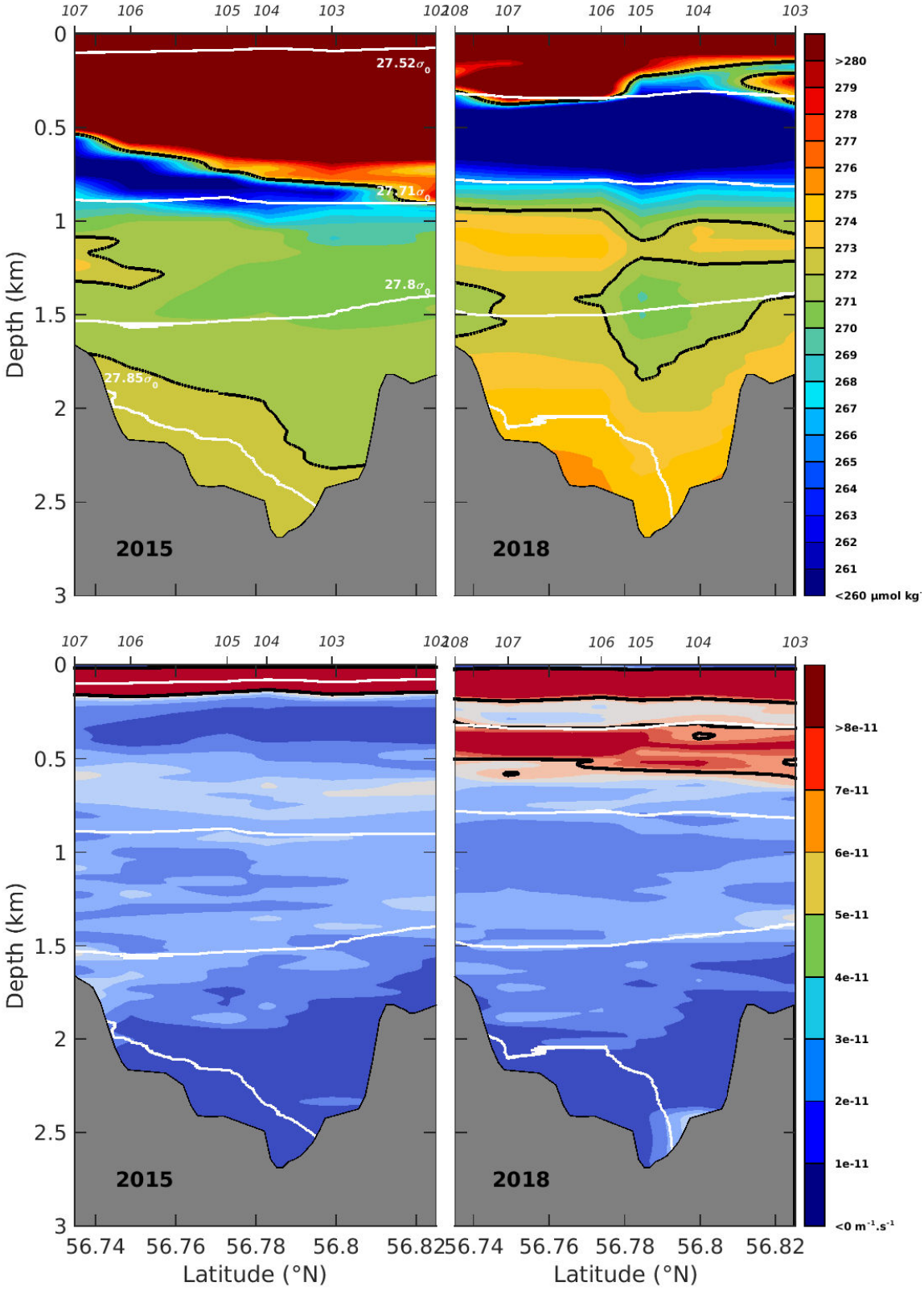

Figure 5.7: Hydrographic sections along the Middle Sections 2015 and 2018 based on CTDO2 data for (upper panels) dissolved oxygen concentration in µmol kg^{-1} and (lower panels) potential vorticity in m^{-1} s^{-1}. The bold black lines represent isoline 272 µmol kg^{-1} for the upper panels and isoline 6 10^{-11} m^{-1} s^{-1} for the lower panels. In all panels, the bold white lines show the potential density anomalies σ_0 = 27.52, 27.71, 27.8 and 27.85 kg m^{-3}. Bathymetry in grey is from the ship surveys. Locations of the hydrographic stations are indicated on the top axis.

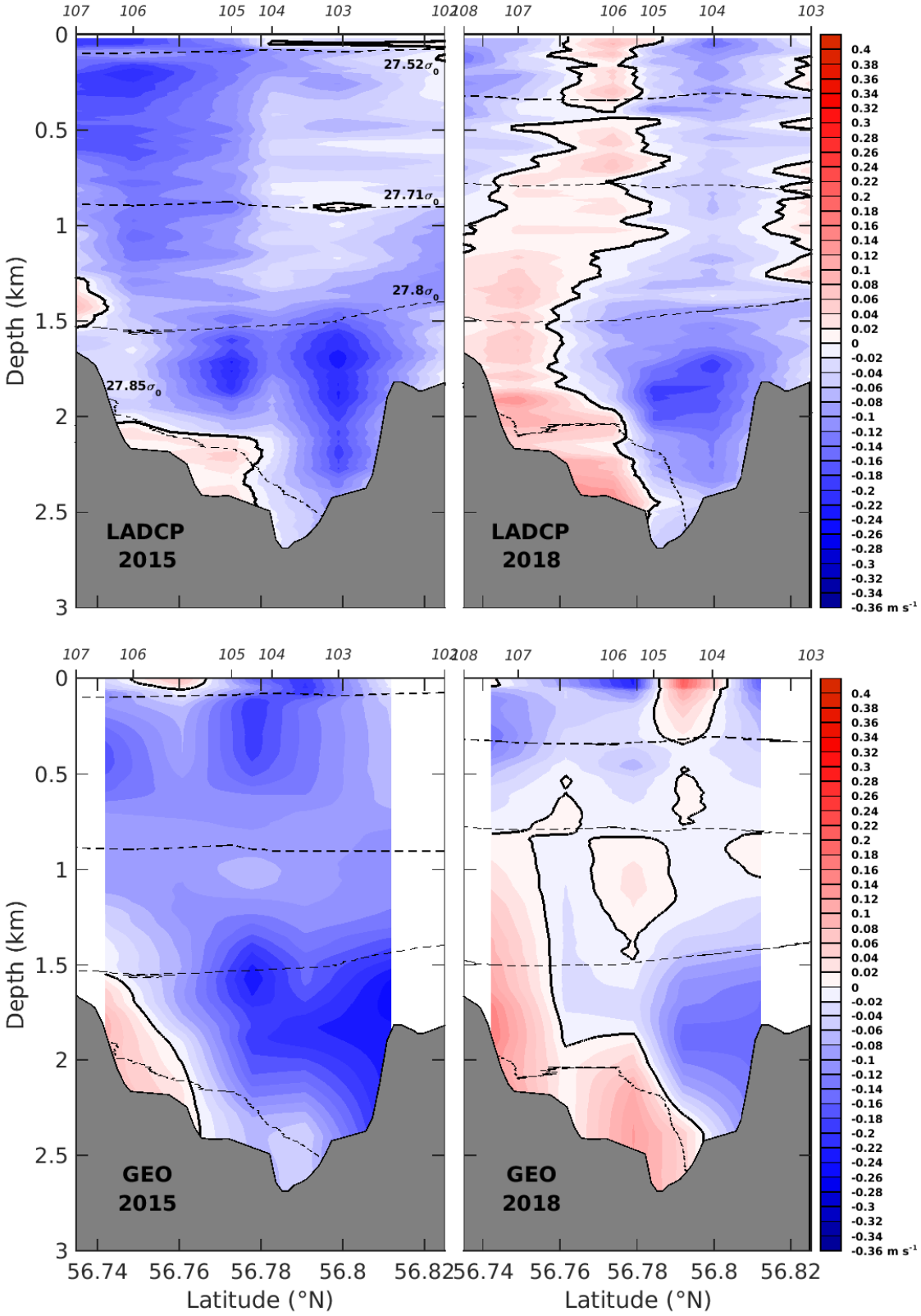

Figure 5.8: (upper panels) L-ADCP and (lower panels) Geostrophic velocity sections along the Middle Sections 2015 and 2018 (m s^{-1}). Positive values correspond to eastward velocities. The black bold line outlines the 0 isotach. The dashed black lines indicate the potential density σ_0 = 27.52, 27.71, 27.8 and 27.85 kg m^{-3}. Bathymetries from the ship surveys are added in grey. Locations of the hydrographic stations are indicated on the top axis.

5.3.3 Exit of ISOW toward the Irminger Sea

Figure 5.9 shows the salinity and potential temperature profiles, as well as the L-ADCP velocities, of the five $CTDO_2$ stations carried out along the West Section in 2015. The circulation in the two western basins was studied from the L-ADCP velocities only because of the low resolution of the West Section. The comparison of the two western basins in Figure 5.9 shows that the thickness of ISOW is larger in the northern basin (deeper than 1400 m) than in the southern basin (deeper than 1700 m), and reached higher density ($\sigma_0 > 27.85$ kg m^{-3}) and higher salinity (> 34.97) in the northern basin. Moreover in each basin, the ISOW salinity of the northern profiles (stations 16 and 18) was higher than the ISOW salinity of the southern profiles (stations 17 and 19), with for instance a salinity of 34.97 at station 16 and 34.95 at station 17 at 2000-m depth.

Based on L-ADCP velocities, Figure 5.9 (c) shows that westward flows of ISOW are localized along the northern walls of each basin, while eastward flows of ISOW are localized along the southern walls, suggesting cyclonic circulations. Moreover, the deep circulation is 0.02 m s^{-1} stronger in the northern basin than in the southern basin.

5.3.4 Circulation of ISOW through the BFZ

The evolution of the averaged θ/S properties of ISOW along the BFZ axis is shown in Figure 5.10. Between the East and Middle Sections 2015, the ISOW salinity and temperature are almost identical (they vary by less than 0.002 in salinity at a given density), which shows a direct link between them, but ISOW is denser by up to 0.02 kg m^{-3} at the East Section than at the Middle Section. This difference in density should be ascribed either to blocking of the deep flow by bathymetry of the BFZ (but this is unlikely because the whole ISOW layer is moving at the East Section), or to diapycnal mixing downstream of the sill. Moreover, the averaged θ/S properties of the East Section 2017 and the Middle Section 2018 are both fresher and colder than those in 2015. Indeed, the East Section 2017 was 0.01 fresher and 0.06°C colder than the East Section 2015 along $27.84\sigma_0$, and the Middle Section 2018 was 0.02 fresher and 0.11°C colder than the Middle Section 2015 along $27.84\sigma_0$. The similar time evolution in ISOW properties at the Middle and East Sections suggests coherent interannual freshening and cooling of ISOW originating from the Iceland Basin.

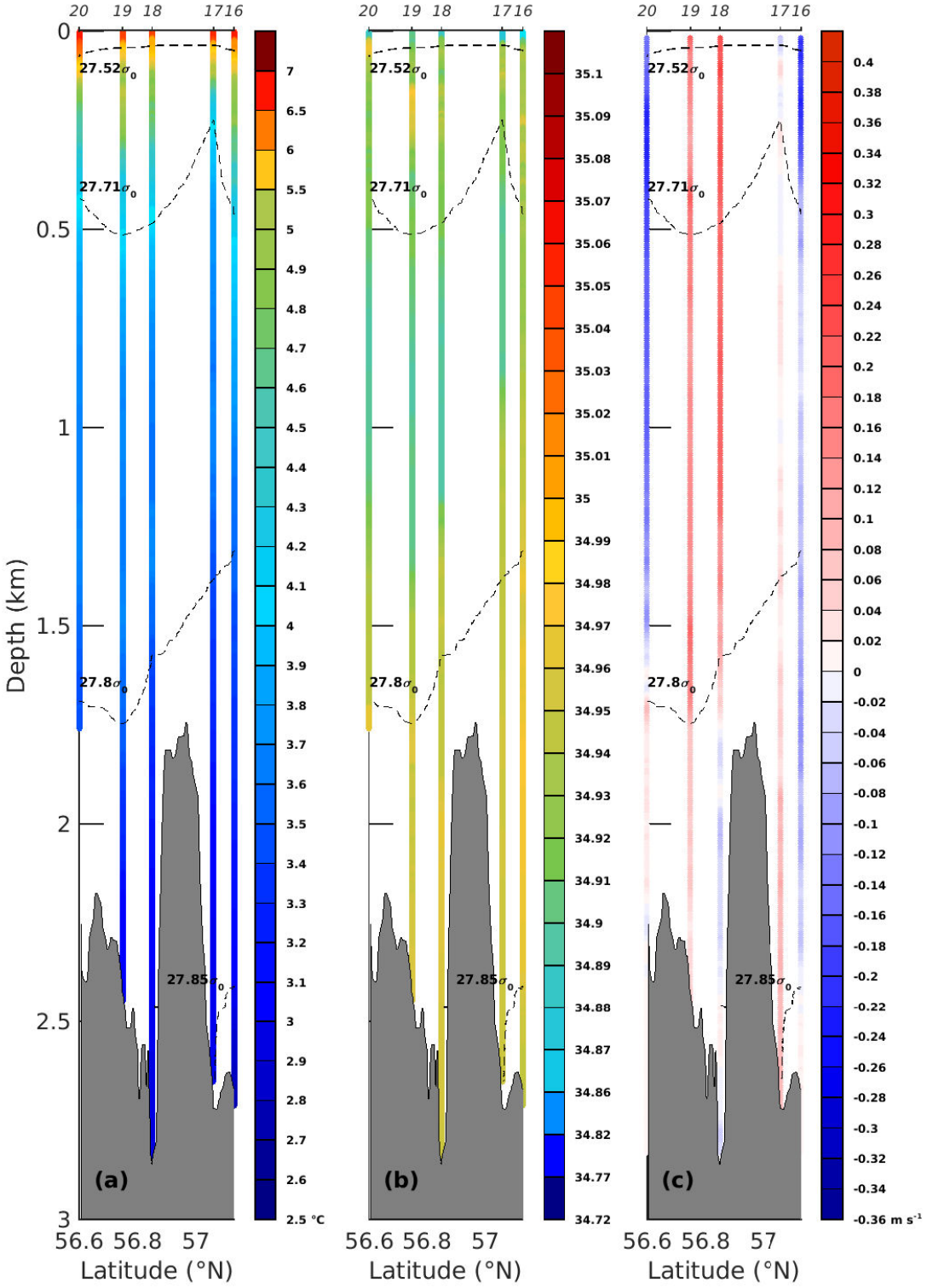

Figure 5.9: (a) Temperature (°C), (b) salinity and (c) L-ADCP (m s^{-1}) profiles along the West Section. Positive values correspond to eastward velocities. The black bold line outlines the 0 isotach. The dashed black lines indicate the potential density σ_0 = 27.52, 27.71, 27.8 and 27.85 kg m^{-3}. Bathymetries from the ship surveys are added in grey. Locations of the hydrographic stations are indicated on the top axis.

By comparing the averaged θ/S properties of the East and Middle Sections 2015 with the θ/S properties of the western basins, Figure 5.10 shows that ISOW in the western basins are fresher and colder than that found upstream. For $\sigma_0 < 27.85$ kg m^{-3}, the northern wall of the northern basin is fresher by about 0.015 and colder by about 0.15°C than at the Middle Section along $27.84\sigma_0$, and the northern wall of the southern basin is fresher by about 0.022 and colder by about 0.2°C than at the Middle Section along $27.84\sigma_0$. The southern walls of the two basins are both 0.03 fresher and 0.25°C colder than at the Middle Section along $27.84\sigma_0$. However for $\sigma_0 > 27.85$ kg m^{-3}, all θ/S profiles of the western basins are identical such that hey are 0.035 fresher and 0.35°C colder than at the East Section along $27.86\sigma_0$. Finally, note that the averaged θ/S profile of the IC at the Ovide Section is identical to those at the southern wall of the western basins, while the averaged θ/S profile of the IC at the South Section is 0.01 saltier along $27.82\sigma_0$.

The westward through-flow of ISOW is thus continuous between the East and Middle Sections but its hydrological properties seem variable over time, with a decrease in salinity of 0.02 between 2015 and 2018. West of the rift valley, the ISOW properties found along the northern walls of the western basins are closer to the upstream ISOW properties than those found along the southern walls ($\sigma_0 < 27.85$ kg m^{-3}), and especially along the northern wall of the northern basin that is 0.02 saltier than the southern walls. This shows that ISOW from the Iceland Basin mixes with fresher and colder ISOW and mainly exits the BFZ by following the northern walls of these basins. The fresh and cold ISOW, found along the southern walls and at high density ($\sigma_0 > 27.85$ kg m^{-3}), cannot be renewed by BFZ through-flow and come from the Irminger Sea, although its exact connections with the IC across the South and Ovide Sections is not clear yet.

5.3.5 Deep-Arvor float trajectories in the BFZ

The Deep-Arvor float trajectories deployed in 2017 and 2018 are shown in Figure 5.11. To study the evolution of the ISOW properties along the float trajectories, Figures 5.12 and 5.13 shows the averaged potential temperature and salinity between $\sigma_0 = 27.805$ and 27.815 kg m^{-3}. This range of density is associated with the maximum of salinity sampled by the floats and thus with the core of ISOW. Indeed, the parking depths of the Deep-Arvor floats were set at the depth of the maximum salinity associated with ISOW (Table 5.1, Figures 5.3 and 5.6).

After being deployed near the eastern sill in 2017, the #6901603 float flowed cyclonically in the rift valley of the Reykjanes Ridge and reached the western sill.

For the #6901603 float, the weak isopycnal property changes highlight the low-level of mixing occurring in the rift valley of the Reykjanes Ridge (Figure 5.12). Localized over a thin range of longitude, the ISOW potential temperature and salinity fluctuate but only decrease of 0.05°C in temperature and 0.007 in salinity between the cycle 1 and cycle 10, the latter cycle being localized at same longitude than the Middle Sections. This low evolution of ISOW properties in 2017 is consistent with the hydrological properties at the East and Middle sections 2015 (Figure 5.10).

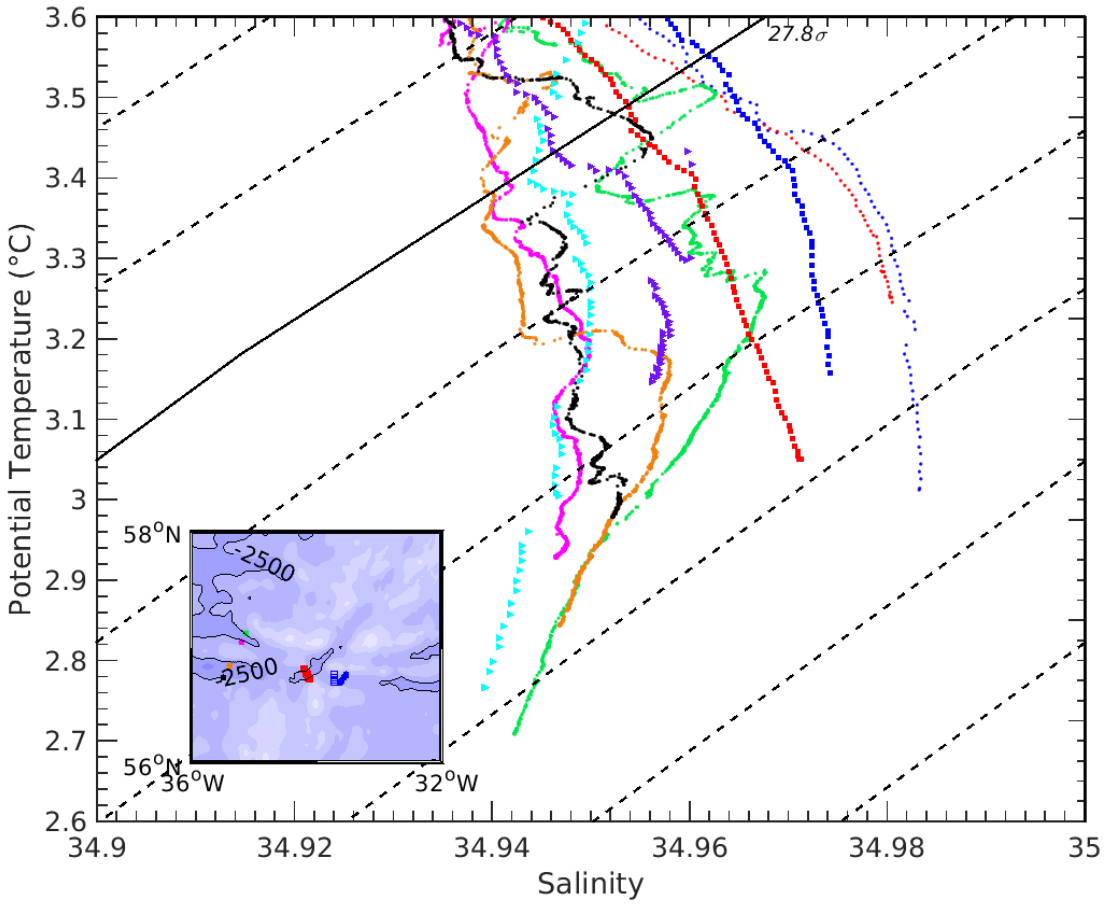

Figure 5.10: Potential temperature θ/S diagram displaying the hydrographic profiles averaged along isopycnals for the East Sections 2015 (blue points) and 2017 (blue squares) and for the Middle Sections 2015 (red points) and 2018 (red squares). The four θ/S profiles of the western basins are also shown with colors that relate to the locations of the $CTDO_2$ stations shown in the inset. The averaged θ/S profiles of the two IC branches at the Ovide Section (cyan triangles) and South Section (purple triangles) showed in chapter 4 are also added. The plain black line shows the isopycnal σ_0 = 27.8 kg m^{-3} and the dashed black lines indicate isopycnals with a step of 0.02 kg m^{-3}. Inserted map: Bathymetry in the BFZ with 500-m isobaths spacing. The deepest bathymetries are represented with the darkest blue. Locations of the $CTDO_2$ stations are indicated with color code.

After being deployed in the rift valley of the Reykjanes Ridge, the #6902881 and #6902882 floats flowed westward over the western sill, between 34.17°W and 35°W, and reached the western basins at the entrance of the Irminger Sea (Figure 5.11). Note the slight southwestward deviation of the #6902882 float trajectory after cycle 2 compare to #6902881, which could be caused by the 4 hours delay in the ascending time between the two floats, revealing a high temporal variability of the dynamics there. West of the western sill, the two floats followed the northern wall of the southern basin, which is consistent with the circulation described in section 5.3.4. At about 35°W (cycle 4), the #6902882 float was apparently blocked and changed direction twice. It first flowed southwestward and reached the southern wall of the southern basin, and then flowed back northward at the center of the basin. Similarly at about 35.5°W (cycle 3), the #6902881 float was apparently blocked and flowed southeastward to reach the southern wall of the southern basin. Then, the #6902881 float flowed westward over the southern wall of the southern basin at shallower depth.

In the western basins, the #6902881 and #6902882 floats show different evolution of the ISOW properties depending on density. The westward evolution of the ISOW temperature and salinity is very weak between $27.8\sigma_0$ and $27.84\sigma_0$ (Figure 5.13), but is stronger between $27.84\sigma_0$ and $27.86\sigma_0$ (Figure 5.14), with a decrease of more than 0.025 in salinity and 0.2°C in temperature for the two floats. Moreover, we note an intensification of the freshening and cooling between 34.4 and 35°N, downstream of the western sill, in coherence with an increasing influence of fresher and colder inflows from the Irminger Sea.

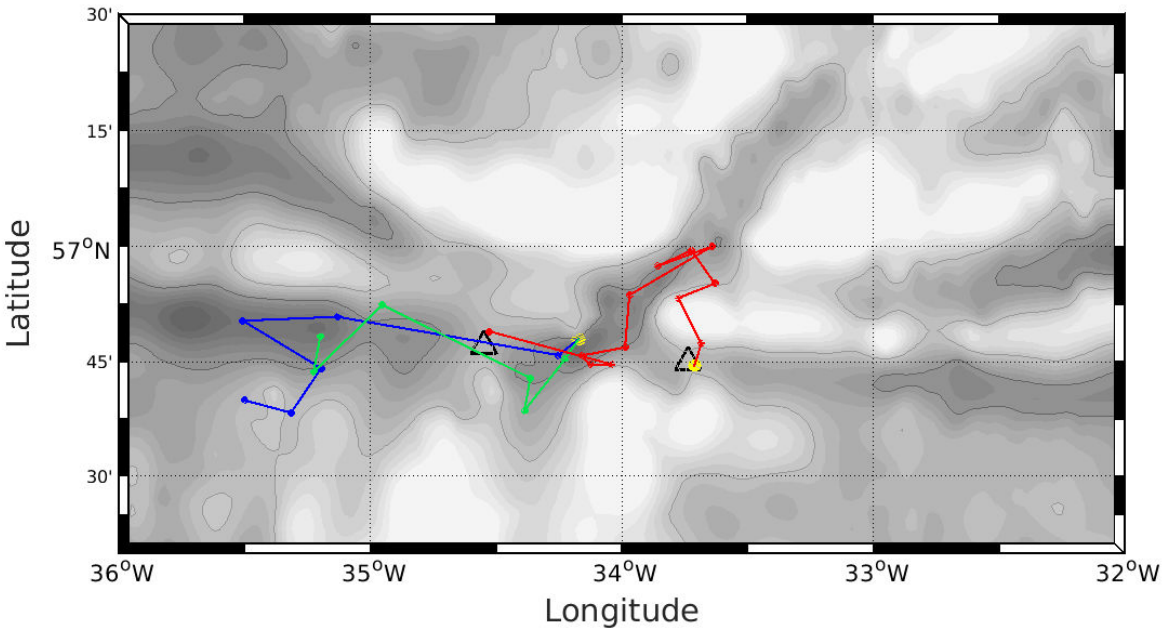

Figure 5.11: Deep Argo float trajectories across the BFZ. The #6901603 float (red) was deployed along the East Section in 2017 (station 89); the #6902881 (blue) and #6902882 (green) floats were deployed along the Middle Section in 2018. Yellow dots indicate the starting position of the floats. Black triangles show the main sills of the BFZ. Bathymetry in the region of the Bight Fracture Zone was obtained by contouring the ETOPO1 data set with 100-m isobaths spacing. The light grey line outlines the 2100-m isobaths. The deepest bathymetries are represented with the darkest grey.

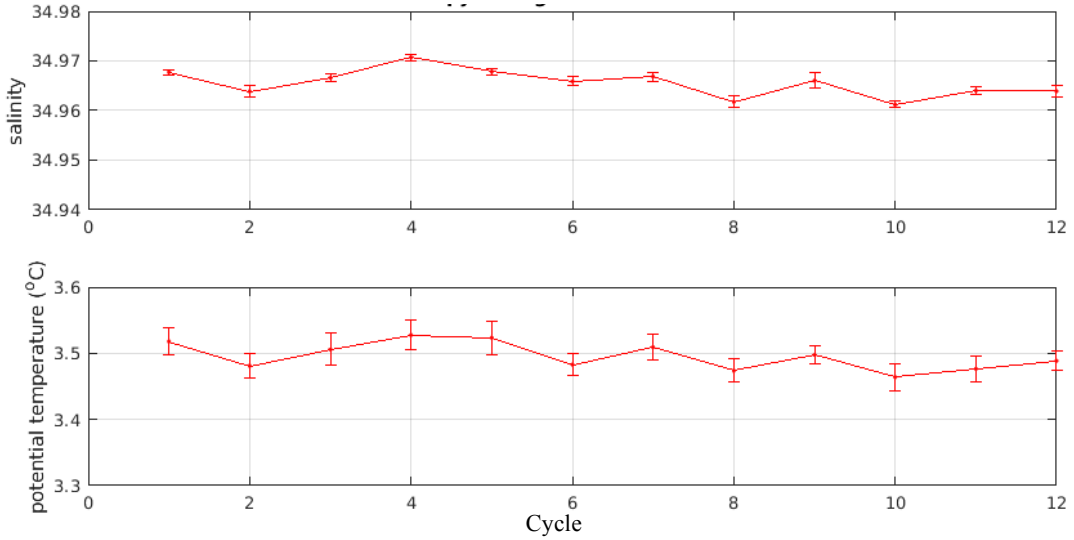

Figure 5.12: Salinity (upper panel) and potential temperature (lower panel) averaged between σ_0 = 27.805 and 27.815 kg m^{-3} for each cycle of the #6901603 Deep-Arvor float.

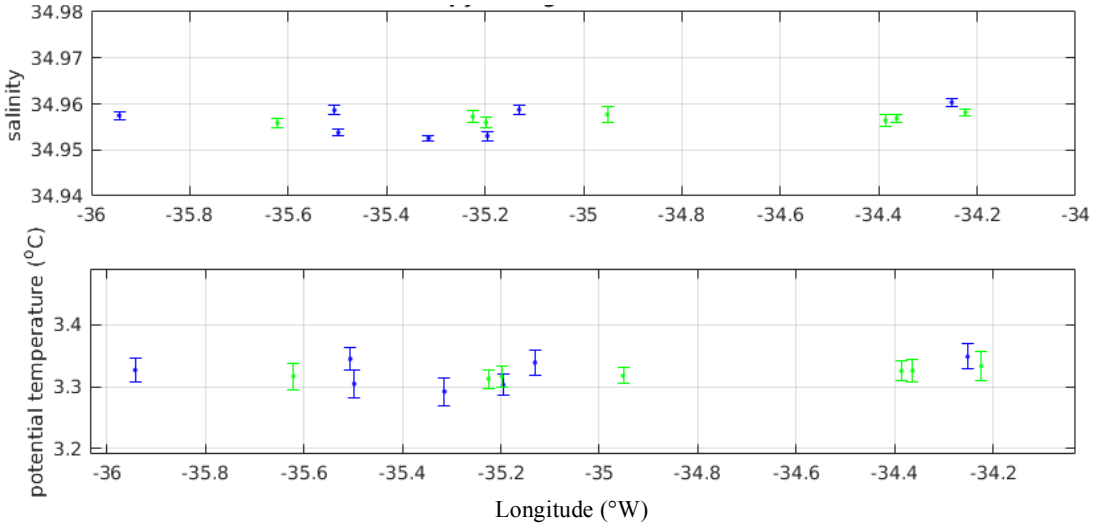

Figure 5.13: Salinity (upper panel) and potential temperature (lower panel) averaged between σ_0 = 27.815 and 27.825 kg m^{-3} along the westward pathway of the #6902881 (blue dots) and #6902882 (green dots) Deep-Arvor floats.

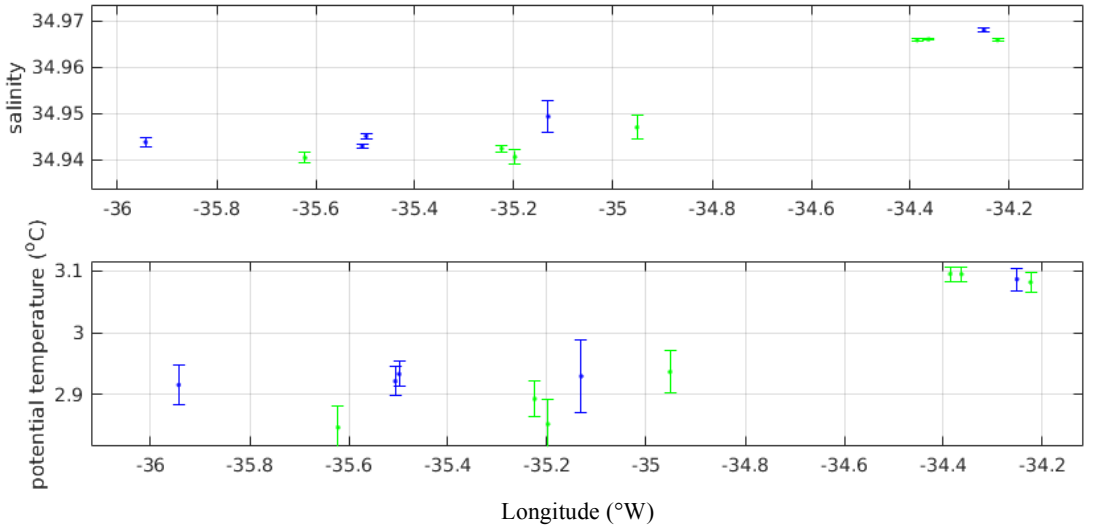

Figure 5.14: Same as in Figure 5.13 with salinity and potential temperature averaged between σ_0 = 27.845 and 27.855 kg m^{-3}

5.4 Discussion

In chapters 3 and 4, we showed that light ISOW from the Iceland Basin preferentially crosses the BFZ to join the Irminger Sea. Based on three hydrographic sections and three Deep-Arvor floats deployed in the BFZ, here we synthetize the hydrological evolution and circulation of the ISOW layer along the BFZ axis. First, we detail the deep circulation in the BFZ schemed in Figure 5.15. Across the East Section, localized at the entrance of the BFZ, ISOW flows westward below 1500 m with homogeneous properties at the eastern sill and in the deep valley north of the sill (Figures 5.2 and 5.4). At the eastern sill, ISOW is first channeled by the narrow and deep bathymetry and then follows the northern wall of the sill (Figure 5.5). By passing westward through the eastern sill, ISOW joins the rift valley of the Reykjanes Ridge. There, the #6901603 float trajectory shows that the deep circulation in the rift valley is cyclonic (Figure 5.11). As shown by the trajectories of floats #6902881 and #6902882, ISOW then crosses the western sill of the BFZ and reaches the western basins. These western basins connect the BFZ to the Irminger Sea. In each basin, an outflow of ISOW preferentially follows the northern walls while an inflow of denser ISOW originating from the Irminger Sea follows the southern walls, in coherence with the deep cyclonic circulation shown by the L-ADCP velocities (Figure 5.9). There, the comparison of the θ/S profiles in Figure 5.10 shows that the eastward inflow of ISOW comes from the Irminger Sea.

By comparing data sets from three different years, we now discuss the time variability of the circulation. At the entrance of the BFZ, almost the entire ISOW transport joined the BFZ through the eastern sill in 2017, while 1/3 of the ISOW transport flows through the valley north of the eastern sill in 2015. Indeed, we found an ISOW transport of -0.66 ± 0.1 Sv at the eastern sill and -0.96 ± 0.1 Sv for the sum of the eastern sill and the valley north of the sill (56.7 – 56.93°N) in 2015. This shows the importance of westward pathways for ISOW north of the eastern sill some years. West of the eastern sill, the ISOW transports in the rift valley of the Reykjanes Ridge were five times weaker in 2018 than in 2015 (Table 5.2) due to an eastward flow along the southern wall of the rift valley that was stronger and wider in 2018 than in 2015 (Figure 5.8).

In term of hydrological properties, there was a decrease in salinity (0.02 along $27.84\sigma_0$) between 2015 and 2017 at the East section and between 2015 and 2018 at the Middle Section (Figure 5.10). This cold and fresh evolution of the ISOW properties could be related to the cold and fresh anomaly of the subpolar gyre showed by Grist et al. (2016) and Zunino et al.

(2017) that started in 2006 and intensified in 2014. This time evolution of the subpolar gyre properties could modify ISOW properties through entrainment south of the Faroe-Bank Channel.

Between the eastern and western sills of the BFZ, the hydrological evolution of the ISOW layer is weak (Figure 5.12), but there is more signal at the exit of the BFZ. Indeed, ISOW found along the northern wall of the southern basin is 0.23°C colder and 0.028 fresher along σ_0 = 27.82 kg m^{-3} than ISOW found in the rift valley (Figure 5.10). The evolution of ISOW properties in Figure 5.10 and along the float trajectories for density higher than 27.84 kg m^{-3} downstream of the western sill (Figures 5.13 and 5.14) reveals inflow of ISOW from the Irminger Sea, which is required to explain that ISOW in the western basins is denser than ISOW at the Middle Section. This ISOW freshening and cooling suggests mixing between the BFZ outflow and inflow. Previous papers highlight the role of the bathymetry and mixing in the evolution of deep waters (De Lavergne et al., 2017). Mercier and Morin (1997) showed that the equatorial densest water masses of the Romanche and Chain fracture zones were strongly modified by vertical mixing. In the Vema Chanel at about 30°S, mixing and entrainments of surrounding waters are other mechanisms responsible for the hydrological evolution of deep waters (Hogg et al., 1982). Mercier and Morin (1997) specified that these mixing are mostly localized downstream of the sills. Here we investigate which of these processes explain the westward evolution of the ISOW properties in the BFZ.

To better illustrate the westward evolution of the ISOW properties in the BFZ, we compare hydrological profiles of each section carried out in 2015 (Figure 5.16). At each section, the profile is associated with the station localized in the main westward core of ISOW. Between the East and Middle Sections, the salinity profiles are identical, but the Middle Section is warmer and less dense than at the East Section below 1800 m. At 2400 m, the Middle Section is 0.4°C warmer and 0.03 less dense than at the East Section. Vertical mixing and entrainment of warmer ISOW at 1500 m is likely to be the primary mechanism explaining the evolution of the ISOW properties between the East and Middle Sections. The mixing only occurs into the ISOW layer and does not include another water mass. The mixing could nevertheless include ISOW from gaps north of the rift valley, which should be of similar properties than at the East Section (dashed arrow in Figure 5.15). Following the water mass balance between the East and Middle Sections 2015, an inflow of ISOW from north of the East Section is consistent with the lower ISOW transport estimated across the East Section (-0.66 ± 0.1 Sv) compared to the Middle Section (-1.25 ± 0.1 Sv). To sum up, the evolution of the ISOW properties in the

BFZ is caused by mixing in the ISOW layer without intrusion of upper water masses, which differ from the mixing of ISOW and LSW observed at the CGFZ by Bower and Furey (2017).

West of the BFZ, we compare the hydrologic profiles in the western basins with the hydrological profiles of the East and Middle Sections (Figure 5.16). Between 1500 and 2400 m, the density profile of the Middle and West Sections are similar, although profiles of the West Section are colder and fresher than those of the Middle Section. Below 2400 m, the profiles of the West Section become denser at a given depth than profiles at the Middle Section. The isopycnal property changes in the western basins, also shown in Figure 5.12, highlight coexistence of ISOW from the Iceland Basin and ISOW from the Irminger Sea, which most likely will mix on isopycnal further downstream due to eddies (Fan et al., 2013; Sy et al., 1997). Below 2400 m, the proportion of ISOW from the Irminger Sea is stronger than above 2400 m. This explains the increase in density at depth between the Middle and West Sections.

To conclude, the westward evolution of the ISOW properties between the Iceland Basin and the Irminger Sea is mainly explained by vertical mixing between the East Section and the rift valley of the Reykjanes Ridge, and between the rift valley and the western basins. In the rift valley, there is no eastward inflow from the Irminger Sea and only ISOW of similar properties mixes, which erodes the denser waters but only slightly change the ISOW properties. On the contrary, downstream of the western sill and in the western basins, dense ISOW comes from the Irminger Sea and most likely mixes with ISOW from the Iceland Basin. To precisely quantify the intensity of the mixing in the BFZ, it might be interesting to compute the vertical mixing coefficient in the rift valley following Mercier et al. (1994), as well as the Thorpe scale of the turbulence in the western basins following Ferron et al. (1998). To complete our analysis, and verify if the mixing mainly occurs downstream of the sills as suggested by Mercier and Morin (1997), it might also be interesting to analysis microstructure data sets located immediately west of the eastern and western sills.

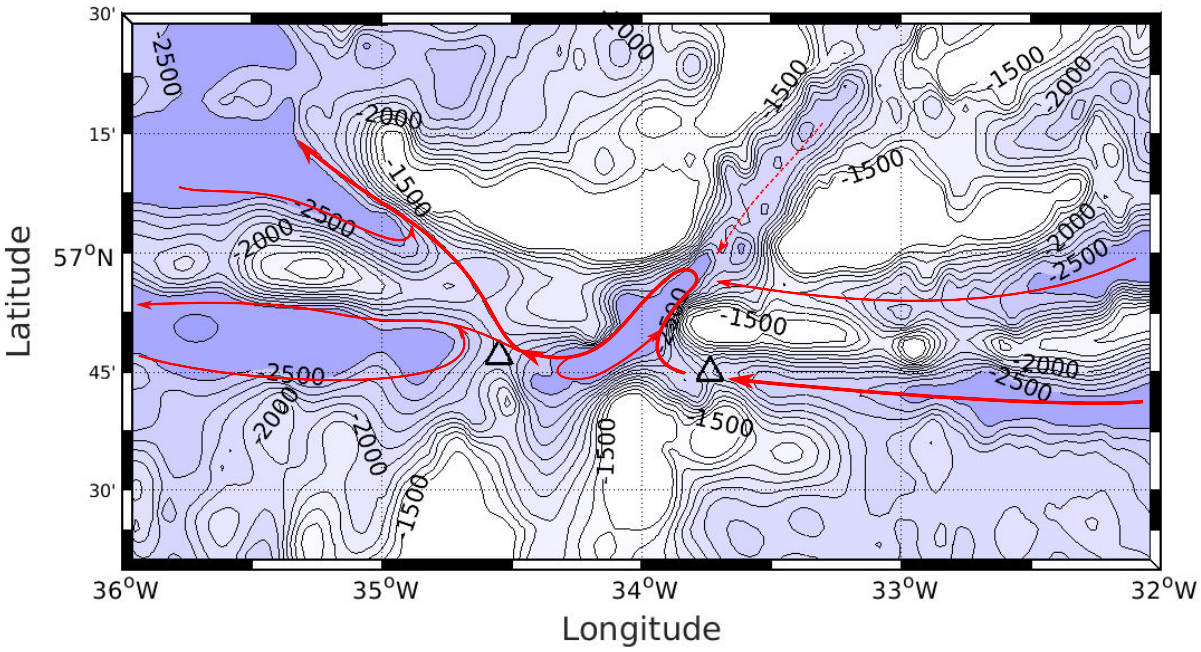

Figure 5.15: Schematic ocean circulation of ISOW in the Bight Fracture Zone. Dashed arrow is uncertain pathway. Black triangles show the main sills of the BFZ.

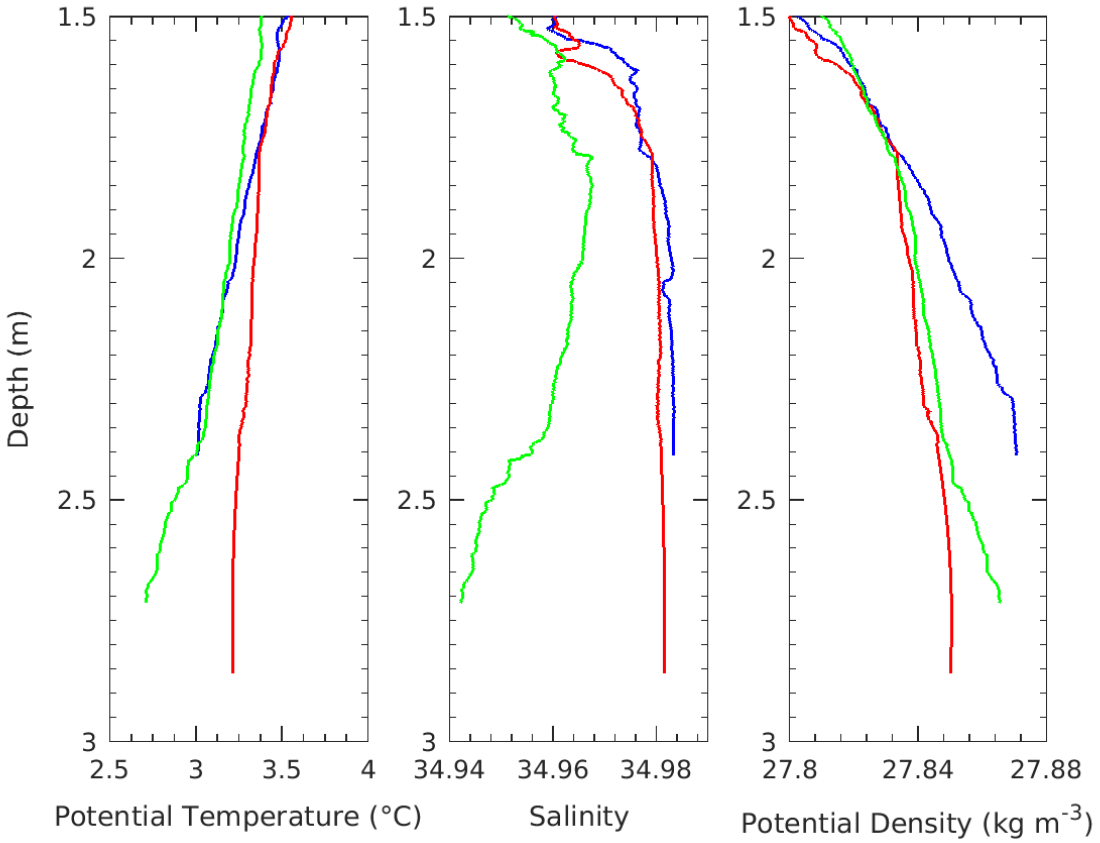

Figure 5.16: Temperature (°C), Salinity and Density (kg m^{-3}) profiles of stations 99 (East Section, blue line), station 103 (Middle Section, red line) and station 16 (West Section, green line) of the RREX2015 cruise.

5.5 Conclusion

From the Iceland Basin to the Irminger Sea, the Iceland-Scotland Overflow Water (ISOW) properties change as ISOW crosses the Reykjanes Ridge. The Bight Fracture Zone (BFZ) was identified to be a major and northernmost pathway of ISOW through the Reykjanes Ridge. The RREX project provided new and insightful data sets to better understand the evolution of the ISOW properties in the BFZ. By analyzing hydrographical sections along the eastern sill of the BFZ and in the rift valley of the Reykjanes Ridge, we first show that vertical mixing in the ISOW layer and entrainment of shallower and warmer ISOW slightly change the ISOW properties exiting the BFZ. Moreover, the Deep-Arvor float deployed in the rift valley highlight a cyclonic circulation of the ISOW layer. By comparing hydrological profiles at the rift valley and at the western basins, we then show that the outflow of ISOW join the Irminger Sea by following the western sill of the rift valley and then the northern walls of each western basin. In the western basins, ISOW from the Iceland Basin encounters dense ISOW from the Irminger Sea, which is fresher and colder than the westward through-flow. Between the rift valley and the western basins, the two Deep-Arvor floats also outline the strong signal of fresh and cold ISOW at high densities. Finally, we note an overall freshening and cooling of the ISOW layer between 2015 and 2017.

6 Conclusions and perspectives

The Reykjanes Ridge is a major topographic feature of the northern North-Atlantic Ocean. Composed of troughs, fracture zones and seamounts, the Reykjanes Ridge extends northeast / southwest from Iceland at about 300-m depth to the Charlie Gibbs Fracture Zone (CGFZ) at about 3000-m depth. Localized between the Iceland Basin and the Irminger Sea, the Reykjanes Ridge affects the large-scale ocean circulation by constraining the westward branch of the North-Atlantic Subpolar Gyre (NASPG) that flow anticyclonically around the ridge. In the Iceland Basin, the westward branch of the NASPG is composed of warm and salty surface waters from the equator, as part of the North-Atlantic Current (NAC), and cold and fresh overflow waters from the Nordic Seas. As part of the Meridional Overturning Circulation, about 50% of light-to-dense conversion of the NASPG occurs in the vicinity of the Reykjanes Ridge (Desbruyères et al., 2013). Indeed, the hydrological properties of the westward branch of the NASPG strongly differ from the eastern side to the western side of the Reykjanes Ridge (Daniault et al., 2016). This suggests strong interaction between flow and bathymetry, which cause the evolution of water masses as they pass over the ridge. However, direct measurements near the Reykjanes Ridge were up to now lacking to fully characterize and understand the 3-D structure and properties of the flows along and across the ridge, and to investigate how they are affected by the bathymetry.

The RREX project provides new data sets in the vicinity of the Reykjanes Ridge to deeply investigate the subpolar gyre circulation there. These data sets combine hydrological sections carried out in June – July 2015 and 2017, but also moorings, microstructure measurements and Deep-Arvor floats deployed in the BFZ and CGFZ. In this PhD thesis, we mainly used the hydrological sections carried out in 2015 to describe the 3-D along and cross-ridge circulation and the associated water mass distribution during summer 2015. For the first time,

the westward branch of the subpolar gyre and the evolution of its water mass properties over and around the ridge were thus directly quantified. Additional data sets collected in the Bight Fracture Zone (BFZ) in 2016, 2017 and 2018 were also analyzed to investigate the circulation and evolution of the overflow properties within the BFZ. Indeed, the BFZ is a major pathway for the overflow water masses and its bathymetry is susceptible to influence the evolution of the overflow properties at smaller-scale.

6.1 Estimation of geostrophic transports

Results of this PhD thesis rely on geostrophic transports estimated for each hydrographic sections carried out along and perpendicular to the Reykjanes Ridge axis during the RREX2015 cruise. As indicated by Petit et al. (2018a), the geostrophic transports were estimated from the geostrophic velocities by using the thermal wind equation between each hydrographic station. The geostrophic velocities were constrained in a selected depth range by S-ADCP data acquired along the ship track. During these computations, one main difficulty was to remove biases in the S-ADCP velocities. We resolved this difficulty by deeply investigating each step of the S-ADCP processing with the software Cascade, and by comparing the OS38 with the OS150 velocities. This first work led to major improvements in the S-ADCP data processing. We improved the quality of the S-ADCP velocities by using new statistical test parameters in the detection of the outliers. These new statistical tests were implemented in the last version of the software Cascade (Version 7.2), and the S-ADCP data acquired during the RREX2017 were successfully processed following this method of treatment.

Beyond the treatment of S-ADCP velocities themselves, another difficulty came from the selection of the depth and thickness of the absolute reference layer, because of its large impact on the final geostrophic transports. Comparisons of S-ADCP and geostrophic profiles at each pair of hydrographic station revealed that the ageostrophic motions are weaker at 600 – 1000-m depth than above and that this layer is adequate for referencing the geostrophic profiles.

Finally, a specific method was required to compute accurate geostrophic transports over the sloping and rough bathymetry of the Reykjanes Ridge. By comparing different methods of extrapolation at depth, we showed that a second-order polynomial fit minimizes the impact of

non-linear variability in the bottom triangles and that it was the best solution in regions with large number of seamounts. This step was particularly important for estimating the geostrophic transport of the deep and overflow water masses across the fracture zones of the Reykjanes Ridge.

6.2 Intensity and structure of the subpolar gyre across the Reykjanes Ridge

In chapter 3 of this PhD thesis, we derived the first direct estimates of volume and water mass transports across the Reykjanes Ridge. By analyzing velocity and hydrography measurement carried out along the crest of the Reykjanes Ridge in June – July 2015, we investigated the intensity and structure of the westward cross-ridge flow. Along the Reykjanes Ridge, the westward branch of the NASPG extended from Iceland to 53.15°N with a top-to-bottom integrated transport of 21.9 ± 2.5 Sv. This cross-ridge circulation was intensified at 57°N near the BFZ and at 59 – 62°N, with associated transports of -8.0 ± 0.5 and -13.6 ± 0.8 Sv, respectively. Although the existence of the westward pathway above the BFZ was already known (Bower & von Appen, 2008), the presence of a second pathway further north was subject to controversy and was precisely quantified in this study.

The aforementioned description and quantification of the cross-ridge flow was estimated from one synoptic data set and should now be combined with other estimations of the cross-ridge flow in order to assess its temporal variability. Figure 6.1 compares the top-to-bottom integrated transports across the Ridge Section in 2015 (chapter 3) and in 2017. The geostrophic transports estimated from the RREX2017 cruise were preliminary computed following the same method than in 2015 (chapter 2). We note that the distributions of the westward branch of the NASPG were similar in regions 3 and 4, but were strongly different in region 2. Indeed in 2017, the flow was not only intensified at the BFZ and at 59 – 61°N, but was also intensified between 52.7°N and 56.1°N, which encompasses non-named gaps between the BFZ and CGFZ as well as the northern valley of the CGFZ. In region 2, the net top-to-bottom transport was of 0 ± 1.4 Sv in 2015 while it was of -20 Sv in 2017. Thus, this result supports the hypothesis that the two pathways at the BFZ and 59 – 61°N are permanent features associated with the bathymetry, while the cross-ridge transport in region 2 is highly variable in time. With this result arise new questions. What mechanisms modulate the variability of these cross-ridge flows? Indeed, the small difference between the 2015 and 2017

transports at the BFZ could only be related to mesoscale features, but the stronger difference between the 2015 and 2017 transports in region 2 should also be related to variability in the large-scale circulation. For instance, is the temporal variability of the cross-ridge transport in region 2 correlated to the temporal variability of the NAC that crosses eastward the Mid-Atlantic Ridge at the CGFZ and south?

For this latter question, it could be interesting to investigate the position of the NAC during the RREX2017 cruise. Indeed, we showed in chapter 3 that the northern branch of the NAC and the Sub-Artic Front crossed the Mid-Atlantic Ridge eastward in a northern position with a transport of 17.4 ± 1.7 and 22.8 ± 1.1 Sv, respectively in June – July 2015. In Figure 6.1, we show that the northern branch of the NAC in 2017 was localized at 51 – 52.3°N with an associated transport of 23 Sv. The location and intensity of the northern branch of the NAC were thus similar in 2017 and 2015, which suggests no correlation between the intensity of the cross-ridge flow in region 2 and of the northern branch of the NAC. Nevertheless, it could be interesting to study the evolution of the NAC and cross-ridge flow from a longer time series based on Aviso altimetry maps. These maps could allow us to analyze the time variability of the cross-ridge flow in region 2, and to link it to the location and intensity of the NAC branches, as well as to the formation of mesoscale structures or to the large-scale circulation of the NASPG. To complete the study, the same analysis could be done with model outputs or oceanic reanalysis such as Mercator. Indeed, it could be interesting to study this correlation from numerical models, as recently done by Xu et al. (2018) who showed the correlation between the transport of ISOW in the CGFZ and the position of the NAC.

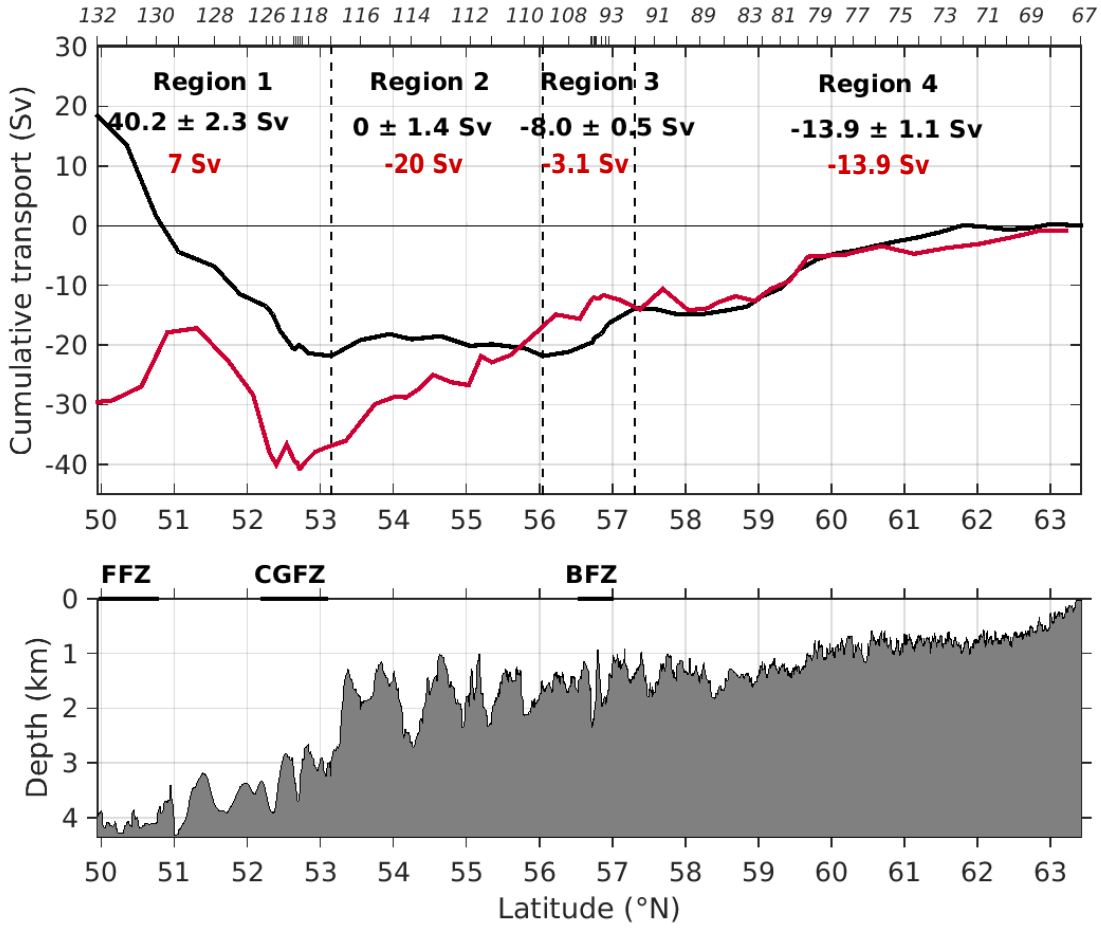

Figure 6.1: Upper panel: Top-to-bottom vertically integrated transport (Sv) along the Ridge Section 2015 (black line) and 2017 (red line) cumulated from Iceland to 50°N. Increasing (decreasing) cumulative transport corresponds to eastward (westward) transport. The dashed lines divide the section into four regions. The locations of the hydrographic stations 2015 are shown on the top axis. Lower panel: Bathymetry along the Ridge Section. CGFZ stands for Charlie Gibbs Fracture Zone, BFZ for Bight Fracture Zone, and FFZ for Faraday Fracture Zone.

6.3 Link between distribution of the cross-ridge flow and large-scale circulation of the subpolar gyre

In chapter 3 of this PhD thesis, we provide the first direct view of the water mass distribution along the Reykjanes Ridge. The three main contributors to the westward branch of the NASPG were SPMW (29.7%), ISW (22.3%), and IW (21.9%), while only 9.1% of ISOW and 5.9% of LSW composed the cross-ridge flow. Among the main water masses, we showed that SPMW was denser at and south of the BFZ (σ_0 = 27.61 kg m^{-3}) than at 59 – 62°N (σ_0 = 27.56 kg m^{-3}). The difference of SPMW density is linked to the cyclonic circulation in the Iceland Basin. Indeed, we note in chapter 3 that the northern branch of the NAC contained a larger

proportion of subpolar water than the Sub-Arctic Front, which is consistent with de Boisséson et al. (2010). In the Iceland Basin, we thus suggest that the Sub-Arctic Front connects to the lighter SPMW found at 59 – 62°N, while the northern branch of the NAC connects to the denser SPMW found at the BFZ. Chapter 4 of this PhD thesis made the link with the cyclonic circulation in the Iceland Basin. We showed that upper and intermediate water masses continuously joined the ERRC from the Iceland Basin and were detrained westward toward the Irminger Sea as soon as they were no longer blocked by the bathymetry. For instance, we showed that ISW crossed the Reykjanes Ridge mainly between 59 and 60°N because of the deepening of the bathymetry at these latitudes. In addition, water mass densifications in the Iceland Basin lead to the formation of weakly stratified SPMW, and then favor the downstream overturning observed in the Irminger Sea and Labrador Sea. Thus, we showed in this PhD thesis that the distribution of the water masses upstream of the convection areas are not only constrained by the bathymetry of the Reykjanes Ridge, but also strongly depends on the vertical mixing and horizontal circulation in the Iceland Basin.

It remains to investigate the impact of the temporal variability of the water mass properties on their circulation around and across the Reykjanes Ridge. Indeed, Grist et al. (2016) and Zunino et al. (2017) documented a cooling and freshening of the subpolar gyre since 2006 with an exceptional acceleration in 2014. What is the impact of this cooling and freshening on the large-scale circulation near the Reykjanes Ridge? A densification of the water masses in the Iceland Basin could modify the intensity and distribution of the associated cross-ridge flow. Modification of the pathways across the ridge as those reported in Figure 6.1, with stronger flow between the BFZ and the CGFZ, could affect the water masses arriving in the Irminger Sea and Labrador Sea. To answer this question, it could be interesting to document the interannual variability of the water mass properties and distributions in region 2, where we observed high interannual variability. Moorings in the deepest gaps of the region 2, for instance near 54.2°N, would be also helpful to quantify the variability of the cross-ridge flow in region 2.

6.4 Circulation and evolution of Iceland-Scotland Overflow Water across the Reykjanes Ridge

In chapters 3, 4 and 5 of this PhD thesis, we investigated the ISOW circulation from the Iceland Basin to the Irminger Sea. For the first time, we described the evolution of its structure and hydrological properties along the eastern side of the ridge as part of the East Reykjanes Ridge Current (ERRC), across the ridge, with a particular focus on the BFZ, and along the western side of the ridge as part of the Irminger Current (IC). In the ERRC, chapter 4 showed that the southward transport of ISOW was composed of several veins directly connected to the westward cross-ridge flow of ISOW shown in chapter 3. The lightest variety of ISOW crossed the ridge at the BFZ while the densest variety of ISOW crossed the ridge through deeper gaps further south. Quantified along the Ridge Section, ISOW crossed the ridge in the BFZ region with an associated transport of -0.8 ± 0.8 Sv and in the CGFZ region with an associated transport of -1.1 ± 0.7 Sv. In the CGFZ, the weak westward transport of ISOW was due to the position of the northern branch of the NAC during the RREX2015 cruise.

Through the BFZ, the circulation and evolution of the ISOW properties were poorly documented, although publications showed the importance of bathymetry in the evolution of deep through-flow properties. In chapter 5 of this PhD thesis, we provided the first description of the circulation and hydrological evolution of the ISOW layer through the BFZ. From the Iceland Basin, ISOW crosses the deepest sills of the BFZ to join the rift valley of the Reykjanes Ridge. There, mixing in the ISOW layer slightly changes its properties along the cyclonic circulation observed in the rift valley. West of the rift valley, ISOW exits the BFZ through a deep western sill and joins the Irminger Sea by following the northern walls of two deep western basins, which are localized at the entrance of the Irminger Sea. Downstream of the western sill and in the western basins, the westward ISOW meets an eastward input of dense, fresh and cold ISOW from the Irminger Sea.

Related perspectives arise from this aforementioned description of the circulation and ISOW properties in the BFZ. Firstly, it could be interesting to quantify the mixing of ISOW in the rift valley of the Reykjanes Ridge and in the western basins. To do so, it might be interesting to quantify the turbulence by computing the Thorpe scale following Ferron et al. (1998), or to study microstructure data set carried out in the BFZ during the RREX2015 and RREX2017 cruises. Moreover, we showed that inflows from the Irminger Sea play a fundamental role in

the modification of the ISOW properties. However, this inflow was not directly connected to the Irminger Current from the south. To localize the origin of this inflow, it could be interesting to carry out small-scale hydrographic sections at the exit of the BFZ, and to use eddy-resolving models in which we follow Lagrangian particles connecting the center of the Irminger Sea and the BFZ.

6.5 Formation, connection and evolution of the East Reykjanes Ridge Current

Repeatedly observed at surface and sub-surface, the top-to-bottom structure of the East Reykjanes Ridge Current (ERRC) was never documented along the eastern side of the Reykjanes Ridge, except along the Ovide transect as shown by Daniault et al. (2016). In chapter 4 of this PhD thesis, we provided the first description of its formation and southward evolution along the ridge, and showed the impact of the bathymetry for its connections with the Irminger Current on the western side of the Reykjanes Ridge. For the first time, we showed that the characteristics of the ERRC observed along the Ovide transect are not found north and south of this latitude. Intensified at depth at northern latitudes, the southward current is composed of different layers either blocked by the bathymetry of the Reykjanes Ridge or able to cross the ridge as part of the westward cross-ridge flow depending on their densities. The deep layers blocked by the bathymetry are joined by westward inflows of NAC waters at surface and continue southward along the Reykjanes Ridge. This convergence of waters locally form the top-to-bottom barotropic ERRC documented along the Ovide transect by Daniault et al. (2016). This major result of the PhD thesis has an important impact in our understanding of the circulation in the Iceland Basin, because it shows for the first time that the ERRC is not a continuous top-to-bottom along-ridge current but a superposition of southward flows in different layers that are controlled by the Reykjanes Ridge. In the layers, water masses are entrained from the Iceland Basin and detrained toward the Irminger Sea depending on their densities.

The aforementioned description of the ERRC shows that the structure of the southward current strongly depends on the proportion and location of inflows from the Iceland Basin. However, the NAC is documented to be strongly turbulent in the Iceland Basin, such that its connections with the ERRC should be strongly variable over time. How this variation impacts

the circulation of the ERRC along the ridge, and subsequently the cross-ridge flow? Altimetric maps could firstly show the variation at surface, and eddy-permitting numerical models could provide a top-to-bottom analysis of this connection.

6.6 Connections between Irminger Current and cross-ridge flow

In chapter 4 of this PhD thesis, we describe for the first time the connections between the westward cross-ridge flow and the northward Irminger Current (IC). Following the same entrainment and detrainment processes than the ERRC, on the other side of the Reykjanes Ridge, the IC is composed of northwestward flows in different layers that consecutively feed the IC from the Iceland Basin and join the Irminger Gyre. Controlled by the bathymetry of the Reykjanes Ridge, the connection between the IC and the cross-ridge flows occurs at different latitudes depending on their densities. In addition to this connection, the IC incorporates waters of the Irminger Gyre and of the NAC from the Irminger Sea south of the Ovide latitudes. These latter inflows preferentially join the western branch of the IC, while the eastern branch is more influenced by the westward cross-ridge flow. One major result of this PhD thesis was thus to show that the two IC branches are differently influenced by inflows from the Iceland Basin and from the Irminger Sea, and thus that their circulation is not always connected and continuous along the Reykjanes Ridge.

These results give rise to new perspectives. Firstly, our data sets did not give us access to the diapycnal exchange between the layers that connect the ERRC with the IC. The light-to-dense conversions enhanced by these entrainments along the Reykjanes Ridge are thus not explained and should be investigated because it preconditioned the densification of the downstream convection areas. Moreover, we did not explain the mechanisms responsible for the intrusion of waters from the Irminger Gyre. Based on previous papers, we argue that they are related to eddy or meander formed between the two northward currents. However, it is fundamental to better understand how these eddies are formed, and more generally, what control their interactions and processes of mixing, because it directly impacts the deep convection of the Irminger Sea, and downstream, of the Labrador Sea. To provide elements of explanation, altimetry and models could be simultaneously used.

To conclude, thanks to the RREX project, this PhD thesis provides the first direct description and quantification of the 3-D circulation of the subpolar gyre around, above and across the Reykjanes Ridge. It reveals the importance of local processes such as eddies and mixing in water mass transformation as well as local features in the bathymetry that constrain the cross-ridge flow. First analysis of the 2017 data set also points to the possible influence of the large-scale circulation pattern on the structure of the cross-ridge flow. Further investigations of the dynamical processes involved in setting the circulation and hydrographic properties near the Reykjanes Ridge are thus necessary. Such investigations are ongoing works conducted as part of the RREX project and are based on the analysis of the RREX data set (hydrography, mixing, moorings data), realistic high-resolution and idealized simulations. Finally, results of this PhD thesis are invaluable for the validation of general circulation models because these results will help to understand the origin of bias generally observed in those models.

A Sequence of operations during the RREX2015 cruise

Num Station	Date	Heure	Latitude	Longitude	Section	Commentaires
0	08/06/2015	15:48:55	52,104	-18,411		Station test Deep Arvor
1	10/06/2015	01:34:21	54,261	-27,456		Centre bassin d'Islande
2	10/06/2015	18:28:56	55,156	-31,336	Sud	
3	10/06/2015	22:19:19	55,310	-31,671	Sud	
4	11/06/2015	01:53:06	55,468	-32,008	Sud	
5	11/06/2015	06:06:28	55,622	-32,344	Sud	VMP
6	11/06/2015	10:12:27	55,777	-32,677	Sud	VMP
7	11/06/2015	15:06:55	55,997	-33,215	Sud	VMP
8	11/06/2015	19:24:05	56,245	-33,685	Sud	
9	11/06/2015	22:36:06	56,400	-34,019	Sud	Idem station 108
10	12/06/2015	02:43:30	56,733	-33,717		Mouillage BFZ-S VMP
11	12/06/2015	08:58:49	56,940	-33,853		Mouillage BFZ-N

						VMP
12	12/06/2015	14:37:14	56,725	-33,759	Sud	VMP
13	12/06/2015	17:53:51	56,760	-33,922	Sud	VMP
14	12/06/2015	23:22:45	56,449	-34,421	Sud	
15	13/06/2015	02:57:39	56,523	-34,999	Sud	
16	13/06/2015	08:02:21	57,131	-35,121	BFZ aval 1	VMP
17	13/06/2015	11:40:16	57,059	-35,182	BFZ aval 1	VMP
18	13/06/2015	15:30:59	56,850	-35,370	BFZ aval 1	VMP
19	13/06/2015	19:25:39	56,749	-35,468	BFZ aval 1	VMP
20	13/06/2015	22:52:49	56,599	-35,629	BFZ aval 1 Sud	PROVOR-DO
21	14/06/2015	06:12:09	56,639	-36,229	Sud	VMP
22	14/06/2015	10:26:27	56,687	-36,829	Sud	VMP
23	14/06/2015	14:53:37	56,727	-37,532	Sud	VMP ARVOR-2DO
24	14/06/2015	19:44:13	56,770	-38,187	Sud	
25	15/06/2015	13:20:35	59,362	-36,399	Ovide	SVP
26	15/06/2015	18:01:21	59,299	-35,763	Ovide	
26	15/06/2015	20:25:16	59,299	-35,760	Ovide	VMP
27	15/06/2015	22:48:45	59,232	-35,116	Ovide	Pb contacteur de fond Pas de bouteille
Pas de CTD	16/06/2015	09:25 :00	59.091	-33,259		Mouillage IRW
28	16/06/2015	14:16:46	59,164	-34,491	Ovide	
29	16/06/2015	18:15:07	59,102	-33,832	Ovide	SVP

30	16/06/2015	21:49:11	59,039	-33,189	Ovide	
30	16/06/2015	21:49:18	59,038	-33,189	Ovide	
31	17/06/2015	01:42:05	58,972	-32,548	Ovide	
32	17/06/2015	05:21:05	58,910	-31,911	Ovide	PROVOR-DO
33	17/06/2015	08:59:22	58,845	-31,269	Ovide	Idem Station 83
34	17/06/2015	12:11:24	58,727	-30,694	Ovide	
35	17/06/2015	14:58:26	58,550	-30,365	Ovide	
36	17/06/2015	18:57:39	58,410	-30,101	Ovide	
37	17/06/2015	22:19:22	58,208	-29,722	Ovide	
38	18/06/2015	01:59:34	57,970	-29,274	Ovide	PROVOR-DO
39	18/06/2015	05:12:47	58,092	-29,394		Mouillage ICM
40	18/06/2015	13:42:45	57,586	-28,448		Mouillage ICE PROVOR-DO VMP
41	18/06/2015	19:27:42	57,675	-28,726	Ovide	
42	18/06/2015	23:43:45	57,379	-28,172	Ovide	
43	19/06/2015	03:46:32	57,150	-27,749	Ovide	
44	19/06/2015	08:03:26	56,930	-27,335	Ovide	
45	20/06/2015	08:52:23	60,300	-20,997	Nord	VMP
46	20/06/2015	13:17:57	60,570	-21,359	Nord	VMP
47	20/06/2015	17:29:26	60,840	-21,720	Nord	VMP PROVOR-DO
48	20/06/2015	21:29:38	61,110	-22,080	Nord	VMP
49	21/06/2015	01:47:49	61,380	-22,438	Nord	VMP
50	21/06/2015	05:43:38	61,650	-22,801	Nord	VMP

51	21/06/2015	09:32:18	61,919	-23,160	Nord	VMP
52	21/06/2015	13:15:27	62,189	-23,521	Nord	VMP
53	21/06/2015	16:43:13	62,460	-23,878	Nord	VMP
54	21/06/2015	20:18:40	62,730	-24,241	Nord	VMP
55	21/06/2015	23:16:08	63,000	-24,750	Nord	Idem station 68
56	22/06/2015	01:32:45	62,998	-25,363	Nord	VMP
57	22/06/2015	04:45:36	63,000	-26,127	Nord	VMP
58	22/06/2015	08:16:40	63,001	-26,892	Nord	VMP
59	22/06/2015	11:47:57	63,000	-27,656	Nord	VMP
60	22/06/2015	15:27:09	63,000	-28,419	Nord	VMP
61	22/06/2015	19:32:30	63,000	-29,182	Nord	VMP
62	22/06/2015	23:20:36	63,000	-29,946	Nord	VMP
63	23/06/2015	03:15:59	63,000	-30,709	Nord	VMP SVP
64	23/06/2015	07:22:40	63,000	-31,473	Nord	VMP
65	23/06/2015	11:34:55	63,000	-32,237	Nord	VMP
66	23/06/2015	15:54:44	63,001	-33,000	Nord	VMP SVP
67	24/06/2015	17:15:53	63,417	-23,917	Axe	Sud islande
68	24/06/2015	22:34:46	63,000	-24,752	Axe	Idem station 55
68	24/06/2015	22:34:51	63,000	-24,752	Axe	
69	25/06/2015	01:04:19	62,699	-25,237	Axe	
70	25/06/2015	03:50:50	62,401	-25,721	Axe	
71	25/06/2015	06:46:10	62,099	-26,205	Axe	
72	25/06/2015	09:39:44	61,800	-26,691	Axe	

73	25/06/2015	12:47:58	61,500	-27,176	Axe	
74	25/06/2015	15:34:53	61,200	-27,659	Axe	
75	26/06/2015	12:02:17	60,903	-28,119	Axe	
76	26/06/2015	14:51:47	60,600	-28,579	Axe	
77	26/06/2015	17:54:57	60,300	-29,037	Axe	SVP
78	26/06/2015	20:39:58	60,050	-29,422	Axe	
79	26/06/2015	23:27:37	59,800	-29,805	Axe	
80	27/06/2015	02:18:20	59,550	-30,187	Axe	
81	27/06/2015	05:21:05	59,301	-30,570	Axe	
82	27/06/2015	08:31:32	59,050	-30,953	Axe	VMP
83	27/06/2015	11:33:47	58,844	-31,268	Axe	Idem station 33
84	27/06/2015	17:08:35	58,429	-30,025		Mouillage ICW VMP
Pas de CTD	27/06/2015	23 :21 :00	58,547	-30,183		ASFAR1
85	28/06/2015	06:40:28	58,982	-32,160		Mouillage IRM VMP
Pas de CTD	28/06/2015	10 :18 :00	58,970	-32,097		ASFAR2
86	28/06/2015	13:21:38	58,924	-31,561		Mouillage IRE VMP
87	28/06/2015	22:09:52	58,772	-30,676		Mouillage RRT VMP
87	28/06/2015	22:10:03	58,772	-30,676	Axe	
88	29/06/2015	03:20:57	58,530	-31,421	Axe	
89	29/06/2015	06:57:03	58,199	-31,751	Axe	

90	29/06/2015	10:29:50	57,880	-32,119	Axe	VMP
91	29/06/2015	14:02:47	57,580	-32,477	Axe	VMP
92	29/06/2015	17:51:20	57,310	-32,821	Axe	VMP
93	29/06/2015	21:46:35	56,950	-33,303	Axe	BFZ nord
94	29/06/2015	23:52:07	56,910	-33,354	Axe	BFZ nord VMP
95	30/06/2015	02:15:34	56,850	-33,433	Axe	BFZ nord
96	30/06/2015	04:14:32	56,780	-33,524	Axe	BFZ sud
97	30/06/2015	05:51:26	56,768	-33,539	Axe	BFZ sud
98	30/06/2015	08:36:37	56,753	-33,559	Axe	BFZ sud VMP
99	30/06/2015	11:01:54	56,725	-33,594	Axe	BFZ sud
100	30/06/2015	13:33:58	56,710	-33,616	Axe	BFZ sud
101	30/06/2015	16:10:35	56,702	-33,627	Axe	BFZ sud
102	30/06/2015	20:02:24	56,825	-34,194	BFZ aval 2	
103	30/06/2015	21:46:58	56,799	-34,169	BFZ aval 2	
104	30/06/2015	23:52:25	56,783	-34,154	BFZ aval 2	VMP
105	01/07/2015	03:10:12	56,773	-34,145	BFZ aval 2	
106	01/07/2015	05:13:43	56,749	-34,123	BFZ aval 2	
107	01/07/2015	06:59:50	56,735	-34,110	BFZ aval 2	
108	01/07/2015	11:48:11	56,400	-34,021	Axe	VMP Idem station 9
109	01/07/2015	15:43:57	56,050	-34,286	Axe	SVP
110	01/07/2015	18:53:47	55,800	-34,474	Axe	VMP
111	01/07/2015	23:38:45	55,350	-34,814	Axe	VMP

112	02/07/2015	03:57:50	55,050	-35,001	Axe	VMP
113	02/07/2015	08:04:09	54,649	-35,080	Axe	
114	02/07/2015	11:11:46	54,249	-35,080	Axe	
115	02/07/2015	14:48:31	53,949	-35,080	Axe	
116	02/07/2015	19:03:49	53,549	-35,079	Axe	VMP
117	02/07/2015	23:04:11	53,150	-35,080	Axe	
118	03/07/2015	06:05:51	52,840	-35,080	Axe	CGFZ
119	03/07/2015	08:38:30	52,745	-35,080	Axe	CGFZ
120	03/07/2015	10:59:34	52,730	-35,079	Axe	CGFZ 3 Deep-Arvor
121	03/07/2015	14:35:00	52,701	-35,080	Axe	CGFZ VMP
122	03/07/2015	18:33:09	52,664	-35,080	Axe	CGFZ SVP
123	03/07/2015	21:40:43	52,631	-35,080	Axe	CGFZ
124	04/07/2015	00:35:23	52,449	-35,079	Axe	
125	04/07/2015	04:10:19	52,350	-35,080	Axe	VMP
126	04/07/2015	08:07:49	52,260	-35,080	Axe	
127	04/07/2015	13:16:55	51,900	-35,080	Axe	VMP
128	04/07/2015	18:15:09	51,550	-35,081	Axe	
129	04/07/2015	23:51:13	51,060	-35,080	Axe	VMP
130	05/07/2015	05:40:18	50,750	-35,080	Axe	VMP
131	05/07/2015	11:40:55	50,348	-35,079	Axe	
132	05/07/2015	16:51:45	49,950	-35,080	Axe	

B Résumé en Français

B.1 Objectifs de la thèse

La dorsale de Reykjanes est une structure topographique majeure de l'océan Atlantique Nord qui s'étend au sud-ouest de l'Islande jusqu'à 55°N, puis à longitude constante jusqu'à la zone de fracture de Charlie Gibbs (CGFZ) à 52.5°N (Figure 1.2). Le sommet de la dorsale de Reykjanes est à environ 300 m au nord de 63°N, puis plonge jusqu'à plus de 3000 m à la CGFZ. Située au cœur du gyre subpolaire, la dorsale de Reykjanes, et les zones de fracture qui la composent, influencent fortement la circulation du gyre (Bower et al., 2002) et les masses d'eau associées (Thierry et al., 2008). En effet, la Figure 1.2 montre que le gyre subpolaire suit une circulation anticyclonique autour de la dorsale de Reykjanes. Située à l'entrée de la mer d'Irminger et de la mer du Labrador, la dorsale de Reykjanes est également une porte d'entrée vers les zones de convection profonde. Desbruyères et al. (2013) ont montré que 50% de la densification associée à la circulation méridienne de retournement se produit à proximité de la dorsale de Reykjanes, ce qui renforce l'importance de cette région dans le système climatique.

Du Groenland au Portugal, la section hydrographique historique d'Ovide (Figure 1.2) fournit une vue moyenne des courants océaniques et des masses d'eau associées le long de la dorsale de Reykjanes, de la surface jusqu'au fond. L'asymétrie des structures et des propriétés de part et d'autre de la dorsale de Reykjanes montre que celle-ci agit comme une barrière entre le bassin d'Islande et la mer d'Irminger en limitant les échanges de volume et de transport de masse d'eau (Figure 1.3 et Figure 1.8). En effet, le courant d'Irminger (IC), situé à l'ouest de la dorsale de Reykjanes, est relativement barocline, tandis que le « East Reykjanes Ridge Current » (ERRC), situé à l'est de la dorsale, est un courant étroit et davantage barotrope (Figure 1.8). En ce qui concerne les masses d'eau, le cœur de l'eau modale subpolaire n'est pas symétrique par rapport à l'axe de la dorsale de Reykjanes, mais est situé sur son flanc est (Figure 1.3). Plus profondément, l'eau de la mer du Labrador (LSW) est observée dans les couches intermédiaires du bassin d'Islande et de la mer d'Irminger, mais n'est pas observée au sommet de la dorsale de Reykjanes. Le long de la section Ovide, les eaux de pente islandaises (ISW) sont situées dans les couches intermédiaires au-dessus de la dorsale de Reykjanes. La

topographie de la dorsale empêche donc la propagation de la LSW entre les deux bassins, et influence la formation de l'ISW. Enfin, l'eau de débordement Islande-Écosse (ISOW) est observé sur la topographie de la dorsale de Reykjanes, mais est plus salé (34,96 - 35) et plus profond (inférieures à 1200 m) du côté est de la dorsale de Reykjanes que du côté ouest (salinité de 34.94 – 34.96 sous 1000-m de profondeur). En traversant la dorsale de Reykjanes, les masses d'eau les plus profondes doivent interagir avec la bathymétrie, de sorte que leurs propriétés hydrologiques évoluent.

Bien que ces observations soulignent clairement le rôle de la dorsale de Reykjanes sur la circulation du gyre subpolaire, la structure des écoulements à travers et le long de la dorsale est encore insuffisamment documentée, et son impact sur l'écoulement des masses d'eau est peu connu. La distribution asymétrique des courants et des propriétés de part et d'autre de la dorsale de Reykjanes n'a donc pas encore été expliquée (Figures 1.3 et 1.8), de même que leur lien avec les masses d'eau du bassin d'Islande.

Dans le cadre du projet RREX, l'objectif de cette thèse est de documenter la circulation synoptique autour et au-dessus de la dorsale de Reykjanes et de mieux comprendre et quantifier la transformation des masses d'eau au voisinage de la dorsale. L'objectif final de cette thèse est de créer un schéma détaillé et de quantifier la circulation océanique en 3-D au voisinage de la dorsale de Reykjanes, de la surface jusqu'au fond. Essentiellement à partir de données hydrographiques et de vitesses enregistrées lors de la campagne RREX2015 en Juin – Juillet 2015, mais également à partir d'autres outils décrits au chapitre 2, nous abordons des questions importantes qui restent sans réponse. Les cinq questions posées par cette thèse sont:

Q1: Quelle est l'intensité et quelle est la structure de la branche ouest du gyre subpolaire à travers la dorsale de Reykjanes?

En utilisant principalement la section qui longe le sommet de la dorsale de Reykjanes en Juin – Juillet 2015, nous avons décrit l'effet de la bathymétrie sur la circulation du gyre subpolaire. Les voies privilégiées à travers la dorsale de Reykjanes sont identifiées par l'intensification de l'écoulement à travers la dorsale. La structure verticale de cet écoulement a également été discutée en lien avec la profondeur de la dorsale. Cette question fait partie du projet RREX O1.3 et est traitée au chapitre 3.

Q2: Est-ce que la distribution des masses d'eau le long de la dorsale de Reykjanes est liée à la circulation à grande échelle du gyre subpolaire et / ou à d'autres processus locaux?

En utilisant principalement la section qui longe le sommet de la dorsale de Reykjanes en Juin – Juillet 2015, nous avons quantifié la transformation des masses d'eau au-dessus de la dorsale et documenté leurs liens avec la circulation cyclonique du courant Nord-Atlantique (NAC) en amont. Liée à cette circulation à grande échelle, une attention particulière a été accordée à la densification des eaux modales subpolaires au-dessus de la dorsale de Reykjanes, ce qui constitue une première étape de densification en amont de celle observée en mer d'Irminger. De plus, nous avons montré que les processus à petite échelle, tels que les mélanges isopycnal et diapycnal, ainsi que les fractures locales dans la bathymétrie de la dorsale, façonnent la distribution des masses d'eau au voisinage de la dorsale de Reykjanes. Cette question fait partie du projet RREX O1.3 et est traitée au chapitre 3.

Q3: Plus précisément, comment la bathymétrie de la dorsale de Reykjanes influence-t-elle l'ISOW? Est-ce que l'ISOW est contrainte de s'écouler uniquement à travers la BFZ et la CGFZ pour rejoindre la mer d'Irminger, ou existe-t-il d'autres chemins empruntés par l'ISOW?

En utilisant principalement la section qui longe le sommet de la dorsale de Reykjanes en Juin – Juillet 2015, nous avons dans un premier temps identifié et quantifié toutes les chemins empruntés par l'ISOW à travers la dorsale de Reykjanes. Ces questions font partie du projet RREX O1.2 et sont abordées dans le chapitre 3. Bien que la BFZ ait déjà été identifiée comme étant un chemin privilégié de l'ISOW à travers la dorsale de Reykjanes, on ignore comment cette étroite bathymétrie affecte la circulation de l'ISOW. Comment évoluent les propriétés de l'ISOW entre l'entrée et la sortie de la zone de fracture? En combinant des sections hydrographiques hautes-résolutions obtenues dans la BFZ au cours de trois campagnes (RREX2015, RREX2017 et OVIDE2018), ainsi que des flotteurs Deep-Argo déployés dans la BFZ, nous avons analysé la circulation et la dynamique profondes, ainsi que le rôle du mélange dans l'évolution des propriétés de l'ISOW. Cette question fait partie du projet RREX O1.2 et est traitée au chapitre 5.

Q4: Comment l'ERRC interagit-il avec le NAC dans le bassin de l'Islande, et quelles sont ses connexions avec l'écoulement qui traverse la dorsale de Reykjanes?

En utilisant principalement les trois sections hydrographiques perpendiculaires au sommet de la dorsale de Reykjanes en Juin – Juillet 2015, nous avons expliqué les mécanismes de formation de l'ERRC tels qu'il a été observé le long de la section Ovide par Daniault et al. (2016). Nous avons également analysé l'évolution de ses structures horizontales et verticales le long de la dorsale de Reykjanes. En terme de masses d'eau, nous avons documenté l'évolution des propriétés des masses d'eau et, plus important encore, nous avons relié ces évolutions à la répartition des masses d'eau en amont dans le bassin d'Islande, et en aval sur la dorsale de Reykjanes. Dans cette thèse, nous examinons donc l'origine et le devenir des masses d'eau au voisinage de la dorsale de Reykjanes. Cette question fait partie du projet RREX O1.1 et est traitée au chapitre 4.

Q5: Est-ce que l'IC est affecté par des apports provenant du gyre d'Irminger et du bassin d'Islande?

En utilisant principalement les trois sections hydrographiques perpendiculaires au sommet de la dorsale de Reykjanes en Juin – Juillet 2015, nous avons étudié l'évolution, depuis la surface jusqu'au fond, des structures et propriétés horizontales et verticales du IC. De la CGFZ à l'Islande, nous mettons en évidence les connexions entre le IC et la branche est du gyre d'Irminger, ainsi qu'avec l'écoulement qui traverse la dorsale de Reykjanes vers l'ouest, et nous montrons que ces connexions affectent différemment la circulation des deux branches du IC en fonction de la densité. Des schémas de circulation à grande échelle au voisinage de la dorsale de Reykjanes sont créés pour chaque masse d'eau identifiée le long de la dorsale. Cette question fait partie du projet RREX O1.1 et est traitée au chapitre 4.

B.2 Données et méthodes

Pour répondre à ces questions, les vitesses et transports géostrophiques ont été calculés à travers les sections hydrographiques réalisées lors des deux campagnes océanographiques du projet RREX (RREX2105 et RREX2017), et lors d'une troisième réalisée en 2018 par le

programme Ovide (OVIDE2018). En effet, les vitesses geostrophiques nous ont permis de quantifier pour la première fois les échanges de volumes et de masses d'eau au-dessus de la dorsale de Reykjanes, et de mieux comprendre le rôle de la dorsale dans la transformation des masses d'eau du gyre subpolaire. Pour estimer des transports géostrophiques précis, un traitement détaillé des mesures de vitesse a été nécessaire, ce qui nous a permis d'apporter des améliorations dans traitement des mesures de bateau S-ADCP (Shipboard-Acoustic Doppler Current Profiler). Une difficulté majeure a été de calculer des vitesses géostrophiques le long de la bathymétrie de la dorsale qui s'approfondit vers le sud et est composée de zones de fracture. Dans les triangles de fond créés par la bathymétrie, nous avons utilisé une extrapolation polynomiale du second ordre. Afin de minimiser l'impact des mouvements ageostrophiques, nous avons ajusté les profils de vitesses géostrophiques à des vitesses S-ADCP filtrées horizontalement et verticalement, sur 2 km × 16 m, en utilisant des filtres de Lanczos dont les valeurs de coupures sont de 1/8 km^{-1} et 1 / 400 m^{-1} respectivement. Enfin, nous avons montré que les transports géostrophiques varient fortement en fonction de la profondeur et de l'épaisseur de la couche de référence absolue que l'on applique, lié à des perturbations agéostrophiques dans les vitesses S-ADCP. De plus, à la BFZ et à la CGFZ, la haute-résolution horizontale des données provoque des mouvements ageostrophiques dans les profils de vitesse géostrophiques. En étudiant les profils S-ADCP et géostrophiques séparément, nous avons choisi d'appliquer la couche de référence absolue L_{ref} = 600 – 1000 m, avec une vitesse de référence absolue moyenne et unique à la BFZ et CGFZ.

B.3 Première estimation directe de transports de volume et de masse d'eau à travers la dorsale de Reykjanes

La dorsale de Reykjanes est une structure topographique majeure de l'océan Atlantique Nord située au sud de l'Islande. Elle influence fortement la circulation du gyre subpolaire. A partir de mesures de vitesses et hydrographiques effectuées le long de la dorsale de Reykjanes depuis l'Islande jusqu'à 50°N lors de la campagne RREX en Juin – Juillet 2015, nous avons calculé les premières estimations directes de cette circulation. Au nord de 53,15°N, la circulation était principalement orientée vers l'ouest, tandis qu'au sud de cette latitude, l'écoulement était principalement orienté vers l'est. Le transport vers l'ouest a été estimé à 21,9 ± 2,5 Sv (Sv = 10 6 m^3 s^{-1}) et représente l'intensité du gyre subpolaire. Cet écoulement a

suivi deux chemins privilégiés à 57°N, près de la BFZ, et à 59 – 62°N. Nous soutenons que ces chemins sont reliés à la branche nord du NAC et au front Subarctique, respectivement, qui ont tous les deux été observés dans la partie sud de la section. En plus de cette circulation horizontale, la distribution des masses d'eau le long de la dorsale de Reykjanes est liée à la bathymétrie et au mélange. En effet, la transformation des masses d'eau dans le bassin d'Islande a conduit à la formation d'eau modale subpolaire faiblement stratifiée (SPMW). Nous expliquons pourquoi la SPMW, qui constitue une large partie de l'écoulement à travers la dorsale de Reykjanes, était plus dense à 57°N qu'à 59 – 62°N. À des densités plus élevées, les eaux intermédiaires (IW) et l'ISW ont chacune contribué davantage au transport vers l'ouest à travers la dorsale de Reykjanes que la somme de la LSW et de l'ISOW.

B.4 Formation et évolution du ERRC et IC

L'étude des structures horizontales et verticales de l'ERRC a montré pour la première fois que ce courant n'a pas de caractéristiques identiques au nord et au sud de la section Ovide. Ce courant, qui s'écoule vers le sud le long du flanc est de la dorsale de Reykjanes, n'est pas un courant continu et barotrope du nord au sud de la dorsale. L'étude de ses caractéristiques hydrologiques a montré que des branches de circulation quitte l'ERRC pour rejoindre la mer d'Irminger à travers la dorsale de Reykjanes dès qu'elles ne sont plus bloquées par la bathymétrie de la dorsale. Ce courant est néanmoins rejoint par des branches du NAC depuis le centre du bassin d'Islande, ce qui compense localement les déperditions d'eau à travers la dorsale, et forme un ERRC très barotrope aux latitudes d'Ovide. Ce courant est donc formé localement par la convergence des flux entrants du NAC en surface et des flux du ERRC bloqués par la dorsale de Reykjanes en profondeur.

De part et d'autre de la dorsale de Reykjanes, le flux d'ERRC qui traverse la dorsale alimente l'IC. Partiellement bloqué par la bathymétrie de la dorsale de Reykjanes, ce flux dépend de la densité des masses d'eau qui le composent, ce qui affecte différemment les couches du IC. De plus, au sud de la section Ovide, les couches de surface et intermédiaire de la branche ouest du IC incorporent également de l'eau du NAC qui rejoint le IC depuis la mer d'Irminger avant de pénétrer dans le bassin d'Islande. Les flux de NAC provenant du bassin d'Islande et de la mer d'Irminger influencent donc différemment les deux branches du IC. Enfin, au nord de la

section Ovide, les couches de surface du IC sont largement détournées vers le centre de la mer d'Irminger, tandis que les couches de fond sont contraintes par la bathymétrie à s'écouler vers le nord le long de la dorsale de Reykjanes à profondeur constante.

B.5 Circulation profonde dans la zone de fracture Bight

Du bassin d'Islande à la mer d'Irminger, les propriétés de l'ISOW changent lorsque celui-ci traverse la dorsale de Reykjanes. Comme la BFZ a été identifiée comme étant un chemin préférentiel de l'ISOW à travers la dorsale, le projet RREX a fourni de nouveaux ensembles de données afin de mieux comprendre l'évolution des propriétés de l'ISOW dans la BFZ. En analysant des sections hydrographiques localisées au seuil est de la BFZ et dans la vallée du rift de la dorsale, nous montrons d'abord que les propriétés dans la couche d'ISOW sont légèrement modifiées dans le rift par mélange vertical et entraînement d'ISOW moins profond et plus chaud. De plus, un flotteur Deep-Arvor montre que la couche d'ISOW suit une circulation cyclonique dans la vallée du rift. En comparant les profils hydrologiques du rift et des bassins ouest, nous montrons ensuite que les écoulements d'ISOW rejoignent la mer d'Irminger en suivant le seuil ouest du rift, puis les murs nord de chaque bassin ouest. Dans les bassins ouest, l'ISOW du bassin d'Islande rencontre de l'ISOW plus dense qui provient de la mer d'Irminger. Dans les bassins ouest, deux flotteurs Deep-Arvor soulignent également le signal d'ISOW moins chaud et moins salé à forte densité que celui observé dans le rift. Enfin, nous notons un rafraîchissement et un refroidissement de la couche d'ISOW entre 2015 et 2017.

Bibliography

Van Aken, H. (2000). *The hydrography of the mid-latitude northeast Atlantic Ocean I: The deep water masses*. *Deep-Sea Research Part I: Oceanographic Research Papers* (Vol. 47). https://doi.org/10.1016/S0967-0637(99)00092-8

Van Aken, H., & De Boer, C. J. (1995). On the synoptic hydrography of intermediate and deep water masses in the Iceland Basin. *Deep-Sea Research Part I*, *42*(2), 165–189. https://doi.org/10.1016/0967-0637(94)00042-Q

Van Aken, H., Femke de Jong, M., & Yashayaev, I. (2011). Decadal and multi-decadal variability of Labrador Sea Water in the north-western North Atlantic Ocean derived from tracer distributions: Heat budget, ventilation, and advection. *Deep-Sea Research Part I: Oceanographic Research Papers*, *58*(5), 505–523. https://doi.org/10.1016/j.dsr.2011.02.008

Álvarez, M., Pérez, F. F., Bryden, H., & Ríos, A. F. (2004). Physical and biogeochemical transports structure in the North Atlantic subpolar gyre. *Journal of Geophysical Research: Oceans*, *109*(C3), C03027. https://doi.org/10.1029/2003JC002015

Amante, C., & Eakins, B. W. (2009). ETOPO1 1 Arc-Minute Global Relief Model: Procedures, Data Sources and Analysis. *NOAA Technical Memorandum NESDIS NGDC-24*. National Geophysical Data Center, NOAA. https://doi.org/10.1594/PANGAEA.769615

Arhan, M. (1990). The North Atlantic Current and Subarctic Intermediate Water. *Journal of Marine Research*, *48*(1), 109–144. https://doi.org/10.1357/002224090784984605

de Boisséson, E. (2010). *Eaux modales subpolaires du Bassin d'Islande: Origine, formation et variabilité*. University of Bretagne Occidentale, Brest, France.

de Boisséson, E., Thierry, V., Mercier, H., & Caniaux, G. (2010). Mixed layer heat budget in

the Iceland Basin from Argo. *Journal of Geophysical Research: Oceans*, *115*(10), C10055. https://doi.org/10.1029/2010JC006283

de Boisséson, E., Thierry, V., Mercier, H., Caniaux, G., & Desbruyères, D. (2012). Origin, formation and variability of the Subpolar Mode Water located over the Reykjanes Ridge. *Journal of Geophysical Research: Oceans*, *117*(C12005). https://doi.org/10.1029/2011JC007519

Böning, C. W., Scheinert, M., Dengg, J., Biastoch, A., & Funk, A. (2006). Decadal variability of subpolar gyre transport and its reverberation in the North Atlantic overturning. *Geophysical Research Letters*, *33*(21), 1–5. https://doi.org/10.1029/2006GL026906

Le Bot, P., Kermabon, C., Lherminier, P., & Gaillard, F. (2011). CASCADE V6.1: Logiciel de validation et de visualisation des mesures ADCP de coque. https://doi.org/http://archimer.ifremer.fr/doc/00342/45285/

Bower, A., & von Appen, W.-J. (2008). Interannual Variability in the Pathways of the North Atlantic Current over the Mid-Atlantic Ridge and the Impact of Topography. *Journal of Physical Oceanography*, *38*(1), 104–120. https://doi.org/10.1175/2007JPO3686.1

Bower, A., & Furey, H. (2017). Iceland-Scotland Overflow Water transport variability through the Charlie-Gibbs Fracture Zone and the impact of the North Atlantic Current. *Journal of Geophysical Research: Oceans*, *122*(9), 6989–7012. https://doi.org/10.1002/2017JC012698

Bower, A., Le Cann, B., Rossby, T., Zenk, W., Gould, J., Speer, K., et al. (2002). Directly measured mid-depth circulation in the northeastern North Atlantic Ocean. *Nature*, *419*(6907), 603–607. https://doi.org/10.1038/nature01078

Brambilla, E., & Talley, L. D. (2008). Subpolar mode water in the northeastern Atlantic: 1. Averaged properties and mean circulation. *Journal of Geophysical Research: Oceans*, *113*(4), 1–18. https://doi.org/10.1029/2006JC004062

Branellec, P., & Thierry, V. (2016). RREX 2015. CTD-02 Data report. *ODE/LOPS/16-26*. https://doi.org/http://doi.org/10.13155/47156

Breckenfelder, T., Rhein, M., Roessler, A., Böning, C. W., Biastoch, A., Behrens, E., & Mertens, C. (2017). Flow paths and variability of the North Atlantic Current: A

comparison of observations and a high-resolution model. *Journal of Geophysical Research: Oceans*, *122*(4), 2686–2708. https://doi.org/10.1002/2016JC012444

Cabanes, C., Thierry, V., & Lagadec, C. (2016). Improvement of bias detection in Argo float conductivity sensors and its application in the North Atlantic. *Deep-Sea Research Part I: Oceanographic Research Papers*, *114*, 128–136. https://doi.org/10.1016/j.dsr.2016.05.007

Cabanes, C., Racapé, V., & Thierry, V. (2018). Delayed mode analysis of Deep Avor Floats. *SO. ARGO – LOPS Report N°LOPS/18-03*. https://doi.org/http://archimer.ifremer.fr/doc/00443/55464/

Chafik, L., Rossby, T., & Schrum, C. (2014). On the spatial structure and temporal variability of poleward transport between Scotland and Greenland. *Journal of Geophysical Research: Oceans*, *119*(2), 824–841. https://doi.org/10.1002/2013JC009287

Childers, K., Flagg, C. N., Rossby, T., & Schrum, C. (2015). Directly measured currents and estimated transport pathways of Atlantic Water between 59.5 8 N and the Iceland Faroes Scotland Ridge. *Tellus*, *67*(28067), 1–9. https://doi.org/10.3402/tellusa.v67.28067

Cuny, J., Rhines, P. B., Niiler, P. P., & Bacon, S. (2002). Labrador Sea Boundary Currents and the Fate of the Irminger Sea Water. *Journal of Physical Oceanography*, *32*(2), 627–647. https://doi.org/10.1175/1520-0485(2002)032%3C0627:lsbcat%3E2.0.co;2

Daniault, N., Mercier, H., Lherminier, P., Sarafanov, A., Falina, A., Zunino, P., et al. (2016). The northern North Atlantic Ocean mean circulation in the early 21st century. *Progress in Oceanography*, *146*(June), 142–158. https://doi.org/10.1016/j.pocean.2016.06.007

Dee, D. P., Uppala, S. M., Simmons, A. J., Berrisford, P., Poli, P., Kobayashi, S., et al. (2011). The ERA-Interim reanalysis: Configuration and performance of the data assimilation system. *Quarterly Journal of the Royal Meteorological Society*, *137*(656), 553–597. https://doi.org/10.1002/qj.828

Delworth, T. L., Zhang, R., & Mann, M. E. (2007). Decadal to centennial variability of the Atlantic from observations and models. In *Geophysical Monograph Series* (Vol. 173, pp. 131–148). https://doi.org/10.1029/173GM10

Desbruyères, D., Thierry, V., & Mercier, H. (2013). Simulated decadal variability of the

meridional overturning circulation across the A25-Ovide section. *Journal of Geophysical Research: Oceans*, *118*(1), 462–475. https://doi.org/10.1029/2012JC008342

Dickson, B., Yashayaev, I., Meincke, J., Turrell, B., Dye, S., & Holfort, J. (2002). Rapid freshening of the deep North Atrlantic Ocean over the ast four decades. *Nature*, *416*, 832–837. Retrieved from http://dx.doi.org/10.1038/416832a

Dickson, R. R., Meincke, J., Malmberg, S.-A., & Lee, A. (1988). The "great salinity anomaly" in the Northern North Atlantic 1968-1982. *Progress in Oceanography*, *20*(2), 103–151. https://doi.org/10.1016/0079-6611(88)90049-3

Egbert, G. D., & Erofeeva, S. Y. (2002). Efficient inverse modeling of barotropic ocean tides. *Journal of Atmospheric and Oceanic Technology*, *19*(2), 183–204. https://doi.org/10.1175/1520-0426(2002)019<0183:EIMOBO>2.0.CO;2

Eldevik, T., Nilsen, J. E. Ø., Iovino, D., Anders Olsson, K., Sandø, A. B., & Drange, H. (2009). Observed sources and variability of Nordic seas overflow. *Nature Geoscience*, *2*(6), 406–410. https://doi.org/10.1038/ngeo518

Fan, X., Send, U., Testor, P., Karstensen, J., & Lherminier, P. (2013). Observations of Irminger Sea Anticyclonic Eddies. *Journal of Physical Oceanography*, *43*(4), 805–823. https://doi.org/10.1175/JPO-D-11-0155.1

Ferron, B., Mercier, H., Speer, K., Gargett, A., & Polzin, K. (1998). Mixing in the Romanche Fracture Zone. *Journal of Physical Oceanography*, *28*(10), 1929–1945. https://doi.org/10.1175/1520-0485(1998)028<1929:MITRFZ>2.0.CO;2

Firing, E., & Hummon, J. M. (2010). Shipboard Adcp Measurements. *Earth Science*, *14*, 1–11. Retrieved from https://www.go-ship.org/Manual/Firing_SADCP.pdf

Flatau, M. K., Talley, L., & Niiler, P. P. (2003). The North Atlantic Oscillation, surface current velocities, and SST changes in the subpolar North Atlantic. *Journal of Climate*, *16*(14), 2355–2369. https://doi.org/10.1175/2787.1

Ganachaud, A. (1999). *Large scale oceanic circulation and fluxes of freshwater, heat, nutrients and oxygen*. Massachusetts Institute of technology-Woods Hole Oceanographic Institution, Cambrige MA02139, USA.

Ganachaud, A. (2003). Error budget of inverse box models: The North Atlantic. *Journal of*

Atmospheric and Oceanic Technology, *20*(11), 1641–1655. https://doi.org/10.1175/1520-0426(2003)020<1641:EBOIBM>2.0.CO;2

García-Ibáñez, M. I., Pardo, P. C., Carracedo, L. I., Mercier, H., Lherminier, P., Ríos, A. F., & Pérez, F. F. (2015). Structure, transports and transformations of the water masses in the Atlantic Subpolar Gyre. *Progress in Oceanography*, *135*, 18–36. https://doi.org/10.1016/j.pocean.2015.03.009

Gourcuff, C., Lherminier, P., Mercier, H., & Le Traon, P. Y. (2011). Altimetry combined with hydrography for ocean transport estimation. *Journal of Atmospheric and Oceanic Technology*, *28*(10), 1324–1337. https://doi.org/10.1175/2011JTECHO818.1

Grist, J. P., Josey, S. A., Jacobs, Z. L., Marsh, R., Sinha, B., & Van Sebille, E. (2016). Extreme air-sea interaction over the North Atlantic subpolar gyre during the winter of 2013--2014 and its sub-surface legacy. *Climate Dynamics*, *46*(11), 4027–4045. https://doi.org/10.1007/s00382-015-2819-3

Hakkinen, S., & Rhines, P. (2004). Decline of Subpolar North Atlantic Circulation During the 1990s. *Science*, *304*(5670), 555–559. https://doi.org/10.1126/science.1094917

Harvey, J., & Arhan, M. (1988). The Water Masses of the Central North Atlantic in 1983—84. *Journal of Physical Oceanography*. https://doi.org/10.1175/1520-0485(1988)018<1855:TWMOTC>2.0.CO;2

Heezen, B. C., Bunce, E. T., Hersey, J. B., & Tharp, M. (1964). Chain and romanche fracture zones. *Deep-Sea Research and Oceanographic Abstracts*, *11*(1), 11–33. https://doi.org/10.1016/0011-7471(64)91079-4

Hogg, N., Biscaye, P., Gardner, W., & Schmitz, W. J. (1982). On the transport and modification of Antarctic Bottom Water in the Vema Channel. *Journal of Marine Research*, *40*, *suppl.*, 231–263.

Holliday, N. P., Cunningham, S. A., Johnson, C., Gary, S. F., Griffiths, C., Read, J. F., & Sherwin, T. (2015). Multidecadal variability of potential temperature, salinity, and transport in the eastern subpolar North Atlantic. *Journal of Geophysical Research: Oceans*, *120*, 1–23. https://doi.org/10.1002/2015JC010762.Received

Holliday, P. N., Pollard, R. T., Read, J. F., & Leach, H. (2000). Water mass properties and

fluxes in the Rockall Trough, 1975-1998. *Deep-Sea Research Part I: Oceanographic Research Papers*, *47*(7), 1303–1332. https://doi.org/10.1016/S0967-0637(99)00109-0

Intergovernmental Panel on Climate Change (Ed.). (2013). *Climate Change 2013 - The Physical Science Basis*. Cambridge: Cambridge University Press. https://doi.org/10.1017/CBO9781107415324

Iselin, C. (1936). The influence of the Mediterranean outflow at mid-depths in the Sargasso Sea. *Transactions, American Geophysical Union*, *17*(1), 219. https://doi.org/10.1029/TR017i001p00219

Jakobsen, P. K., Ribergaard, M. H., Quadfasel, D., Schmith, T., & Hughes, C. W. (2003). Near-surface circulation in the northern North Atlantic as inferred from Lagrangian drifters: Variability from the mesoscale to interannual. *Journal of Geophysical Research*, *108*(C8), 3251. https://doi.org/10.1029/2002JC001554

de Jong, M. F., Oltmanns, M., Karstensen, J., & de Steur, L. (2018). Deep Convection in the Irminger Sea Observed with a Dense Mooring Array. *Oceanography*, *31*(1), 50–59. https://doi.org/10.5670/oceanog.2018.109

Joyce, T. M., Hernández-Guerra, A., & Smethie, W. M. (2001). Zonal circulation in the NW Atlantic and Caribbean from a meridional World Ocean Circulation Experiment hydrographic section at 66°W. *Journal of Geophysical Research: Oceans*, *106*(C10), 22095–22113. https://doi.org/10.1029/2000JC000268

Kalnay, E., Kanamitsu, M., Kistler, R., Collins, W., Deaven, D., Gandin, L., et al. (1996). The NCEP/NCAR 40-year reanalysis project. *Bulletin of the American Meteorological Society*. https://doi.org/10.1175/1520-0477(1996)077<0437:TNYRP>2.0.CO;2

Kanzow, T., & Zenk, W. (2014). Structure and transport of the Iceland Scotland Overflow plume along the Reykjanes Ridge in the Iceland Basin. *Deep-Sea Research Part I: Oceanographic Research Papers*, *86*, 82–93. https://doi.org/10.1016/j.dsr.2013.11.003

King, B. A., & Cooper, E. B. (1993). Comparison of ship's heading determined from an array of GPS antennas with heading from conventional gyrocompass measurements. *Deep-Sea Research Part I*, *40*(11–12), 2207–2216. https://doi.org/10.1016/0967-0637(93)90099-O

Knight, J. R., Allan, R. J., Folland, C. K., Vellinga, M., & Mann, M. E. (2005). A signature of

persistent natural thermohaline circulation cycles in observed climate. *Geophysical Research Letters*, *32*(20), 1–4. https://doi.org/10.1029/2005GL024233

Knight, J. R., Folland, C. K., & Scaife, A. A. (2006). Climate impacts of the Atlantic Multidecadal Oscillation. *Geophysical Research Letters*, *33*(17), L17706. https://doi.org/10.1029/2006GL026242

Knutsen, Ø., Svendsen, H., Østerhus, S., Rossby, T., & Hansen, B. (2005). Direct measurements of the mean flow and eddy kinetic energy structure of the upper ocean circulation in the NE Atlantic. *Geophysical Research Letters*, *32*(14), n/a-n/a. https://doi.org/10.1029/2005GL023615

Krauss, W. (1995). Currents and mixing in the Irminger Sea and in the Iceland Basin. *Journal of Geophysical Research*, *100*(C6), 10851. https://doi.org/10.1029/95JC00423

Lankhorst, M., & Zenk, W. (2006). Lagrangian Observations of the Middepth and Deep Velocity Fields of the Northeastern Atlantic Ocean. *Journal of Physical Oceanography*, *36*(1), 43–63. https://doi.org/10.1175/JPO2869.1

Lavender, K. L., Davis, R. E., & Owens, W. B. (2000). Mid-depth recirculation observed in the interior Labrador and Irminger seas by direct velocity measurements. *Nature*, *407*(6800), 66–69. https://doi.org/10.1038/35024048

Lavender, K. L., Brechner Owens, W., & Davis, R. E. (2005). The mid-depth circulation of the subpolar North Atlantic Ocean as measured by subsurface floats. *Deep-Sea Research Part I: Oceanographic Research Papers*, *52*(5), 767–785. https://doi.org/10.1016/j.dsr.2004.12.007

De Lavergne, C., Madec, G., Roquet, F., Holmes, R. M., & McDougall, T. J. (2017). Abyssal ocean overturning shaped by seafloor distribution. *Nature*, *551*(7679), 181–186. https://doi.org/10.1038/nature24472

Lazarevich, P., Rossby, T., & McNeil, C. (2004). Oxygen variability in the near-surface waters of the northern North Atlantic: Observations and a model. *Journal of Marine Research*, *62*, 663–683 ST–Oxygen variability in the near–surfa. https://doi.org/10.1357/0022240042387547

Lherminier, P., Mercier, H., Gourcuff, C., Alvarez, M., Bacon, S., & Kermabon, C. (2007).

Transports across the 2002 Greenland-Portugal Ovide section and comparison with 1997. *Journal of Geophysical Research: Oceans*, *112*(7), C07003. https://doi.org/10.1029/2006JC003716

Lherminier, P., Mercier, H., Huck, T., Gourcuff, C., Perez, F. F., Morin, P., et al. (2010). The Atlantic Meridional Overturning Circulation and the subpolar gyre observed at the A25-OVIDE section in June 2002 and 2004. *Deep-Sea Research Part I: Oceanographic Research Papers*, *57*(11), 1374–1391. https://doi.org/10.1016/j.dsr.2010.07.009

Lohmann, K., Drange, H., & Bentsen, M. (2009). A possible mechanism for the strong weakening of the North Atlantic subpolar gyre in the mid-1990s. *Geophysical Research Letters*, *36*(15), 2–6. https://doi.org/10.1029/2009GL039166

Lozier, M. S. (2010). Deconstructing the conveyor belt. *Science*, *328*(5985), 1507–1511. https://doi.org/10.1126/science.1189250

Lozier, M. S., Bacon, S., Bower, A. S., Cunningham, S. A., De Jong, M. F., De Steur, L., et al. (2017). Overturning in the Subpolar north Atlantic program: A new international ocean observing system. *Bulletin of the American Meteorological Society*, *98*(4), 737–752. https://doi.org/10.1175/BAMS-D-16-0057.1

McCartney, M. (1992). Recirculating components to the deep boundary current of the northeern North Atlantic. *Progress in Oceanography*, *29*(4), 283–383. https://doi.org/10.1016/0079-6611(92)90006-L

Mercier, H., & Morin, P. (1997). Hydrography of the Romanche and Chain Fracture Zones. *Journal of Geophysical Research: Oceans*, *102*(C5), 10373–10389. https://doi.org/10.1029/97JC00229

Mercier, H., Speer, K. G., & Honnorez, J. (1994). Flow pathways of bottom water through the Romanche and chain fracture zones. *Deep-Sea Research Part I*, *41*(10), 1457–1477. https://doi.org/10.1016/0967-0637(94)90055-8

Mercier, H., Lherminier, P., Sarafanov, A., Gaillard, F., Daniault, N., Desbruyères, D., et al. (2015). Variability of the meridional overturning circulation at the Greenland-Portugal OVIDE section from 1993 to 2010. *Progress in Oceanography*, *132*, 250–261. https://doi.org/10.1016/j.pocean.2013.11.001

Myers, P. G., Josey, S. A., Wheler, B., & Kulan, N. (2007). Interdecadal variability in Labrador Sea precipitation minus evaporation and salinity. *Progress in Oceanography*, *73*(3–4), 341–357. https://doi.org/10.1016/j.pocean.2006.06.003

Ollitrault, M., & Colin de Verdière, A. (2014). The Ocean General Circulation near 1000-m Depth. *Journal of Physical Oceanography*, *44*(1), 384–409. https://doi.org/10.1175/JPO-D-13-030.1

Otto, L., & Van Aken, H. M. (1996). Surface circulation in the northeast Atlantic as observed with drifters. *Deep-Sea Research Part I: Oceanographic Research Papers*, *43*(4), 467–499. https://doi.org/10.1016/0967-0637(96)00017-9

Penduff, T., Le Sommer, J., Barnier, B., Treguier, A.-M., Molines, J.-M., & Madec, G. (2007). Influence of numerical schemes on current-topography interactions in 1/4° global ocean simulations. *Ocean Science*, *3*(4), 509–524. https://doi.org/10.5194/os-3-509-2007

Petit, T., Mercier, H., & Thierry, V. (2018b). First direct estimates of volume and water mass transports across the Reykjanes Ridge. *Journal of Geophysical Research: Oceans*, 123. https://doi.org/10.1029/2018JC013999

Petit, T., Thierry, V., & Mercier, H. (2018a). RREX 2015. S-ADCP data processing report. *LOPS/18-01 (March 2018)*. https://doi.org/http://doi.org/10.13155/53471

Pickart, R. S., Straneo, F., & Moore, G. W. K. (2003). Is Labrador Sea Water formed in the Irminger basin? *Deep-Sea Research Part I: Oceanographic Research Papers*, *50*(1), 23–52. https://doi.org/10.1016/S0967-0637(02)00134-6

Piron, A., Thierry, V., Mercier, H., & Caniaux, G. (2016). Argo float observations of basin-scale deep convection in the Irminger sea during winter 2011–2012. *Deep-Sea Research Part I: Oceanographic Research Papers*, *109*, 76–90. https://doi.org/10.1016/j.dsr.2015.12.012

Piron, A., Thierry, V., Mercier, H., & Caniaux, G. (2017). Gyre-scale deep convection in the subpolar North Atlantic Ocean during winter 2014–2015. *Geophysical Research Letters*, *44*(3), 1439–1447. https://doi.org/10.1002/2016GL071895

Pollard, R. T., Read, J. F., Holliday, N. P., & Leach, H. (2004). Water masses and circulation pathways through the Iceland basin during Vivaldi 1996. *Journal of Geophysical*

Research C: Oceans, *109*(4), 1–10. https://doi.org/10.1029/2003JC002067

Rattan, S., Myers, P. G., Treguier, A. M., Theetten, S., Biastoch, A., & Böning, C. (2010). Towards an understanding of Labrador Sea salinity drift in eddy-permitting simulations. *Ocean Modelling*, *35*(1–2), 77–88. https://doi.org/10.1016/j.ocemod.2010.06.007

Read, J. F. (2001). CONVEX-91: Water masses and circulation of the Northeast Atlantic subpolar gyre. *Progress in Oceanography*, *48*(4), 461–510. https://doi.org/10.1016/S0079-6611(01)00011-8

Le Reste, S., Dutreuil, V., André, X., Thierry, V., Renaut, C., Le Traon, P. Y., & Maze, G. (2016). "Deep-Arvor": A new profiling float to extend the argo observations down to 4000-m depth. *Journal of Atmospheric and Oceanic Technology*, *33*(5), 1039–1055. https://doi.org/10.1175/JTECH-D-15-0214.1

Reverdin, G., Niiler, P. P., & Valdimarsson, H. (2003). North Atlantic Ocean surface currents. *Journal of Geophysical Research*, *108*(C1), 3002. https://doi.org/10.1029/2001JC001020

Rhein, M., Fischer, J., Smethie, W. M., Smythe-Wright, D., Weiss, R. F., Mertens, C., et al. (2002). Labrador Sea Water: Pathways, CFC Inventory, and Formation Rates. *Journal of Physical Oceanography*, *32*(2), 648–665. https://doi.org/10.1175/1520-0485(2002)032<0648:LSWPCI>2.0.CO;2

Robson, J., Sutton, R., Lohmann, K., Smith, D., & Palmer, M. D. (2012). Causes of the Rapid Warming of the North Atlantic Ocean in the Mid-1990s. *Journal of Climate*, *25*(12), 4116–4134. https://doi.org/10.1175/JCLI-D-11-00443.1

Roessler, A., Rhein, M., Kieke, D., & Mertens, C. (2015). Long-term observations of North Atlantic Current transport at the gateway western and eastern Atlantic. *Journal of Geophysical Research: Oceans*, *120*(6), 4003–4027. https://doi.org/10.1002/2014JC010662

Rossby, T., Reverdin, G., Chafik, L., & Søiland, H. (2017). A direct estimate of poleward volume, heat, and freshwater fluxes at 59.5°N between Greenland and Scotland. *Journal of Geophysical Research: Oceans*, *122*(7), 5870–5887. https://doi.org/10.1002/2017JC012835

Sarafanov, A., Falina, A., Mercier, H., Sokov, A., Lherminier, P., Gourcuff, C., et al. (2012).

Mean full-depth summer circulation and transports at the northern periphery of the Atlantic Ocean in the 2000s. *Journal of Geophysical Research: Oceans*, *117*(1), C01014. https://doi.org/10.1029/2011JC007572

Saunders, P. M. (1994). The flux of overflow water through the Charlie-Gibbs Fracture Zone. *Journal of Geophysical Research*, *99*(C6), 12343. https://doi.org/10.1029/94JC00527

Schott, F., Stramma, L., & Fischer, J. (1999). Interaction of the North Atlantic Current with the deep Charlie Gibbs Fracture Zone throughflow. *Geophysical Research Letters*, *26*(3), 369–372. https://doi.org/10.1029/1998GL900223

Sherwin, T. J., & Turrell, W. R. (2005). Mixing and advection of a cold water cascade over the Wyville Thomson Ridge. *Deep-Sea Research Part I: Oceanographic Research Papers*, *52*(8), 1392–1413. https://doi.org/10.1016/j.dsr.2005.03.002

Smith, D. M., Eade, R., Dunstone, N. J., Fereday, D., Murphy, J. M., Pohlmann, H., & Scaife, A. A. (2010). Skilful multi-year predictions of Atlantic hurricane frequency. *Nature Geoscience*, *3*, 846. Retrieved from http://dx.doi.org/10.1038/ngeo1004

Straneo, F., Pickart, R. S., & Lavender, K. (2003). Spreading of Labrador sea water: An advective-diffusive study based on Lagrangian data. *Deep-Sea Research Part I: Oceanographic Research Papers*, *50*(6), 701–719. https://doi.org/10.1016/S0967-0637(03)00057-8

Sutton, R. T., & Hodson, D. L. R. (2005). Atlantic Ocean Forcing of North American and European Summer Climate. *Science*, *309*(5731), 115–118. https://doi.org/10.1126/science.1109496

Swift, J. H. (1984). The circulation of the Denmark Strait and Iceland-Scotland overflow waters in the North Atlantic. *Deep Sea Research Part A, Oceanographic Research Papers*, *31*(11), 1339–1355. https://doi.org/10.1016/0198-0149(84)90005-0

Sy, A., Rheint, M., Lazier, J. R. N., Koltermann, K. P., Meincke, J., Putzka, A., & Bersch, M. (1997). Surprisingly rapid spreading of newly formed intermediate waters across the North Atlantic Ocean. *Nature*. https://doi.org/10.1038/386675a0

Talley, L. (1999). Mode waters in the subpolar North Atlantic in historical data and during the WOCE period. *International WOCE Newsletter*, (37), 3–6. Retrieved from

http://scholar.google.com/scholar?hl=en&btnG=Search&q=intitle:Mode+waters+in+the+subpolar+North+Atlantic+in+historical+data+and+during+the+WOCE+period#0

Talley, L. D., & McCartney, M. S. (1982). Distribution and Circulation of Labrador Sea Water. *Journal of Physical Oceanography*. https://doi.org/10.1175/1520-0485(1982)012<1189:DACOLS>2.0.CO;2

Thierry, V., de Boisséon, E., & Mercier, H. (2008). Interannual variability of the Subpolar Mode Water properties over the Reykjanes Ridge during 1990-2006. *Journal of Geophysical Research: Oceans*, *113*(4), C04016. https://doi.org/10.1029/2007JC004443

Thierry, V., Mercier, H., Petit, T., Branellec, P., Balem, K., & Lherminier, P. (2018). Reykjanes Ridge Experiment (RREX) dataset. *SEANOE*. https://doi.org/http://doi.org/10.17882/55445

Treguier, A. M., Theetten, S., Chassignet, E. P., Penduff, T., Smith, R., Talley, L., et al. (2005). The North Atlantic Subpolar Gyre in Four High-Resolution Models. *Journal of Physical Oceanography*, *35*(5), 757–774. https://doi.org/10.1175/JPO2720.1

Våge, K., Pickart, R. S., Sarafanov, A., Knutsen, Ø., Mercier, H., Lherminier, P., et al. (2011). The Irminger Gyre: Circulation, convection, and interannual variability. *Deep-Sea Research Part I: Oceanographic Research Papers*, *58*(5), 590–614. https://doi.org/10.1016/j.dsr.2011.03.001

Valdimarsson, H., & Malmberg, S. (1999). Near-surface circulation in Icelandic waters derived from satellite tracked drifters. *Rit Fiskideildar*, *16*, 23–39. Retrieved from papers://f554698c-bc30-43aa-8c0c-c8de8adb48e4/Paper/p1548

Visbeck, M. (2002). Deep velocity profiling using lowered acoustic Doppler current profilers: Bottom track and inverse solutions. *Journal of Atmospheric and Oceanic Technology*, *19*(5), 794–807. https://doi.org/10.1175/1520-0426(2002)019<0794:DVPULA>2.0.CO;2

Xu, X., Schmitz, W. J., Hurlburt, H. E., Hogan, P. J., & Chassignet, E. P. (2010). Transport of Nordic Seas overflow water into and within the Irminger Sea: An eddy-resolving simulation and observations. *Journal of Geophysical Research: Oceans*, *115*(12), C12048. https://doi.org/10.1029/2010JC006351

Xu, X., Bower, A., Furey, H., & Chassignet, E. (2018). Variability of the Iceland-Scotland

overflow water transport through the Charlie-Gibbs Fracture Zone: results from an eddying simulation and observations. *Journal of Geophysical Research: Oceans*, *123*. https://doi.org/10.1029/2018JC013895

Yashayaev, I., & Loder, J. W. (2016). Recurrent replenishment of Labrador Sea Water and associated decadal-scale variability. *Journal of Geophysical Research: Oceans*, *121*(11), 8095–8114. https://doi.org/10.1002/2016JC012046

Yashayaev, I., & Loder, J. W. (2017). Further intensification of deep convection in the Labrador Sea in 2016. *Geophysical Research Letters*, *44*(3), 1429–1438. https://doi.org/10.1002/2016GL071668

Yashayaev, I., Bersch, M., & van Aken, H. M. (2007). Spreading of the Labrador Sea Water to the Irminger and Iceland basins. *Geophysical Research Letters*, *34*(10), 1–8. https://doi.org/10.1029/2006GL028999

Yeager, S., Karspeck, A., Danabasoglu, G., Tribbia, J., & Teng, H. (2012). A Decadal Prediction Case Study: Late Twentieth-Century North Atlantic Ocean Heat Content. *Journal of Climate*, *25*(15), 5173–5189. https://doi.org/10.1175/JCLI-D-11-00595.1

Zhang, R., & Delworth, T. L. (2006). Impact of Atlantic multidecadal oscillations on India/Sahel rainfall and Atlantic hurricanes. *Geophysical Research Letters*, *33*(17), L17712. https://doi.org/10.1029/2006GL026267

Zou, S., Lozier, S., Zenk, W., Bower, A., & Johns, W. (2017). Observed and modeled pathways of the Iceland Scotland Overflow Water in the eastern North Atlantic. *Progress in Oceanography*, *159*, 211–222. https://doi.org/10.1016/j.pocean.2017.10.003

Zunino, P., Lherminier, P., Mercier, H., Daniault, N., García-Ibáñez, M. I., & Pérez, F. F. (2017). The GEOVIDE cruise in May-June 2014 reveals an intense Meridional Overturning Circulation over a cold and fresh subpolar North Atlantic. *Biogeosciences*, *14*(23), 5323–5342. https://doi.org/10.5194/bg-14-5323-2017

Acronyms

AAIW	Antarctic Intermediate Water
ADCP	Acoustic Doppler Current Profiler
AVISO	Archiving, Validation and Interpretation of Satellite Oceanographic
BB	Broad Band
BFZ	Bight Fracture Zone
BT	Bottom Tracking
CASCADE	Chaine Automatisée de Suivi des Courantomètres Acoustiques Doppler Embarqués
CGFZ	Charlie-Gibbs Fracture Zone
CMEMS	Copernicus Marine Environment Monitoring Service
CTD	Conductivity-Temperature-Depth
DCL	Deepest Common Level
DSOW	Denmark Strait Overflow Water
EGIC	East-Greenland Irminger Current

Acronyms

ERRC	East Reykjanes Ridge Current
FFZ	Faraday Fracture Zone
IC	Irminger Current
IG	Irminger Gyre
ISOW	Iceland-Scotland Overflow Water
ISW	Icelandic Slope Water
IW	Intermediate Water
LDW	Lower Deep Water
LNEADW	Lower North East Atlantic Deep Water
LSW	Labrador Sea Water
MADT	Merged-Absolute Dynamic Topography
MAR	Mid-Atlantic Ridge
MFZ	Maxwell Fracture Zone
MOC	Meridional Overturning Circulation
MW	Mediterranean Water
NAC	North-Atlantic Current
NACW	North-Atlantic Central Water
NAO	North-Atlantic Oscillation

NASPG	North-Atlantic SubPolar Gyre
NB	Narrow-Band
NS	North Section
NWC	Northwest Corner
OS	Ovide Section
OVIDE	Observatoire de la variabilité Interannuelle et Décennale en Atlantique Nord
RMS	Root-Mean-Square
RREX	Reykjanes Ridge Experiment
RRMW	Reykjanes Ridge Mode Water
RS	Ridge Section
RT	Rockall Trough
SAF	Sub-Arctic Front
SAIW	Sub-Arctic Intermediate Water
SAW	Sub-Arctic Water
SPG	SubPolar Gyre
SPMW	Subpolar Mode Water
SS	South Section
WT	Water Tracking

UNIVERSITE SCIENCES BRETAGNE DE LA MER LOIRE ET DU LITTORAL

UBO Université de Bretagne Occidentale

Titre : Caractérisation de la circulation autour, au-dessus et à travers (via des zones de fracture) la dorsale de Reykjanes.

Mots clés : gyre subpolaire Nord-Atlantique, bathymétrie, masses d'eau, circulation, observations

Résumé : La dorsale de Reykjanes est une structure topographique majeure de l'océan Atlantique Nord qui s'étend de l'Islande à la zone de fracture de Charlie Gibbs. Située entre le bassin d'Islande et la mer d'Irminger, la dorsale de Reykjanes influence fortement la circulation du gyre subpolaire et est une porte d'entrée vers les zones de convection profondes. Cependant, la circulation et la répartition des masses d'eau à travers la dorsale de Reykjanes n'ont jamais été directement quantifiées, de sorte que la caractérisation de la connexion entre le bassin d'Islande et la mer d'Irminger est encore incomplète. Dans le cadre du projet « Reykjanes Ridge Experiment », nous avons été capables d'analyser la circulation autour, au-dessus et à travers la dorsale de Reykjanes. Essentiellement à partir de sections hydrographiques perpendiculaires et le long de l'axe de la dorsale, l'objectif de cette thèse a été de quantifier et caractériser la circulation 3-D et les propriétés des courants qui longent et traversent la dorsale de Reykjanes. Nous avons commencé par quantifier précisément le transport géostrophique à travers les sections, ce qui a permis d'améliorer le traitement des données S-ADCP. A travers la dorsale de Reykjanes, l'intensité de la branche du gyre subpolaire qui rejoint la mer d'Irminger a été estimée à 21.9 ± 2.5 Sv en Juin – Juillet, avec des intensifications dans la zone de fracture Bight (BFZ) et à 59 – 62°N. Dans la BFZ, les masses d'eau profondes sont influencées par la bathymétrie, de sorte que leurs propriétés hydrologiques se modifient lorsqu'elles traversent la dorsale de Reykjanes. Enfin, la bathymétrie et la circulation horizontale cyclonique du bassin d'Islande contrôlent les courants qui longent la dorsale en bloquant certaines masses d'eau, et donc sont à l'origine de la répartition de ces masses d'eau le long de la dorsale. En plus des masses d'eau du Bassin d'Islande, le Courant d'Irminger comprend également des masses d'eau qui proviennent de la mer d'Irminger.

Title : Characterization of the circulation around, above and across (through fracture zones) the Reykjanes Ridge.

Keywords : North-Atlantic, subpolar gyre, bathymetry, water masses, circulation, observations.

Abstract : The Reykjanes Ridge is a major topographic feature of the North-Atlantic Ocean that extends from Iceland to the Charlie Gibbs Fracture Zone. Located between the Iceland Basin and the Irminger Sea, the Reykjanes Ridge strongly influences the subpolar gyre circulation and is a gate toward the deep convection areas. However, the circulation and distribution across the Reykjanes Ridge has never been directly quantified such that the characterization of the connection between the Iceland Basin and the Irminger Sea is still incomplete. As part of the Reykjanes Ridge Experiment project, we were able to analyze the circulation around, above and across the Reykjanes Ridge. Mainly based on hydrographic sections along and perpendicular to the ridge axis, the aim of this PhD thesis was thus to characterize the 3-D circulation and properties of the flow along and across the Reykjanes Ridge. We started by accurately quantifying geostrophic transports across the sections, which led to improvements in the treatment of S-ADCP data. Acorss the Reykjanes Ridge, the intensity of the wesward branch of the subpolar gyre was estimated at 21.9 ± 2.5 Sv in June – July 2015 with intensifications at the Bight Fracture Zone (BFZ) and at 59 – 62°N. At the BFZ, overflow waters are influenced by the bathymetry such as their hydrological properties evolve as they cross the Reykjanes Ridge. Finally, both the bathymetry and the cyclonic horizontal circulation of the Iceland Basin regulate the evoluton of the along-ridge flows by blocking water masses, and thus shaping the water mass distribution over the Reykjanes Ridge. In addition to waters from the cross-ridge flow, the Irminger Current incorporates waters from the center of the Irminger Sea.